

**An Analytical Theory for the Perturbative Effect of Solar
Radiation Pressure on Natural and Artificial Satellites**

by

Jay W. McMahon

B.S., University of Michigan, 2004

M.S.E, University of Southern California, 2006

A thesis submitted to the
Faculty of the Graduate School of the
University of Colorado in partial fulfillment
of the requirements for the degree of
Doctor of Philosophy
Department of Aerospace Engineering Sciences

2011

This thesis entitled:
An Analytical Theory for the Perturbative Effect of Solar Radiation Pressure on Natural and Artificial
Satellites
written by Jay W. McMahon
has been approved for the Department of Aerospace Engineering Sciences

Daniel J. Scheeres

Hanspeter Schaub

George Born

Date _____

The final copy of this thesis has been examined by the signatories, and we find that both the content and the form meet acceptable presentation standards of scholarly work in the above mentioned discipline.

McMahon, Jay W. (Ph.D., Aerospace Engineering Sciences)

An Analytical Theory for the Perturbative Effect of Solar Radiation Pressure on Natural and Artificial Satellites

Thesis directed by Professor Daniel J. Scheeres

Solar radiation pressure is the largest non-gravitational perturbation for most satellites in the solar system, and can therefore have a significant influence on their orbital dynamics. This work presents a new method for representing the solar radiation pressure force acting on a satellite, and applies this theory to natural and artificial satellites. The solar radiation pressure acceleration is modeled as a Fourier series which depends on the Sun's location in a body-fixed frame; a new set of Fourier coefficients are derived for every latitude of the Sun in this frame, and the series is expanded in terms of the longitude of the Sun. The secular effects due to the solar radiation pressure perturbations are given analytically through the application of averaging theory when the satellite is in a synchronous orbit. This theory is then applied to binary asteroid systems to explain the Binary YORP effect. Long term predictions of the evolution of the near-Earth asteroid 1999 KW4 are discussed under the influence of solar radiation pressure, J_2 , and 3rd body gravitational effects from the Sun. Secular effects are shown to remain when the secondary asteroid becomes non-synchronous due to a librational motion. The theory is also applied to Earth orbiting spacecraft, and is shown to be a valuable tool for improved orbit determination. The Fourier series solar radiation pressure model derived here is shown to give comparable results for orbit determination of the GPS IIR-M satellites as JPL's solar radiation pressure model. The theory is also extended to incorporate the effects of the Earth's shadow analytically. This theory is briefly applied to the evolution of orbital debris to explain the assumptions that are necessary in order to use the cannonball model for debris orbit evolution, as is common in the literature. Finally, the averaging theory methodology is applied to a class of Earth orbiting solar sail spacecraft to show the orbital effects when the sails are made to cone at orbit rates in the local horizontal frame.

Dedication

To my wife, Sarah, for always supporting me and keeping me on task; to my dog, Kona, for always recognizing when I have been working for too long and need to go for a walk; and to my first-born daughter, Maggie Rose, for ensuring that I finish this degree in a timely manner.

Acknowledgements

In some respects, this is the hardest section to write as I would like to adequately express my thanks for everyone that helped me finish this dissertation. None of this work would have happened without Dan Scheere's guidance and support. In fact, I may not have even ended up at CU if Dan hadn't decided to come here at the same time! So many thanks to the best advisor I could have asked for. Next, I'd like to thank my colleagues in the Celestial and Spaceflight Mechanics Laboratory. There are few things more valuable than having good, smart colleagues to bounce ideas off of. In particular, Marcus, Christine, and Seth - it has been three wonderful years of working closely together. The faculty in the Aerospace Engineering Mechanics department is amazing. I have learned, and continue to learn, an enormous amount from them. These lessons, both inside and outside of the classroom, have gone a long way in shaping this dissertation.

My main motivation in life is driven by my family, and as of yesterday (June 7th, 2011) that family has grown due to the birth of my daughter Maggie! Knowing she was on the way helped me complete this dissertation on time. To Sarah, my beautiful, amazing wife - I can't thank you enough for everything that you've done for me over the past three years. There is no doubt in my mind that I would be a total mess without you in my life. My parents, Jim and Kathy - without the examples you set and the sacrifices you made to support me throughout my life, I wouldn't even have the chance to pursue a PhD! Thank you so much. Finally, to my brother and sister, Cory and Gina, and to my many wonderful friends - thank you for supporting me and making my life wonderful to live. Having wonderful distractions like all of you doesn't directly help me get work done, but it does make me a much happier person.

Contents

Chapter

1	Introduction	1
1.1	Orbital Perturbations due to Solar Radiation Pressure	1
1.1.1	SRP Models	6
1.1.2	Natural Bodies	7
1.1.3	Artificial Bodies	9
1.2	Organization and Contributions	11
1.2.1	Contributions	13
1.2.2	Publications	14
2	Solar Radiation Pressure Model	17
2.1	Coordinate Frame Definitions	17
2.2	Solar Radiation Force Representation	23
2.3	Comparison with other Solar Radiation Pressure Models	25
3	Orbit Variational Equations	28
3.1	Dynamical Elements	28
3.2	Keplerian Orbital Elements	32
3.3	Delaunay Elements	34
4	Attitude Dynamics Coupling in the Force Model	35
4.1	Synchronous Rotation	35

4.2	Periodic Rotation	39
4.3	Higher Order Resonances	40
4.4	Non-resonant Rotation	41
5	Averaging Theory	42
5.1	Averaging Methodology	43
5.1.1	Orbit Averaging	43
5.1.2	Offset Due to Periodic Terms	45
5.1.3	Year Averaging	46
5.1.4	Long Term Averaging	51
5.2	Application to a Circular Orbit	52
5.2.1	Circular Orbit Average Equation Derivation	52
5.2.2	Initial Offset Correction	56
5.2.3	Circular Orbit Simulation	58
5.2.4	Averaging the Circular Results Over 1 year	62
5.3	Application to an Elliptical Orbit	63
5.3.1	Orbit Averaged Equations	63
5.3.2	Initial Offset Correction	76
5.3.3	Eccentric Orbit Simulation	76
5.3.4	Averaging Eccentric Equations Over a Year	79
6	Application to Natural Bodies: BYORP	82
6.1	Nominal Predictions	84
6.1.1	Non-dimensionalized BYORP Model	85
6.1.2	BYORP on Doubly Synchronous Binary Systems	85
6.1.3	Secular Evolution of Binary Asteroid Systems	87
6.1.4	Application to Binary System 1999 KW4	97
6.1.5	Discussion of Binary Asteroid Results	114

6.2	Effects of Libration	116
6.2.1	Librational Dynamics	117
6.2.2	Fourier Coefficients for a Librating Secondary	118
6.2.3	Libration Averaging	121
7	Application to Artificial Bodies	126
7.1	Satellite Application Example: GRACE	128
7.1.1	Shadowing	134
7.1.2	Shadow Approach	134
7.1.3	Orbital Effect of the Shadow	135
7.1.4	Penumbra Models	136
7.2	GPS SRP Model	138
7.2.1	JPL Model	139
7.2.2	University of Bern	140
7.2.3	Rotating Frame Coefficients	141
7.3	SRP Estimation for GPS Orbit Determination	145
7.4	Orbital Debris	152
7.4.1	Tumbling Debris at Unique Rates	152
7.4.2	Tumbling Debris with Resonant Rates	154
7.5	Solar Sails	155
7.5.1	System Definition	156
7.5.2	Attitude Motion	157
7.5.3	Orbital Effects	158
7.5.4	Applications	167
7.5.5	Conclusion	169
8	Conclusion and Future Work	173

Bibliography	176
---------------------	-----

Appendix

A Mathematical Relationships	183
A.1 Trigonometric Functions	183
A.2 Fourier Series	184
A.3 Bessel Functions	184

Tables

Table

6.1	Physical properties of the KW4 system. All data is reproduced from [76], except those marked with a * which are from [73], and those marked with a # which are from [92].	105
6.2	These values have either been derived from the previously cited data according to equations in [65], or they were set arbitrarily for the simulation. The vectors are expressed in inertial coordinates.	106
6.3	Drift in mean anomaly and period computed using the current KW4 expansion rate, along with estimation errors for n and \dot{n} over these time spans.	111
6.4	Scaled orbit expansion results for well observed binaries. Binary data including heliocentric orbit semi-major axis (a_s) and eccentricity (e_s), primary and secondary diameters (D_{pri} and D_{sec} respectively), orbit semi-major axis (a) and orbit period (T_{orb}) obtained from [117]. Mass fraction (ν) derived by Eq. (6.96). Semi-major axis growth rate (\dot{a}) for all binaries scaled from KW4 according to Eq. (6.95). Mean anomaly drift calculated from Eq. (6.85). Time for the orbit to expand to the Hill radius (Δt_{Hill}) calculated based on the Hill radius at perihelion and the assumption that the expanding orbit remains circular. Comparison to KW4 simulation results in §6.1.4.2 gives an idea of the difference expected from this assumption.	113
6.5	Time for the orbit of 1999 KW4 to expand to a given semi-major axis based on an initial libration amplitude that increases adiabatically as the orbit expands. The first row gives the nominal case with no libration at all, and the subsequent rows show how much longer the expansion takes given some initial libration amplitude.	125

7.1	GRACE optical properties.	128
7.2	Parameter values for JPL SRP model for GPS IIR-M spacecraft, from Ref. [4].	139
7.3	Relationship between JPL coefficients and single-prime coefficients when attitude motion is nominal.	142
7.4	GPS IR-M satellites not in eclipse and their associated β values on August 5 and 14, 2009.	145
7.5	RSS [m] for 10 days August 5 - 14, 2009. The outlier marked with a * is discussed in the text.	147
7.6	10 day arc RMS [m] for August 5 - 14, 2009.	148
7.7	4 day arc plus 4 day prediction RMS [m] for August 12, 2009.	148
7.8	4 day arc plus 4 day prediction RMS [m] for August 13, 2009.	148
7.9	4 day arc plus 4 day prediction RMS [m] for August 14, 2009.	149
7.10	Y-bias values ($\times 10^{-9}$ m/s ²) estimated by the JPL model estimation for August 9, 2009.	151

Figures

Figure

1.1	Illustration of the role of the different gravity models in orbital dynamics. The first order point mass model leads to Keplerian dynamics. Describing a non-point mass planet's gravity field requires perturbation theory; numerical N-body descriptions are used in special perturbation techniques, and the analytical spherical harmonics models are general perturbation techniques. Semi-analytical theories combine both high-fidelity methods.	4
1.2	Illustration of the role of the analytical theory developed in this dissertation (the Fourier series) to previous solar radiation pressure models.	12
2.1	Illustration of the Sun orbit parameters in the body frame. The node vector is at the intersection of the $\hat{\mathbf{x}}_b - \hat{\mathbf{y}}_b$ plane and the $\hat{\mathbf{X}}_H - \hat{\mathbf{Y}}_H$ plane. The heliocentric orbit plane will rotate in the body frame as the body spins, thus making the node vector process around $\hat{\mathbf{z}}_b$. Ω_s is the angle between $\hat{\mathbf{x}}_b$ and the node vector, and $\bar{\omega}_s$ is the angle between the node vector and $\hat{\mathbf{X}}_H$	21
2.2	Illustration of the Sun vector ($\hat{\mathbf{u}}$) in the body frame with the solar latitude (δ_s) and longitude (λ_s).	22

4.1	Illustration of the variation of the solar position in the body frame over time. The Sun appears to move in a circle as the body spins, tracing out the tube. During this time, the Sun vector ($\hat{\mathbf{u}}$) would trace out the surface of the cone. As the year passes, the tube will vary between the highest and lowest positions based on the solar inclination (i_s) following the surface of the cylinder.	39
5.2	Orbital energy of the example secondary over 10 orbits about the primary.	59
5.3	Orbital angular momentum of the example secondary over 10 orbits about the primary.	59
5.4	Orbit angular momentum vector components in the primary-centered inertial frame for the example secondary over 10 orbits about the primary.	60
5.5	Eccentricity of the example secondary over 10 orbits about the primary.	61
5.6	Eccentricity vector components in the primary-centered inertial frame for the example secondary over 10 orbits about the primary.	62
5.7	Orbital energy of the example secondary over 10 orbits about the primary.	77
5.8	Orbit angular momentum magnitude of the example secondary over 10 orbits about the primary.	77
5.9	Orbit angular momentum vector components in the primary-centered inertial frame for the example secondary over 10 orbits about the primary.	78
5.10	Eccentricity of the example secondary over 10 orbits about the primary.	78
5.11	Eccentricity vector components in the primary-centered inertial frame for the example secondary over 10 orbits about the primary.	79
5.1	Illustration of a generic function time-varying function, shown in red. Removing the short-period terms leaves the function shown in blue. Removing the long-period terms leaves only the secular portion, shown in black.	81

6.1 This cartoon shows an example asymmetric secondary body that clearly has different geometries exposed to sunlight as it orbits the primary originating from the Sun to the left. The arrows represent the direction of the force imparted on the secondary by solar radiation pressure. It is clear that in this example, the force is not constant in magnitude or direction. This will result in secular changes to the orbit. 83

6.2 Top view of the KW4 Beta shape model with the body axes illustrated. 98

6.3 Isometric view of the KW4 Beta shape model with the body axes illustrated. 99

6.4 Front view of the KW4 Beta shape model with the body axes illustrated. 99

6.5 Side view of the KW4 Beta shape model with the body axes illustrated. 100

6.6 Plot of \mathbf{A}'_0 over zenith angle (measured from the body's north pole) in body frame components denoted by the basis vectors $\hat{\mathbf{x}}_b, \hat{\mathbf{y}}_b, \hat{\mathbf{z}}_b$ 101

6.7 Plot of \mathbf{A}'_n for KW4 over zenith angle in body frame components. The first four orders are defined by the following color scheme: $n = 1$ is blue; $n = 2$ is green; $n = 3$ is red; $n = 4$ is cyan. 101

6.8 Plot of \mathbf{B}'_n for KW4 over zenith angle in body frame components. The first four orders are defined by the following color scheme: $n = 1$ is blue; $n = 2$ is green; $n = 3$ is red; $n = 4$ is cyan. 102

6.9 Plot of \mathbf{A}''_0 over zenith angle (measured from the body's north pole) in orbit frame components denoted by the basis vectors $\hat{\mathbf{e}}, \hat{\mathbf{e}}_\perp, \hat{\mathbf{h}}$ 102

6.10 Plot of \mathbf{A}''_n for KW4 over zenith angle in body frame components. The first four orders are defined by the following color scheme: $n = 1$ is blue; $n = 2$ is green; $n = 3$ is red; $n = 4$ is cyan. 103

6.11 Plot of \mathbf{B}''_n for KW4 over zenith angle in body frame components. The first four orders are defined by the following color scheme: $n = 1$ is blue; $n = 2$ is green; $n = 3$ is red; $n = 4$ is cyan. 103

6.12 This figure shows the body-frame components of $\overline{\mathbf{A}}_n$, the year-averaged Fourier coefficients of KW4. These values were computed with a fixed heliocentric inclination and rotation pole (values are given in Table 6.1). Only the first few orders are shown as these are the dominant terms. 104

6.13	This figure shows the body-frame components of $\overline{\mathbf{B}}_n$, the year-averaged Fourier coefficients of KW4. These values were computed with a fixed heliocentric inclination and rotation pole (values are given in Table 6.1). Only the first few orders are shown as these are the dominant terms.	104
6.14	Predicted evolution of the semi-major axis under BYORP, J_2 , and 3rd body perturbations from the Sun. This integration was carried out with the long-term averaged evolutionary equations.	107
6.15	Predicted evolution of the eccentricity under BYORP, J_2 , and 3rd body perturbations from the Sun. This integration was carried out with the long-term averaged evolutionary equations.	107
6.16	Predicted evolution of the semi-major axis under BYORP, J_2 , and 3rd body perturbations from the Sun. This integration was carried out with the long-term averaged evolutionary equations, and the secondary body flipped 180.	108
6.17	Predicted evolution of the eccentricity under BYORP, J_2 , and 3rd body perturbations from the Sun. This integration was carried out with the long-term averaged evolutionary equations, and the secondary body flipped 180.	108
6.18	Illustration showing the libration angle of an elongated secondary asteroid in the plane of its orbit. The libration angle is defined as the angle between the long axis of the secondary and the orbital radius vector.	117
6.19	Necessary condition for the libration period to be the same as the orbit period. Note that the range of values for KW4 show that it is possible for there to be a periodic libration.	119
6.20	Libration periods for varying libration amplitude.	119
6.21	Averaged values of libration angle coefficients.	122
6.22	Orbit expansion for KW4 with different initial libration amplitudes. The libration amplitude is evolved adiabatically following Eq. (6.133).	124
7.1	Illustration of the GRACE model, with the body axes shown.	130
7.2	$\mathbf{A}_n(1)$ coefficient components. The most prominent orders are labeled.	130

7.3	$\mathbf{A}_n(3)$ coefficient components. The most prominent orders are labeled.	131
7.4	$\mathbf{B}_n(2)$ coefficient components. The most prominent orders are labeled.	131
7.5	Change in the orbital energy from its initial mean value over 10 orbits for the numerical integration and the orbit averaged theory. The initial mean value is approximately $-28.98 \text{ km}^2/\text{s}^2$. The dashed lines represent the bounds of the short period variations.	132
7.6	Change in the orbital angular momentum magnitude from its initial mean value over 10 orbits for the numerical integration and the orbit averaged theory. The initial mean value is approximately $52,360 \text{ km}^2/\text{s}$. The dashed lines represent the bounds of the short period variations.	132
7.7	Orbital eccentricity over 10 orbits for the numerical integration and the orbit averaged theory. The dashed lines represent the bounds of the short period variations.	133
7.8	Example of the effect of the Earth's shadow on GRACE in orbit frame coordinates. The shadow acceleration cancels out the original SRP acceleration for $M_1 \leq M \leq M_2$ so that the total acceleration is zero over this range. The mean anomaly is measured from the sub-solar point on the orbit.	135
7.9	The nominal GPS II/IIA frame is illustrated, along with the rotating frame from Chapter 2. The yaw angle, that between $\hat{\mathbf{h}}$ and $\hat{\mathbf{x}}_b$, is shown here to have a negative value. Note that the GPS IIR frame has the $\hat{\mathbf{x}}_b$ and $\hat{\mathbf{y}}_b$ body axes in the negative directions of those illustrated here, however the yaw angle can still be defined between the vectors shown.	138
7.10	Rotating frame coefficients for GPS IIR-M plotted as a function of β (or δ_s) as computed using the JPL body-fixed SRP model and the nominal attitude motion. (Part I)	143
7.11	Rotating frame coefficients for GPS IIR-M plotted as a function of β (or δ_s) as computed using the JPL body-fixed SRP model and the nominal attitude motion. (Part II)	143
7.12	Rotating frame coefficients for GPS IIR-M plotted as a function of β (or δ_s) as computed using the JPL body-fixed SRP model and the nominal attitude motion. (Part III)	144
7.13	Rotating frame coefficients for GPS IIR-M due to $C_{Y_0} = 10^{-9} \text{ m/s}^2$ plotted as a function of β (or δ_s) as computed using the JPL body-fixed SRP model and the nominal attitude motion.	144

7.14	The RMS values for each of the four estimation schemes tested for August 9, 2009	147
7.15	The $A'_0(2)$ scale factors estimated for each 1 day arc for each of the satellites in Case 1.	150
7.16	The $B'_1(3)$ scale factors estimated for each 1 day arc for each of the satellites in Case 1.	150
7.17	The general scale factors estimated for each 1 day arc for each of the satellites in Case 1.	151
7.18	Illustration of the LVLH frame and the cone (β) and clock (ϕ) angles.	157
7.19	Illustration of the normal vector coning in the LVLH frame for $\phi_{eq} = \pi$	158
7.20	Scaled change of the angular momentum vector components, $\bar{\mathbf{h}} \cdot \hat{\mathbf{Q}}/(a_c r)$ (top) and $\bar{\mathbf{h}} \cdot \hat{\mathbf{R}}/(a_c r)$ (bottom), for coning cases with $\phi_{eq} = \pi$	165
7.21	Scaled change of the eccentricity vector $\bar{\mathbf{e}} \cdot \hat{\mathbf{P}} / \left(a_c \sqrt{\frac{r}{\mu}} \right)$ (top), and the energy $\bar{\mathcal{E}} / \left(a_c \sqrt{\frac{\mu}{r}} \right)$ (bottom) for coning cases with $\phi_{eq} = \pi$	166
7.22	Nodal drift errors caused by off-nominal semi-major axis and inclination values that can be overcome by a solar sail with a variety of characteristic accelerations. a_c varies from 0.05 mm/s ² (dark blue) to 0.75 mm/s ² (dark red). The solar sail can overcome the error if it lies between the bands of the same color. The white line indicates where the semi-major axis and inclination errors offset each other. The orbit radius used to obtain these results was 8008 km.	170
7.23	Nodal drift error plot for a 6600 km orbit (left) and a 9900 km orbit (right).	170
7.24	The nodal drift per orbit created for solar sails of varying characteristic accelerations over a variety of altitudes are shown as solid lines with the same color scheme as Fig. 7.22. The dotted lines represent the nodal drift that would need to be overcome for given changes in the orbit radius to keep the orbit Sun-synchronous.	171
7.25	Nodal drift caused by 3σ injection errors from a Pegasus launch vehicle are drawn as a red box. Solar sails moving in coning motion can overcome errors within each color band, varying from $a_c = 0.05 - 0.25$ mm/s ²	172

Chapter 1

Introduction

1.1 Orbital Perturbations due to Solar Radiation Pressure

The study of orbital motion has a long and illustrious history of which only the highlights are outlined in this chapter. The modern field of celestial mechanics (or equivalently astrodynamics or orbital mechanics) is founded on the work of two great scientists of the 17th century, Johannes Kepler and Isaac Newton. Kepler's three laws of motion [5] describe the motion of the planets in the Solar System around the Sun, while Newton's law of gravitation [74] gave the mathematical proof of why these laws are obeyed in nature. The problem for which Kepler's laws apply considers two bodies that are modeled as point masses and attract each other gravitationally. The motion is described in a relative coordinate frame with one of the bodies at the origin (typically the larger/more massive body); in this frame, when one body is much more massive than the other, the motion of the second body will move along a conic orbit. In this work, the more massive body is referred to as the primary, and the smaller, "orbiting" body as the secondary. This problem is an integrable, and the resulting orbital motion is commonly referred to as "Keplerian motion."

Introducing any forces beyond point mass gravity makes the problem non-Keplerian in nature. However, if the additional forces are small in magnitude compared to the point mass gravity, perturbation theory can be used to study the subsequent orbital motion. Perturbation theory is a mathematical methodology in which the solution of the perturbed system is described by relating it to small deviations from the solution of the unperturbed system. Many different types of perturbation theory have been used to describe orbital motion in the presence of disturbing forces. These methods are generally broken into three categories: special

perturbation techniques, general perturbation techniques, and semianalytical techniques [111].

Special perturbation techniques are concerned with numerically integrating the equations of motion of an object, including any perturbing accelerations. Early methods of special perturbations were developed by Encke and later by Cowell [111]. Given the availability of computing power now, numerical integration of the exact equations of motion is commonly used in two ways. First, many problems are extremely complicated and do not allow for a tractable analytical analysis, therefore numerical integration is the only recourse to study the behavior of these systems. An example of this is the integration of a satellite orbit subject to a perturbing acceleration due to atmospheric drag where the model of the atmospheric density is not an analytical function. The second major use for numerical methods is to act as a truth model for comparison with a simplified analytical theory. It is in this capacity that special perturbations will be used in this work.

General perturbation techniques are of specific interest to this work as these methods form the basis of the perturbative analysis presented. The main procedure for analytically studying the perturbations of Keplerian dynamics is known as the method of variation of parameters. In Keplerian dynamics, since the problem is integrable, there are six constants of the motion, one for each dimension in the problem. The variation of parameters technique looks at the effect of the disturbing force on these constants of the motion, which then defines how the conic orbit is changing. Lagrange developed this method with application to conservative effects through the use of the disturbing potential function. The result, known as Lagrange's Planetary Equations [6], are still commonly used, in particular to study the effects of higher order gravity terms of a primary body. Gauss' approach to the variation of parameters used an arbitrary disturbing acceleration, making the resulting Gauss' variational equations useful for any disturbing force [6]. However, these equations are regularly used today to analyze how non-conservative forces that can't easily be written in terms of a disturbing potential, such as the thrust of a spacecraft, change the orbital elements. In both of the cases of Lagrange and Gauss, the result is a set of six differential equations for the rates of the Keplerian orbital elements.

In situations where long term orbit evolution is of concern, the secular terms in the dynamics are of particular interest. Secular terms are those which appear as a constant term in the variational equations. In order to extract the secular terms from the total dynamical equations, the method of averaging is used.

This is a perturbative technique which averages the system over the time scale of the periodic terms, which results in these terms averaging to zero, and only secular terms remaining. Depending on the system and the perturbations present, averaging may be carried out over several distinct time scales to remove short and long periodic terms.

Kozai, [47] based on the method of averaging which he credits to Tisserand, developed a first-order theory for the variation of a satellite's orbit due to J_2 in Keplerian elements. Kozai recognized that the solution of the perturbed set of Keplerian elements could have secular, long period, and short period dynamics. Kozai used series expansions to express the variational equations in terms of the mean anomaly. Then, by averaging the first (and in some case second) order terms over the mean anomaly, he was able to separate out the secular rates in particular, as well as identify the short and long period rates. Similar averaging methodology is applied in this work.

Hamilton reformulated the two-body problem in terms of his Hamiltonian dynamics, and used the canonical set of orbital elements developed by Delaunay [111]. This formulation has advantages over using Keplerian elements in that the structure of the problem can make the mathematical development more tractable. Von Ziepel [12] developed a technique by which canonical transformations are applied in order to separate certain periodic components from the solution of the orbital elements in the presence of a perturbation such as the higher order gravity terms. Brouwer [11] created an analytical theory for satellite orbits under the perturbation of J_2 - J_5 using Von Ziepel's method (Brouwer's paper was actually published in the same issue as Kozai's original paper; in fact, it was on the pages directly following Kozai's article). Brouwer used two canonical transformations; the first separated the short period terms dependent on the mean anomaly, and the second separated the long period terms dependent on the argument of periapse. The periodic terms were determined up to first order in J_2 , while the secular terms were expanded to second order. Kozai [48] later improved upon his and Brouwer's theories (and adopted the Von Ziepel method as it is advantageous for carrying out higher order theories in the process) by extending the periodic terms to second order and the secular terms to third order while including harmonics up to J_8 . Brouwer's theory was later extended further by Lyddane [55] to be applicable and zero eccentricity and the critical inclination, and again by Brouwer and Hori [13] to account for a basic model of drag. The culmination of this type of

canonical reformulation was developed by Deprit [25], [26]. He was able to use Lie algebra to functionalize the canonical transformations in such a way that a computer could generate the analytical theory to arbitrary order.

Semianalytical methods combine the special and general perturbation ideas by developing some form of analytical theory and integrating these equations numerically. This technique is very commonly applied in modern astrodynamics research as new analytical theories are developed, they are integrated numerically and tested against truth models of numerically integrating the full equations of motion as discussed previously. There are two well known semianalytical theories for satellite motion that are used regularly today, the Goddard Trajectory Determination System [51] and the Draper Semianalytical Satellite Theory [23]. Both of these semianalytical techniques give very accurate results for the propagation of satellite orbits.

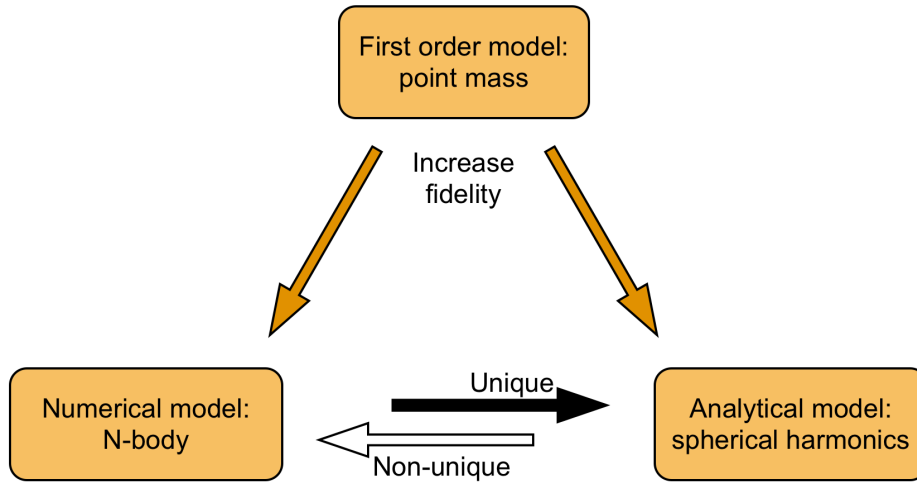


Figure 1.1: Illustration of the role of the different gravity models in orbital dynamics. The first order point mass model leads to Keplerian dynamics. Describing a non-point mass planet’s gravity field requires perturbation theory; numerical N-body descriptions are used in special perturbation techniques, and the analytical spherical harmonics models are general perturbation techniques. Semi-analytical theories combine both high-fidelity methods.

Given the available techniques for studying the effect of perturbations on Keplerian orbits, the effect of specific perturbations can be studied. Much of the focus of perturbation studies has been gravitational effects beyond the Keplerian two-body problem. This includes the effects of the masses having finite size and shape [71, 119], as well as 3rd body gravitational effects [84]. Many studies have looked at different

non-gravitational perturbations in attempt to categorize them in some manner [33, 34, 24]. Atmospheric drag is a very important perturbative effect for low Earth orbiting spacecraft and has been the subject of much work [19, 35, 105]. Another non-gravitational effect that can be important for Earth orbiting satellites is the albedo effect, where radiation from the Earth perturbs the orbit in a similar fashion to solar radiation effects [53, 45, 85]. Similarly, the effect of the perturbation caused by the re-radiation of heat has been studied for both spacecraft [86] and asteroids [87] in related works. Finally, the study of the spacecraft thrust effects have been studied in detail. Recently, with the advent and use of low-thrust propulsion such as ion engines and solar sails, the study of spacecraft thrust has begun to overlap more with the study of natural perturbative effects since the accelerations are of a similar magnitude and are acting for long periods of time [40].

Solar radiation effects have become an increasingly important perturbation to understand over the past several decades. The dynamical evolution of main belt and near-Earth asteroids is strongly influenced by different processes which originate with solar radiation. Analytical studies of the different aspects of the solar radiation interaction with asteroids has lead to great advances in the understanding of the solar system [72, 10]. Likewise, solar radiation interactions with spacecraft are of great interest right now. Increased knowledge of the Earth's gravity field has lead to solar radiation pressure being one of the largest unknown factors that must be accounted for in orbit propagation and orbit determination [3, 102]. In both cases, the perturbative effects of solar radiation pressure have been studied analytically through the use of relatively simplistic models. The importance of high-fidelity predictions for the perturbative effects of solar radiation pressure (SRP) for natural bodies and spacecraft orbits naturally leads to the following thesis statement:

Thesis Statement

A general model for solar radiation pressure forces acting on celestial bodies enables them to be analyzed independent of their specific properties. Analytical perturbation theory using this model improves understanding of the secular, long-period, and short-period effects of solar radiation pressure on the orbit of a secondary object. Application of the theory to spacecraft orbits about Earth improves orbit propagation and determination, and application to binary asteroid systems allows for long term predictions of the system evolution.

To support this thesis statement, this study of solar radiation pressure perturbations is concerned with three main topics: modeling the solar radiation pressure force, application to natural bodies, and application

to artificial bodies.

1.1.1 SRP Models

A variety of models have been used to study solar radiation pressure for various applications. The simplest model, which has been used for most analytical studies to date, states that the force caused by solar radiation pressure acts along the object-Sun line, directly away from the Sun. In the spacecraft community, this model is often referred to as the cannonball model [53] because a) this is how solar radiation would affect a cannonball-like spherical object with uniform optical properties in space, and b) because this model was created for the LAGEOS mission, and that particular spacecraft looked very similar to a cannonball. This model is used as the baseline for many missions [18, 111] and has also been applied to the debris problem [54, 99]. One of the advantages for the cannonball model is that its simplicity allows it to be expressed as a potential disturbing function [23, 100], which allows easy analytical investigation of the perturbative effects through the use of Lagrange’s planetary equations. Similarly, Roth [83] formulated a first order theory using Gauss’ equations for the equinoctial elements using the cannonball model.

Spacecraft missions often desire much higher fidelity in their solar radiation pressure model than the cannonball model. The next step is still a simple model characterized by a small number of facets to capture the general geometry of the spacecraft. Many spacecraft can be modeled as a “box-wing” model such as that produced for TOPEX/Poseidon [61] or the GRACE model [17]. With a small number of facets, it is still tractable to approach the problem analytically. However, the solar radiation pressure force is computed per facet for each Sun position as needed, which requires a numerical implementation. As the models of the spacecraft become more and more detailed, they are more and more reliant on numerical methods and are referred to as micro models [80]. These micro models can be extremely detailed, approaching full CAD models with the shape of the spacecraft reproduced and each component being assigned its own optical properties. The effect of solar radiation pressure for such high fidelity models is determined through extremely detailed ray-tracing methods which can include all self-shadowing and secondary incidence effects [124].

The original model used to study the BYORP (Binary-Yarkovsky-O’Keefe-Radviskii-Paddack) effect by Ćuk [21] was similar to the cannonball model. Ćuk averaged the time-varying solar radiation pressure

over the rotation body to come up with a force that was constant in the asteroid’s body-fixed frame. The effect of this model was analyzed analytically, however for many systems where the rotation rate is near or equal to the orbit rate, applying the averaged model to the variational equations does not reveal all of the correct dynamical implications.

In general, the literature to date lacks an analytical model that is used for studies of the perturbative effects of SRP to arbitrary bodies which are not accurately represented by the cannonball model. Details of different studies of the perturbative effects of SRP using these (and other) models are discussed in the following sections.

1.1.2 Natural Bodies

In the study of natural bodies in the solar system, particularly main-belt and near-Earth asteroids, the effects of solar radiation are very important to their dynamical evolution. The direct impact of solar radiation pressure largely determines the evolution of interplanetary dust falling into the Sun through Poynting-Robertson drag [24], however this effect is usually considered insignificant for larger bodies. Solar radiation pressure scales with the area-to-mass ratio, which is very high for dust particles, but is very low for even low density rock that is formed into a somewhat spherical body. Therefore, the direct solar radiation pressure accelerations acting on asteroids is generally much less important than 3rd body gravity effects, and therefore neglected. A much more important effect due to solar radiation for many natural bodies is the study of thermal reemission which is intimately linked with SRP for natural bodies since the SRP is main source of incoming heat. This is most apparent for comets whose jets are caused by heating from solar radiation. Heating of asteroids through radiation pressure and the reemission effects have been studied for some time.

Early studies were conducted by Yarkovsky, where he suggested that, due to the fact that an asteroid has non-zero thermal inertia, the afternoon side of a rotating asteroid will be hotter than the morning side, and therefore there will be an asymmetric re-radiation causing a prograde rotator to speed up and a retrograde rotator to slow down [39]. This effect is called the “diurnal” Yarkovsky effect, and has a maximum effect when the asteroid rotation pole is at 0° or 180° from the ecliptic north direction. Another component

of the Yarkovsky effect acting on asteroids was discovered by Rubincam [87] after defining a similar effect for the LAGEOS satellite [86]. This secondary effect is called the “seasonal” Yarkovsky effect, arising from the same thermal inertia but now when the asteroid has a non-zero (or 180°) obliquity. In this case, the hemisphere that is in autumn will be hotter and radiate more heat than the hemisphere in spring, leading to a net force which causes a decrease in semi-major axis of the asteroid.

O’Keefe [75], Radvieskii [79], and Paddack [77] individually studied various aspects of how incident light can change the spin of objects in space, looking at how spinning up an object can cause it to fragment or burst into smaller pieces. Their various studies were recognized by Rubincam [88] when he coined the name for the YORP effect. The YORP effect arises from a net torque being applied to the asteroid as it rotates with respect to the Sun due to the scattering of solar radiation pressure off of an asymmetric object (e.g. asteroids). Rubincam studied how differently shaped objects can have different spin evolutions which cause them to increase or decrease their spin rates and orient their spin axes at either $0^\circ/180^\circ$ or 90° obliquity. While Rubincam assumes no thermal conductivity to simplify his analysis, Čapek and Vokrouhlický [112] show that the inclusion of finite thermal conductivity causes YORP to evolve asteroids preferentially toward $0^\circ/180^\circ$ obliquity while leaving the spin rate evolution largely unchanged. Subsequently, there have been many detailed studies modeling the YORP effect. In particular, Scheeres [92] and Scheeres and Mirahimi [98] use an analytical model to analyze the YORP torques that is similar to the one used in this work. One of the major outcomes of the YORP research is that it has been confirmed observationally [109, 52, 44] to change asteroids spins appreciably.

In 2005, Čuk and Burns [21] proposed the BYORP effect. The name comes from the fact that this effect is a natural extension of the YORP effect to binary asteroids. In binary asteroid systems (and many planetary systems such as the Earth-Moon system), the secondary asteroid typically orbits the primary synchronously, meaning that the same face of the secondary always faces the primary. Thus, as the secondary orbits the primary once, it also spins once in inertial space and with respect to the Sun. The time varying torques that are the root of the YORP effect also create a time varying force on the secondary which will modify its orbit with respect to the primary; thus the BYORP effect. Čuk later discussed the fact that BYORP evolution can disrupt binary asteroid systems on short timescales (10^5 years) so that there must

be a fast method of binary creation in order to maintain the population of binaries observed (approximately 16%) in the near-Earth asteroid population [20, 60]. These predictions have been subsequently modified in a study by Āuk and Nesvorný [22] where they state that the inclusion of the secondary’s attitude dynamics leads to a situation where the secondary starts spinning chaotically, thus turning off the BYORP effect and arresting the destruction of binary systems. The weakness in Āuk’s studies is the simplistic model used to represent the SRP acceleration which, as mentioned previously, is a constant force in the body-fixed frame. Regardless, BYORP is now thought to be a major component of binary asteroid evolution, and accurate modeling of the effect is key to understanding the life-cycle of binary asteroid systems.

1.1.3 Artificial Bodies

Solar radiation effects are also extremely important for modeling the orbits of spacecraft and orbital debris. There are two major differences with respect to studies of solar radiation acting on natural bodies. First, thermal re-radiation is generally considered as a separate effect. This is due to the fact that for spacecraft, the flow of heat is controlled to some degree so that it acts in a very different manner than on a natural body. Second, most spacecraft are Earth orbiting satellites, and therefore there has always been a concern with how SRP affects the orbit about Earth (similar to the BYORP effect), rather than the heliocentric orbit as is the focus of the Yarkovsky effect. Also, many of these Earth orbiting spacecraft reside in orbits that have significant shadow periods, which can have a large effect on the solar radiation pressure on the orbit.

Most spacecraft studies have used the cannonball model. However, in recent years the combination of improved tracking capabilities and an improved gravity model have made the solar radiation pressure models the largest source of errors in orbital determination. This becomes more apparent for higher altitude satellites; solar radiation pressure is the largest non-gravitational perturbation of GPS satellites and also has the largest uncertainty [3]. This is even more true for satellites at geosynchronous altitudes [18], where higher-order gravity terms have a diminished effect due to the high altitude and the fact that the satellite moves very little in the geocentric frame.

Due to the uncertainty in the solar radiation pressure model for GPS satellites, a large number of

researchers have spent significant time and resources attempting to rectify the problem. The first improvement on the analytical models were made by Fliegel and Gallini [31] where they modeled the spacecraft more accurately. The resulting force model was then parametrized as a function of the angle between the Earth facing side of the spacecraft and the Sun. They also introduced the idea of the Y-bias, which is a constant acceleration in the spacecraft fixed Y direction due to unmodeled dynamics. Two main groups located at JPL [3] and the University of Bern [102] extended this work into higher fidelity models which were derived from orbit determination residuals that were attributed to solar radiation pressure. In both cases, the data derived “best-fit” models were parametrized in terms of an orbit angle and a Sun latitude and truncated Fourier series in these angles were written. These models have been repeatedly updated, and represent the state of the art models for orbit determination of the GPS satellites. Independent tests show that these models are extremely good for GPS orbit estimation and subsequent prediction [15]. There are two drawbacks of these models. First, the frames they are defined in are great for parametrizing the data they had, but they are not convenient for making analytical predictions of the solar radiation pressure effects. Second, the large amount of work required to derive these models makes it difficult to extend to other spacecraft.

While low Earth orbiters may not be quite as sensitive to SRP due to the stronger effect of higher-order gravity terms and drag, it is still important if high accuracy orbit determination is required. The LAGEOS mission, which is the source of the cannonball model, was a low Earth orbiting mission whose point was extremely high accuracy orbit determination. This was one of the first missions to include significant SRP modeling, and the analytical effects of the cannonball model were explored [53]. Several other low Earth orbit missions that required accurate SRP modeling were TOPEX/Poseidon [61] and GRACE [17]; the former measured ocean surface topography, while the later mission constructed accurate gravity and atmospheric density models.

Earth orbiting spacecraft can also experience periods of shadow, which necessarily turns off the solar radiation for the spacecraft. The presence of a shadow can completely change the analytical effects of SRP on a spacecraft [18], even when the force is modeled with only the cannonball model. The most apparent difference in the analytical results is that the semi-major axis, which won’t change on average with no shadow, but with a shadow can change secularly. In reality, addressing the complexity of the Earth’s shadow can

make this problem significantly harder. Basic analyses model the Earth’s shadow as a cylinder [18, 23], while a more accurate study of the shadow’s effect is made by using a conical shadow originating at the center of the Earth [67]. While these analyses illustrate the importance of accounting for the shadow, a highly detailed accounting of the penumbra effects [113, 114, 115, 116] can virtually rule out strictly analytical results.

Another class of spacecraft which requires special mention for modeling and use of solar radiation pressure are solar sail propelled spacecraft. Until the recent demonstration of the IKAROS mission by JAXA/ISAS [43], these craft were still largely theoretical. Even so, there are a large number of works analyzing the orbital effects of solar radiation pressure in changing orbits in a controlled manner. Extremely detailed models for SRP interacting with a solar sail are available [62], however most trajectory studies only consider the sail to be a flat plate [90, 106, 32]. In reality, the SRP force produced on the solar sail spacecraft depends intrinsically on the exact shape of the sail and the geometry with the Sun. A more general model was developed by Rios-Reyes and Scheeres [81] which can describe any sail shape with a finite set of coefficients. These coefficients can be estimated by executing basic attitude maneuvers so that the various geometries with the Sun are realized [82]. The same SRP force that creates the propulsive forces on a solar sail will also create torques on the spacecraft. This aspect has been explored for general spacecraft without solar sails as well [70], and in fact attitude control systems using solar radiation pressure torques have been designed and used [27].

The final class of artificial bodies for which solar radiation pressure effects are important is Earth orbiting debris. The SRP perturbations can be very important at GPS [14] and geosynchronous (GEO) altitudes [101]. In fact, it is predicted that much of the debris at GEO has a high area to mass ratio (HAMR) [101], meaning that the SRP perturbations are even more important. While most analysis to date has used only simple cannonball models, [54], it can be shown that even this type of force can cause very significant changes to the debris orbits [100].

1.2 Organization and Contributions

Similar to the methods of analyzing an object’s gravity analytically, as illustrated in Fig. 1.1, the analytical theory developed for solar radiation pressure in this dissertation fills in the hole which marries the

high fidelity predictions from CAD models with the analytical theory for the prediction of the orbital effects. This is illustrated in Fig. 1.2. The similarity between the two previously mentioned figures is intentional as the Fourier series model developed here plays the same role in describing the solar radiation pressure effects as the spherical harmonics models do for gravitational effects.

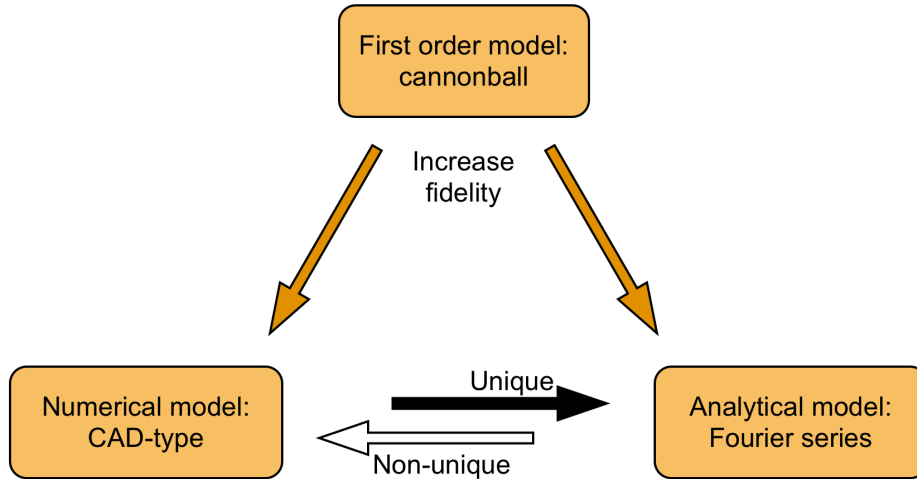


Figure 1.2: Illustration of the role of the analytical theory developed in this dissertation (the Fourier series) to previous solar radiation pressure models.

This dissertation is organized such that the analytical theory is outlined in Chapters 2-5. Specifically, Chapter 2 presents the general analytical theory for modeling solar radiation pressure. The SRP force can be determined from a detailed physical perspective to arbitrary accuracy based on the detail of the shape model of the secondary body. The force is then decomposed as a Fourier series, based on the location of the Sun in a body fixed frame. In Chapter 3 variational equations for three different sets of orbit elements (dynamical, Keplerian, and Delaunay) are derived in terms of the general analytical theory. Chapter 4 discusses the coupling between the attitude and translational dynamics in this problem. The relationship between the body attitude and the SRP force provides a bridge to the correct method of analysis to determine the secular effects on the secondary's orbit due to SRP. Finally, in Chapter 5 averaging theory is discussed and applied to this problem to determine the secular effects from SRP. The variational equations are averaged explicitly over the secondary orbit period, and the system's heliocentric orbit period. The short period dynamics are discussed, and the results are applied to both circular and fully elliptical orbits.

The applications of the analytical theory are separated into two parts. Chapter 6 is concerned with the implications of this theory to natural bodies under the guise of the BYORP effect. §6.1 outlines the details of the BYORP effect using the general analytical model. The theory is extended in a number of ways to more accurately model a binary asteroid system, and results are obtained for simulation of the near-Earth asteroid system 1999 KW4. These results are discussed, and scaled for application to other known binary systems. §6.2 extends to this theory by considering the effects of libration on the predictions made in §6.1.

Chapter 7 elucidates the application of the analytical theory to artificial bodies. The general application of the model to spacecraft is discussed in §7.1, while using this model for spacecraft orbit determination, with specific application to GPS satellites, is discussed in §7.2. §7.4 discusses the application of this theory to modeling the orbits of orbital debris, and §7.5 discusses how this theory can be leveraged for use with solar sail spacecraft.

1.2.1 Contributions

The main contributions of this dissertation are summarized in the following three categories:

Analytical Theory

- Developed an analytical methodology to model the effects of a disturbing force which is tied to the attitude of the orbiting body.
- Applied averaging theory to the effects of solar radiation pressure and determined the secular changes to an orbit (over multiple timescales) for an arbitrary body in synchronous rotation through the use of first-order averaging theory.
- Analytically incorporated the effects of the primary's shadow seamlessly into the solar radiation pressure model.

Natural Bodies

- Improved upon previous BYORP theory by increasing the modeling fidelity and determined under what conditions previous theories are applicable.

- Modeled the BYORP effect in detail based upon real binary asteroid shape models, and made predictions for NEA systems which can be tested from Earth observations.
- Expanded upon BYORP effect theory through the addition of the effects of librational motion of the secondary asteroid.

Artificial Bodies

- Developed a solar radiation pressure force model that can reproduce the orbit determination performance of JPL's GPS model while being usable for any spacecraft.
- Stated the conditions under which the cannonball model can be used for the solar radiation pressure effects on debris orbits.
- Analytically modeled the orbital control space for a solar sail spacecraft that is coning in the local horizontal frame at orbit rates.

1.2.2 Publications

For reference purposes, journal and conference papers forming the basis for this dissertation are listed below in reverse chronological order (newest to oldest).

Journals

- J. McMahon and D. Scheeres, Application of a New Solar Radiation Pressure Model to GPS Orbit Determination, to be submitted to the Journal of Guidance, Control, and Dynamics
- [66] J. McMahon and D. Scheeres, A New Navigation Force Model for Solar Radiation Pressure, Journal of Guidance, Control, and Dynamics, Vol. 33, No. 5, 2010, pp. 1418-1428
- [64] J. McMahon and D. Scheeres, Detailed Prediction for the BYORP Effect on Binary Near-Earth Asteroid (66391) 1999 KW4 and Implications for the Binary Population, Icarus, Vol. 209, No. 2, 2010, pp. 494-509

- [65] J. McMahon and D. Scheeres, Secular Orbit Variation due to Solar Radiation Effects: A Detailed Model for BYORP, *Celestial Mechanics and Dynamical Astronomy*, Vol. 106, No. 3, 2010, pp. 261-300

Conferences Papers

- D. Scheeres, J. McMahon and A. Rosengren, The Dynamics of High Area-to-Mass Ratio Objects in Earth Orbit: The Effect of Solar Radiation Pressure, AAS/AIAA Space Flight Mechanics Meeting, New Orleans, LA. Paper No. AAS 11-178
- J. McMahon and D. Scheeres, A New Navigation Force Model for Solar Radiation Pressure, IAF International Astronautical Congress, Prague, Czech Republic, 2010. Paper No. IAC-10.C1.2.5
- J. McMahon and D. Scheeres, The Secular Effects of Solar Radiation Pressure on the Orbits of GPS Satellites, AIAA/AAS Astrodynamics Specialist Conference, Toronto, Ontario, Canada 2010.
- J. McMahon and D. Lawrence, Orbital Maneuvering with a Solar Sail Through the Use of Natural Attitude Coning, AAS/AIAA Astrodynamics Specialist Meeting, Pittsburgh, PA, 2009. Paper No. AAS 09-345
- J. McMahon and D. Scheeres, A New Navigation Force Model for Solar Radiation Pressure, AAS/AIAA Astrodynamics Specialist Meeting, Pittsburgh, PA, 2009. Paper No. AAS 09-346

Conferences and Workshop Abstracts

- J. McMahon and D. Scheeres, Dynamical Limits on Planar Libration-Orbit Coupling Around an Oblate Primary with Application to BYORP Evolution, 42nd Meeting of the American Astronomical Society Division of Dynamical Astronomy, Austin, TX, 2011. Abstract No. 2.01
- J. McMahon and D. Scheeres, Measuring the BYORP Effect and the Influence of Librations on Binary Asteroid Evolution, 42nd Meeting of the American Astronomical Society Division for Planetary Sciences, Pasadena, CA, 2010. Abstract No. 63.06

- J. McMahon and D. Scheeres, A Detailed Model for BYORP, Second Workshop on Binaries in the Solar System, Poznan, Poland, July 2010
- J. McMahon and D. Scheeres, The Effects of Libration on BYORP Induced Secular Evolution, 41st Meeting of the American Astronomical Society Division of Dynamical Astronomy, Boston, MA, 2010. Abstract No. 3.04
- J. McMahon and D. Scheeres, Predictions for the Effects of BYORP on 1999 KW4, 41st Meeting of the American Astronomical Society Division for Planetary Sciences, Fajardo, Puerto Rico, 2009. Abstract No. 56.09
- J. McMahon and D. Scheeres, Secular Orbit Variation due to Solar Radiation Effects: A Detailed Model for BYORP, 40th Meeting of the American Astronomical Society Division of Dynamical Astronomy, Virginia Beach, VA, 2009. Abstract No. 10.03

Chapter 2

Solar Radiation Pressure Model

The acceleration imparted on a body in space by solar radiation pressure is dependent on the shape, orientation, and optical properties of the body in question. In this chapter, the physical process of impacting light producing an acceleration on a given body is discussed and expressed as an analytical function. §2.1 gives the mathematical background needed to describe the layout of the body and system in question through the definition of a number of coordinate frames and quantities of interest. §2.2 gives the derivation of the solar radiation pressure acceleration and decomposes the time varying force into a Fourier series dependent on the Sun's location in the body frame. The chapter is summarized in §2.3 where the new analytical representation is compared to other solar radiation pressure models in the literature.

2.1 Coordinate Frame Definitions

Describing the effect of solar radiation pressure on the orbit of a secondary body requires five coordinate frames. The first is an inertial frame to which all other frames are related. The second is an inertial coordinate frame describing the heliocentric orbit of the entire system. The third is a coordinate frame that describes the body frame of the body of interest. The fourth, the orbit frame, describes orientation of the orbit of the secondary body about the primary. Finally, the fifth frame is the called the rotating frame, which rotates at the mean motion rate about the angular momentum vector.

The inertial frame can be described by the unit vectors $\hat{\mathbf{X}}_I$, $\hat{\mathbf{Y}}_I$, and $\hat{\mathbf{Z}}_I$. This frame can be designed according to whichever convention is convenient. The heliocentric orbit frame is defined by $\hat{\mathbf{X}}_H$, which is the unit vector pointing along the perihelion radius vector, $\hat{\mathbf{Z}}_H$, which is the unit vector pointing along the orbit

angular momentum vector, and $\hat{\mathbf{Y}}_H$, which is the unit vector pointing along the perihelion velocity vector which completes the triad. The heliocentric orbit frame can then be described according to the inertial frame using the classical orbit elements as follows.

$$\begin{aligned}\hat{\mathbf{X}}_H &= [\cos \bar{\omega}_H \cos \Omega_H - \sin \bar{\omega}_H \sin \Omega_H \cos i_H] \hat{\mathbf{X}}_I \\ &+ [\cos \bar{\omega}_H \sin \Omega_H + \sin \bar{\omega}_H \cos \Omega_H \cos i_H] \hat{\mathbf{Y}}_I \\ &+ \sin \bar{\omega}_H \sin i_H \hat{\mathbf{Z}}_I\end{aligned}\tag{2.1}$$

$$\begin{aligned}\hat{\mathbf{Y}}_H &= -[\sin \bar{\omega}_H \cos \Omega_H + \cos \bar{\omega}_H \sin \Omega_H \cos i_H] \hat{\mathbf{X}}_I \\ &+ [-\sin \bar{\omega}_H \sin \Omega_H + \cos \bar{\omega}_H \cos \Omega_H \cos i_H] \hat{\mathbf{Y}}_I \\ &+ \cos \bar{\omega}_H \sin i_H \hat{\mathbf{Z}}_I\end{aligned}\tag{2.2}$$

$$\hat{\mathbf{Z}}_H = \sin \Omega_H \sin i_H \hat{\mathbf{X}}_I - \cos \Omega_H \sin i_H \hat{\mathbf{Y}}_I + \cos i_H \hat{\mathbf{Z}}_I\tag{2.3}$$

where i_H is the inclination, Ω_H is the right ascension of the ascending node, and $\bar{\omega}_H$ is the argument of perihelion.

The body frame is related to the inertial frame by the right ascension, α , and declination, δ , of the body rotation pole, as well as the rotation angle, ϕ , about the pole. The body fixed axes are denoted by $\hat{\mathbf{x}}_b$, $\hat{\mathbf{y}}_b$, $\hat{\mathbf{z}}_b$, where $\hat{\mathbf{z}}_b$ is the rotation pole of the body. The body frame unit vectors are related to the inertial frame by,

$$\begin{aligned}\hat{\mathbf{x}}_b &= -[\sin \alpha \cos \phi + \cos \alpha \sin \phi \sin \delta] \hat{\mathbf{X}}_I \\ &+ [\cos \alpha \cos \phi - \sin \alpha \sin \phi \sin \delta] \hat{\mathbf{Y}}_I \\ &+ \sin \phi \cos \delta \hat{\mathbf{Z}}_I\end{aligned}\tag{2.4}$$

$$\begin{aligned}\hat{\mathbf{y}}_b &= [\sin \alpha \sin \phi - \cos \alpha \cos \phi \sin \delta] \hat{\mathbf{X}}_I \\ &- [\cos \alpha \sin \phi + \sin \alpha \cos \phi \sin \delta] \hat{\mathbf{Y}}_I \\ &+ \cos \phi \cos \delta \hat{\mathbf{Z}}_I\end{aligned}\tag{2.5}$$

$$\hat{\mathbf{z}}_b = \cos \alpha \cos \delta \hat{\mathbf{X}}_I + \sin \alpha \cos \delta \hat{\mathbf{Y}}_I + \sin \delta \hat{\mathbf{Z}}_I\tag{2.6}$$

The body frame at the defining epoch will be denoted $\hat{\mathbf{x}}_{b0}$, $\hat{\mathbf{y}}_{b0}$, $\hat{\mathbf{z}}_{b0}$ which are defined by the epoch angles α_0 , δ_0 , and ϕ_0 .

The secondary's orbital frame is defined in a similar manner as the heliocentric orbit. The basis vectors are $\hat{\mathbf{e}}$, the unit vector along the eccentricity vector, which is in the direction of periapsis, $\hat{\mathbf{h}}$, the unit vector in the direction of the angular momentum, and $\hat{\mathbf{e}}_{\perp}$ which is in the direction of the velocity at periapsis and completes the triad. These vectors can be expressed with respect to the orbital frame by the classical orbital elements as,

$$\begin{aligned}\hat{\mathbf{e}} &= [\cos \bar{\omega} \cos \Omega - \sin \bar{\omega} \sin \Omega \cos i] \hat{\mathbf{X}}_I \\ &+ [\cos \bar{\omega} \sin \Omega + \sin \bar{\omega} \cos \Omega \cos i] \hat{\mathbf{Y}}_I \\ &+ \sin \bar{\omega} \sin i \hat{\mathbf{Z}}_I\end{aligned}\tag{2.7}$$

$$\begin{aligned}\hat{\mathbf{e}}_{\perp} &= -[\sin \bar{\omega} \cos \Omega + \cos \bar{\omega} \sin \Omega \cos i] \hat{\mathbf{X}}_I \\ &+ [-\sin \bar{\omega} \sin \Omega + \cos \bar{\omega} \cos \Omega \cos i] \hat{\mathbf{Y}}_I \\ &+ \cos \bar{\omega} \sin i \hat{\mathbf{Z}}_I\end{aligned}\tag{2.8}$$

$$\hat{\mathbf{h}} = \sin \Omega \sin i \hat{\mathbf{X}}_I - \cos \Omega \sin i \hat{\mathbf{Y}}_I + \cos i \hat{\mathbf{Z}}_I\tag{2.9}$$

where i is the inclination, Ω is the right ascension of the ascending node, and $\bar{\omega}$ is the argument of periapsis.

The rotating frame is defined with respect to the satellite orbit frame by a rotation of the mean anomaly angle about the angular momentum vector. Therefore its basis vectors are $\hat{\mathbf{p}}$, $\hat{\mathbf{q}}$, and $\hat{\mathbf{h}}$. These vectors are defined by

$$\hat{\mathbf{p}} = \cos M \hat{\mathbf{e}} + \sin M \hat{\mathbf{e}}_{\perp}\tag{2.10}$$

$$\hat{\mathbf{q}} = -\sin M \hat{\mathbf{e}} + \cos M \hat{\mathbf{e}}_{\perp}\tag{2.11}$$

$$\hat{\mathbf{h}} = \hat{\mathbf{h}}\tag{2.12}$$

where M is the mean anomaly of the satellite in its orbit. The rotating frame is similar to the local vertical local horizontal frame, and in fact the two are the same for circular orbits.

It will be beneficial for the solar radiation pressure model derived here to express the orientation of the heliocentric orbit and the position of the Sun in the body frame. In this perspective, the Sun seems to be orbiting the body, and the motion is defined by the body's spin and its movement on the heliocentric orbit. The inclination of the heliocentric orbit in the body frame is defined by the angle between $\hat{\mathbf{Z}}_H$ and

$\hat{\mathbf{z}}_b$, which can be described as,

$$\cos i_s = \hat{\mathbf{Z}}_H \cdot \hat{\mathbf{z}}_b = \sin \delta \cos i_H + \cos \delta \sin i_H \sin(\Omega_H - \alpha) \quad (2.13)$$

The node vector of the orbit in the body frame is defined by

$$\hat{\mathbf{n}}_{\Omega_s} = \frac{\hat{\mathbf{z}}_b \times \hat{\mathbf{Z}}_H}{|\hat{\mathbf{z}}_b \times \hat{\mathbf{Z}}_H|} = \cos \Omega_s \hat{\mathbf{x}}_b + \sin \Omega_s \hat{\mathbf{y}}_b \quad (2.14)$$

The right ascension of the ascending node of the Sun in the body frame is

$$\tan \Omega_s = \frac{\hat{\mathbf{y}} \cdot (\hat{\mathbf{z}}_b \times \hat{\mathbf{Z}}_H)}{\hat{\mathbf{x}} \cdot (\hat{\mathbf{z}}_b \times \hat{\mathbf{Z}}_H)} = \frac{\hat{\mathbf{Z}}_H \cdot \hat{\mathbf{x}}_b}{-\hat{\mathbf{Z}}_H \cdot \hat{\mathbf{y}}_b} = \tan(\Omega_{s_0} - \phi) \quad (2.15)$$

where the initial value is

$$\tan \Omega_{s_0} = \frac{\sin i_H \cos(\Omega_H - \alpha)}{\cos \delta \cos i_H - \sin \delta \sin i_H \sin(\Omega_H - \alpha)} \quad (2.16)$$

Note the relationship $\Omega_s = \Omega_{s_0} - \phi$, which states that as the body rotates, the node will regress in the body-fixed frame.

Finally, the argument of perihelion is defined in the body-fixed frame by expressing the orbit perihelion vector, $\hat{\mathbf{X}}_H$, in the body-fixed frame, and measuring the angle between it and the node vector. First note the transverse vector which lies in the orbit plane perpendicular to the node vector, is defined as

$$\hat{\mathbf{n}}_T = \hat{\mathbf{Z}}_H \times \hat{\mathbf{n}}_{\Omega_s} \quad (2.17)$$

Then, the argument of perihelion is defined as

$$\tan \bar{\omega}_s = \frac{\hat{\mathbf{X}}_H \cdot \hat{\mathbf{n}}_T}{\hat{\mathbf{X}}_H \cdot \hat{\mathbf{n}}_{\Omega_s}} = \frac{\hat{\mathbf{X}}_H \cdot \hat{\mathbf{z}}_b}{\hat{\mathbf{Y}}_H \cdot \hat{\mathbf{z}}_b} = \tan(\bar{\omega}_0 + \bar{\omega}_H) \quad (2.18)$$

where the initial value is

$$\tan \bar{\omega}_0 = \frac{\cos \delta \cos(\Omega_H - \alpha)}{\sin \delta \sin i_H - \cos \delta \cos i_H \sin(\Omega_H - \alpha)} \quad (2.19)$$

Again, note the simple relationship $\bar{\omega}_s = \bar{\omega}_0 + \bar{\omega}_H$, where $\bar{\omega}_H$ is the original orbit perihelion argument and $\bar{\omega}_0$ is the shift due to the new coordinate frame. The angles defining the Sun's orbit in the body frame are illustrated in Fig. 2.1.

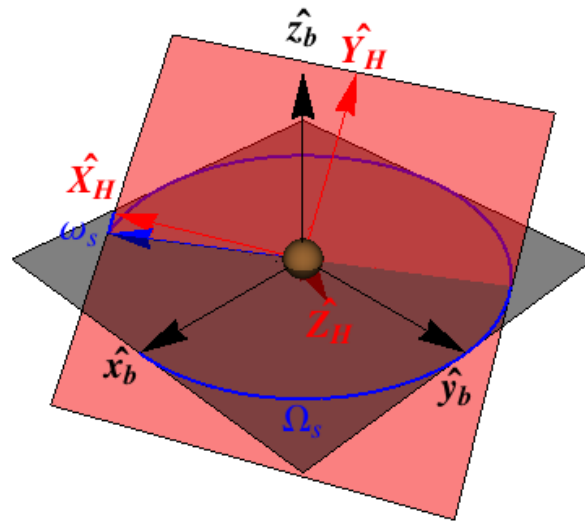


Figure 2.1: Illustration of the Sun orbit parameters in the body frame. The node vector is at the intersection of the $\hat{x}_b - \hat{y}_b$ plane and the $\hat{X}_H - \hat{Y}_H$ plane. The heliocentric orbit plane will rotate in the body frame as the body spins, thus making the node vector process around \hat{z}_b . Ω_s is the angle between \hat{x}_b and the node vector, and $\bar{\omega}_s$ is the angle between the node vector and \hat{X}_H .

The location of the Sun in the body-fixed frame, $\hat{\mathbf{u}}$ (see Fig. 2.2), can now be described using the above orbital elements as,

$$\hat{\mathbf{u}} = \cos(\bar{\omega}_s + \nu_s) \hat{\mathbf{n}}_{\Omega_s} + \sin(\bar{\omega}_s + \nu_s) \hat{\mathbf{n}}_T \quad (2.20)$$

$$\hat{\mathbf{u}} = \cos \delta_s \cos \lambda_s \hat{\mathbf{x}}_b + \cos \delta_s \sin \lambda_s \hat{\mathbf{y}}_b + \sin \delta_s \hat{\mathbf{z}}_b \quad (2.21)$$

where ν_s is the heliocentric orbit true anomaly. In the body-fixed frame, the position of the Sun is represented by δ_s and λ_s , which are called the solar latitude and longitude, respectively. When the secondary spin axis, $\hat{\mathbf{z}}_b$, is assumed to be fixed in inertial space, the angles are defined as,

$$\sin \delta_s = \sin i_s \sin(\bar{\omega}_s + \nu_s) \quad (2.22)$$

$$\lambda_s = \Omega_{s_0} + \lambda_\nu - (\phi + \phi_0) = \Omega_{s_0} + \lambda_\nu - \phi_{total} \quad (2.23)$$

where λ_ν is the longitude of the Sun due to the true anomaly, which is equal to

$$\tan \lambda_\nu = \cos i_s \tan(\bar{\omega}_s + \nu_s) \quad (2.24)$$

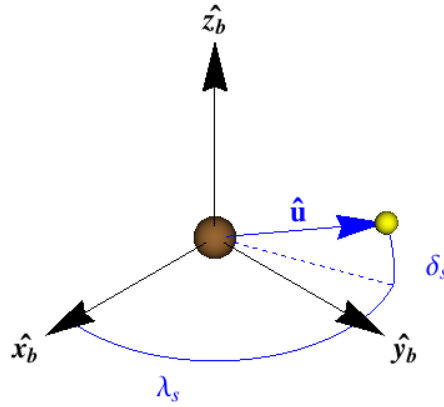


Figure 2.2: Illustration of the Sun vector ($\hat{\mathbf{u}}$) in the body frame with the solar latitude (δ_s) and longitude (λ_s).

The previous relationships can be used to group several terms into the initial solar longitude,

$$\lambda_{s_0} = \Omega_{s_0} + \lambda_\nu \quad (2.25)$$

which allows the equation for the solar longitude to be rewritten as

$$\lambda_s = \lambda_{s_0} - (\phi + \phi_0) = \lambda_{s_0} - \phi_{total} \quad (2.26)$$

Finally, the asteroid-Sun distance is assumed to vary with the true anomaly in a Keplerian fashion, which gives

$$R = \frac{a_s(1 - e_s^2)}{1 + e_s \cos \nu_s} \quad (2.27)$$

where a_s and e_s are the semi-major axis and eccentricity of the heliocentric orbit.

2.2 Solar Radiation Force Representation

The solar radiation force can be expressed as a Fourier series, as derived by Scheeres [92].

$$\mathbf{F}_{SRP} = P(R) \sum_{i=1}^N \mathbf{f}_i(\lambda_s) = P(R) \sum_{n=0}^{\infty} [\mathbf{A}_n(\delta_s) \cos(n\lambda_s) + \mathbf{B}_n(\delta_s) \sin(n\lambda_s)] \quad (2.28)$$

where N is the number of surface elements used to describe the body and $P(R)$ is the solar radiation pressure at a given distance from the Sun R , given to first order as,

$$P(R) = \frac{G_1}{R^2} \quad (2.29)$$

where G_1 is the solar radiation constant and is approximately equal to $1 \times 10^{14} \text{kg km/s}^2$.

The Fourier coefficients, \mathbf{A}_n and \mathbf{B}_n have units of area and are functions of the body shape, reflective properties, and the position of the Sun in the body frame defined by the solar latitude and longitude. The full derivation of the Fourier coefficients is in Scheeres [92]. The interaction between the solar radiation pressure and a surface element of the body is given by,

$$\mathbf{f}_i = - \left[\left\{ \rho_i s_i \left(2\hat{\mathbf{n}}_i \hat{\mathbf{n}}_i - \bar{\bar{U}} \right) + \bar{\bar{U}} \right\} \cdot \hat{\mathbf{u}} \hat{\mathbf{u}} \cdot \hat{\mathbf{n}}_i + a_{2i} \hat{\mathbf{n}}_i \hat{\mathbf{n}}_i \cdot \hat{\mathbf{u}} \right] H_i(\hat{\mathbf{u}}) A_i \quad (2.30)$$

with

$$a_{2i} = B(1 - s_i)\rho_i + (1 - \rho_i)B \quad (2.31)$$

where i is an index that identifies each surface element of the satellite. Each surface has a normal unit vector, $\hat{\mathbf{n}}_i$, a surface area, A_i , and specular and diffuse reflectivity coefficients, s_i and ρ_i respectively. B is the Lambertian scattering coefficient of the surface (ideally equal to $2/3$), $\hat{\mathbf{u}}$ is the Sun unit vector from the surface element to the Sun, $\bar{\bar{U}}$ is the identity dyad, and $H(\hat{\mathbf{u}})$ is the visibility function that accounts for self-shadowing and equals 1 when the Sun is above the horizon of the surface (when the angle between $\hat{\mathbf{u}}$ and $\hat{\mathbf{n}}_i$ is less than 90°) and 0 otherwise.

In general, the solar radiation force is also a function of the solar latitude, δ_s , as shown in Eq. (2.28). However this dependence will be suppressed from here forward because we assume that the secondary spin axis can be considered inertially fixed over longer than one orbit. Then, for a given number of body rotations, the solar latitude is effectively constant as the position on the heliocentric orbit changes much more slowly than body spins. The dependence on the solar latitude will be reintroduced in §5.1.3 when the analysis for the effects over a heliocentric orbit is conducted and the solar latitude is not constant for the timeframe of interest.

Using Eq. (2.26), the Fourier series can be represented as a function of the satellite spin angle as

$$\sum_{i=1}^N \mathbf{f}_i(\phi) = \sum_{n=0}^{\infty} [\mathbf{A}'_n \cos(n\phi) + \mathbf{B}'_n \sin(n\phi)] \quad (2.32)$$

where the single-prime Fourier coefficients are defined in terms of the no-prime Fourier coefficients (\mathbf{A} and \mathbf{B}) as

$$\mathbf{A}'_n = \cos(n(\lambda_{s_0} - \phi_0))\mathbf{A}_n + \sin(n(\lambda_{s_0} - \phi_0))\mathbf{B}_n \quad (2.33)$$

$$\mathbf{B}'_n = \cos(n(\lambda_{s_0} - \phi_0))\mathbf{B}_n - \sin(n(\lambda_{s_0} - \phi_0))\mathbf{A}_n \quad (2.34)$$

Since these generalized Fourier coefficients are a function of λ_ν (from Eq. (2.25)), they are only valid for one location on the heliocentric orbit.

The Fourier coefficients are vector quantities that are defined in the body-fixed frame. However, in order to investigate the effects of this force on the secondary's orbit, they need to be transformed to the secondary's orbital frame. Applying an arbitrary rotation matrix, the Fourier series will become,

$$\sum_{i=1}^N T\mathbf{f}_i(\phi) = \sum_{n=0}^{\infty} [T\mathbf{A}'_n \cos(n\phi) + T\mathbf{B}'_n \sin(n\phi)] \quad (2.35)$$

where T is the rotation matrix from the body frame to the desired orbital frame. If the rotation matrix is distributed inside the Fourier series, a new series expression in terms of Fourier coefficients written directly in the orbit frame is given as

$$\sum_{i=1}^N T\mathbf{f}_i(\phi) = \mathbf{A}_0'' + \sum_{n=1}^{\infty} [\mathbf{A}_n'' \cos(n\phi) + \mathbf{B}_n'' \sin(n\phi)] \quad (2.36)$$

where the new, double-prime Fourier coefficients are functions of the single-prime coefficient vectors. In either case, Eq. (2.35) or (2.36) express the same SRP acceleration in the orbital frame.

2.3 Comparison with other Solar Radiation Pressure Models

A discussion of standard SRP models must begin with the cannonball model. Also recognized as the LAGEOS model due to the fact that it was used for that cannonball shaped spacecraft, this model is based on the spacecraft being a simple sphere with all incident radiation being reflected directly back at the Sun. It is written as

$$\mathbf{a}_{SRP} = -C_R \frac{P(R)}{m} A \hat{\mathbf{u}} \quad (2.37)$$

where A is the cross sectional area seen by the Sun, and C_R is an SRP strength scale factor, nominally equal to $1 + \rho$ to account for the momentum transferred to the object by the initial impact and subsequent reflection of light. It is immediately obvious upon comparison to Eq. (2.30) that this is a zeroth order model for any object which is not actually spherical in shape with constant optical properties. All tangential forces from specular reflection and re-radiation of absorbed light are assumed to cancel exactly. In spacecraft applications, however, these tangential forces can be very important and should not be ignored.

A more detailed spacecraft model was derived for GRACE. The GRACE model [17] looks much more like Eq. (2.30). The spacecraft is represented by the six major surfaces with each surface having its own optical properties. This model is written as

$$\mathbf{a}_{SRP} = -C_R \frac{P(R)}{m} \sum_{k=1}^6 A_k \cos \theta_k \left[(1 - s_k) \hat{\mathbf{u}} + 2 \left(\frac{\rho_k}{3} + s_k \cos \theta_k \right) \hat{\mathbf{n}}_k \right] \quad (2.38)$$

where k is the index for each surface of the satellite. Each surface has a normal unit vector, $\hat{\mathbf{n}}_k$, a surface area, A_k , and specular and diffuse reflectivity coefficients, s_k and ρ_k respectively. Finally, $\cos \theta_k = \hat{\mathbf{u}} \cdot \hat{\mathbf{n}}_k$

and θ_k is the angle between the two unit vectors of interest. In this case, C_R represents a scale factor to be estimated, and has a nominal value of 1.

There are also two semi-analytical models in use to represent the SRP force on GPS spacecraft, one developed by JPL [3] and the other by the University of Bern [102]. These models are different in that the functional form was derived to fit residuals from orbit estimation which were attributed to the SRP force, and therefore are not necessarily similar to the discussion presented here since they are not based in the physical SRP interactions. The details of these models, and a comparison to the model presented in this work is given in §7.2.

The SRP model presented in §2.2 is very similar to the macro-models built with geometric primitives such as those developed for GPS [30], GRACE [17], TOPEX/Poseidon [61], and ICESat [80]. If only one facet is kept in our model, we are effectively reproducing the cannonball model from LAGEOS [53]. By increasing the number of facets used in our model, the accuracy of the true shape and properties of the spacecraft can be retained similar to detailed ray-tracing models [124]. However, one difference between the highly detailed ray-tracing models is that our model does not account for secondary impact of photons due to the reflected light impacting another part of the spacecraft. Using ray-tracing models to reproduce this effect is a numerical process that requires significant computational power, which does not coincide with the goals of our analytical model.

The main benefits of our model, however, do not come from the **a priori** model, but rather from the Fourier analysis we apply to this force in the rotating frame. This analysis allows us to move from a model of the SRP physics, to an observation of how this force can affect the orbit through an intelligent observation of the orbit-attitude coupling. By estimating the coefficients based on the changes to the orbit, the model can account for unmodeled processes (such as secondary photon impact), as well as differences between the physical properties used to derive the **a priori** coefficients and those actually on the spacecraft.

It is also instructive to compare this model to those originally proposed for the BYORP effect by Ćuk [21] and Goldreich [37]. In those papers, the solar radiation pressure force was averaged alone without regard to the orbit, giving a resultant force that is constant in the body frame. This is similar to the cannonball model, except that the constant force need to be along $\hat{\mathbf{u}}$. If this force were expressed as a Fourier series, the

only non-zero components would be $\mathbf{A}'_0(1)$ and $\mathbf{A}'_0(2)$ in the body frame, or in the orbit frame the non-zero components would be $\mathbf{A}''_1(1) = \mathbf{B}''_1(2)$ and $\mathbf{A}''_1(2) = -\mathbf{B}''_1(1)$. There could also be a constant force out of plane represented by $\mathbf{A}'_0(3) = \mathbf{A}''_0(3)$, however the previous studies assumed this component was zero and the orbit plane lay in the ecliptic.

Chapter 3

Orbit Variational Equations

In order to apply any analytical theory to describe the perturbative effect of solar radiation pressure on Keplerian orbits, we must start with variational equations. In this section, variational equations for a set of non-singular orbital elements are derived for use in our analytical development under the presence of an arbitrary disturbing acceleration vector. This is followed by forms of variational equations for the Keplerian and Delaunay orbital elements, in terms of the original equations. This will allow us to immediately have results in terms of any of these element sets once we have solved the problem for the first case.

3.1 Dynamical Elements

In this section, Gauss' equations are solved for specific orbit energy, the specific orbit angular momentum vector, and the eccentricity vector. These elements are chosen because they are well-defined for all orbits, including circular orbits. These elements result in simpler variational equations than the original Gauss equations for the classical orbit elements, but the classical orbit elements are all easily derived from the energy, angular momentum, and eccentricity vector.

To begin, the equations for specific energy (\mathcal{E}), specific angular momentum (\mathbf{h}), and the eccentricity vector (\mathbf{e}) are

$$\mathcal{E} = \frac{\mathbf{v} \cdot \mathbf{v}}{2} - \frac{\mu}{r} \quad (3.1)$$

$$\mathbf{h} = \mathbf{r} \times \mathbf{v} \quad (3.2)$$

$$\mathbf{e} = \frac{1}{\mu} \mathbf{v} \times (\mathbf{r} \times \mathbf{v}) - \hat{\mathbf{r}} \quad (3.3)$$

where μ is the gravitational parameter of the system ($\mu = G(m_1 + m_2)$ where G is the gravitational constant and m_1 and m_2 are the masses of the two bodies in the system), \mathbf{r} is the orbit radius vector, $\hat{\mathbf{r}}$ is the unit vector pointing along the radius vector, and r is the orbit radius magnitude, \mathbf{v} is the orbital velocity vector, and \mathbf{a} is the acceleration being applied to the secondary. Throughout this dissertation a bold term is a vector, the un-bolded is the magnitude, and a bold with a hat over it is a unit vector along the vector, such as

$$\mathbf{r} = r\hat{\mathbf{r}} \quad (3.4)$$

$$\mathbf{v} = v\hat{\mathbf{v}} \quad (3.5)$$

$$\mathbf{h} = h\hat{\mathbf{h}} \quad (3.6)$$

Taking the inertial time derivatives of these equations gives

$$\dot{\mathcal{E}} = \mathbf{v} \cdot \mathbf{a} \quad (3.7)$$

$$\dot{\mathbf{h}} = \mathbf{r} \times \mathbf{a} \quad (3.8)$$

$$\dot{\mathbf{e}} = \frac{1}{\mu} [\mathbf{a} \times \mathbf{h} + \mathbf{v} \times (\mathbf{r} \times \mathbf{a})] \quad (3.9)$$

The following osculating orbit definitions will be used extensively throughout the derivations below.

$$p = \frac{h^2}{\mu} = a(1 - e^2) \quad (3.10)$$

$$r = \frac{p}{1 + e \cos(\nu)} \quad (3.11)$$

$$v = \sqrt{\frac{\mu}{p} [1 + e \cos(\nu) + e^2]} \quad (3.12)$$

$$\hat{\mathbf{r}} = \cos(\nu)\hat{\mathbf{e}} + \sin(\nu)\hat{\mathbf{e}}_{\perp} \quad (3.13)$$

$$\hat{\mathbf{v}} = \sin(\gamma)\hat{\mathbf{r}} + \cos(\gamma)\hat{\boldsymbol{\theta}} \quad (3.14)$$

$$\hat{\boldsymbol{\theta}} = -\sin(\nu)\hat{\mathbf{e}} + \cos(\nu)\hat{\mathbf{e}}_{\perp} \quad (3.15)$$

$$\hat{\mathbf{e}}_{\perp} = \hat{\mathbf{h}} \times \hat{\mathbf{e}} \quad (3.16)$$

where p is the semilatus rectum, ν is the true anomaly and γ is the flight path angle, which is defined by

the following relationships,

$$\sin(\gamma) = \frac{e \sin(\nu)}{\sqrt{1 + 2e \cos(\nu) + e^2}} \quad (3.17)$$

$$\cos(\gamma) = \frac{1 + e \cos(\nu)}{\sqrt{1 + 2e \cos(\nu) + e^2}} \quad (3.18)$$

$$\tan(\gamma) = \frac{e \sin(\nu)}{1 + e \cos(\nu)} \quad (3.19)$$

The above equations are now substituted into the derivative equations to express them in terms of ν .

First we will work on the energy derivative, which after substituting Eqs. (3.13) - (3.15) and rearranging becomes,

$$\dot{\mathcal{E}} = \frac{h}{a(1 - e^2)} [(-\sin(\nu))\hat{\mathbf{e}} + (e + \cos(\nu))\hat{\mathbf{e}}_{\perp}] \cdot \mathbf{a} \quad (3.20)$$

We can directly carry out similar substitutions in the angular momentum derivative by rearranging and substituting Eqs. (3.11) and (3.13) to obtain

$$\begin{aligned} \dot{\mathbf{h}} &= r\hat{\mathbf{r}} \times \mathbf{a} = r\tilde{\mathbf{r}} \cdot \mathbf{a} = r\tilde{\mathbf{r}} \cdot \tilde{\mathbf{a}} \\ &= \frac{a(1 - e^2)}{1 + e \cos(\nu)} [\cos(\nu)\hat{\mathbf{e}} + \sin(\nu)\hat{\mathbf{e}}_{\perp}] \cdot \tilde{\mathbf{a}} \end{aligned} \quad (3.21)$$

The terms $\tilde{\mathbf{r}}$ and $\tilde{\mathbf{a}}$ are the cross product matrices of the associated vectors. For example, for the vector $\mathbf{e} = [e(1) \ e(2) \ e(3)]^T$, the cross product matrix is

$$\tilde{\mathbf{e}} = \begin{bmatrix} 0 & -e(3) & e(2) \\ e(3) & 0 & -e(1) \\ -e(2) & e(1) & 0 \end{bmatrix} \quad (3.22)$$

For the derivative of the eccentricity vector, we can rearrange the equation using dyadic notation to write,

$$\dot{\mathbf{e}} = \frac{1}{\mu} [-\tilde{\mathbf{h}} + \tilde{\mathbf{v}} \cdot \tilde{\mathbf{r}}] \cdot \mathbf{a} \quad (3.23)$$

Use the dyadic identity

$$\tilde{\mathbf{v}} \cdot \tilde{\mathbf{r}} = \mathbf{r}\mathbf{v} - (\mathbf{r} \cdot \mathbf{v})\overline{\overline{U}} \quad (3.24)$$

where $\overline{\overline{U}}$ is the identity dyad and two vectors written as $\mathbf{r}\mathbf{v}$ denote a dyad. This results in

$$\dot{\mathbf{e}} = \frac{1}{\mu} [-\tilde{\mathbf{h}} + \mathbf{r}\mathbf{v} - (\mathbf{r} \cdot \mathbf{v})\overline{\overline{U}}] \cdot \mathbf{a} \quad (3.25)$$

Next, note that by inserting Eqs. (3.13) and (3.15) into Eq. (3.14), we get

$$\hat{\mathbf{v}} = [\sin(\gamma) \cos(\nu) - \cos(\gamma) \sin(\nu)]\hat{\mathbf{e}} + [\sin(\gamma) \sin(\nu) + \cos(\gamma) \cos(\nu)]\hat{\mathbf{e}}_{\perp} \quad (3.26)$$

Combining the previous relationships gives a final form for the eccentricity vector rate as,

$$\begin{aligned} \dot{\mathbf{e}} = \frac{1}{\mu} \left\{ -\tilde{\mathbf{h}} + \frac{h}{1 + e \cos(\nu)} \left[-\cos(\nu) \sin(\nu)\hat{\mathbf{e}}\hat{\mathbf{e}} - \sin^2(\nu)\hat{\mathbf{e}}_{\perp}\hat{\mathbf{e}} \right. \right. \\ \left. \left. + \cos(\nu)[e + \cos(\nu)]\hat{\mathbf{e}}\hat{\mathbf{e}}_{\perp} + \sin(\nu)[e + \cos(\nu)]\hat{\mathbf{e}}_{\perp}\hat{\mathbf{e}}_{\perp} - e \sin(\nu)\bar{\bar{U}} \right] \right\} \cdot \mathbf{a} \end{aligned} \quad (3.27)$$

At this point, the expression for the solar radiation pressure can be inserted into Eqs. (3.20), (3.21), and (3.27) to obtain explicit expressions for the effect the solar radiation pressure has on the secondary's orbit. First note that the acceleration caused by the solar radiation on the secondary is represented by

$$\mathbf{a}_{SRP} = \frac{P(R)}{m} \sum_{n=0}^{\infty} [T\mathbf{A}'_n \cos(n\phi) + T\mathbf{B}'_n \sin(n\phi)] \quad (3.28)$$

where m is the mass of the secondary.

This expression can now be substituted into Eqs. (3.20), (3.21), and (3.27) to obtain,

$$\dot{\mathcal{E}} = \frac{P(R)h}{ma(1 - e^2)} [-\sin(\nu)\hat{\mathbf{e}} + (e + \cos(\nu))\hat{\mathbf{e}}_{\perp}] \cdot T \sum_{n=0}^{\infty} [\mathbf{A}'_n \cos(n\phi) + \mathbf{B}'_n \sin(n\phi)] \quad (3.29)$$

$$\dot{\mathbf{h}} = \frac{P(R)}{m} \frac{a(1 - e^2)}{1 + e \cos(\nu)} [\cos(\nu)\tilde{\mathbf{e}} + \sin(\nu)\tilde{\mathbf{e}}_{\perp}] \cdot T \sum_{n=0}^{\infty} [\mathbf{A}'_n \cos(n\phi) + \mathbf{B}'_n \sin(n\phi)] \quad (3.30)$$

$$\begin{aligned} \dot{\mathbf{e}} = \frac{1}{\mu} \left\{ -h\tilde{\mathbf{h}} + \frac{h}{1 + e \cos(\nu)} \left[-\cos(\nu) \sin(\nu)\hat{\mathbf{e}}\hat{\mathbf{e}} - \sin^2(\nu)\hat{\mathbf{e}}_{\perp}\hat{\mathbf{e}} + \cos(\nu)[e + \cos(\nu)]\hat{\mathbf{e}}\hat{\mathbf{e}}_{\perp} \right. \right. \\ \left. \left. + \sin(\nu)[e + \cos(\nu)]\hat{\mathbf{e}}_{\perp}\hat{\mathbf{e}}_{\perp} - e \sin(\nu)\bar{\bar{U}} \right] \right\} \cdot T \sum_{n=0}^{\infty} [\mathbf{A}'_n \cos(n\phi) + \mathbf{B}'_n \sin(n\phi)] \end{aligned} \quad (3.31)$$

Alternatively, the acceleration caused by the solar radiation on the secondary can be represented directly in the orbit frame by

$$\mathbf{a}_{SRP} = \frac{P(R)}{m} \left[\mathbf{A}''_0 + \sum_{n=1}^{\infty} [\mathbf{A}''_n \cos(n\phi) + \mathbf{B}''_n \sin(n\phi)] \right] \quad (3.32)$$

Using this notation and Eqs. (3.20), (3.21), and (3.27), the effect of the solar radiation on the secondary's

orbit can be written as,

$$\dot{\mathcal{E}} = \frac{P(R)}{m} \frac{h}{a(1-e^2)} [-\sin(\nu)\hat{\mathbf{e}} + (e + \cos(\nu))\hat{\mathbf{e}}_{\perp}] \cdot \left[\mathbf{A}_0'' + \sum_{n=1}^{\infty} [\mathbf{A}_n'' \cos(n\phi) + \mathbf{B}_n'' \sin(n\phi)] \right] \quad (3.33)$$

$$\dot{\mathbf{h}} = \frac{P(R)}{m} \frac{a(1-e^2)}{1+e\cos(\nu)} [\cos(\nu)\tilde{\hat{\mathbf{e}}} + \sin(\nu)\tilde{\hat{\mathbf{e}}}_{\perp}] \cdot \left[\mathbf{A}_0'' + \sum_{n=1}^{\infty} [\mathbf{A}_n'' \cos(n\phi) + \mathbf{B}_n'' \sin(n\phi)] \right] \quad (3.34)$$

$$\dot{\mathbf{e}} = \frac{P(R)}{m} \frac{h}{\mu} \left\{ -\tilde{\hat{\mathbf{h}}} + \frac{1}{1+e\cos(\nu)} \left[-\cos(\nu)\sin(\nu)\hat{\mathbf{e}}\hat{\mathbf{e}} - \sin^2(\nu)\hat{\mathbf{e}}_{\perp}\hat{\mathbf{e}} + \cos(\nu)[e + \cos(\nu)]\hat{\mathbf{e}}\hat{\mathbf{e}}_{\perp} + \sin(\nu)[e + \cos(\nu)]\hat{\mathbf{e}}_{\perp}\hat{\mathbf{e}}_{\perp} - e\sin(\nu)\bar{\bar{U}} \right] \right\} \cdot \left[\mathbf{A}_0'' + \sum_{n=1}^{\infty} [\mathbf{A}_n'' \cos(n\phi) + \mathbf{B}_n'' \sin(n\phi)] \right] \quad (3.35)$$

The two formulations shown in Eqs. (3.29) - (3.31) and (3.33) - (3.35) are useful in different circumstances. Using the first formulation with the single-prime coefficients explicitly shows how the body parameters affect the orbit, assuming that the function form for T is known. The second formulation with the double-prime coefficients is easier to work with especially when considering an eccentric orbit, however it requires an expression of the SRP acceleration in the orbital frame, which is less physically intuitive, but can be derived with T .

3.2 Keplerian Orbital Elements

It is often of interest to see how the Keplerian orbital elements change due to perturbations as this is how most people think about orbits. The evolutionary equations for the standard Keplerian orbit elements can be derived directly from the results shown in §3.1. The downside of analyzing the variation of the orbit in terms of Keplerian orbital elements, as opposed to those presented previously, is that the variational equations will have the well-known singularities for equatorial and circular orbits.

Expressions for the Keplerian elements in terms of energy, angular momentum, and the eccentricity vector are,

$$a = -\frac{\mu}{2\mathcal{E}} \quad (3.36)$$

$$e = |\mathbf{e}| \quad (3.37)$$

$$\cos i = \hat{\mathbf{h}} \cdot \hat{\mathbf{Z}}_I \quad (3.38)$$

$$\tan \Omega = -\frac{\hat{\mathbf{h}} \cdot \hat{\mathbf{X}}_I}{\hat{\mathbf{h}} \cdot \hat{\mathbf{Y}}_I} \quad (3.39)$$

$$\tan \omega = \frac{\hat{\mathbf{e}} \cdot \hat{\mathbf{Z}}_I}{\hat{\mathbf{e}} \cdot \hat{\mathbf{Y}}_I} \quad (3.40)$$

The time derivatives of these equations are taken to determine the variational equations. The variational equation for semi-major axis easily falls out of in terms of energy as,

$$\dot{a} = \frac{2a^2 \dot{\mathcal{E}}}{\mu} \quad (3.41)$$

The angular momentum magnitude and eccentricity evolutions can be determined from the vector quantities by differentiating the magnitude itself,

$$\frac{d}{dt} (h^2) = \frac{d}{dt} (\mathbf{h} \cdot \mathbf{h}) = 2\mathbf{h} \cdot \dot{\mathbf{h}} \quad (3.42)$$

$$\frac{d}{dt} (e^2) = \frac{d}{dt} (\mathbf{e} \cdot \mathbf{e}) = 2\mathbf{e} \cdot \dot{\mathbf{e}} \quad (3.43)$$

Equivalently we can write,

$$\frac{d}{dt} (h^2) = 2h\dot{h} \quad (3.44)$$

$$\frac{d}{dt} (e^2) = 2e\dot{e} \quad (3.45)$$

therefore, by equating the two results we get,

$$\dot{h} = \hat{\mathbf{h}} \cdot \dot{\mathbf{h}} \quad (3.46)$$

$$\dot{e} = \hat{\mathbf{e}} \cdot \dot{\mathbf{e}} \quad (3.47)$$

Suppressing the intervening algebra, we find the variational equations of the orbit angles in terms of \mathcal{E} , \mathbf{h} , and \mathbf{e} to be,

$$\dot{i} = \frac{1}{h \sin i} \left[\dot{h} \cos i - \hat{\mathbf{h}} \cdot \hat{\mathbf{Z}}_I \right] \quad (3.48)$$

$$\dot{\Omega} = \frac{\left[(\hat{\mathbf{h}} \cdot \hat{\mathbf{Y}}_I)(\hat{\mathbf{h}} \cdot \hat{\mathbf{X}}_I) - (\hat{\mathbf{h}} \cdot \hat{\mathbf{X}}_I)(\hat{\mathbf{h}} \cdot \hat{\mathbf{Y}}_I) \right] \cos^2 \Omega}{h(\hat{\mathbf{h}} \cdot \hat{\mathbf{Y}}_I)^2} \quad (3.49)$$

$$\dot{\omega} = \frac{\left[(\dot{\mathbf{e}} \cdot \hat{\mathbf{Z}}_I)(\hat{\mathbf{e}} \cdot \hat{\mathbf{Y}}_I) - (\dot{\mathbf{e}} \cdot \hat{\mathbf{Y}}_I)(\hat{\mathbf{e}} \cdot \hat{\mathbf{Z}}_I) \right] \cos^2 \omega}{e(\hat{\mathbf{e}} \cdot \hat{\mathbf{Y}}_I)^2} \quad (3.50)$$

3.3 Delaunay Elements

Some secular theories, such as Brouwer's [11], prefer the use of canonical variables. In particular, many applications use the Delaunay elements, which are most easily defined in terms of the Keplerian orbital elements as,

$$L = \sqrt{\mu a} \quad (3.51)$$

$$G = L\sqrt{1 - e^2} \quad (3.52)$$

$$H = G \cos i \quad (3.53)$$

$$g = \omega \quad (3.54)$$

$$h_D = \Omega \quad (3.55)$$

The derivatives can be written as,

$$\dot{L} = \frac{1}{2}\sqrt{\frac{\mu}{a}}\dot{a} \quad (3.56)$$

$$\dot{G} = \frac{1}{2}\sqrt{\frac{\mu(1 - e^2)}{a}}\dot{a} - \frac{1}{2}\sqrt{\frac{\mu a e^2}{1 - e^2}}\dot{e} \quad (3.57)$$

$$\dot{H} = \dot{G} \cos i - iG \sin i \quad (3.58)$$

$$\dot{g} = \dot{\omega} \quad (3.59)$$

$$\dot{h}_D = \dot{\Omega} \quad (3.60)$$

Chapter 4

Attitude Dynamics Coupling in the Force Model

The solar radiation pressure force can be termed a body or surface force, in that the force depends on the physical properties and attitude of the secondary body. Eqs. (2.35) and (2.36) show that the SRP force that is determined through the physical properties of the must be mapped to the orbit frame through the rotation matrix, T , in order to see what effect it has on the orbit. In this chapter, dynamical systems are classified based on the attitude motion of the secondary as it orbits the primary. This in turn defines the transformation matrix, which is necessary for the averaging process carried out in Chapter 5.

4.1 Synchronous Rotation

Synchronous rotation is that when the secondary body rotates once with respect to inertial space in the same period as it orbits the primary body about a fixed rotation axis so that one face of the secondary is always toward the primary body. This is a very specific attitude motion, however it is found in many natural and satellite systems. Many moons, such as the Earth's moon, display synchronous rotation due to the fact that they are tidally locked to the primary. Likewise, most binary asteroid systems found to date contain a secondary in synchronous rotation. Finally, many Earth orbiting satellites, such as the GRACE satellite, fall into this category as they are constantly pointing their instruments in the nadir direction. Clearly, therefore, this type of orbit-attitude motion is important to study.

Stating that the secondary is in synchronous rotation has several important implications. First, the rotation pole of the body, $\hat{\mathbf{z}}_b$, is aligned with the orbit angular momentum vector, $\hat{\mathbf{h}}$.

$$\hat{\mathbf{z}}_b = \hat{\mathbf{h}} \quad (4.1)$$

Second, the secondary rotates at a constant rate of one rotation per orbit. Therefore we can write,

$$\phi_{total} = \omega t + \phi_0 \quad (4.2)$$

$$\phi = \omega t \quad (4.3)$$

$$\omega = n = \sqrt{\frac{\mu}{a^3}} \quad (4.4)$$

where ω is the rotation rate of the secondary, ϕ_{total} is the secondary's current rotation angle, ϕ is the rotation angle change since $t = 0$ when the rotation angle was ϕ_0 , n is the mean motion of the secondary's orbit, μ is the gravitational parameter of the primary (or in the case of a binary asteroid, the pair), and a is the semi-major axis of the mutual orbit. Note that ω is positive; this is intentional as synchronous rotation requires that the spin about $\hat{\mathbf{z}}_b$ is positive in order for the facing restriction to be met.

Finally, making the assertion that ϕ_0 is defined at periapsis, then t is the time since periapsis passage, and it can also be stated that

$$\phi_{total} = M + \phi_0 \quad (4.5)$$

$$\phi = M \quad (4.6)$$

where M is the mean anomaly of the secondary. Recall that the definition of the single-prime coefficients in Eqs. (2.33) and (2.34) contain the initial rotation state, ϕ_0 . Therefore, the expressions of the SRP force in terms of the single-prime or double-prime coefficients shown in Eqs. (2.32) and (2.36) can have the Fourier angle, ϕ , replaced with the mean anomaly directly due to Eq. (4.6).

Note that under synchronous rotation, the body frame and the rotating frame are exactly equal. In particular, $\hat{\mathbf{x}}_b = \hat{\mathbf{p}}$ and $\hat{\mathbf{y}}_b = \hat{\mathbf{q}}$, along with the already noted relationship in Eq. (4.1).

When the secondary is in a state of synchronous rotation, it is straightforward to write the rotation matrix from the body frame to the orbit frame as,

$$T = \begin{bmatrix} \cos(\phi) & -\sin(\phi) & 0 \\ \sin(\phi) & \cos(\phi) & 0 \\ 0 & 0 & 1 \end{bmatrix} \quad (4.7)$$

or in dyadic notation as

$$T = \cos(\phi)\hat{\mathbf{e}}\hat{\mathbf{x}}_b - \sin(\phi)\hat{\mathbf{e}}\hat{\mathbf{y}}_b + \sin(\phi)\hat{\mathbf{e}}_{\perp}\hat{\mathbf{x}}_b + \cos(\phi)\hat{\mathbf{e}}_{\perp}\hat{\mathbf{y}}_b + \hat{\mathbf{h}}\hat{\mathbf{z}}_b \quad (4.8)$$

Inserting this definition for the rotation matrix, T , into Eqs. (3.29) - (3.31), we find the variational equations for the energy, angular momentum vector and eccentricity vector in terms of the single-prime coefficients to be

$$\dot{\mathcal{E}} = \frac{P(R)h}{ma(1-e^2)} \left[-\sin(\nu)(\cos(\phi)\hat{\mathbf{x}}_b - \sin(\phi)\hat{\mathbf{y}}_b) \right. \\ \left. + (e + \cos(\nu))(\sin(\phi)\hat{\mathbf{x}}_b + \cos(\phi)\hat{\mathbf{y}}_b) \right] \cdot \sum_{n=0}^{\infty} [\mathbf{A}'_n \cos(n\phi) + \mathbf{B}'_n \sin(n\phi)] \quad (4.9)$$

$$\dot{\mathbf{h}} = \frac{P(R)}{m} \frac{a(1-e^2)}{1+e\cos(\nu)} \left[\cos(\nu) [\sin(\phi)\hat{\mathbf{h}}\hat{\mathbf{x}}_b + \cos(\phi)\hat{\mathbf{h}}\hat{\mathbf{y}}_b - \hat{\mathbf{e}}_{\perp}\hat{\mathbf{z}}_b] \right. \\ \left. + \sin(\nu) [-\cos(\phi)\hat{\mathbf{h}}\hat{\mathbf{x}}_b + \sin(\phi)\hat{\mathbf{h}}\hat{\mathbf{y}}_b + \hat{\mathbf{e}}_{\perp}\hat{\mathbf{z}}_b] \right] \cdot \sum_{n=0}^{\infty} [\mathbf{A}'_n \cos(n\phi) + \mathbf{B}'_n \sin(n\phi)] \quad (4.10)$$

$$\dot{\mathbf{e}} = \frac{h}{\mu} \left\{ -(\cos(\phi)\hat{\mathbf{e}}_{\perp}\hat{\mathbf{x}}_b - \sin(\phi)\hat{\mathbf{e}}_{\perp}\hat{\mathbf{y}}_b - \sin(\phi)\hat{\mathbf{e}}\hat{\mathbf{x}}_b - \cos(\phi)\hat{\mathbf{e}}\hat{\mathbf{y}}_b) \right. \\ \left. + \frac{1}{1+e\cos(\nu)} \left[-\cos(\nu)\sin(\nu)(\cos(\phi)\hat{\mathbf{e}}\hat{\mathbf{x}}_b - \sin(\phi)\hat{\mathbf{e}}\hat{\mathbf{y}}_b) - \sin^2(\nu)(\cos(\phi)\hat{\mathbf{e}}_{\perp}\hat{\mathbf{x}}_b - \sin(\phi)\hat{\mathbf{e}}_{\perp}\hat{\mathbf{y}}_b) \right. \right. \\ \left. \left. + \cos(\nu)[e + \cos(\nu)](\sin(\phi)\hat{\mathbf{e}}\hat{\mathbf{x}}_b + \cos(\phi)\hat{\mathbf{e}}\hat{\mathbf{y}}_b) + \sin(\nu)[e + \cos(\nu)](\sin(\phi)\hat{\mathbf{e}}_{\perp}\hat{\mathbf{x}}_b + \cos(\phi)\hat{\mathbf{e}}_{\perp}\hat{\mathbf{y}}_b) \right. \right. \\ \left. \left. - e\sin(\nu)(\cos(\phi)\hat{\mathbf{e}}\hat{\mathbf{x}}_b - \sin(\phi)\hat{\mathbf{e}}\hat{\mathbf{y}}_b + \sin(\phi)\hat{\mathbf{e}}_{\perp}\hat{\mathbf{x}}_b + \cos(\phi)\hat{\mathbf{e}}_{\perp}\hat{\mathbf{y}}_b + \hat{\mathbf{h}}\hat{\mathbf{z}}_b) \right] \right\} \\ \cdot \sum_{n=0}^{\infty} [\mathbf{A}'_n \cos(n\phi) + \mathbf{B}'_n \sin(n\phi)] \quad (4.11)$$

Alternatively, we can now explicitly define the double-prime coefficients in terms of the single-prime coefficients using the definition of T . By distributing the rotation matrix into the Fourier series as illustrated in Eq. (2.36), the double-prime coefficients simply become functions of the single-prime coefficients. The convention $\mathbf{A}''_n = [A'_n(1) A'_n(2) A'_n(3)]^T$ is used to show the components of a vector. The double-prime coefficients are expressed as

$$\mathbf{A}''_0 = \frac{1}{2} \begin{bmatrix} A'_1(1) - B'_1(2) \\ A'_1(2) + B'_1(1) \\ 2A'_0(3) \end{bmatrix} \quad (4.12)$$

$$\mathbf{A}_1'' = \frac{1}{2} \begin{bmatrix} 2A_0'(1) + A_2'(1) - B_2'(2) \\ 2A_0'(2) + A_2'(2) + B_2'(1) \\ 2A_1'(3) \end{bmatrix} \quad (4.13)$$

$$\mathbf{B}_1'' = \frac{1}{2} \begin{bmatrix} -2A_0'(2) + A_2'(2) + B_2'(1) \\ 2A_0'(1) - A_2'(1) + B_2'(2) \\ 2B_1'(3) \end{bmatrix} \quad (4.14)$$

$$\mathbf{A}_n'' = \frac{1}{2} \begin{bmatrix} A'_{n-1}(1) + A'_{n+1}(1) + B'_{n-1}(2) - B'_{n+1}(2) \\ A'_{n-1}(2) + A'_{n+1}(2) - B'_{n-1}(1) + B'_{n+1}(1) \\ 2A'_n(3) \end{bmatrix} \quad (4.15)$$

$$\mathbf{B}_n'' = \frac{1}{2} \begin{bmatrix} -A'_{n-1}(2) + A'_{n+1}(2) + B'_{n-1}(1) + B'_{n+1}(1) \\ A'_{n-1}(1) - A'_{n+1}(1) + B'_{n-1}(2) + B'_{n+1}(2) \\ 2B'_n(3) \end{bmatrix} \quad (4.16)$$

for $n = 2, 3, \dots, \infty$. The first-order coefficients have a different form due to the reflection of $\sin(\phi)$ and $\cos(\phi)$ for negative ϕ and the fact that $\mathbf{B}'_0 = 0$. The Fourier coefficients, \mathbf{A}_0'' , \mathbf{A}_n'' , and \mathbf{B}_n'' are vectors in the orbital frame.

The motion of the Sun in the body frame under synchronous rotation, which is key for the development of the Fourier series in Chapter 2, can be illustrated through Figs. 2.2 and 4.1. Fig. 2.2 shows the position of the Sun in the body frame. As was mentioned in Chapter 2, if the rotation axis, $\hat{\mathbf{z}}_b$, is fixed inertially then the Sun will appear to orbit the body at a constant latitude. In the case of synchronous rotation, we can also add that the Sun will move in a retrograde motion in the body frame, and will appear to orbit the secondary once per rotation, which is also once per secondary orbit.

Furthermore, the $\hat{\mathbf{x}}_b$ - $\hat{\mathbf{y}}_b$ plane is equivalent to the secondary's orbit plane. This plane is nominally fixed in orientation in inertial space, however the location of the Sun with respect to this plane changes as the system moves along its heliocentric orbit, which changes the latitude of the Sun over the course of the year as given in Eq. (2.22). Therefore as the secondary spins once per orbit, the Sun latitude is effectively

fixed, but over the course of days that latitude slowly changes, bounded by $|\delta_s| \leq \pm i_s$. This process is illustrated in Fig. 4.1.

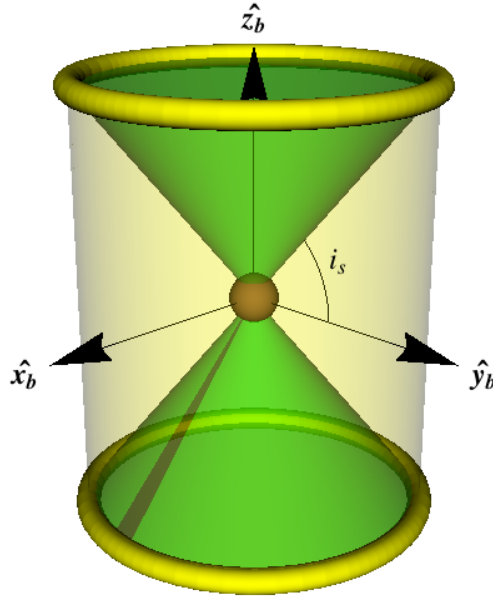


Figure 4.1: Illustration of the variation of the solar position in the body frame over time. The Sun appears to move in a circle as the body spins, tracing out the tube. During this time, the Sun vector ($\hat{\mathbf{u}}$) would trace out the surface of the cone. As the year passes, the tube will vary between the highest and lowest positions based on the solar inclination (i_s) following the surface of the cylinder.

4.2 Periodic Rotation

In this case, the rotation of the secondary is periodic with the orbit, however, it is not synchronous. This means that the restrictions from §4.1 that constrain the rotation such that the same component of the body always face the primary and that the spin axis be fixed are not met. In general this encompasses motions that do not meet Eqs. (4.1) and (4.4). Both the spin axis and spin rate can change over the course of the orbit, however since the motion is constrained to be periodic, the spin axis will repeat its motion from orbit to orbit, and therefore the spin rate is repeated necessarily.

An easy illustration of a body that experiences periodic rotation is seen in the GPS spacecraft. GPS spacecraft do always have one side facing the Earth, similar to a synchronous rotator. However, as the spacecraft orbits, it yaws back and forth about the axis pointed toward Earth to facilitate the solar panel

exposure to the Sun. This means that the spin axis always has one component in the angular momentum direction as with a synchronous rotator, but it has a second component in the $\pm\hat{\mathbf{f}}$ direction which varies in magnitude over the course of the orbit.

One of the consequences of the breaking of synchronous rotation is that it is no longer true that body and rotating frames are equivalent; however this is also the solution of being able to handle these cases with our current model. Note that the rotating frame always satisfies the conditions for synchronous rotation as outlined in §4.1. The motion of the body frame is periodic with respect to the rotating frame as well, meaning that the solar radiation pressure force (which depends on the body frame motion) is periodic in the rotating frame. Putting this all together means that we can still derive the Fourier series expression used in the previous discussion for synchronous rotation; the single-prime coefficients are defined for this case in the rotating frame instead of the body frame, but are mathematically equivalent. The double-prime coefficients can then be determined based on the rotating frame single-prime coefficients exactly as in the synchronous case.

There is one further issue that often arises in the periodic rotation case. It is generally assumed that the normal vector for a surface facet, $\hat{\mathbf{n}}_i$, will be constant in the body frame as would be the case for both LAGEOS and GRACE. However, many satellites have parts that will move in the body frame, for example solar panels that track the Sun (as is the case for GPS). If this motion follows the Sun, it is straightforward to incorporate as the normal vectors for these facets will always be equal to the Sun position unit vector. In the more general case, when the motion is periodic with the orbit but not tracking the Sun's movement, the time varying force can still be computed for every location of the Sun by taking into account the time-varying normal vectors for the moving parts. In either case, the results of this section are fully applicable.

4.3 Higher Order Resonances

In the previous sections, we have been considering cases where there is a 1:1 resonance between the orbit period and the rotation period of the secondary body. Here, we investigate the possibility that the rotation occurs at a different resonance so that the rotation rate is some rational fraction multiple of the

orbit rate. This implies that,

$$\phi = pM \tag{4.17}$$

where $p \in \mathbb{Q}$ is the number of rotations the body makes per orbit. The spin axis is restricted as in §4.1 so that $\hat{\mathbf{z}}_b = \hat{\mathbf{h}}$.

Given this type of rotation, the transformation matrix from the body frame to the orbit frame is given by,

$$T = \begin{bmatrix} \cos(\phi) & -\sin(\phi) & 0 \\ \sin(\phi) & \cos(\phi) & 0 \\ 0 & 0 & 1 \end{bmatrix} = \begin{bmatrix} \cos(pM) & -\sin(pM) & 0 \\ \sin(pM) & \cos(pM) & 0 \\ 0 & 0 & 1 \end{bmatrix} \tag{4.18}$$

This type of rotation motion is not common. However it is delineated here because if this type of motion does occur, secular rates can arise due to the solar radiation pressure. This will be discussed in Chapter 5. Also, this type of motion could have implications for certain dynamical situations, such as spin-stabilized spacecraft and fast spinning binary asteroid primaries.

4.4 Non-resonant Rotation

This is by far the largest and most general set of cases, as it includes all motion that doesn't fall into one of the previous three categories. Despite the name, however, this does not necessarily mean that there are no cases in this category that lead to secular effects from the solar radiation pressure. Two cases that do lead to secular effects are discussed later in this work. §7.4 discusses how the attitude can be modeled for tumbling objects, and §6.2 discusses the case when a secondary body is in near synchronous rotation but librates in-plane about the synchronous attitude.

Chapter 5

Averaging Theory

The process of averaging a dynamical system has been around since the work of Clairaut, Lagrange and Laplace in the 18th century [89]. The basic idea can be illustrated through Fig. 5.1; there is in this case an arbitrary orbital element that changes over time, and contains short-period, long-period, and secular terms. The averaging process is used to separate these terms. In particular, by averaging the differential equation governing the dynamics of the orbital element over one period, the secular term is determined. Mathematically this is stated as,

$$\overline{\dot{\mathbf{e}}} = \frac{1}{T} \int_0^T f(\mathbf{x}(\tau), \tau) d\tau \quad (5.1)$$

where T is the longest period in the system. The method of averaging is a perturbation theory; it assumes that the magnitude of the differential equation, $f(\mathbf{x}(\tau), \tau)$, is very small so that the orbital element does not vary appreciable over the averaging period, T . The secular rate recovered from this process, $\overline{\dot{\mathbf{e}}}$, is a constant, which leads to a linear change in the orbital element. The dynamics of the orbital elements due to these secular terms is often referred to in literature as tracking the mean orbital element evolution [91].

In a system based on Keplerian motion with small perturbations, time may be converted to mean anomaly through the mean motion which is nearly constant over the orbital period, generally taken as the averaging period for these problems. This process of averaging the orbital element evolution over an orbit to find the secular rates is often attributed to Tisserand [47].

In this chapter, this straightforward method of averaging the orbital elements to find the secular terms is employed for our problem of determining the secular effects of solar radiation pressure. §5.1 details the averaging process used, which was outlined here. §5.2 then applies this theory to systems where the

secondary is in a circular orbit, followed by the discussion of elliptical orbits in §5.3.

5.1 Averaging Methodology

The problem of analyzing the orbital effects of SRP is a multi-scale problem. In general, there are three main time scales: the secondary’s spin period, the secondary’s orbit period, and the system’s heliocentric orbit period. In this section, we assume that the secondary is in synchronous rotation about the primary, so that the assumptions explained in §4.1 hold. This causes the spin period and orbit period to become the same, and thus only two time scales remain. The faster time scale is the orbit of the primary about the secondary, while the slower time scale is the orbit of the binary system about the Sun. These two time scales are generally different by orders of magnitude, therefore analyze the system by looking at each time scale in turn. The goal is to find the secular evolution of the secondary’s orbit under the influence of solar radiation pressure. Therefore, we first average over the orbit about the primary, and then average those results over the binary system’s heliocentric orbit.

This section discusses the mathematical process of averaging over these two distinct time scales. §5.1.1 discusses the methodology used to average over the secondary’s orbit, §5.1.2 shows how the offset due to the non-zero mean periodic terms are applied, and §5.1.3 discusses the methodology used to average over the heliocentric orbit.

5.1.1 Orbit Averaging

The methodology for averaging the rate of change of energy, angular momentum, and eccentricity over the secondary’s orbit is straight forward. The averaging is done over the mean anomaly as follows

$$\overline{\dot{\mathcal{E}}} = \frac{1}{2\pi} \int_0^{2\pi} \dot{\mathcal{E}}(M) dM \quad (5.2)$$

$$\overline{\dot{\mathbf{h}}} = \frac{1}{2\pi} \int_0^{2\pi} \dot{\mathbf{h}}(M) dM \quad (5.3)$$

$$\overline{\dot{\mathbf{e}}} = \frac{1}{2\pi} \int_0^{2\pi} \dot{\mathbf{e}}(M) dM \quad (5.4)$$

As shown in the above equations, this requires expressing the rates (Eqs. (3.29) - (3.31) or (3.33) - (3.35)) as functions of mean anomaly, which also implies that the inertial acceleration due to the solar

radiation pressure must be expressed in terms of mean anomaly.

This change of variables from the secondary spin angle, ϕ , to the mean anomaly is made by applying the relationships developed in Chapter 4. In the case of synchronous rotation, the change is simple due to Eq. (4.6). The acceleration is written as

$$\begin{aligned} \mathbf{a}_{SRP}(M) &= \frac{P(R)}{m} \sum_{n=0}^{\infty} [T\mathbf{A}'_n \cos(nM) + T\mathbf{B}'_n \sin(nM)] \\ &= \frac{P(R)}{m} \left[\mathbf{A}''_0 + \sum_{n=1}^{\infty} [\mathbf{A}''_n \cos(nM) + \mathbf{B}''_n \sin(nM)] \right] \end{aligned} \quad (5.5)$$

which results in variational equations that are identical to Eqs. (4.9) - (4.11), except that ϕ is replaced with M . If the attitude motion is periodic, as outlined in §4.2, the acceleration appears exactly the same as above. The only difference is that SRP acceleration is expressed in the rotating frame instead of the body frame.

In the third case, where the attitude motion is in a higher order resonance with the orbit as outlined in §4.3, the relationships from Eqs. (4.17) and (4.18) are used. This results in an extra factor of p appearing in the solar radiation pressure acceleration as

$$\begin{aligned} \mathbf{a}_{SRP}(M) &= \frac{P(R)}{m} \sum_{n=0}^{\infty} [T\mathbf{A}'_n \cos(npM) + T\mathbf{B}'_n \sin(npM)] \\ &= \frac{P(R)}{m} \left[\mathbf{A}''_0 + \sum_{n=1}^{\infty} [\mathbf{A}''_n \cos(npM) + \mathbf{B}''_n \sin(npM)] \right] \end{aligned} \quad (5.6)$$

It is useful to understand the different effects of Eq. (5.5) and (5.6), which is simplest to see through the use of the double-prime formulation. The SRP acceleration is inserted into the variational equations, as in Eqs. (3.33) - (3.35), and averaged over the orbit through the mean anomaly. Noting that the portions of the variational equations which depend on the true anomaly can be represented as a power series in mean anomaly (this is shown in detail in §5.3), the averaging process effectively boils down to matching arguments of like trigonometric series as only these terms will survive the averaging process due to the trigonometric orthogonality equations given in Appendix A.

In the synchronous case, this will be a straightforward matching of terms from the Fourier series of order n with the same order terms in the mean anomaly power series. In the higher order resonance, however, this is made more complicated by the presence of the resonance factor, p . The resonance condition

now requires the orders in the mean anomaly power series to match np . The basic result is that the terms which survive the averaging will have a higher order from one of the two series; since the coefficients for both of these series tend to decrease quickly after the first few orders, this will result in weaker secular terms.

In light of the similarities of process between the three resonant cases, only synchronous rotation will be discussed from here on unless specifically noted. This is also justified for this work because the situations we are mainly concerned with are in either synchronous or periodic rotation, which have effectively the same results.

5.1.2 Offset Due to Periodic Terms

The value of an orbital element can be expressed at any time as a sum of the initial conditions, the secular term, and the periodic term as, [40]

$$\alpha(t) = \alpha_0 + \overline{\dot{\alpha}}t + \alpha_p \quad (5.7)$$

The average value of the orbital element over one orbit is then given by,

$$\overline{\alpha} = \alpha_0 + \overline{\dot{\alpha}}\frac{P}{2} + \overline{\alpha}_p \quad (5.8)$$

where P is the orbit period.

We assume that α_0 is a given starting condition, and we can determine $\overline{\dot{\alpha}}$ by carrying out the averaging discussed in Section 5.1.1. We have not yet considered $\overline{\alpha}_p$, which is the average value of the periodic terms. In most cases, this term will have some non-zero value, and will need to be included to have the secular value track the average of the changing orbital element.

The time derivative of (5.7) is rearranged to give a differential equation for the periodic term as,

$$\dot{\alpha}_p = f(\mathbf{x}, t) - \overline{\dot{\alpha}}(\mathbf{x}) \quad (5.9)$$

where $f(\mathbf{x}, t)$ is the full dynamics for the orbital element, and \mathbf{x} represents the vector of orbital elements.

Integrating this result over time gives the periodic term over that period, and averaging the result gives the average of the periodic term as,

$$\overline{\alpha}_p = \frac{1}{2\pi} \int_0^{2\pi} \left[\int_0^t f(\mathbf{x}(\tau), \tau) d\tau - \overline{\dot{\alpha}}(\mathbf{x}_0)t \right] dM \quad (5.10)$$

Note that the secular rate is evaluated at the initial conditions, \mathbf{x}_0 . This is assumed valid because the second order effects of the change of the orbital elements over one period should be very small here due to the fact that the perturbation is small in magnitude.

After a change of variables from time to mean anomaly, the average of the periodic term becomes,

$$\overline{\alpha}_p = \frac{1}{2\pi} \int_0^{2\pi} \left[\int_{M_0}^M \frac{1}{n} f(\mathbf{x}_0, M') dM' - \overline{\alpha}(\mathbf{x}_0) \frac{M}{n} \right] dM \quad (5.11)$$

where the mean motion is $n = \sqrt{\mu/a^3}$. This results in the useful expression,

$$\overline{\alpha}_p = \frac{1}{2\pi} \int_0^{2\pi} \left[\int_{M_0}^M \sqrt{\frac{a^3}{\mu}} f(\mathbf{x}_0, M') dM' \right] dM - \pi \sqrt{\frac{a^3}{\mu}} \overline{\alpha}(\mathbf{x}_0) \quad (5.12)$$

Using this result, a corrected initial condition can be evaluated from Eq. (5.7),

$$\overline{\alpha}(t_0) = \alpha_0 + \overline{\alpha}_p \quad (5.13)$$

5.1.3 Year Averaging

The Fourier coefficients used in the orbit averaging are calculated for one particular solar latitude value, δ_s , at a time. Therefore the orbit averaged results are only valid when the binary system is at the position in the heliocentric orbit such that the Sun is at this assumed latitude in the body frame. By averaging the rate equations again over the solar orbit, we remove this dependency and get results valid for long term predictions.

Following the method set out in [92], the yearly average can be determined by first recognizing that each of our orbital element equations can be expressed in the form

$$\dot{\bar{x}} = P(R) \bar{f}(x, \nu'_s) \quad (5.14)$$

where ν_s is the true anomaly of the satellite in it's solar orbit, $\bar{\omega}_s$ is the argument of perihelion, $\nu'_s = \bar{\omega}_s + \nu_s$ which is the angle along the orbit from the ascending node, and $\bar{f}()$ is the functional form of the orbit averaged rate equations.

To obtain the averaged value of the rate over one solar orbit $\left(\overline{\dot{x}}\right)$, we take

$$\overline{\dot{x}} = \frac{1}{2\pi} \int_0^{2\pi} P(R) \bar{f}(x, \nu'_s) dM \quad (5.15)$$

but the classical result $dM = R^2/a_s^2\sqrt{1-e_s^2}d\nu'_s$ can be substituted (where a_s and e_s are the semi-major axis and eccentricity of the heliocentric orbit), which results in

$$\bar{\bar{x}} = \frac{1}{2\pi} \frac{G_1}{a_s^2\sqrt{1-e_s^2}} \int_0^{2\pi} \bar{f}(x, \nu'_s) d\nu'_s \quad (5.16)$$

Examining Eqs. (3.29) - (3.31), it is clear that the only terms which depend on ν'_s are the Fourier coefficients. Therefore, when the year averaging integral is performed, it is only the Fourier coefficients that are actually integrated. The final result for the yearly averaged rate equations will have the form,

$$\bar{\bar{x}} = \frac{1}{2\pi} \frac{G_1}{a_s^2\sqrt{1-e_s^2}} \bar{f}(x, \bar{C}_n) \quad (5.17)$$

where the functional form, $\bar{f}()$, will be the same as the orbit averaged results but the coefficients are now replaced with the year averaged versions. This is an important result because it allows us to average the coefficients offline for a given orbit and then substitute the results into the year averaged equations for that case. The results of the form in Eq. (5.17) are written with the no-prime Fourier coefficients, which have their direct dependence on the heliocentric orbit expressed clearly. Due to the fact that the single-prime and double-prime coefficients are derived from the no-prime coefficient, expressions for the year averaged values for all three types of coefficients can be derived. These derivations are shown in the following sub-sections.

5.1.3.1 No-prime Fourier Coefficients

The dependence of the Fourier coefficients on the heliocentric orbit is apparent in the no-prime Fourier coefficients. These coefficients were constructed based on the position of the Sun in the body-fixed frame. This position is given in Eq. (2.21) in terms of the latitude and longitude. The latitude of the Sun changes as the binary system moves in it's heliocentric orbit, and the averaging of this motion is discussed here.

Due to the relationships in Eqs. (2.33) and (2.34), along with the relationship $\lambda_{s_0} = \Omega_{s_0} + \lambda_\nu$, the no-prime coefficients will always appear multiplied by $\sin(\Omega_{s_0} + \lambda_\nu - \phi_0)$ or $\cos(\Omega_{s_0} + \lambda_\nu - \phi_0)$. These terms are rearranged using trigonometric properties to isolate the $\sin(\lambda_\nu)$ and $\cos(\lambda_\nu)$ terms as λ_ν also varies with the heliocentric orbit. The averaging of the no-prime coefficients therefore actually involves averaging the multiplication of these two terms that vary over the heliocentric orbit. This averaging can be made simpler by investigating the properties of these different values.

The Fourier coefficients are purely a function of the solar latitude, δ_s , and the solar latitude is even about the values $\nu'_s = \pi/2, 3\pi/2$ over the ranges $[0, \pi]$ and $[\pi, 2\pi]$, respectively, via Eq. (2.22). Therefore, the Fourier coefficients are symmetric such that $C(\nu'_s) = C(\pi - \nu'_s)$ over those ranges, where $C(-)$ is an arbitrary (A or B) Fourier coefficient. Note, however, that the same claim can not be made over the entire range $[0, 2\pi]$ because the Fourier coefficients are not symmetric for positive and negative solar latitudes.

Furthermore, considering the following equations for λ_ν ,

$$\cos(\lambda_\nu) = \frac{\cos(\nu'_s)}{\cos(\delta_s)} \quad (5.18)$$

$$\sin(\lambda_\nu) = \frac{\cos(i_s) \sin(\nu'_s)}{\cos(\delta_s)} \quad (5.19)$$

Since i_s is assumed constant for this averaging process to be valid, and in light of the relationship of δ_s discussed above, Eqs. (5.18) and (5.19) show that $\cos(\lambda_\nu)$ is odd and $\sin(\lambda_\nu)$ is even about $\nu'_s = \pi/2, 3\pi/2$.

This relationship can be extended to higher frequencies as well. The value of $\cos(n\lambda_\nu)$, where n is the frequency, is even about $\nu'_s = \pi/2, 3\pi/2$ for even frequencies, and odd about these values for odd frequencies. Similarly, $\sin(n\lambda_\nu)$ is even about $\nu'_s = \pi/2, 3\pi/2$ for odd frequencies, and odd about these values for even frequencies.

Thus, when we average over the true anomaly, terms of $C(\nu'_s) \cos(\lambda_\nu)$ will average to zero for odd frequencies, and will average to some non-zero value for even frequencies. On the other hand, terms of $C(\nu'_s) \sin(\lambda_\nu)$ will average to some non-zero value for odd frequencies, and will average to zero for even frequencies.

The year averaged values of the no-prime Fourier coefficients are expressed as,

$$\bar{\mathbf{C}}_n = \begin{cases} \frac{1}{2\pi} \int_0^{2\pi} \mathbf{A}_0 d\nu'_s & n = 0 \\ \frac{1}{2\pi} \int_0^{2\pi} \sin(n\lambda_\nu) \mathbf{C}_n d\nu'_s & n \text{ is odd} \\ \frac{1}{2\pi} \int_0^{2\pi} \cos(n\lambda_\nu) \mathbf{C}_n d\nu'_s & n \text{ is even} \end{cases} \quad (5.20)$$

The Fourier coefficients vary over the orbit about the Sun because different parts of the asteroid are exposed to sunlight as it spins, or the same faces are exposed from different angles. These variations are often non-smooth due to the fact that new faces are being exposed or hidden. Therefore, the averaged Fourier

coefficients generally need to be carried out numerically. A description of how this can be done is given in [92].

5.1.3.2 Single-prime Fourier Coefficients

The year averaged single-prime coefficients are derived by mapping them back to the no-prime set through Eqs. (2.33) and (2.34). The year averaged no-prime coefficients can then be used to come up with expressions for the year averaged single-prime coefficients.

Averaging \mathbf{A}'_0

Investigating Eq. (2.33) for $n = 0$ quickly reveals that $\mathbf{A}'_0 = \mathbf{A}_0$. Therefore, the year averaged value is,

$$\overline{\mathbf{A}'_0} = \overline{\mathbf{A}_0} \quad (5.21)$$

Averaging \mathbf{A}'_n

Using Equation (2.33), along with the relationship $\lambda_{s_0} = \Omega_{s_0} + \lambda_\nu$, we can write,

$$\mathbf{A}'_n = \cos(n(\Omega_{s_0} + \lambda_\nu - \phi_0))\mathbf{A}_n + \sin(n(\Omega_{s_0} + \lambda_\nu - \phi_0))\mathbf{B}_n \quad (5.22)$$

which can be rearranged as,

$$\begin{aligned} \mathbf{A}'_n = & \left[\cos(n(\Omega_{s_0} - \phi_0)) \cos(n\lambda_\nu) - \sin(n(\Omega_{s_0} - \phi_0)) \sin(n\lambda_\nu) \right] \mathbf{A}_n \\ & + \left[\sin(n(\Omega_{s_0} - \phi_0)) \cos(n\lambda_\nu) + \cos(n(\Omega_{s_0} - \phi_0)) \sin(n\lambda_\nu) \right] \mathbf{B}_n \end{aligned} \quad (5.23)$$

or finally as,

$$\begin{aligned} \mathbf{A}'_n = & \left[\cos(n(\Omega_{s_0} - \phi_0))\mathbf{A}_n + \sin(n(\Omega_{s_0} - \phi_0))\mathbf{B}_n \right] \cos(n\lambda_\nu) \\ & + \left[-\sin(n(\Omega_{s_0} - \phi_0))\mathbf{A}_n + \cos(n(\Omega_{s_0} - \phi_0))\mathbf{B}_n \right] \sin(n\lambda_\nu) \end{aligned} \quad (5.24)$$

Carrying out the year averaging results in,

$$\overline{\mathbf{A}'_n} = \begin{cases} -\sin(n(\Omega_{s_0} - \phi_0))\overline{\mathbf{A}}_n + \cos(n(\Omega_{s_0} - \phi_0))\overline{\mathbf{B}}_n & n \text{ is odd} \\ \cos(n(\Omega_{s_0} - \phi_0))\overline{\mathbf{A}}_n + \sin(n(\Omega_{s_0} - \phi_0))\overline{\mathbf{B}}_n & n \text{ is even} \end{cases} \quad (5.25)$$

Averaging \mathbf{B}'_n

Using Equation (2.34), along with the relationship $\lambda_{s_0} = \Omega_{s_0} + \lambda_\nu$, we can write,

$$\mathbf{B}'_n = \cos(n(\Omega_{s_0} + \lambda_\nu - \phi_0))\mathbf{B}_n - \sin(n(\Omega_{s_0} + \lambda_\nu - \phi_0))\mathbf{A}_n \quad (5.26)$$

which can be rearranged as,

$$\begin{aligned} \mathbf{B}'_n &= \left[\cos(n(\Omega_{s_0} - \phi_0)) \cos(n\lambda_\nu) - \sin(n(\Omega_{s_0} - \phi_0)) \sin(n\lambda_\nu) \right] \mathbf{B}_n \\ &\quad - \left[\sin(n(\Omega_{s_0} - \phi_0)) \cos(n\lambda_\nu) + \cos(n(\Omega_{s_0} - \phi_0)) \sin(n\lambda_\nu) \right] \mathbf{A}_n \end{aligned} \quad (5.27)$$

or finally as,

$$\begin{aligned} \mathbf{B}'_n &= \left[\cos(n(\Omega_{s_0} - \phi_0))\mathbf{B}_n - \sin(n(\Omega_{s_0} - \phi_0))\mathbf{A}_n \right] \cos(n\lambda_\nu) \\ &\quad - \left[\sin(n(\Omega_{s_0} - \phi_0))\mathbf{B}_n + \cos(n(\Omega_{s_0} - \phi_0))\mathbf{A}_n \right] \sin(n\lambda_\nu) \end{aligned} \quad (5.28)$$

Carrying out the year averaging results in,

$$\bar{\mathbf{B}}'_n = \begin{cases} -\sin(n(\Omega_{s_0} - \phi_0))\bar{\mathbf{B}}_n - \cos(n(\Omega_{s_0} - \phi_0))\bar{\mathbf{A}}_n & n \text{ is odd} \\ \cos(n(\Omega_{s_0} - \phi_0))\bar{\mathbf{B}}_n - \sin(n(\Omega_{s_0} - \phi_0))\bar{\mathbf{A}}_n & n \text{ is even} \end{cases} \quad (5.29)$$

5.1.3.3 Double-prime Fourier Coefficients

The double-prime coefficients are functions of the single-prime coefficients only, as illustrated in Eqs. (4.12) - (4.16). Therefore, the year averaged values of the double-prime coefficients can be described as functions of the results in Section 5.1.3.2.

Averaging \mathbf{A}''_0

The relationship to the single-prime coefficients is given by Eq. (4.12). Averaging these components over a year gives the following result,

$$\bar{\mathbf{A}}''_0 = \frac{1}{2} \begin{bmatrix} \bar{A}'_1(1) - \bar{B}'_1(2) \\ \bar{A}'_1(2) + \bar{B}'_1(1) \\ 2\bar{A}'_0(3) \end{bmatrix} \quad (5.30)$$

Averaging the $n = 1$ Frequency Coefficients

The relationship to the single-prime coefficients is given by Eqs. (4.13) and (4.14). Averaging these

components over a year gives the following result,

$$\bar{\mathbf{A}}_1'' = \frac{1}{2} \begin{bmatrix} 2\bar{A}'_0(1) + \bar{A}'_2(1) - \bar{B}'_2(2) \\ 2\bar{A}'_0(2) + \bar{A}'_2(2) + \bar{B}'_2(1) \\ 2\bar{A}'_1(3) \end{bmatrix} \quad (5.31)$$

$$\bar{\mathbf{B}}_1'' = \frac{1}{2} \begin{bmatrix} -2\bar{A}'_0(2) + \bar{A}'_2(2) + \bar{B}'_2(1) \\ 2\bar{A}'_0(1) - \bar{A}'_2(1) + \bar{B}'_2(2) \\ 2\bar{B}'_1(3) \end{bmatrix} \quad (5.32)$$

Averaging $n > 1$ Frequency Coefficients

The relationship to the single-prime coefficients is given by Eqs. (4.15) and (4.16). Averaging these components over a year gives the following result,

$$\bar{\mathbf{A}}_n'' = \frac{1}{2} \begin{bmatrix} \bar{A}'_{n-1}(1) + \bar{A}'_{n+1}(1) + \bar{B}'_{n-1}(2) - \bar{B}'_{n+1}(2) \\ \bar{A}'_{n-1}(2) + \bar{A}'_{n+1}(2) - \bar{B}'_{n-1}(1) + \bar{B}'_{n+1}(1) \\ 2\bar{A}'_n(3) \end{bmatrix} \quad (5.33)$$

$$\bar{\mathbf{B}}_n'' = \frac{1}{2} \begin{bmatrix} -\bar{A}'_{n-1}(2) + \bar{A}'_{n+1}(2) + \bar{B}'_{n-1}(1) + \bar{B}'_{n+1}(1) \\ \bar{A}'_{n-1}(1) - \bar{A}'_{n+1}(1) + \bar{B}'_{n-1}(2) + \bar{B}'_{n+1}(2) \\ 2\bar{B}'_n(3) \end{bmatrix} \quad (5.34)$$

Care should be taken when evaluating this coefficient. If n is even, the year averaged single-prime coefficients from Section 5.1.3.2 that are used are **odd**. Likewise, if n is odd, the year averaged single-prime coefficients that are used are **even**.

5.1.4 Long Term Averaging

Extremely long term predictions may require another level of averaging. As is shown in Eqs. (5.21), (5.25), and (5.29), the Sun's node position (Ω_{s0}) appears with every order of single-prime coefficient other than zero. In the development so far, the node is assumed to be constant. However, we know that due to dynamics not considered in this dissertation, this node will precess over time. Therefore, very long term predictions of orbit evolution would require taking this movement into account. For the single-prime coefficients, averaging over the node will result in all terms disappearing except for \mathbf{A}'_0 .

While this long term averaging may seem reasonable, it may not be completely valid. This is because that averaging would assume that the secondary's orbital elements are assumed constant over the time span in order to average, and this may not be the case.

5.2 Application to a Circular Orbit

In this section, perturbation theory will be applied to a circular orbit and averaged. The resulting equations will then be compared to a full dynamics simulation to determine how accurately they estimate the secular effects of the solar radiation pressure.

5.2.1 Circular Orbit Average Equation Derivation

For a circular orbit, the eccentricity is zero, and therefore $\hat{\mathbf{e}}$ and ν are undefined. To resolve this, an arbitrary vector $\hat{\mathbf{a}}$ in the orbital plane is chosen, and ν is replaced with θ , which is just the angle between the current secondary position vector and $\hat{\mathbf{a}}$, measured in the positive direction about the angular momentum vector. Given this, θ is the same as the mean anomaly, M , and Eq. (4.6) is modified to become,

$$\phi = \theta \quad (5.35)$$

A third unit vector, $\hat{\mathbf{b}} = \hat{\mathbf{h}} \times \hat{\mathbf{a}}$ completes the basis set $\{\hat{\mathbf{a}}, \hat{\mathbf{b}}, \hat{\mathbf{h}}\}$.

Using these definitions, and recognizing that for a circular orbit $e = 0$, Eqs. (3.29), (3.30), and (3.31) simplify to:

$$\dot{\mathcal{E}} = \frac{P(R)}{m} \frac{h}{a} \hat{\mathbf{y}}_b \cdot \sum_{n=0}^{\infty} [\mathbf{A}'_n \cos(n\theta) + \mathbf{B}'_n \sin(n\theta)] \quad (5.36)$$

$$\dot{\mathbf{h}} = \frac{P(R)}{m} a \left[\sin(\theta) \hat{\mathbf{a}} \hat{\mathbf{z}}_b - \cos(\theta) \hat{\mathbf{b}} \hat{\mathbf{z}}_b + \hat{\mathbf{h}} \hat{\mathbf{y}}_b \right] \cdot \sum_{n=0}^{\infty} [\mathbf{A}'_n \cos(n\theta) + \mathbf{B}'_n \sin(n\theta)] \quad (5.37)$$

$$\dot{\mathbf{e}} = \frac{P(R)}{m} \frac{h}{\mu} \left[\sin(\theta) \hat{\mathbf{a}} \hat{\mathbf{x}}_b + 2 \cos(\theta) \hat{\mathbf{a}} \hat{\mathbf{y}}_b - \cos(\theta) \hat{\mathbf{b}} \hat{\mathbf{x}}_b + 2 \sin(\theta) \hat{\mathbf{b}} \hat{\mathbf{y}}_b \right] \cdot \sum_{n=0}^{\infty} [\mathbf{A}'_n \cos(n\theta) + \mathbf{B}'_n \sin(n\theta)] \quad (5.38)$$

where $\{\tilde{\hat{\mathbf{a}}}, \tilde{\hat{\mathbf{b}}}, \tilde{\hat{\mathbf{h}}}\}$ are the cross product matrices of the basis vectors $\{\hat{\mathbf{a}}, \hat{\mathbf{b}}, \hat{\mathbf{h}}\}$. Note that the change in the angular momentum vector has components in all three orbital frame directions, while the change in eccentricity is confined to the orbital plane.

For the circular synchronous case the mean anomaly and θ are the same, thus

$$dM = d\theta \quad (5.39)$$

Therefore the orbital elements variations can be averaged over θ instead of the mean anomaly to obtain the secular variation over one orbit as

$$\overline{\dot{\mathcal{E}}} = \frac{1}{2\pi} \int_0^{2\pi} \dot{\mathcal{E}} d\theta \quad (5.40)$$

$$\overline{\dot{\mathbf{h}}} = \frac{1}{2\pi} \int_0^{2\pi} \dot{\mathbf{h}} d\theta \quad (5.41)$$

$$\overline{\dot{\mathbf{e}}} = \frac{1}{2\pi} \int_0^{2\pi} \dot{\mathbf{e}} d\theta \quad (5.42)$$

Inserting Eqs. (5.36) - (5.38) into Eqs. (5.40) - (5.42) and carrying out the averaging using the orthogonality conditions for trigonometric functions, the result is

$$\overline{\dot{\mathcal{E}}} = \frac{P(R)}{m} \frac{h}{a} \hat{\mathbf{y}}_b \cdot \mathbf{A}'_0 \quad (5.43)$$

$$\overline{\dot{\mathbf{h}}} = \frac{P(R)}{m} \frac{a}{2} \left[\hat{\mathbf{a}} \hat{\mathbf{z}}_b \cdot \mathbf{B}'_1 - \hat{\mathbf{b}} \hat{\mathbf{z}}_b \cdot \mathbf{A}'_1 + 2\hat{\mathbf{h}} \hat{\mathbf{y}}_b \cdot \mathbf{A}'_0 \right] \quad (5.44)$$

$$\overline{\dot{\mathbf{e}}} = \frac{P(R)}{m} \frac{h}{2\mu} \left[\hat{\mathbf{a}} \hat{\mathbf{x}}_b \cdot \mathbf{B}'_1 + 2\hat{\mathbf{a}} \hat{\mathbf{y}}_b \cdot \mathbf{A}'_1 - \hat{\mathbf{b}} \hat{\mathbf{x}}_b \cdot \mathbf{A}'_1 + 2\hat{\mathbf{b}} \hat{\mathbf{y}}_b \cdot \mathbf{B}'_1 \right] \quad (5.45)$$

Therefore, for the circular case, we can determine the secular variation of the orbital energy, angular momentum, and the eccentricity vector, with only the first 3 vector quantities of the Fourier series of the solar radiation force. Actually, we don't even need the full vector of the constant term; we only need the second component, $\mathbf{A}'_0(2)$, for a total of 7 components.

Alternatively, the variable substitutions for the circular case could be made to Eqs. (3.33) - (3.35) to get,

$$\dot{\mathcal{E}} = \frac{P(R)}{m} \frac{h}{a} \left[-\sin(\theta) \hat{\mathbf{a}} + \cos(\theta) \hat{\mathbf{b}} \right] \cdot \left[\mathbf{A}''_0 + \sum_{n=1}^{\infty} [\mathbf{A}''_n \cos(n\theta) + \mathbf{B}''_n \sin(n\theta)] \right] \quad (5.46)$$

$$\dot{\mathbf{h}} = \frac{P(R)}{m} a \left[\cos(\theta) \tilde{\hat{\mathbf{a}}} + \sin(\theta) \tilde{\hat{\mathbf{b}}} \right] \cdot \left[\mathbf{A}''_0 + \sum_{n=1}^{\infty} [\mathbf{A}''_n \cos(n\theta) + \mathbf{B}''_n \sin(n\theta)] \right] \quad (5.47)$$

$$\begin{aligned} \dot{\mathbf{e}} = \frac{P(R)}{m} \frac{h}{\mu} \left[-\tilde{\hat{\mathbf{h}}} - \cos(\theta) \sin(\theta) \hat{\mathbf{a}} \hat{\mathbf{a}} - \sin^2(\theta) \hat{\mathbf{b}} \hat{\mathbf{a}} + \cos^2(\theta) \hat{\mathbf{a}} \hat{\mathbf{b}} \right. \\ \left. + \sin(\theta) \cos(\theta) \hat{\mathbf{b}} \hat{\mathbf{b}} \right] \cdot \left[\mathbf{A}''_0 + \sum_{n=1}^{\infty} [\mathbf{A}''_n \cos(n\theta) + \mathbf{B}''_n \sin(n\theta)] \right] \end{aligned} \quad (5.48)$$

These equations can then be inserted into Eqs. (5.40) - (5.42) to obtain the secular rates in terms of the double-prime coefficients as,

$$\overline{\dot{e}} = \frac{P(R)}{m} \frac{h}{2a} \left[-\hat{\mathbf{a}} \cdot \mathbf{B}_1'' + \hat{\mathbf{b}} \cdot \mathbf{A}_1'' \right] \quad (5.49)$$

$$\overline{\dot{\mathbf{h}}} = \frac{P(R)}{m} \frac{a}{2} \left[\tilde{\hat{\mathbf{a}}} \cdot \mathbf{A}_1'' + \tilde{\hat{\mathbf{b}}} \cdot \mathbf{B}_1'' \right] \quad (5.50)$$

$$\overline{\dot{\mathbf{e}}}} = \frac{P(R)}{m} \frac{h}{2\mu} \left[-2\tilde{\hat{\mathbf{h}}} \cdot \mathbf{A}''_0 - \frac{1}{2}\hat{\mathbf{a}}\hat{\mathbf{a}} \cdot \mathbf{B}_2'' - \hat{\mathbf{b}}\hat{\mathbf{a}} \cdot \mathbf{A}''_0 + \frac{1}{2}\hat{\mathbf{b}}\hat{\mathbf{a}} \cdot \mathbf{A}''_2 + \hat{\mathbf{a}}\hat{\mathbf{b}} \cdot \mathbf{A}''_0 + \frac{1}{2}\hat{\mathbf{a}}\hat{\mathbf{b}} \cdot \mathbf{A}''_2 + \frac{1}{2}\hat{\mathbf{b}}\hat{\mathbf{b}} \cdot \mathbf{B}_2'' \right] \quad (5.51)$$

It can be shown by substituting Eqs. (4.12) - (4.16) into the above that Eqs. (5.49) - (5.51) are equivalent to Eqs. (5.43) - (5.45).

5.2.1.1 Averaged Keplerian Orbital Elements

Note that the over-line indicating the orbit averaging can be applied immediately to the previously derived variational equations due to the first-order assumption in the averaging process that the orbit elements are constant over the orbit. Therefore, using Eqs. (2.7) - (2.9), and (5.43) - (5.45), the evolutionary equations for the Keplerian orbit elements due to SRP can be written as,

$$\overline{\dot{a}} = 2 \frac{P(R)}{m} n \left[\hat{\mathbf{q}} \cdot \mathbf{A}'_0 \right] \quad (5.52)$$

$$\overline{\dot{e}} = \frac{1}{2} \frac{P(R)}{m} n \left[\hat{\mathbf{p}} \cdot \mathbf{B}'_1 + 2\hat{\mathbf{q}} \cdot \mathbf{A}'_1 \right] \quad (5.53)$$

$$\overline{\dot{i}} = -\frac{1}{2} \frac{P(R)}{m} \sqrt{\frac{a}{\mu}} \left[\sin \Omega \hat{\mathbf{h}} \cdot \mathbf{B}'_1 + \cos \Omega \hat{\mathbf{h}} \cdot \mathbf{A}'_1 \right] \quad (5.54)$$

$$\overline{\dot{\Omega}} = -\frac{1}{2} \frac{P(R)}{m} \sqrt{\frac{a}{\mu}} \frac{\cos^2 \Omega}{\sin i \cos^2 \omega} \left[\cos \Omega \hat{\mathbf{h}} \cdot \mathbf{B}'_1 + \sin \Omega \hat{\mathbf{h}} \cdot \mathbf{A}'_1 \right] \quad (5.55)$$

$$\overline{\dot{\omega}} = \frac{P(R)}{m} \frac{1}{2e} \sqrt{\frac{a}{\mu}} \frac{\cos^2 \omega \sin i \sin \omega}{(\cos i \cos \omega \sin \Omega + \cos \Omega \sin \omega)^2} \left[-\hat{\mathbf{p}} \cdot \mathbf{A}'_1 + 2\hat{\mathbf{q}} \cdot \mathbf{B}'_1 \right] \quad (5.56)$$

where $n = \sqrt{a^3/\mu}$ is the mean motion. The fact that $h = \sqrt{\mu a}$ for a circular orbit was also used.

5.2.1.2 Averaged Delaunay Elements

The variational equations derived in §3.3 were still written in terms of the Keplerian orbital elements, so before averaging we would like to remove this dependence. Using the following relationships,

$$\sin(\arccos(x)) = \sqrt{1 - x^2} \quad (5.57)$$

so that

$$\sin i = \sin(\arccos(\cos i)) = \sqrt{1 - \cos^2 i} \quad (5.58)$$

and

$$\cos i = \frac{H}{G} \quad (5.59)$$

so finally

$$\sin i = \sqrt{1 - (H/G)^2} \quad (5.60)$$

Recall that,

$$\sqrt{1 - e^2} = \frac{G}{L} \quad (5.61)$$

which gives

$$e^2 = 1 - \frac{G^2}{L^2} \quad (5.62)$$

$$a = \frac{L^2}{\mu} \quad (5.63)$$

$$\sqrt{\frac{a}{\mu}} = \frac{L}{\mu} \quad (5.64)$$

$$n = \frac{L^3}{\mu^2} \quad (5.65)$$

and substituting Eqs. (3.41), (3.46) - (3.50) into Eqs. (3.56) - (3.60), we get self-consistent variational equations for the Delaunay elements. Skipping the algebra, the orbit averaged variational equations for a circular orbit are,

$$\dot{\bar{L}} = \frac{P(R)}{m} \frac{L^2}{\mu} \left[\hat{\mathbf{q}} \cdot \mathbf{A}'_0 \right] \quad (5.66)$$

$$\dot{\bar{G}} = \frac{P(R)}{m} \left\{ \frac{GL}{\mu} \left[\hat{\mathbf{q}} \cdot \mathbf{A}'_0 \right] - \frac{1}{4} \frac{L^5}{G\mu^2} \sqrt{1 - \frac{G^2}{L^2}} \left[\hat{\mathbf{p}} \cdot \mathbf{B}'_1 + 2\hat{\mathbf{q}} \cdot \mathbf{A}'_1 \right] \right\} \quad (5.67)$$

$$\bar{H} = \frac{P(R)}{m} \left\{ \frac{HL}{\mu} \left[\hat{\mathbf{q}} \cdot \mathbf{A}'_0 \right] - \frac{1}{4} \frac{HL^5}{G^2 \mu^2} \sqrt{1 - \frac{G^2}{L^2}} \left[\hat{\mathbf{p}} \cdot \mathbf{B}'_1 + 2\hat{\mathbf{q}} \cdot \mathbf{A}'_1 \right] + \frac{1}{2} \sqrt{G^2 - H^2} \frac{L}{\mu} \left[\sin h_D \hat{\mathbf{h}} \cdot \mathbf{B}'_1 + \cos h_D \hat{\mathbf{h}} \cdot \mathbf{A}'_1 \right] \right\} \quad (5.68)$$

$$\bar{g} = \frac{P(R)}{m} \frac{1}{2\sqrt{L^2 - G^2}} \frac{L^2}{\mu} \frac{\cos^2 g \sin g \sqrt{1 - (H/G)^2}}{\left(\frac{H}{G} \cos g \sin h_D + \cos h_D \sin g \right)^2} \left[-\hat{\mathbf{p}} \cdot \mathbf{A}'_1 + 2\hat{\mathbf{q}} \cdot \mathbf{B}'_1 \right] \quad (5.69)$$

$$\bar{h}_D = -\frac{1}{2} \frac{P(R)}{m} \frac{L}{\mu} \frac{\cos^2 h_D}{\sqrt{1 - (H/G)^2} \cos^2 g} \left[\cos h_D \hat{\mathbf{h}} \cdot \mathbf{B}'_1 + \sin h_D \hat{\mathbf{h}} \cdot \mathbf{A}'_1 \right] \quad (5.70)$$

5.2.2 Initial Offset Correction

Recall that for the circular case under discussion here, $\theta = M$, and therefore this substitution can be made in Eqs. (5.36) - (5.38) before plugging them into Eq. (5.12). The averages of the periodic terms for each orbital element will now be evaluated. Each component of the angular momentum and eccentricity vectors can be evaluated independently.

The functional equation for the change in energy in terms of mean anomaly can be seen from Eq. (5.36) to be

$$\dot{\mathcal{E}} = \frac{P(R)}{m} \frac{h}{a} \hat{\mathbf{y}}_b \cdot \left\{ \mathbf{A}'_0 + \sum_{n=1}^{\infty} [\mathbf{A}'_n \cos(nM) + \mathbf{B}'_n \sin(nM)] \right\} \quad (5.71)$$

The secular rate of change is given in Eq. (5.43). Plugging these equations into Eq. (5.12), and carrying out the inside integration, the periodic term for energy becomes

$$\begin{aligned} \bar{\mathcal{E}}_p = \frac{P(R)}{m} \frac{h}{a} \sqrt{\frac{a^3}{\mu}} \hat{\mathbf{y}}_b \cdot \frac{1}{2\pi} \int_0^{2\pi} \left\{ \mathbf{A}'_0 (M - M_0) + \sum_{n=1}^{\infty} \frac{1}{n} \left[\mathbf{A}'_n \sin(nM) - \mathbf{B}'_n \cos(nM) \right. \right. \\ \left. \left. - \mathbf{A}'_n \sin(nM_0) + \mathbf{B}'_n \cos(nM_0) \right] \right\} dM - \pi \sqrt{\frac{a^3}{\mu}} \bar{\mathcal{E}}(\mathbf{x}_0) \end{aligned} \quad (5.72)$$

Now, without loss of generality for the circular case, we will assume that $M_0 = 0$ and integrate to get the periodic energy term,

$$\bar{\mathcal{E}}_p = \frac{P(R)}{m} \frac{h}{a} \sqrt{\frac{a^3}{\mu}} \hat{\mathbf{y}}_b \cdot \left[\pi \mathbf{A}'_0 + \sum_{n=1}^{\infty} \frac{1}{n} \mathbf{B}'_n \right] - \pi \sqrt{\frac{a^3}{\mu}} \bar{\mathcal{E}}(\mathbf{x}_0) \quad (5.73)$$

Finally, notice that the \mathbf{A}'_0 term cancels exactly with the $\overline{\mathcal{E}}$ (see Eq. (5.43)), and therefore the final result is,

$$\overline{\mathcal{E}}_p = \frac{P(R)}{m} \frac{h}{a} \sqrt{\frac{a^3}{\mu}} \hat{\mathbf{y}}_b \cdot \sum_{n=1}^{\infty} \left[\frac{1}{n} \mathbf{B}'_n \right] \quad (5.74)$$

The same process is now carried out for each component of the angular momentum and eccentricity vectors. As the methodology is identical to that shown above for energy, the intermediate steps are not shown for these vectors.

The functional equation for the change in angular momentum in terms of mean anomaly can be seen from Eq. (5.37) to be

$$\dot{\mathbf{h}}_1 = \frac{P(R)}{m} a \hat{\mathbf{z}}_b \cdot \left\{ \mathbf{A}'_0 \sin(M) + \sum_{n=1}^{\infty} [\mathbf{A}'_n \sin(M) \cos(nM) + \mathbf{B}'_n \sin(M) \sin(nM)] \right\} \quad (5.75)$$

$$\dot{\mathbf{h}}_2 = \frac{P(R)}{m} a \hat{\mathbf{b}}_b \cdot \left\{ -\mathbf{A}'_0 \cos(M) + \sum_{n=1}^{\infty} [-\mathbf{A}'_n \cos(M) \cos(nM) - \mathbf{B}'_n \cos(M) \sin(nM)] \right\} \quad (5.76)$$

$$\dot{\mathbf{h}}_3 = \frac{P(R)}{m} a \hat{\mathbf{h}}_b \cdot \left\{ \mathbf{A}'_0 + \sum_{n=1}^{\infty} [\mathbf{A}'_n \cos(nM) + \mathbf{B}'_n \sin(nM)] \right\} \quad (5.77)$$

The secular rate of change is given in Eq. (5.44). Plugging these equations into Eq. (5.12) and carrying out the integrations results in the average of the periodic angular momentum term,

$$\bar{\mathbf{h}}_{p1} = \frac{P(R)}{m} a \sqrt{\frac{a^3}{\mu}} \hat{\mathbf{z}}_b \cdot \left\{ \mathbf{A}'_0 + \frac{1}{4} \mathbf{A}'_1 + \sum_{n=2}^{\infty} \left[\frac{-\mathbf{A}'_n}{(n-1)(n+1)} \right] \right\} \quad (5.78)$$

$$\bar{\mathbf{h}}_{p2} = \frac{P(R)}{m} a \sqrt{\frac{a^3}{\mu}} \hat{\mathbf{b}}_b \cdot \left\{ -\frac{1}{4} \mathbf{B}'_1 + \sum_{n=2}^{\infty} \left[\frac{-n \mathbf{B}'_n}{(n-1)(n+1)} \right] \right\} \quad (5.79)$$

$$\bar{\mathbf{h}}_{p3} = \frac{P(R)}{m} a \sqrt{\frac{a^3}{\mu}} \hat{\mathbf{h}}_b \cdot \left[\sum_{n=1}^{\infty} \frac{1}{n} \mathbf{B}'_n \right] \quad (5.80)$$

The functional equation for the change in eccentricity in terms of mean anomaly can be seen from Eq. (5.38) to be

$$\dot{\mathbf{e}}_1 = \frac{P(R)}{m} \frac{h}{\mu} \left[\sin(M) \hat{\mathbf{a}}_b + 2 \cos(M) \hat{\mathbf{y}}_b \right] \cdot \left\{ \mathbf{A}'_0 + \sum_{n=1}^{\infty} [\mathbf{A}'_n \cos(nM) + \mathbf{B}'_n \sin(nM)] \right\} \quad (5.81)$$

$$\dot{\mathbf{e}}_2 = \frac{P(R)}{m} \frac{h}{\mu} \left[-\cos(M) \hat{\mathbf{b}}_b + 2 \sin(M) \hat{\mathbf{y}}_b \right] \cdot \left\{ \mathbf{A}'_0 + \sum_{n=1}^{\infty} [\mathbf{A}'_n \cos(nM) + \mathbf{B}'_n \sin(nM)] \right\} \quad (5.82)$$

$$\dot{\mathbf{e}}_3 = 0 \quad (5.83)$$

The secular rate of change is given in Eq. (5.45). Plugging these equations into Eq. (5.12), and carrying out the integrations results in the average of the periodic eccentricity term,

$$\begin{aligned} \bar{\mathbf{e}}_{p1} = \frac{P(R)}{m} \frac{h}{\mu} \sqrt{\frac{a^3}{\mu}} \left\{ \hat{\mathbf{a}}\hat{\mathbf{x}}_b \cdot \left\{ \mathbf{A}'_0 + \frac{1}{4}\mathbf{A}'_1 + \sum_{n=2}^{\infty} \left[\frac{-\mathbf{A}'_n}{(n-1)(n+1)} \right] \right\} \right. \\ \left. + \hat{\mathbf{a}}\hat{\mathbf{y}}_b \cdot \left\{ \frac{1}{2}\mathbf{B}'_1 + \sum_{n=2}^{\infty} \left[\frac{2n\mathbf{B}'_n}{(n-1)(n+1)} \right] \right\} \right\} \end{aligned} \quad (5.84)$$

$$\begin{aligned} \bar{\mathbf{e}}_{p2} = \frac{P(R)}{m} \frac{h}{\mu} \sqrt{\frac{a^3}{\mu}} \left\{ \hat{\mathbf{b}}\hat{\mathbf{x}}_b \cdot \left\{ -\frac{1}{4}\mathbf{B}'_1 + \sum_{n=2}^{\infty} \left[\frac{-n\mathbf{B}'_n}{(n-1)(n+1)} \right] \right\} \right. \\ \left. + \hat{\mathbf{b}}\hat{\mathbf{y}}_b \cdot \left\{ 2\mathbf{A}'_0 + \frac{1}{2}\mathbf{A}'_1 + \sum_{n=2}^{\infty} \left[\frac{-2\mathbf{A}'_n}{(n-1)(n+1)} \right] \right\} \right\} \end{aligned} \quad (5.85)$$

$$\bar{\mathbf{e}}_{p3} = 0 \quad (5.86)$$

5.2.3 Circular Orbit Simulation

A simulation has been constructed to validate the orbit averaged results in Eqs. (5.43) - (5.45). This simulation represents a small body orbiting Earth at an altitude of 500 km. The only forces considered in this simulation are the two-body point mass gravity and solar radiation pressure. The initial offset correction derived in Section 5.2.2 was included.

For this validation case, the solar radiation pressure is modeled with 25 randomly generated coefficients chosen to yield a random acceleration with an order of magnitude of 10^{-5} m/s². The signs of each Fourier coefficient component are also randomly assigned. Therefore, no conclusions about the behavior of real bodies should be drawn from the results shown in Figs. 5.2 - 5.6 since it is very unlikely that any real body has similar coefficients to those arbitrarily generated for this example. The point here is to show that the secular theory closely follows the mean value of the numerical simulation.

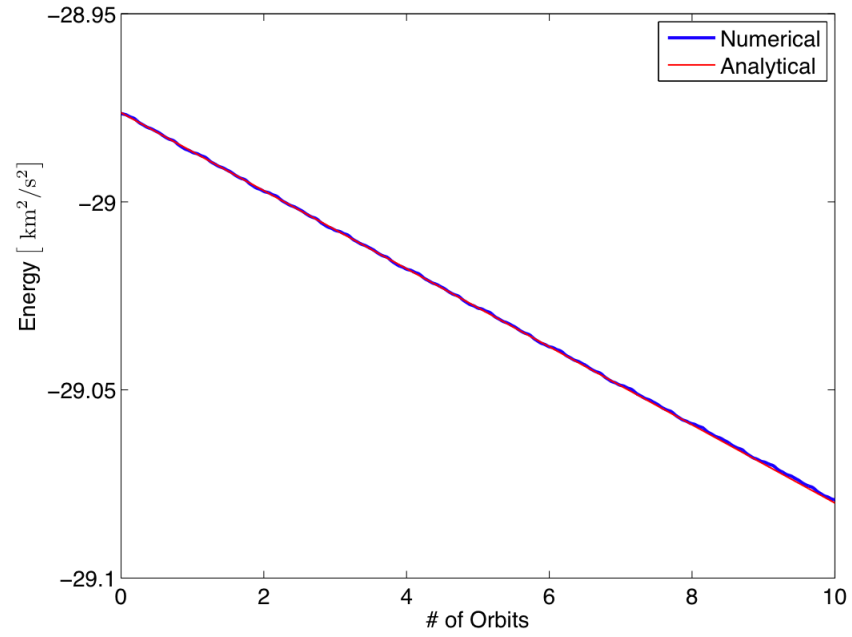


Figure 5.2: Orbital energy of the example secondary over 10 orbits about the primary.

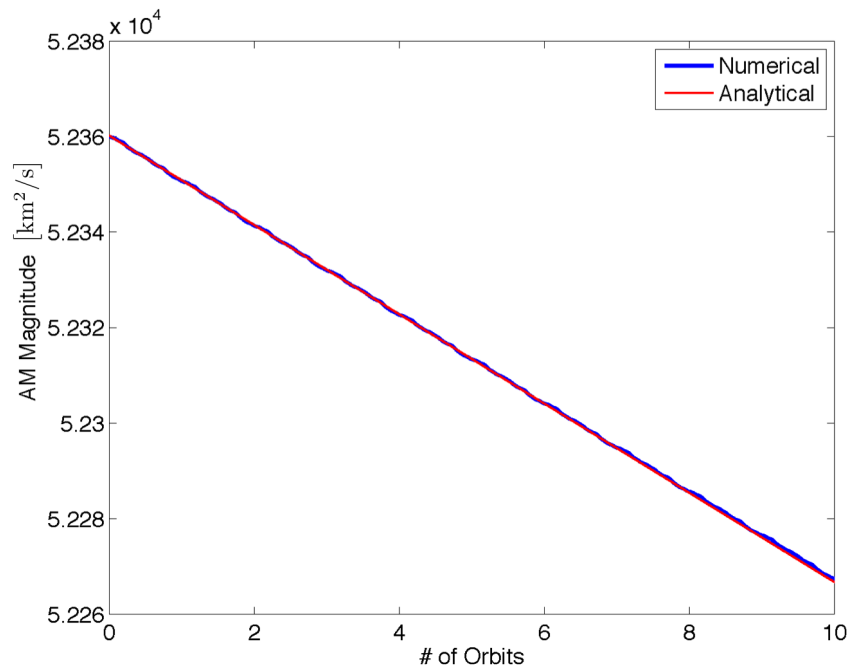


Figure 5.3: Orbital angular momentum of the example secondary over 10 orbits about the primary.

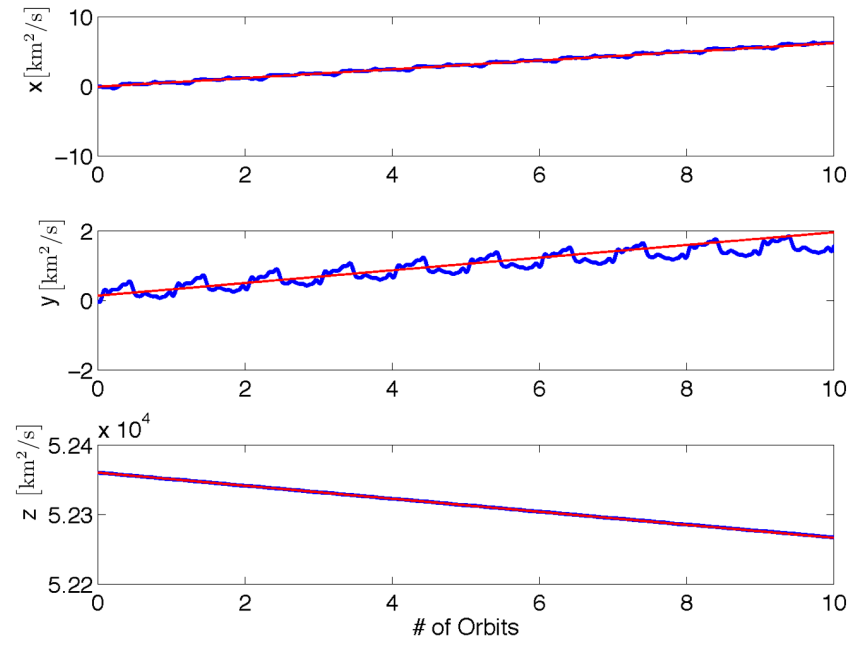


Figure 5.4: Orbit angular momentum vector components in the primary-centered inertial frame for the example secondary over 10 orbits about the primary.

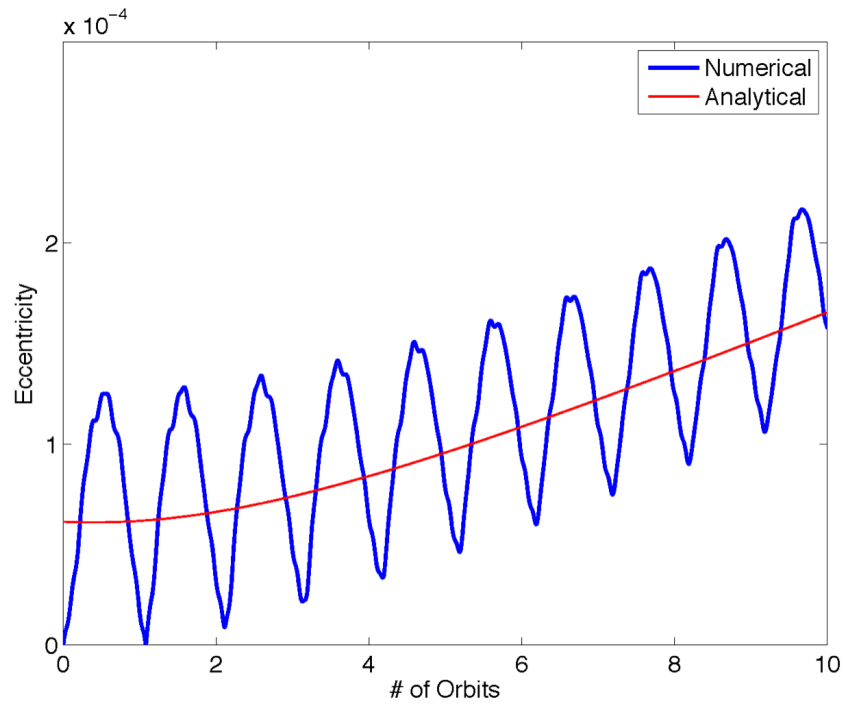


Figure 5.5: Eccentricity of the example secondary over 10 orbits about the primary.

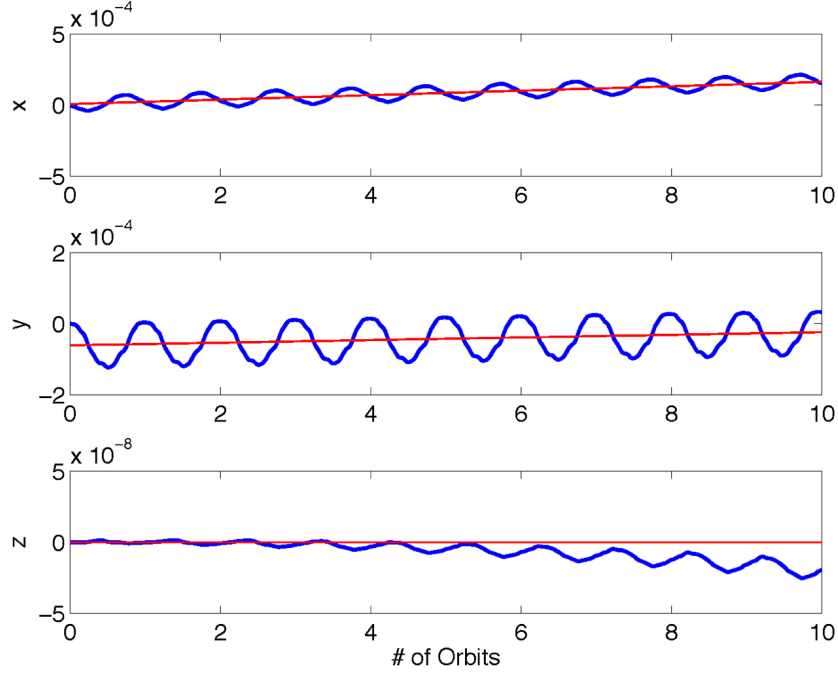


Figure 5.6: Eccentricity vector components in the primary-centered inertial frame for the example secondary over 10 orbits about the primary.

The figures show that the analytical and dynamic results show good agreement. The numerically integrated analytical results start to diverge at one part in 10^{-8} after several orbits in the z-axis of the eccentricity vector. This is due to the fact that as the eccentricity grows, the orbit is becoming non-circular, and the assumptions made for Eqs. (5.43) - (5.45) are no longer valid. In fact, the circular equations predict that the z-component of the eccentricity will never change.

5.2.4 Averaging the Circular Results Over 1 year

Eqs. (5.43) - (5.45) can be written for the year averaged results by inserting the year averaged coefficients from Section 5.1.3.2. The results are,

$$\overline{e}_s = \frac{G_1}{a_s^2 \sqrt{1 - e_s^2}} \frac{h}{ma} [A'_0(2)] \quad (5.87)$$

$$\overline{\mathbf{h}}_s = \frac{G_1}{a_s^2 \sqrt{1 - e_s^2}} \frac{a}{2m} \left[\hat{\mathbf{a}}\hat{\mathbf{z}}_b \cdot \overline{\mathbf{B}}'_1 - \hat{\mathbf{b}}\hat{\mathbf{z}}_b \cdot \overline{\mathbf{A}}'_1 + 2\hat{\mathbf{h}}\hat{\mathbf{y}}_b \cdot \overline{\mathbf{A}}'_0 \right] \quad (5.88)$$

$$\overline{\mathbf{e}}_s = \frac{G_1}{a_s^2 \sqrt{1 - e_s^2}} \frac{h}{2m\mu} \left[\hat{\mathbf{a}}\hat{\mathbf{x}}_b \cdot \overline{\mathbf{B}}'_1 + 2\hat{\mathbf{a}}\hat{\mathbf{y}}_b \cdot \overline{\mathbf{A}}'_1 - \hat{\mathbf{b}}\hat{\mathbf{x}}_b \cdot \overline{\mathbf{A}}'_1 + 2\hat{\mathbf{b}}\hat{\mathbf{y}}_b \cdot \overline{\mathbf{B}}'_1 \right] \quad (5.89)$$

Note that for the circular case, all of the Fourier coefficients appear at zero or first order frequency. Therefore the year averaged Fourier coefficients used from Eqs. (5.25) and (5.29) are always the odd terms.

Alternatively, the year averaged results can be written in terms of the double-prime coefficients. Using Eqs. (5.49) - (5.51) and the Fourier coefficients from Section 5.1.3.3, the results are,

$$\overline{\dot{e}}_s = \frac{G_1}{a_s^2 \sqrt{1-e_s^2}} \frac{h}{2ma} \left[-\hat{\mathbf{a}} \cdot \overline{\mathbf{B}}_1'' + \hat{\mathbf{b}} \cdot \overline{\mathbf{A}}_1'' \right] \quad (5.90)$$

$$\overline{\dot{\mathbf{h}}}_s = \frac{G_1}{a_s^2 \sqrt{1-e_s^2}} \frac{a}{2m} \left[\tilde{\hat{\mathbf{a}}} \cdot \overline{\mathbf{A}}_1'' + \tilde{\hat{\mathbf{b}}} \cdot \overline{\mathbf{B}}_1'' \right] \quad (5.91)$$

$$\overline{\dot{e}}_s = \frac{G_1}{a_s^2 \sqrt{1-e_s^2}} \frac{h}{2m\mu} \left[-2\tilde{\hat{\mathbf{h}}} \cdot \overline{\mathbf{A}}_0'' - \frac{1}{2}\hat{\mathbf{a}}\hat{\mathbf{a}} \cdot \overline{\mathbf{B}}_2'' - \hat{\mathbf{b}}\hat{\mathbf{a}} \cdot \overline{\mathbf{A}}_0'' + \frac{1}{2}\hat{\mathbf{b}}\hat{\mathbf{a}} \cdot \overline{\mathbf{A}}_2'' + \hat{\mathbf{a}}\hat{\mathbf{b}} \cdot \overline{\mathbf{A}}_0'' + \frac{1}{2}\hat{\mathbf{a}}\hat{\mathbf{b}} \cdot \overline{\mathbf{A}}_2'' + \frac{1}{2}\hat{\mathbf{b}}\hat{\mathbf{b}} \cdot \overline{\mathbf{B}}_2'' \right] \quad (5.92)$$

5.3 Application to an Elliptical Orbit

In this section, the perturbation theory will be applied to an elliptical orbit and averaged. The resulting equations will then be compared to a full dynamics simulation to determine how accurately they estimate the secular effects of the solar radiation pressure.

5.3.1 Orbit Averaged Equations

In order to carry out the orbit averaging from Section 5.1.1, the solar radiation pressure acceleration and the variation equations (Eqs. (3.20), (3.21), and (3.27)) must be written in terms of the mean anomaly. Due to the assumption in Eq. (4.6), the solar radiation pressure acceleration can be expressed in terms of the mean anomaly as,

$$\mathbf{a}_{SRP} = \frac{P(R)}{m} \left[\mathbf{A}_0'' + \sum_{n=1}^{\infty} [\mathbf{A}_n'' \cos(nM) + \mathbf{B}_n'' \sin(nM)] \right] \quad (5.93)$$

The variation equations are expressed in terms of ν . To express these in terms of M , first rewrite Eqs. (3.21) and (3.27) as,

$$\dot{\mathbf{h}} = a \left[\frac{r}{a} \cos(\nu) \hat{\mathbf{e}} + \frac{r}{a} \sin(\nu) \hat{\mathbf{e}}_{\perp} \right] \cdot \tilde{\mathbf{a}} \quad (5.94)$$

$$\dot{\mathbf{e}} = \left\{ -\frac{\tilde{\mathbf{h}}}{\mu} + \frac{a}{h} \frac{r}{a} \left[-\cos(\nu) \sin(\nu) \hat{\mathbf{e}}\hat{\mathbf{e}} - \sin^2(\nu) \hat{\mathbf{e}}_{\perp} \hat{\mathbf{e}} + \cos(\nu) [e + \cos(\nu)] \hat{\mathbf{e}}\hat{\mathbf{e}}_{\perp} + \sin(\nu) [e + \cos(\nu)] \hat{\mathbf{e}}_{\perp} \hat{\mathbf{e}}_{\perp} - e \sin(\nu) \overline{\overline{U}} \right] \right\} \cdot \mathbf{a} \quad (5.95)$$

Terms of the true anomaly can be written as a series in terms of the mean anomaly (found in both Taff [107] and Brower and Clemence [12]) as,

$$\frac{r}{a} \cos(\nu) = -\frac{3e}{2} + \sum_{n=1}^{\infty} \left(\frac{2}{n^2}\right) J'_n(ne) \cos(nM) \quad (5.96)$$

$$\frac{r}{a} \sin(\nu) = (1 - e^2)^{1/2} \sum_{n=1}^{\infty} \left(\frac{2}{ne}\right) J_n(ne) \sin(nM) \quad (5.97)$$

$$\cos(\nu) = -e + \frac{2(1 - e^2)}{e} \sum_{n=1}^{\infty} J_n(ne) \cos(nM) \quad (5.98)$$

$$\sin(\nu) = (1 - e^2)^{1/2} \sum_{n=1}^{\infty} \left(\frac{2}{n}\right) J'_n(ne) \sin(nM) \quad (5.99)$$

where $J_n(ne)$ is the Bessel function of the first kind of argument e and order n , and $J'_n(ne) = \partial J_n(ne)/\partial e$.

Due to the fact that these relationships will be used in numerical simulations for systems that will often have small eccentricities, having the $1/e$ terms is undesirable. Using well known Bessel function relationships listed in Appendix A, Eqs. (5.97) and (5.98) can be rewritten as,

$$\frac{r}{a} \sin(\nu) = (1 - e^2)^{1/2} \sum_{n=1}^{\infty} \frac{1}{n} (J_{n-1}(ne) + J_{n+1}(ne)) \sin(nM) \quad (5.100)$$

$$\cos(\nu) = -e + (1 - e^2) \sum_{n=1}^{\infty} (J_{n-1}(ne) + J_{n+1}(ne)) \cos(nM) \quad (5.101)$$

The previous relationships can be used to write the Eqs. (3.20), (5.94), and (5.95) in terms of the mean anomaly, M ,

$$\begin{aligned} \dot{\mathcal{E}}(M) = & \frac{P(R)}{m} \frac{h}{a} \left[\left(- (1 - e^2)^{-1/2} \sum_{n=1}^{\infty} \left(\frac{2}{n}\right) J'_n(ne) \sin(nM) \right) \hat{\mathbf{e}} \right. \\ & \left. + \left(\sum_{n=1}^{\infty} (J_{n-1}(ne) + J_{n+1}(ne)) \cos(nM) \right) \hat{\mathbf{e}}_{\perp} \right] \cdot \left[\mathbf{A}_0'' + \sum_{n=1}^{\infty} [\mathbf{A}_n'' \cos(nM) + \mathbf{B}_n'' \sin(nM)] \right] \end{aligned} \quad (5.102)$$

$$\begin{aligned} \dot{\mathbf{h}}(M) = & \frac{P(R)a}{m} \left[\left(-\frac{3e}{2} + \sum_{n=1}^{\infty} \left(\frac{2}{n^2}\right) J'_n(ne) \cos(nM) \right) \hat{\mathbf{e}} \right. \\ & \left. + \left((1 - e^2)^{1/2} \sum_{n=1}^{\infty} \frac{1}{n} (J_{n-1}(ne) + J_{n+1}(ne)) \sin(nM) \right) \hat{\mathbf{e}}_{\perp} \right] \\ & \cdot \left[\tilde{\mathbf{A}}_0'' + \sum_{n=1}^{\infty} [\tilde{\mathbf{A}}_n'' \cos(nM) + \tilde{\mathbf{B}}_n'' \sin(nM)] \right] \end{aligned} \quad (5.103)$$

$$\begin{aligned}
\dot{\mathbf{e}}(M) = & \frac{P(R)}{m} \left\{ -\frac{\tilde{\mathbf{h}}}{\mu} + \frac{a}{h} \left[\left(\frac{3e}{2} - \sum_{n=1}^{\infty} \left(\frac{2}{n^2} \right) J'_n(ne) \cos(nM) \right) \left((1-e^2)^{1/2} \sum_{n=1}^{\infty} \left(\frac{2}{n} \right) J'_n(ne) \sin(nM) \right) \hat{\mathbf{e}} \right. \right. \\
& - (1-e^2) \left(\sum_{n=1}^{\infty} \frac{1}{n} (J_{n-1}(ne) + J_{n+1}(ne)) \sin(nM) \right) \left(\sum_{n=1}^{\infty} \left(\frac{2}{n} \right) J'_n(ne) \sin(nM) \right) \hat{\mathbf{e}}_{\perp} \hat{\mathbf{e}} \\
& + \left(-\frac{3e}{2} + \sum_{n=1}^{\infty} \left(\frac{2}{n^2} \right) J'_n(ne) \cos(nM) \right) \left((1-e^2) \sum_{n=1}^{\infty} (J_{n-1}(ne) + J_{n+1}(ne)) \cos(nM) \right) \hat{\mathbf{e}}_{\perp} \\
+ & \left((1-e^2)^{1/2} \sum_{n=1}^{\infty} \frac{1}{n} (J_{n-1}(ne) + J_{n+1}(ne)) \sin(nM) \right) \left((1-e^2) \sum_{n=1}^{\infty} (J_{n-1}(ne) + J_{n+1}(ne)) \cos(nM) \right) \hat{\mathbf{e}}_{\perp} \hat{\mathbf{e}}_{\perp} \\
& \left. - \left((1-e^2)^{1/2} \sum_{n=1}^{\infty} \left(\frac{2}{n} \right) J_n(ne) \sin(nM) \right) \bar{U} \right\} \cdot \left[\mathbf{A}_0'' + \sum_{n=1}^{\infty} [\mathbf{A}_n'' \cos(nM) + \mathbf{B}_n'' \sin(nM)] \right] \quad (5.104)
\end{aligned}$$

The orbit averaging is then carried out on Eqs. (5.102) - (5.104), using the acceleration expression in Eq. (5.93) to find,

$$\bar{\mathcal{E}} = \frac{P(R)}{2m} \frac{h}{a} \left[- (1-e^2)^{-1/2} \sum_{n=1}^{\infty} \left(\frac{2}{n} \right) J'_n(ne) B_n''(1) + \sum_{n=1}^{\infty} (J_{n-1}(ne) + J_{n+1}(ne)) A_n''(2) \right] \quad (5.105)$$

$$\begin{aligned}
\bar{\mathbf{h}} = & \frac{P(R)a}{2m} \left[\left((1-e^2)^{1/2} \sum_{n=1}^{\infty} \frac{1}{n} (J_{n-1}(ne) + J_{n+1}(ne)) B_n''(3) \right) \hat{\mathbf{e}} \right. \\
& + \left(3eA_0''(3) - \sum_{n=1}^{\infty} \left(\frac{2}{n^2} \right) J'_n(ne) A_n''(3) \right) \hat{\mathbf{e}}_{\perp} \\
& \left. + \left(-3eA_0''(2) + \sum_{n=1}^{\infty} \left(\frac{2}{n^2} \right) J'_n(ne) A_n''(2) - (1-e^2)^{1/2} \sum_{n=1}^{\infty} \frac{1}{n} (J_{n-1}(ne) + J_{n+1}(ne)) B_n''(1) \right) \hat{\mathbf{h}} \right] \quad (5.106)
\end{aligned}$$

The eccentricity equation does not collapse quite as nicely because there is multiplication of infinite series for the coefficients. The general form of the averaged eccentricity equation can be written as,

$$\begin{aligned}
\bar{\mathbf{e}} = & \frac{P(R)}{2m} \left\{ -\frac{\tilde{\mathbf{h}}}{\mu} \cdot 2\mathbf{A}_0'' + \frac{a}{h} \left[\left(3e(1-e^2)^{1/2} \sum_{n=1}^{\infty} \left(\frac{1}{n} \right) J'_n(ne) B_n''(1) - \sum_{n=1}^{\infty} C_n B_n''(1) \right) \hat{\mathbf{e}} \right. \right. \\
& - \left(2D_0 A_0''(1) + \sum_{n=1}^{\infty} D_n A_n''(1) \right) \hat{\mathbf{e}}_{\perp} + \left(-3(1-e^2) \sum_{n=1}^{\infty} J_n(ne) A_n''(2) + 2F_0 A_0''(2) + \sum_{n=1}^{\infty} F_n A_n''(2) \right) \hat{\mathbf{e}} \\
& \left. + \left(\sum_{n=1}^{\infty} G_n B_n''(2) \right) \hat{\mathbf{e}}_{\perp} - (1-e^2)^{1/2} \sum_{n=1}^{\infty} \left(\frac{2}{n} \right) J_n(ne) \cdot \mathbf{B}_n'' \right\} \quad (5.107)
\end{aligned}$$

where C_n , D_n , D_0 , F_n , F_0 , and G_n represent the terms with multiplied infinite series of Bessel functions.

The multiplication of the infinite series from (5.104) is made more complicated by the fact that these series are trigonometric functions, and when multiplied they follow the well known relationships given in Eqs.

(A.3) - (A.6). These equations show that when the series are multiplied, the multiplied term will appear at a different frequency of the mean anomaly than the original terms. In order to average the equations, the coefficients need to be written in terms of the sin and cos of mean anomaly. This is best illustrated by a generic example. If the following multiplication is carried out and simplified,

$$\sum_{n=1}^{\infty} Z_n \sin(nM) = \sum_{n=1}^{\infty} X_n \cos(nM) \sum_{m=1}^{\infty} Y_m \sin(mM) \quad (5.108)$$

Then the coefficient is determined as

$$Z_m = \frac{1}{2} \left[\sum_{n=1}^{\infty} X_n Y_{n+m} - \sum_{n=1}^{\infty} X_{n+m} Y_n + \sum_{n=1}^{m-1} X_n Y_{m-n} \right] \quad (5.109)$$

Note that when two sin or cos terms are multiplied to result in a cos series, there will be a zeroth order term. This is illustrated with a second example,

$$Z_0 + \sum_{n=1}^{\infty} Z_n \cos(nM) = \sum_{n=1}^{\infty} X_n \cos(nM) \sum_{m=1}^{\infty} Y_m \cos(mM) \quad (5.110)$$

Then the coefficients are determined as

$$Z_0 = \frac{1}{2} \sum_{n=1}^{\infty} X_n Y_n \quad (5.111)$$

$$Z_m = \frac{1}{2} \left[\sum_{n=1}^{\infty} X_n Y_{n+m} + \sum_{n=1}^{\infty} X_{n+m} Y_n + \sum_{n=1}^{m-1} X_n Y_{m-n} \right] \quad (5.112)$$

Note that in both examples, this notation implies that if $m = 1$, the third summation (up to $m - 1$) is zero.

Using these examples, the coefficients from (5.107) can be written as,

$$\begin{aligned} C_n = \frac{1}{2}(1 - e^2)^{1/2} \left\{ \sum_{m=1}^{\infty} \left[\left(\frac{2}{m^2} \right) J'_m(me) \left(\frac{2}{n+m} \right) J'_{n+m}((n+m)e) \right] \right. \\ \left. - \sum_{m=1}^{\infty} \left[\left(\frac{2}{(n+m)^2} \right) J'_{n+m}((n+m)e) \left(\frac{2}{m} \right) J'_m(me) \right] \right. \\ \left. + \sum_{m=1}^{n-1} \left[\left(\frac{2}{m^2} \right) J'_m(me) \left(\frac{2}{n-m} \right) J'_{n-m}((n-m)e) \right] \right\} \quad (5.113) \end{aligned}$$

$$\begin{aligned}
D_n = \frac{1}{2}(1 - e^2) \left\{ \sum_{m=1}^{\infty} \left[\frac{1}{m} (J_{m-1}(me) + J_{m+1}(me)) \left(\frac{2}{n+m} \right) J'_{n+m}((n+m)e) \right] \right. \\
+ \sum_{m=1}^{\infty} \left[\frac{1}{n+m} (J_{n+m-1}((n+m)e) + J_{n+m+1}((n+m)e)) \left(\frac{2}{m} \right) J'_m(me) \right] \\
\left. - \sum_{m=1}^{n-1} \left[\frac{1}{m} (J_{m-1}(me) + J_{m+1}(me)) \left(\frac{2}{n-m} \right) J'_{n-m}((n-m)e) \right] \right\} \quad (5.114)
\end{aligned}$$

$$D_0 = \frac{1}{2}(1 - e^2) \sum_{m=1}^{\infty} \left[\frac{1}{m} (J_{m-1}(me) + J_{m+1}(me)) \left(\frac{2}{m} \right) J'_m(me) \right] \quad (5.115)$$

$$\begin{aligned}
F_n = \frac{1}{2}(1 - e^2) \left\{ \sum_{m=1}^{\infty} \left[\left(\frac{2}{m^2} \right) J'_m(me) (J_{n+m-1}((n+m)e) + J_{n+m+1}((n+m)e)) \right] \right. \\
+ \sum_{m=1}^{\infty} \left[\left(\frac{2}{(n+m)^2} \right) J'_{n+m}((n+m)e) (J_{m-1}(me) + J_{m+1}(me)) \right] \\
\left. + \sum_{m=1}^{n-1} \left[\left(\frac{2}{m^2} \right) J'_m(me) (J_{n-m-1}((n-m)e) + J_{n-m+1}((n-m)e)) \right] \right\} \quad (5.116)
\end{aligned}$$

$$F_0 = \frac{1}{2} \sum_{m=1}^{\infty} \left[\left(\frac{2}{m^2} \right) J'_m(me) (1 - e^2) (J_{m-1}(me) + J_{m+1}(me)) \right] \quad (5.117)$$

$$\begin{aligned}
G_n = \frac{1}{2}(1 - e^2)^{3/2} \left\{ - \sum_{m=1}^{\infty} \left[\frac{1}{m} (J_{m-1}(me) + J_{m+1}(me)) (J_{n+m-1}((n+m)e) + J_{n+m+1}((n+m)e)) \right] \right. \\
+ \sum_{m=1}^{\infty} \left[\frac{1}{n+m} (J_{n+m-1}((n+m)e) + J_{n+m+1}((n+m)e)) (J_{m-1}(me) + J_{m+1}(me)) \right] \\
\left. + \sum_{m=1}^{n-1} \left[\frac{1}{m} (J_{m-1}(me) + J_{m+1}(me)) (J_{n-m-1}((n-m)e) + J_{n-m+1}((n-m)e)) \right] \right\} \quad (5.118)
\end{aligned}$$

Eqs. (5.105) - (5.107) can be expanded up to an arbitrary order of eccentricity due to the fact that Bessel functions have well known series expansions in terms of their argument. The following three subsections will show the details for energy, angular momentum, and eccentricity expanded up to the fourth order of eccentricity.

5.3.1.1 Energy Series Expressions

The series expansion of the orbit averaged energy (Eq. (5.105)), with terms up to the 4th power of eccentricity shown, is

$$\begin{aligned} \bar{\mathcal{E}} = \frac{P(R)}{2m} \frac{h}{a} \left\{ \left[-1 - \frac{e^2}{8} - \frac{41e^4}{192} \right] B_1''(1) + \left[1 - \frac{e^2}{8} - \frac{e^4}{192} \right] A_1''(2) \right. \\ + \left[-e + \frac{e^3}{6} \right] B_2''(1) + \left[e - \frac{e^3}{3} \right] A_2''(2) + \left[-\frac{9e^2}{8} + \frac{63e^4}{128} \right] B_3''(1) + \left[\frac{9e^2}{8} - \frac{81e^4}{128} \right] A_3''(2) \\ \left. + \left[-\frac{4e^3}{3} \right] B_4''(1) + \left[\frac{4e^3}{3} \right] A_4''(2) + \left[-\frac{625e^4}{384} \right] B_5''(1) + \left[\frac{625e^4}{384} \right] A_5''(2) + \dots \right\} \quad (5.119) \end{aligned}$$

The series in eccentricity for energy start one order below the order of the Fourier coefficient, and progress in steps of e^2 .

The averaged equation for energy can then be rewritten out in terms of the order of eccentricity chosen as,

$$\bar{\mathcal{E}} = \frac{P(R)}{2m} \frac{h}{a} \left\{ \bar{\mathcal{E}}_0 + e\bar{\mathcal{E}}_1 + e^2\bar{\mathcal{E}}_2 + e^3\bar{\mathcal{E}}_3 + e^4\bar{\mathcal{E}}_4 + \dots \right\} \quad (5.120)$$

where the first 4 orders are,

$$\bar{\mathcal{E}}_0 = -B_1''(1) + A_1''(2) \quad (5.121)$$

$$\bar{\mathcal{E}}_1 = -B_2''(1) + A_2''(2) \quad (5.122)$$

$$\bar{\mathcal{E}}_2 = -\frac{1}{8}B_1''(1) - \frac{9}{8}B_3''(1) - \frac{1}{8}A_1''(2) + \frac{9}{8}A_3''(2) \quad (5.123)$$

$$\bar{\mathcal{E}}_3 = \frac{1}{6}B_2''(1) - \frac{4}{3}B_4''(1) - \frac{1}{3}A_2''(2) + \frac{4}{3}A_4''(2) \quad (5.124)$$

$$\bar{\mathcal{E}}_4 = -\frac{41}{192}B_1''(1) + \frac{63}{128}B_3''(1) - \frac{625}{384}B_5''(1) + \frac{1}{192}A_1''(2) - \frac{81}{128}A_3''(2) + \frac{625}{384}A_5''(2) \quad (5.125)$$

It is important to note that the zeroth order expansion exactly matches Eq. (5.49) that was derived independently for the circular case.

5.3.1.2 Angular Momentum Series Expressions

The series expansion of the orbit averaged angular momentum (Eq. (5.106)), with terms up to the 4th power of eccentricity shown, is (note that I have separated each component of the angular momentum into separate equations for ease of reading),

$$\begin{aligned} \bar{h}(1) = \frac{P(R)a}{2m} \left\{ \left[1 - \frac{5e^2}{8} - \frac{11e^4}{192} \right] B_1''(3) + \left[\frac{e}{2} - \frac{5e^3}{12} \right] B_2''(3) \right. \\ \left. + \left[\frac{3e^2}{8} - \frac{51e^4}{128} \right] B_3''(3) + \left[\frac{e^3}{3} \right] B_4''(3) + \left[\frac{125e^4}{384} \right] B_5''(3) + \dots \right\} \quad (5.126) \end{aligned}$$

$$\begin{aligned} \bar{h}(2) = \frac{P(R)a}{2m} \left\{ \left[3 \right] A_0''(3) - \left[1 - \frac{3e^2}{8} + \frac{5e^4}{192} \right] A_1''(3) - \left[\frac{e}{2} - \frac{e^3}{3} \right] A_2''(3) \right. \\ \left. - \left[\frac{3e^2}{8} - \frac{45e^4}{128} \right] A_3''(3) - \left[\frac{e^3}{3} \right] A_4''(3) - \left[\frac{125e^4}{384} \right] A_5''(3) + \dots \right\} \quad (5.127) \end{aligned}$$

$$\begin{aligned} \bar{h}(3) = \frac{P(R)a}{2m} \left\{ \left[-3 \right] A_0''(2) + \left[1 - \frac{3e^2}{8} + \frac{5e^4}{192} \right] A_1''(2) + \left[\frac{e}{2} - \frac{e^3}{3} \right] A_2''(2) \right. \\ \left. + \left[\frac{3e^2}{8} - \frac{45e^4}{128} \right] A_3''(2) + \left[\frac{e^3}{3} \right] A_4''(2) + \left[\frac{125e^4}{384} \right] A_5''(2) \right. \\ \left. - \left[1 - \frac{5e^2}{8} - \frac{11e^4}{192} \right] B_1''(1) - \left[\frac{e}{2} - \frac{5e^3}{12} \right] B_2''(1) \right. \\ \left. - \left[\frac{3e^2}{8} - \frac{51e^4}{128} \right] B_3''(1) - \left[\frac{e^3}{3} \right] B_4''(1) - \left[\frac{125e^4}{384} \right] B_5''(1) + \dots \right\} \quad (5.128) \end{aligned}$$

The series in eccentricity for angular momentum start one order below the order of the Fourier coefficient, and progress in steps of e^2 .

The averaged equations for angular momentum can then be rewritten out in terms of the order of eccentricity chosen as,

$$\bar{h}(1) = \frac{P(R)a}{2m} \left\{ \bar{h}_0(1) + e\bar{h}_1(1) + e^2\bar{h}_2(1) + e^3\bar{h}_3(1) + e^4\bar{h}_4(1) + \dots \right\} \quad (5.129)$$

$$\bar{h}(2) = \frac{P(R)a}{2m} \left\{ \bar{h}_0(2) + e\bar{h}_1(2) + e^2\bar{h}_2(2) + e^3\bar{h}_3(2) + e^4\bar{h}_4(2) + \dots \right\} \quad (5.130)$$

$$\bar{h}(3) = \frac{P(R)a}{2m} \left\{ \bar{h}_0(3) + e\bar{h}_1(3) + e^2\bar{h}_2(3) + e^3\bar{h}_3(3) + e^4\bar{h}_4(3) + \dots \right\} \quad (5.131)$$

where the first 4 orders are,

$$\bar{h}_0(1) = B_1''(3) \quad (5.132)$$

$$\bar{h}_1(1) = \frac{1}{2}B_2''(3) \quad (5.133)$$

$$\bar{h}_2(1) = -\frac{5}{8}B_1''(3) + \frac{3}{8}B_3''(3) \quad (5.134)$$

$$\bar{h}_3(1) = -\frac{5}{12}B_2''(3) + \frac{1}{3}B_4''(3) \quad (5.135)$$

$$\bar{h}_4(1) = -\frac{11}{192}B_1''(3) - \frac{51}{128}B_3''(3) + \frac{125}{384}B_5''(3) \quad (5.136)$$

$$\bar{h}_0(2) = -A_1''(3) \quad (5.137)$$

$$\bar{h}_1(2) = 3A_0''(3) - \frac{1}{2}A_2''(3) \quad (5.138)$$

$$\bar{h}_2(2) = \frac{3}{8}A_1''(3) - \frac{3}{8}A_3''(3) \quad (5.139)$$

$$\bar{h}_3(2) = \frac{1}{3}A_2''(3) - \frac{1}{3}A_4''(3) \quad (5.140)$$

$$\bar{h}_4(2) = -\frac{5}{192}A_1''(3) + \frac{45}{128}A_3''(3) - \frac{125}{384}A_5''(3) \quad (5.141)$$

$$\bar{h}_0(3) = A_1''(2) - B_1''(1) \quad (5.142)$$

$$\bar{h}_1(3) = -3A_0''(2) + \frac{1}{2}A_2''(2) - \frac{1}{2}B_2''(1) \quad (5.143)$$

$$\bar{h}_2(3) = -\frac{3}{8}A_1''(2) + \frac{3}{8}A_3''(2) + \frac{5}{8}B_1''(1) - \frac{3}{8}B_3''(1) \quad (5.144)$$

$$\bar{h}_3(3) = -\frac{1}{3}A_2''(2) + \frac{1}{3}A_4''(2) + \frac{5}{12}B_2''(1) - \frac{1}{3}B_4''(1) \quad (5.145)$$

$$\bar{h}_4(3) = \frac{5}{192}A_1''(2) - \frac{45}{128}A_3''(2) + \frac{125}{384}A_5''(2) + \frac{11}{192}B_1''(1) + \frac{51}{128}B_3''(1) - \frac{125}{384}B_5''(1) \quad (5.146)$$

It is important to note that the zeroth order expansion exactly matches Eq. (5.50) that was derived independently for the circular case.

5.3.1.3 Eccentricity Series Expressions

The series expansion of the orbit averaged eccentricity (Eq. (5.107)), with terms up to the 4th power of eccentricity shown, is (again, each component is shown in separate equations for ease of reading),

$$\begin{aligned}
\bar{\mathbf{e}}(1) = \frac{P(R)}{2m} \left\{ \frac{2}{\mu} \left(A_0''(2)h(3) - A_0''(3)h(2) \right) \right. \\
+ \frac{a}{h} \left[\left(1 - e^2 \right) A_0''(2) + \left(-\frac{57}{4}e + \frac{385}{24}e^3 \right) A_1''(2) \right. \\
+ \left(\frac{1}{2} - 15e^2 + \frac{309}{16}e^4 \right) A_2''(2) + \left(\frac{3}{4}e - \frac{555}{32}e^3 \right) A_3''(2) \\
+ \left(e^2 - 21e^4 \right) A_4''(2) + \left(\frac{125}{96}e^3 \right) A_5''(2) + \left(\frac{27}{16}e^4 \right) A_6''(2) \\
+ \left(\frac{55}{4}e - \frac{293}{24}e^3 \right) B_1''(1) + \left(-\frac{1}{2} + \frac{59}{4}e^2 - \frac{403}{24}e^4 \right) B_2''(1) \\
+ \left(-\frac{3}{4}e + \frac{549}{32}e^3 \right) B_3''(1) + \left(-e^2 + \frac{125}{6}e^4 \right) B_4''(1) \\
\left. \left. + \left(-\frac{125}{96}e^3 \right) B_5''(1) + \left(-\frac{27}{16}e^4 \right) B_6''(1) \right] + \dots \right\} \quad (5.147)
\end{aligned}$$

$$\begin{aligned}
\bar{\mathbf{e}}(2) = \frac{P(R)}{2m} \left\{ \frac{2}{\mu} \left(A_0''(3)h(1) - A_0''(1)h(3) \right) \right. \\
+ \frac{a}{h} \left[\left(-1 + e^2 \right) A_0''(1) + \left(-\frac{3}{4}e + \frac{41}{48}e^3 \right) A_1''(1) \right. \\
+ \left(\frac{1}{2} - \frac{3}{2}e^2 + \frac{21}{16}e^4 \right) A_2''(1) + \left(\frac{3}{4}e - \frac{69}{32}e^3 \right) A_3''(1) \\
+ \left(e^2 - 3e^4 \right) A_4''(1) + \left(\frac{125}{96}e^3 \right) A_5''(1) + \left(\frac{27}{16}e^4 \right) A_6''(1) \\
+ \left(-\frac{5}{4}e + \frac{49}{48}e^3 \right) B_1''(2) + \left(\frac{1}{2} - \frac{7}{4}e^2 + \frac{35}{24}e^4 \right) B_2''(2) \\
+ \left(\frac{3}{4}e - \frac{75}{32}e^3 \right) B_3''(2) + \left(e^2 - \frac{19}{6}e^4 \right) B_4''(2) \\
\left. \left. + \left(\frac{125}{96}e^3 \right) B_5''(2) + \left(\frac{27}{16}e^4 \right) B_6''(2) \right] + \dots \right\} \quad (5.148)
\end{aligned}$$

$$\begin{aligned}
\bar{\mathbf{e}}(3) = \frac{P(R)}{2m} \left\{ \frac{2}{\mu} \left(A_0''(1)h(2) - A_0''(2)h(1) \right) + \frac{a}{h} \left[\left(-e + \frac{5}{8}e^3 \right) B_1''(3) + \left(-\frac{1}{2}e^2 + \frac{5}{12}e^4 \right) B_2''(3) \right. \right. \\
\left. \left. + \left(-\frac{3}{8}e^3 \right) B_3''(3) + \left(-\frac{1}{3}e^4 \right) B_4''(3) \right] + \dots \right\} \quad (5.149)
\end{aligned}$$

The series in eccentricity for the eccentricity vector do not have the same form as energy and angular momentum due to the fact that there were trigonometric products. Because of this, the first two components of the eccentricity vector include Fourier coefficients two orders higher than the order of the eccentricity expansion. The eccentricity does still progress in steps of e^2 for each coefficient.

The averaged equations for eccentricity can then be rewritten out in terms of the order of eccentricity chosen as,

$$\bar{e}(1) = \frac{P(R)}{2m} \frac{a}{h} \left\{ \bar{e}_0(1) + e\bar{e}_1(1) + e^2\bar{e}_2(1) + e^3\bar{e}_3(1) + e^4\bar{e}_4(1) + \dots \right\} \quad (5.150)$$

$$\bar{e}(2) = \frac{P(R)}{2m} \frac{a}{h} \left\{ \bar{e}_0(2) + e\bar{e}_1(2) + e^2\bar{e}_2(2) + e^3\bar{e}_3(2) + e^4\bar{e}_4(2) + \dots \right\} \quad (5.151)$$

$$\bar{e}(3) = \frac{P(R)}{2m} \frac{a}{h} \left\{ \bar{e}_0(3) + e\bar{e}_1(3) + e^2\bar{e}_2(3) + e^3\bar{e}_3(3) + e^4\bar{e}_4(3) + \dots \right\} \quad (5.152)$$

where the first 4 orders are,

$$\bar{e}_0(1) = \frac{2}{\mu} \frac{h}{a} \left[A_0''(2)h(3) - A_0''(3)h(2) \right] + \left[A_0''(2) + \frac{1}{2}A_2''(2) - \frac{1}{2}B_2''(1) \right] \quad (5.153)$$

$$\bar{e}_1(1) = -\frac{57}{4}A_1''(2) + \frac{3}{4}A_3''(2) + \frac{55}{4}B_1''(1) - \frac{3}{4}B_3''(1) \quad (5.154)$$

$$\bar{e}_2(1) = -A_0''(2) - 15A_2''(2) + A_4''(2) + \frac{59}{4}B_2''(1) - B_4''(1) \quad (5.155)$$

$$\bar{e}_3(1) = \frac{385}{24}A_1''(2) - \frac{555}{32}A_3''(2) + \frac{125}{96}A_5''(2) - \frac{293}{24}B_1''(1) + \frac{549}{32}B_3''(1) - \frac{125}{96}B_5''(1) \quad (5.156)$$

$$\bar{e}_4(1) = \frac{309}{16}A_2''(2) - 21A_4''(2) + \frac{27}{16}A_6''(2) - \frac{403}{24}B_2''(1) + \frac{125}{6}B_4''(1) - \frac{27}{16}B_6''(1) \quad (5.157)$$

$$\bar{e}_0(2) = \frac{2}{\mu} \frac{h}{a} \left[A_0''(3)h(1) - A_0''(1)h(3) \right] + \left[-A_0''(1) + \frac{1}{2}A_2''(1) + \frac{1}{2}B_2''(2) \right] \quad (5.158)$$

$$\bar{e}_1(2) = -\frac{3}{4}A_1''(1) + \frac{3}{4}A_3''(1) - \frac{5}{4}B_1''(2) + \frac{3}{4}B_3''(2) \quad (5.159)$$

$$\bar{e}_2(2) = A_0''(1) - \frac{3}{2}A_2''(1) + A_4''(1) - \frac{7}{4}B_2''(2) + B_4''(2) \quad (5.160)$$

$$\bar{e}_3(2) = \frac{41}{48}A_1''(1) - \frac{69}{32}A_3''(1) + \frac{125}{96}A_5''(1) + \frac{49}{48}B_1''(2) - \frac{75}{32}B_3''(2) + \frac{125}{96}B_5''(2) \quad (5.161)$$

$$\bar{e}_4(2) = \frac{21}{16}A_2''(1) - 3A_4''(1) + \frac{27}{16}A_6''(1) + \frac{35}{24}B_2''(2) - \frac{19}{6}B_4''(2) + \frac{27}{16}B_6''(2) \quad (5.162)$$

$$\bar{\mathbf{e}}_0(3) = \frac{2}{\mu} \frac{h}{a} \left[A_0''(1)h(2) - A_0''(2)h(1) \right] \quad (5.163)$$

$$\bar{\mathbf{e}}_1(3) = -B_1''(3) \quad (5.164)$$

$$\bar{\mathbf{e}}_2(3) = -\frac{1}{2}B_2''(3) \quad (5.165)$$

$$\bar{\mathbf{e}}_3(3) = \frac{5}{8}B_1''(3) - \frac{3}{8}B_3''(3) \quad (5.166)$$

$$\bar{\mathbf{e}}_4(3) = \frac{5}{12}B_2''(3) - \frac{1}{3}B_4''(3) \quad (5.167)$$

These results seem to show that the zeroth order expansion does not match Eq. (5.51) that was derived independently for the circular case. However, recall the classical result,

$$\frac{h}{\mu} = \frac{a(1 - e^2)}{h} \quad (5.168)$$

Therefore, in the circular case with $e = 0$,

$$\frac{h}{\mu} = \frac{a}{h} \quad (5.169)$$

and the zeroth order solution is identical to Eq. (5.51). Technically, the $-e^2$ term of Eq. (5.168) is included in the second order solution for the non-circular case.

5.3.1.4 Elliptical Averaged Keplerian Orbital Elements

It is also useful to have expansions in eccentricity for the secular rates when the orbit is not circular. The full expressions for the eccentric case of energy, angular momentum, and the eccentricity vector, as well as expansions in eccentricity, are given in Ref. [65]. Using these expressions, the expansions in eccentricity for the Keplerian elements are,

$$\bar{a} = \frac{P(R)}{m} n \left\{ \bar{a}_0 + e\bar{a}_1 + e^2\bar{a}_2 + e^3\bar{a}_3 + \dots \right\} \quad (5.170)$$

$$\bar{\mathbf{e}} = \frac{P(R)}{2m} \sqrt{\frac{a}{\mu}} \left\{ \bar{\mathbf{e}}_0 + e\bar{\mathbf{e}}_1 + e^2\bar{\mathbf{e}}_2 + e^3\bar{\mathbf{e}}_3 + \dots \right\} \quad (5.171)$$

$$\bar{\mathbf{i}} = -\frac{P(R)}{2m} \sqrt{\frac{a}{\mu}} \left\{ \bar{\mathbf{i}}_0 + e\bar{\mathbf{i}}_1 + e^2\bar{\mathbf{i}}_2 + e^3\bar{\mathbf{i}}_3 + \dots \right\} \quad (5.172)$$

$$\bar{\Omega} = -\frac{P(R)}{2m} \sqrt{\frac{a}{\mu}} \frac{\cos^2 \Omega}{\sin i \cos^2 \omega} \left\{ \bar{\Omega}_0 + e\bar{\Omega}_1 + e^2\bar{\Omega}_2 + e^3\bar{\Omega}_3 + \dots \right\} \quad (5.173)$$

$$\bar{\omega} = \frac{P(R)}{2m} \sqrt{\frac{a}{\mu}} \frac{\cos^2 \omega}{(\cos i \cos \omega \sin \Omega + \cos \Omega \sin \omega)^2} \left\{ \frac{1}{e}\bar{\omega}_{-1} + \bar{\omega}_0 + e\bar{\omega}_1 + e^2\bar{\omega}_2 + e^3\bar{\omega}_3 + \dots \right\} \quad (5.174)$$

The first three orders for the semi-major axis are,

$$\bar{a}_0 = -B_1''(1) + A_1''(2) \quad (5.175)$$

$$\bar{a}_1 = -\frac{1}{2}B_2''(1) + A_2''(2) \quad (5.176)$$

$$\bar{a}_2 = \frac{3}{8}B_1''(1) - \frac{3}{8}B_3''(1) - \frac{5}{8}A_1''(2) + \frac{9}{8}A_3''(2) \quad (5.177)$$

$$\bar{a}_3 = \frac{1}{3}B_2''(1) - \frac{1}{3}B_4''(1) - \frac{5}{6}A_2''(2) + \frac{4}{3}A_4''(2) \quad (5.178)$$

The first three orders for the eccentricity are,

$$\bar{e}_0 = -\frac{3}{2}A_0''(2) + \frac{1}{2}A_2''(2) - \frac{1}{2}B_2''(1) \quad (5.179)$$

$$\bar{e}_1 = -\frac{155}{8}A_1''(2) + \frac{5}{8}A_3''(2) + \frac{111}{8}B_1''(1) - \frac{3}{8}B_3''(1) \quad (5.180)$$

$$\bar{e}_2 = \frac{5}{8}A_0''(2) - \frac{119}{8}A_2''(2) + \frac{3}{4}A_4''(2) + \frac{29}{4}B_2''(1) - \frac{5}{16}B_4''(1) \quad (5.181)$$

$$\bar{e}_3 = \frac{141}{16}A_1''(2) - \frac{3215}{192}A_3''(2) + \frac{175}{192}A_5''(2) - \frac{1034}{192}B_1''(1) + \frac{1059}{192}B_3''(1) - \frac{55}{192}B_5''(1) \quad (5.182)$$

The first three orders for the inclination are,

$$\bar{i}_0 = \sin \Omega B_1''(3) - \cos \Omega A_1''(3) \quad (5.183)$$

$$\bar{i}_1 = \sin \Omega \left[\frac{1}{2}B_2''(3) + \cos \Omega \left[3A_0''(3) - \frac{1}{4}A_2''(3) \right] \right] \quad (5.184)$$

$$\bar{i}_2 = \sin \Omega \left[-\frac{1}{8}B_1''(3) + \frac{3}{8}B_3''(3) \right] + \cos \Omega \left[-\frac{1}{8}A_1''(3) - \frac{1}{8}A_3''(3) \right] \quad (5.185)$$

$$\bar{i}_3 = \sin \Omega \left[-\frac{1}{6}B_2''(3) + \frac{1}{3}B_4''(3) \right] + \cos \Omega \left[\frac{3}{2}A_0''(3) + \frac{1}{24}A_2''(3) - \frac{1}{12}A_4''(3) \right] \quad (5.186)$$

The first three orders for the right ascension of the ascending node are,

$$\bar{\Omega}_0 = \cos \Omega B_1''(3) - \sin \Omega A_1''(3) \quad (5.187)$$

$$\bar{\Omega}_1 = \cos \Omega \frac{1}{2} B_2''(3) + \sin \Omega \left[3A_0''(3) - \frac{1}{4} A_2''(3) \right] \quad (5.188)$$

$$\bar{\Omega}_2 = \cos \Omega \left[-\frac{1}{8} B_1''(3) + \frac{3}{8} B_3''(3) \right] + \sin \Omega \left[-\frac{1}{8} A_1''(3) - \frac{1}{8} A_3''(3) \right] \quad (5.189)$$

$$\bar{\Omega}_3 = \cos \Omega \left[-\frac{1}{6} B_2''(3) + \frac{1}{3} B_4''(3) \right] + \sin \Omega \left[\frac{3}{2} A_0''(3) + \frac{1}{24} A_2''(3) - \frac{1}{12} A_4''(3) \right] \quad (5.190)$$

Notice that the series expression coefficients for inclination and the node are very similar; the only difference is the switching of $\sin \Omega$ and $\cos \Omega$.

The argument of perigee has a singularity at an eccentricity of zero, which is represented by the presence of the term that is proportional to $1/e$. The first three orders for the argument of perigee are,

$$\bar{\omega}_{-1} = \sin i \sin \omega \left[-\frac{5}{2} A_0''(1) + \frac{1}{2} A_2''(1) + \frac{1}{2} B_2''(2) \right] \quad (5.191)$$

$$\bar{\omega}_0 = \sin i \sin \omega \left[-\frac{1}{2} A_1''(1) + \frac{1}{2} A_3''(1) - \frac{1}{4} B_1''(2) + \frac{3}{4} B_3''(2) \right] + (\sin \Omega \cos \omega + \cos \Omega \sin \omega \cos i) B_1''(3) \quad (5.192)$$

$$\begin{aligned} \bar{\omega}_1 = \sin i \sin \omega & \left[\frac{11}{8} A_0''(1) - \frac{7}{8} A_2''(1) + \frac{1}{2} A_4''(1) - B_2''(2) + B_4''(2) \right] \\ & + (\sin \Omega \cos \omega + \cos \Omega \sin \omega \cos i) \frac{1}{2} B_2''(3) \end{aligned} \quad (5.193)$$

$$\begin{aligned} \bar{\omega}_2 = \sin i \sin \omega & \left[\frac{21}{48} A_1''(1) - \frac{23}{24} A_3''(1) + \frac{25}{48} A_5''(1) - \frac{13}{48} B_1''(2) - \frac{51}{32} B_3''(2) + \frac{125}{96} B_5''(2) \right] \\ & + (\sin \Omega \cos \omega + \cos \Omega \sin \omega \cos i) \left[-\frac{1}{8} B_1''(3) + \frac{3}{8} B_3''(3) \right] \end{aligned} \quad (5.194)$$

$$\begin{aligned} \bar{\omega}_3 = \sin i \sin \omega & \left[\frac{17}{64} A_0''(1) + \frac{191}{384} A_2''(1) - \frac{413}{384} A_4''(1) + \frac{9}{16} A_6''(1) + \frac{29}{48} B_2''(2) - \frac{7}{3} B_4''(2) + \frac{27}{16} B_6''(2) \right] \\ & + (\sin \Omega \cos \omega + \cos \Omega \sin \omega \cos i) \left[-\frac{1}{6} B_2''(3) + \frac{1}{3} B_4''(3) \right] \end{aligned} \quad (5.195)$$

5.3.2 Initial Offset Correction

The initial offset for the elliptical orbit averaged results (Eqs. (5.105) - (5.107)) can be derived analytically via the process outlined in Section 5.1.2. While possible, this is time consuming due to the complexity of the orbit averaged results for an eccentric orbit.

A second alternative is to determine the offset numerically. This can be done by integrating the full non-linear dynamics for one orbit and subtracting the initial conditions and the secular change due to the orbit averaged results. This is effectively solving Eq. (5.8) for the periodic offset term numerically. The result is then inserted into Eq. (5.13) to determine the initial value.

5.3.3 Eccentric Orbit Simulation

A simulation has been constructed to validate the orbit averaged results in Eqs. (5.43) - (5.45). This simulation is exactly the same as that in Section 5.2.3, except the initial conditions put the secondary on an elliptical orbit. The same set of arbitrary Fourier coefficients are used. Again, no conclusions about the behavior of real bodies should be drawn from the results shown in Figs. 5.7 - 5.10. The point here is to show that the secular theory closely follows the mean value of the numerical simulation.

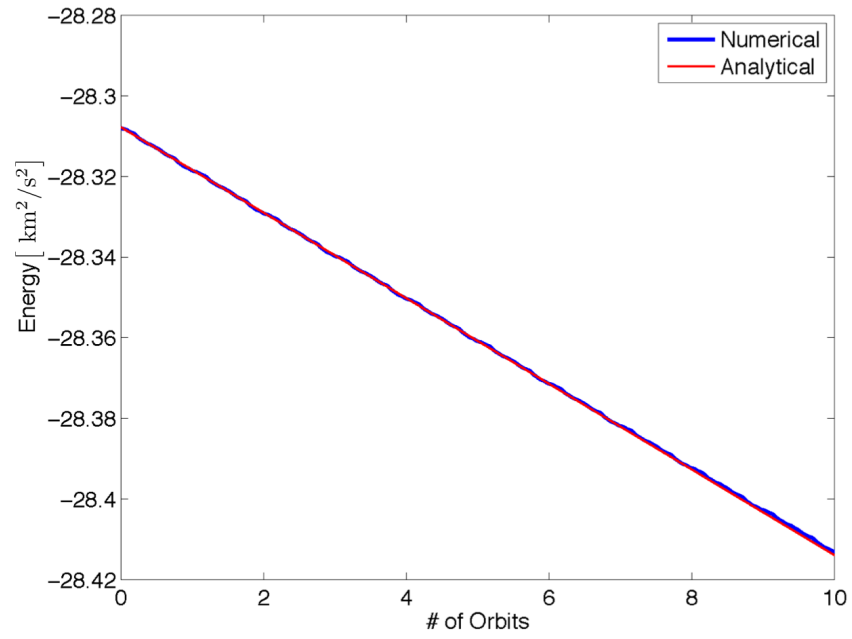


Figure 5.7: Orbital energy of the example secondary over 10 orbits about the primary.

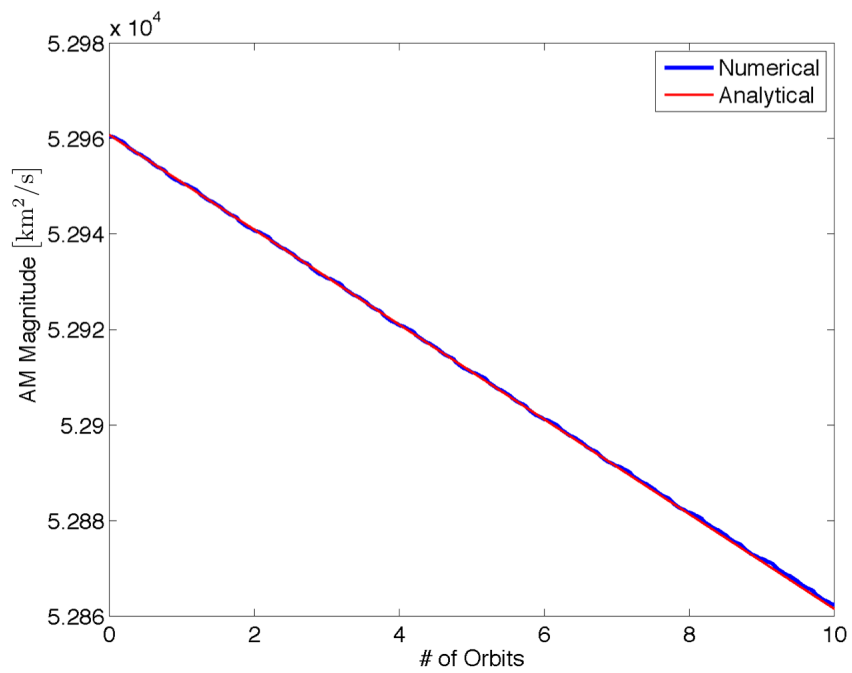


Figure 5.8: Orbit angular momentum magnitude of the example secondary over 10 orbits about the primary.

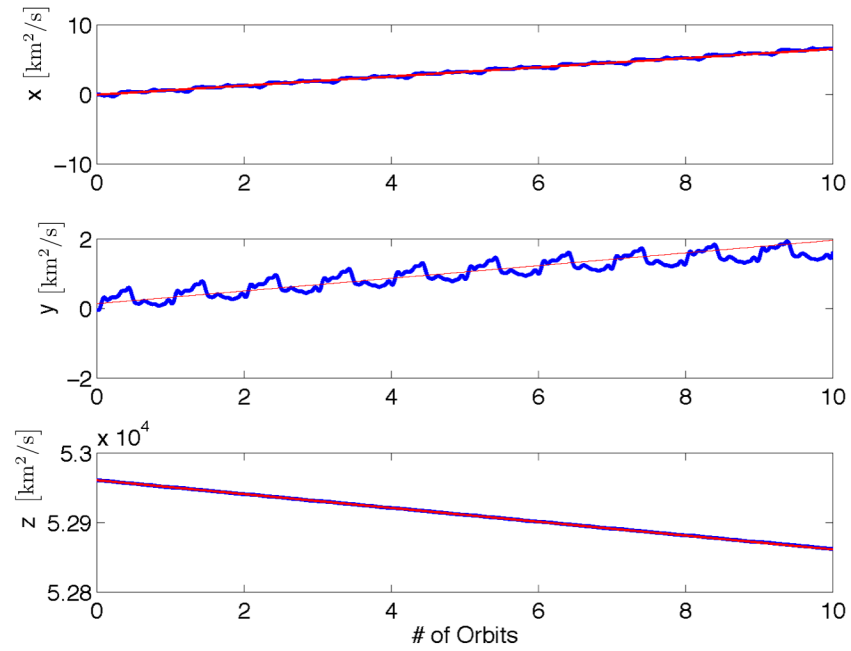


Figure 5.9: Orbit angular momentum vector components in the primary-centered inertial frame for the example secondary over 10 orbits about the primary.

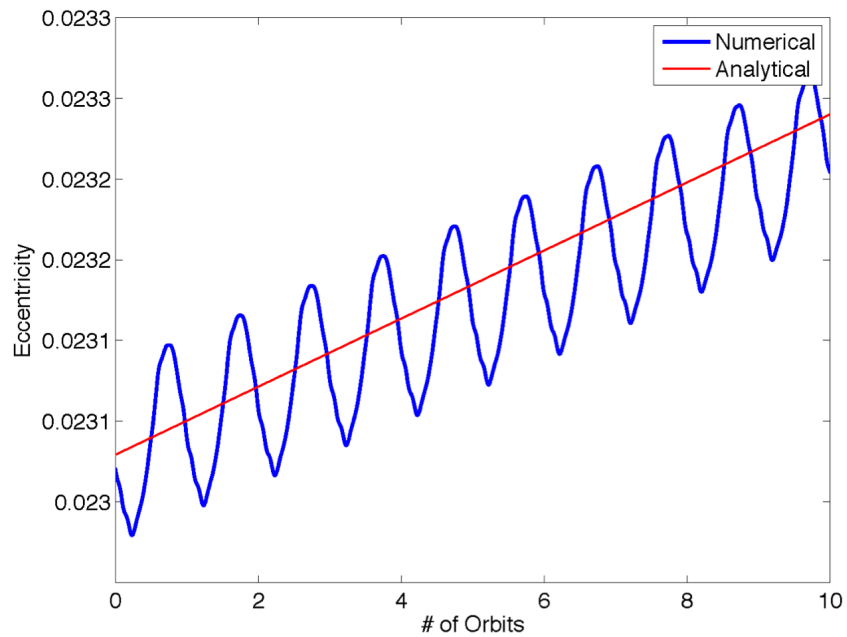


Figure 5.10: Eccentricity of the example secondary over 10 orbits about the primary.

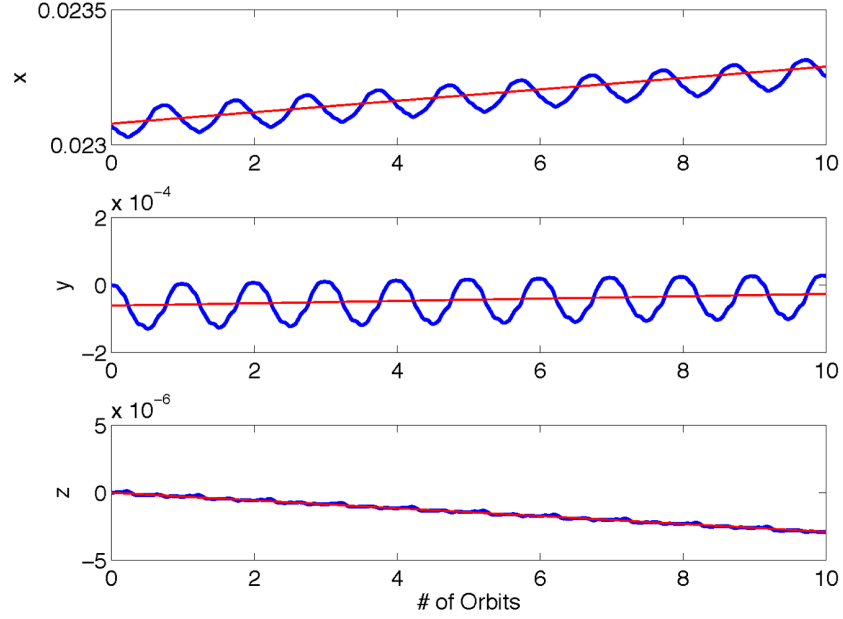


Figure 5.11: Eccentricity vector components in the primary-centered inertial frame for the example secondary over 10 orbits about the primary.

The figures show that the analytical and dynamic results show good agreement for the eccentric case.

5.3.4 Averaging Eccentric Equations Over a Year

The yearly averaging follows the methodology outlined in Section 5.1.3. In the orbit averaged equations ((5.105) - (5.107)), the pressure term, $P(R)$, is replaced and the year averaged Fourier coefficients derived in Section 5.1.3.3 are inserted. Therefore, the resulting year averaged equations become,

$$\overline{\dot{e}}_s = \frac{1}{2m} \frac{G_1}{a_s^2 \sqrt{1-e_s^2}} \frac{h}{a} \left[-(1-e^2)^{-1/2} \sum_{n=1}^{\infty} \left(\frac{2}{n} \right) J'_n(ne) \overline{B}_n''(1) + \frac{2}{e} \sum_{n=1}^{\infty} J_n(ne) \overline{A}_n''(2) \right] \quad (5.196)$$

$$\begin{aligned} \overline{\dot{\mathbf{h}}}_s = & \frac{a}{2m} \frac{G_1}{a_s^2 \sqrt{1-e_s^2}} \left[\left((1-e^2)^{1/2} \sum_{n=1}^{\infty} \left(\frac{2}{ne} \right) J_n(ne) \overline{B}_n''(3) \right) \hat{\mathbf{e}} + \left(3e \overline{A}_0''(3) - \sum_{n=1}^{\infty} \left(\frac{2}{n^2} \right) J'_n(ne) \overline{A}_n''(3) \right) \hat{\mathbf{e}}_{\perp} \right. \\ & \left. + \left(-3e \overline{A}_0''(2) + \sum_{n=1}^{\infty} \left(\frac{2}{n^2} \right) J'_n(ne) \overline{A}_n''(2) - (1-e^2)^{1/2} \sum_{n=1}^{\infty} \left(\frac{2}{ne} \right) J_n(ne) \overline{B}_n''(1) \right) \hat{\mathbf{h}} \right] \quad (5.197) \end{aligned}$$

$$\begin{aligned}
\overline{\dot{\mathbf{e}}_s} = \frac{1}{2m} \frac{G_1}{a_s^2 \sqrt{1-e_s^2}} & \left\{ -\frac{\tilde{\mathbf{h}}}{\mu} \cdot 2\overline{\mathbf{A}}_0'' + \frac{a}{h} \left[\left(3e(1-e^2)^{1/2} \sum_{n=1}^{\infty} \left(\frac{1}{n}\right) J'_n(ne) \overline{\mathbf{B}}_n''(1) - \sum_{n=1}^{\infty} C_n \overline{\mathbf{B}}_n''(1) \right) \hat{\mathbf{e}} \right. \right. \\
& - \left(2D_0 \overline{\mathbf{A}}_0''(1) + \sum_{n=1}^{\infty} D_n \overline{\mathbf{A}}_n''(1) \right) \hat{\mathbf{e}}_{\perp} + \left(-3(1-e^2) \sum_{n=1}^{\infty} J_n(ne) \overline{\mathbf{A}}_n''(2) + 2F_0 \overline{\mathbf{A}}_0''(2) + \sum_{n=1}^{\infty} F_n \overline{\mathbf{A}}_n''(2) \right) \hat{\mathbf{e}} \\
& \left. \left. + \left(\sum_{n=1}^{\infty} G_n \overline{\mathbf{B}}_n''(2) \right) \hat{\mathbf{e}}_{\perp} - (1-e^2)^{1/2} \sum_{n=1}^{\infty} \left(\frac{2}{n}\right) J_n(ne) \cdot \overline{\mathbf{B}}_n'' \right] \right\} \quad (5.198)
\end{aligned}$$

Notice that because the year averaged results have the same form as the orbit averaged results, the series expressions developed above can be used here as well, with the year averaged Fourier coefficients inserted in place of the original coefficients.

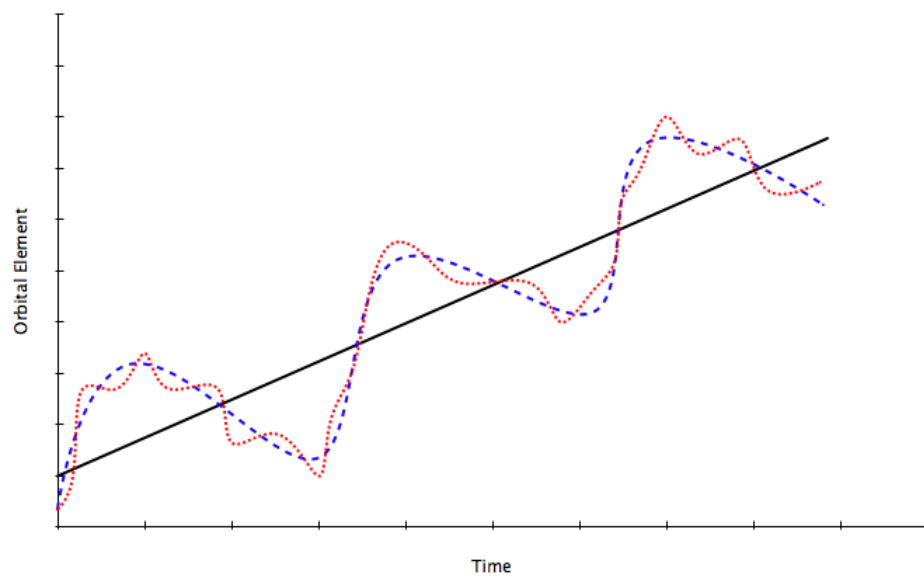


Figure 5.1: Illustration of a generic function time-varying function, shown in red. Removing the short-period terms leaves the function shown in blue. Removing the long-period terms leaves only the secular portion, shown in black.

Chapter 6

Application to Natural Bodies: BYORP

A rotating asymmetric body has a time-varying force imparted on it from solar radiation pressure interacting with the surface of the body. This force imparts a net moment on the body, which results in the well known YORP effect [77, 88], which increases or decreases an object's spin rate over time. It has been hypothesized that when an asymmetric body is in orbit about another body and is rotating synchronously with the orbit, the net force will result in secular changes to the orbit. This effect has been termed the Binary YORP (BYORP) effect [21]. A cartoon illustrating this idea is shown in Fig. 6.1. As different geometries of the body are exposed to sunlight, a different force acts on the body at each point in the orbit. The synchronous spin of the body makes this force periodic with the orbit, which causes secular changes in the orbit to appear.

In early research on representative test objects in planar circular orbits, the timescales predicted for the BYORP effect are very short, yielding binary lifetimes on the order of 10^5 years or less in some cases [20]. Goldreich and Sari [37] have shown that the BYORP timescales for orbit expansion dominate tidal expansions by 2-3 orders of magnitude in many cases. These results indicate that BYORP may be very important for the evolution of binary asteroids. Such a short lifetime for binaries combined with their orbit lifetime (10 Myrs [36]) and population statistics (16% [60]) implies that to maintain this population of binaries a single NEA must, on average, become a binary multiple times over its life.

These implications provide the motivation for further research into BYORP. However the original BYORP theory [21, 37] averages the solar radiation pressure alone first, leaving a constant force in the body frame. The dynamics are then averaged to determine long-term secular effects. This process is incorrect,

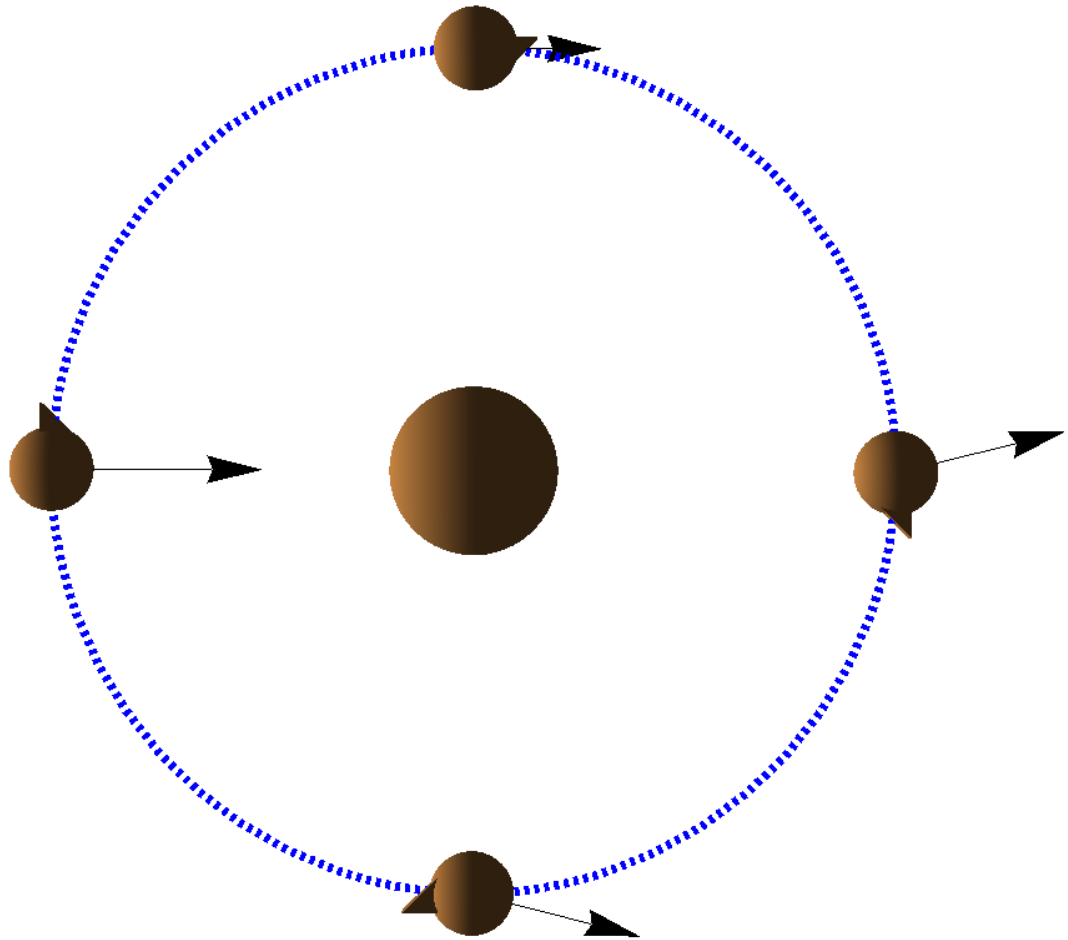


Figure 6.1: This cartoon shows an example asymmetric secondary body that clearly has different geometries exposed to sunlight as it orbits the primary originating from the Sun to the left. The arrows represent the direction of the force imparted on the secondary by solar radiation pressure. It is clear that in this example, the force is not constant in magnitude or direction. This will result in secular changes to the orbit.

as the disturbing acceleration in this case is periodic in time, but is not a disturbing potential. Therefore averaging the disturbing acceleration outside of the dynamics is not appropriate in this case. In §6.1 the theory developed in Chapter 5 is applied to the binary asteroid problem, resulting in an analysis similar to the that done by Scheeres for the YORP effect [92]. The appeal of this theory is that the secular change of the orbit due to the BYORP effect can be described analytically by a set of coefficients which depend on the body’s physical properties and the current orbit description. Once the coefficients are computed based on the body properties, they can be used to determine the secular effects on the orbit at any time. This theory was developed for fully eccentric orbits of any orientation (i.e. not limited to planar orbits as with previous literature).

§6.1 also extends the theory developed in Chapter 5 in order to account for the dynamics present in near-Earth binary asteroid systems. We average the effects of J_2 and the Sun’s 3rd body gravitational effects. After accounting for these major dynamical effects, the analytical results are compared to those from previous works [21, 37]. The conditions under which previous works provide appropriate approximations are discussed. The theory is then applied to the near-Earth asteroid system 1999 KW4 based on the available shape model, and these results are scaled to make predictions for a number of other systems.

Ćuk and Nesvorný [22] have investigated the long-term evolution of binary asteroids through numerical simulations. The evolution of binary systems was explored under the influence of primary oblateness (J_2), evection resonance (due to the Sun’s 3rd body gravity effects), rigid body perturbations on both the orbit and attitude motion, and BYORP. This study showed that BYORP can drive orbit expansion, however the libration is also driven to become chaotic which interrupts BYORP. §6.2 provides an analysis of the changes in the analytical theory for BYORP when the secondary asteroid is librating. Predictions for the evolutions of 1999 KW4 are modified to include the new analytical theory for libration.

6.1 Nominal Predictions

Basic predictions for the BYORP effect can be made by constructing the Fourier coefficients for the system of interest, and applying the secular results from Chapter 5. In this section, several additions to the theory developed to this point will be added which are especially useful for long term predictions of binary

asteroid systems. Then an application to the binary near-Earth asteroid 1999 KW4 is shown, and the results are scaled for other known binary systems.

6.1.1 Non-dimensionalized BYORP Model

It will be useful to write the Fourier coefficients in a non-dimensional form in order to compare how the orbit of bodies of differing shapes are modified under the influence of BYORP. Another reason this is useful is that it will allow us to use coefficients from one shape model and apply it to a different system where a shape model is not yet available [78]. This can allow us to make first order approximations at the secular orbit evolution due to the BYORP effect without having a detailed model of that system.

The Fourier coefficients have units of area. Therefore, we have chosen to use the square of the mean radius as our normalizing factor. The normalized coefficients are,

$$\mathcal{A}_n = \frac{\mathbf{A}_n}{r_m^2} \quad (6.1)$$

$$\mathcal{B}_n = \frac{\mathbf{B}_n}{r_m^2} \quad (6.2)$$

Note that the single and double-prime coefficients are normalized in the same manner.

The mean radius is determined by using the volume of the asteroid, and solving for what the radius of a sphere of equivalent volume would be such that,

$$r_m = \sqrt[3]{\frac{3V}{4\pi}} \quad (6.3)$$

The secular effects of BYORP shown in Eqs. (5.196) - (5.198) can be written in terms of the normalized coefficients by inserting the relevant normalized coefficients into the equations and multiplying each equation by r_m^2 .

6.1.2 BYORP on Doubly Synchronous Binary Systems

Doubly synchronous binary systems, such as the Hermes system [78], have been found to exist. In this case, BYORP will act on each of the asteroids of the system to modify the mutual orbit. By reexamining the definition of the relative orbit, we can see how the accelerations that act on each of the bodies combine to change the mutual orbit.

The inertial dynamics of each of the asteroids is written as,

$$m_1 \ddot{\mathbf{r}}_1 = \frac{Gm_1m_2}{|\mathbf{r}_2 - \mathbf{r}_1|^3}(\mathbf{r}_2 - \mathbf{r}_1) + \mathbf{F}_1 \quad (6.4)$$

$$m_2 \ddot{\mathbf{r}}_2 = -\frac{Gm_1m_2}{|\mathbf{r}_2 - \mathbf{r}_1|^3}(\mathbf{r}_2 - \mathbf{r}_1) + \mathbf{F}_2 \quad (6.5)$$

where \mathbf{F}_1 and \mathbf{F}_2 are disturbing forces such as solar radiation pressure.

We will assume we are looking at the orbit of m_2 around m_1 , so we define $\mathbf{r} = \mathbf{r}_2 - \mathbf{r}_1$ and write

$$\ddot{\mathbf{r}} = \ddot{\mathbf{r}}_2 - \ddot{\mathbf{r}}_1 = -\frac{G(m_1 + m_2)}{r^3}\mathbf{r} + \frac{\mathbf{F}_2}{m_2} - \frac{\mathbf{F}_1}{m_1} \quad (6.6)$$

Now the disturbing acceleration can be written as a combination of the accelerations on the two bodies as,

$$\mathbf{a} = \frac{\mathbf{F}_2}{m_2} - \frac{\mathbf{F}_1}{m_1} = \frac{1}{m_r} \left[(1 - f_m)\mathbf{F}_2 - f_m\mathbf{F}_1 \right] \quad (6.7)$$

where

$$m_r = \frac{m_1m_2}{m_1 + m_2} \quad (6.8)$$

$$f_m = \frac{m_2}{m_1 + m_2} \quad (6.9)$$

Using the theory developed in [65], we can combine the effects of the SRP pressure acting on each of the asteroids of the binary pair. Given that the forces on each of the asteroids is represented by a Fourier series of the form,

$$\mathbf{F}_{1,SRP} = P(R) \left[\mathbf{A}\mathbf{1}''_0 + \sum_{n=1}^{\infty} \mathbf{A}\mathbf{1}''_n \cos(nM) + \mathbf{B}\mathbf{1}''_n \sin(nM) \right] \quad (6.10)$$

$$\mathbf{F}_{2,SRP} = P(R) \left[\mathbf{A}\mathbf{2}''_0 + \sum_{n=1}^{\infty} \mathbf{A}\mathbf{2}''_n \cos(nM) + \mathbf{B}\mathbf{2}''_n \sin(nM) \right] \quad (6.11)$$

and the total SRP acceleration acting on the orbit of m_2 is

$$\begin{aligned} \mathbf{a}_{SRP} = \frac{P(R)}{m} \left[(1 - f_m)\mathbf{A}\mathbf{2}''_0 - f_m\mathbf{A}\mathbf{1}''_0 \right] + \frac{P(R)}{m} \sum_{n=1}^{\infty} \left((1 - f_m)\mathbf{A}\mathbf{2}''_n - f_m\mathbf{A}\mathbf{1}''_n \right) \cos(nM) \\ + \left((1 - f_m)\mathbf{B}\mathbf{2}''_n - f_m\mathbf{B}\mathbf{1}''_n \right) \sin(nM) \end{aligned} \quad (6.12)$$

From this expression we can write a new set of combined coefficients as

$$\mathbf{AC}''_0 = (1 - f_m)\mathbf{A2}''_0 - f_m\mathbf{A1}''_0 \quad (6.13)$$

$$\mathbf{AC}''_n = (1 - f_m)\mathbf{A2}''_n - f_m\mathbf{A1}''_n \quad (6.14)$$

$$\mathbf{BC}''_n = (1 - f_m)\mathbf{B2}''_n - f_m\mathbf{A1}''_n \quad (6.15)$$

which allows us to write,

$$\mathbf{a}_{SRP} = \frac{P(R)}{m} \left[\mathbf{AC}''_0 + \sum_{n=1}^{\infty} \mathbf{AC}''_n \cos(nM) + \mathbf{BC}''_n \sin(nM) \right] \quad (6.16)$$

This expression is of exactly the same form as the SRP acceleration used in [65], therefore these coefficients can be put directly into the orbit averaged secular equations to define the effect of BYORP on the orbit due to both bodies. In order to find the year averaged results, the year averaged values of the double-prime coefficients for each body will need to be determined. Then those year averaged coefficients can be combined using Eqs. (6.13) - (6.15), and the resulting year averaged combined coefficients can be directly inserted into Eqs. (5.196) - (5.198).

There are several interesting implications of these results. The first thing to note is that our theory can easily incorporate doubly synchronous systems by only modifying the coefficients. Thus, if a system transitions between singly and doubly synchronous states, it can be handled by only changing the coefficients of the evolutionary equations. The main point of interest, however, is that in a doubly synchronous system, the BYORP effect can either be enhanced or reduced. If the bodies have the opposite sign on the most significant coefficients, then the BYORP effect will be enhanced, while the same signs in these coefficients can cause the majority of the BYORP effect to be canceled out if the bodies are of similar mass.

6.1.3 Secular Evolution of Binary Asteroid Systems

The theory discussed in Chapter 5 describes the secular changes in the mutual orbit energy, angular momentum, and eccentricity vector under the influence of BYORP only. In this section, we also consider the effect that the other major disturbing forces for binary NEA systems, J_2 and 3rd body effects from the Sun, have on the secular evolution of the system. We start by describing the secular effect of BYORP on

the semi-major axis, angular momentum magnitude, and the eccentricity of the system in §6.1.3.1. These variables may be more useful in many circumstances, especially when considering J_2 . The averaging of the BYORP secular effects under the influence of J_2 is derived in §6.1.3.2. Finally, the averaging of the BYORP secular effects under the influence of the 3rd body perturbations from the Sun are discussed in §6.1.3.3. Which perturbation dominates the binary system depends on the size of the mutual orbit.

6.1.3.1 Secular rates of e and h and a

In many circumstances, it may be more interesting or useful to look at the evolution of the angular momentum magnitude, the eccentricity, and the semi-major axis evolution. These results were derived in §3.2. Here, we apply the year-averaging to these equations for use in making long-term predictions.

The year averaged semi-major axis evolution is simply dependent on the year averaged energy rate as,

$$\overline{\dot{a}} = \frac{2a^2 \overline{\dot{e}}}{\mu} \quad (6.17)$$

The year averaged angular momentum magnitude and eccentricity rates are,

$$\overline{\dot{h}} = \hat{\mathbf{h}} \cdot \overline{\dot{\mathbf{h}}} \quad (6.18)$$

$$\overline{\dot{e}} = \hat{\mathbf{e}} \cdot \overline{\dot{\mathbf{e}}} \quad (6.19)$$

because the orbit frame unit vectors are considered constant for the averaging process. To consider the circular and elliptical cases in turn now only requires us to input the appropriate year-averaged rates.

Circular Case

The year averaged rates of the energy, angular momentum and eccentricity vectors for this case are given in Eqs. (5.87) - (5.89). Taking the appropriate dot products above gives,

$$\overline{\dot{a}} = \frac{P_\Phi}{a_s^2 \sqrt{1 - e_s^2}} \frac{2ah}{m\mu} \left[\hat{\mathbf{y}}_b \cdot \overline{\mathbf{A}}_0' \right] \quad (6.20)$$

$$\overline{\dot{h}} = \frac{P_\Phi}{a_s^2 \sqrt{1 - e_s^2}} \frac{a}{m} \left[\hat{\mathbf{y}}_b \cdot \overline{\mathbf{A}}_0' \right] \quad (6.21)$$

$$\overline{\dot{e}} = \frac{P_\Phi}{a_s^2 \sqrt{1 - e_s^2}} \frac{h}{2m\mu} \left[\hat{\mathbf{x}}_b \cdot \overline{\mathbf{B}}_1' + 2\hat{\mathbf{y}}_b \cdot \overline{\mathbf{A}}_1' \right] \quad (6.22)$$

Alternatively, if one wanted to use the double-prime coefficients, then Eqs. (5.90) - (5.92) would be used, which result in,

$$\bar{\bar{a}} = \frac{P_\Phi}{a_s^2 \sqrt{1-e_s^2}} \frac{ah}{m\mu} \left[-\hat{\mathbf{a}} \cdot \bar{\mathbf{B}}_1'' + \hat{\mathbf{b}} \cdot \bar{\mathbf{A}}_1'' \right] \quad (6.23)$$

$$\bar{\bar{h}} = \frac{P_\Phi}{a_s^2 \sqrt{1-e_s^2}} \frac{a}{2m} \left[-\hat{\mathbf{a}} \cdot \bar{\mathbf{B}}_1'' + \hat{\mathbf{b}} \cdot \bar{\mathbf{A}}_1'' \right] \quad (6.24)$$

$$\bar{\bar{e}} = \frac{P_\Phi}{a_s^2 \sqrt{1-e_s^2}} \frac{h}{2m\mu} \left[-2\hat{\mathbf{b}} \cdot \bar{\mathbf{A}}_0'' - \frac{1}{2}\hat{\mathbf{a}} \cdot \bar{\mathbf{B}}_2'' + \frac{1}{2}\hat{\mathbf{b}} \cdot \bar{\mathbf{A}}_2'' \right] \quad (6.25)$$

where $\hat{\mathbf{a}}$ and $\hat{\mathbf{b}}$ define the orbital plane, $\hat{\mathbf{a}}$ being the preferred direction from which the angular position is measured ($\hat{\mathbf{a}}$ is analogous to $\hat{\mathbf{e}}$ except for a circular orbit).

It is instructive to compare these results to those previously analyzed in [21] and [37]. In those papers, the solar radiation pressure force was averaged alone without regard to the orbit, giving a resultant force that is constant in the body frame. If this force were expressed as a Fourier series, the only non-zero components would be $\bar{\mathbf{A}}_0'(1)$ and $\bar{\mathbf{A}}_0'(2)$ in the body frame, or in the orbit frame the non-zero components would be $\bar{\mathbf{A}}_1''(1) = \bar{\mathbf{B}}_1''(2)$ and $\bar{\mathbf{A}}_1''(2) = -\bar{\mathbf{B}}_1''(1)$. It can be seen from Eq. (6.20) or (6.23) that there would be a secular rate for the semi-major axis, but there would be no secular change in the eccentricity for circular orbits, as was expressed by previous studies. However, Eqs. (6.22) and (6.25) show that it would be quite possible for there to be a secular change in the eccentricity for circular orbits if higher order coefficients have non-zero values.

Elliptical Case

The elliptical case uses Eqs. (5.196) - (5.198). The expressions for the semi-major axis, angular momentum magnitude, and the eccentricity are,

$$\bar{\bar{a}} = \frac{P_\Phi}{a_s^2 \sqrt{1-e_s^2}} \frac{ah}{m\mu} \left[\sum_{n=1}^{\infty} \left(J_{n-1}(ne) + J_{n+1}(ne) \right) \bar{\mathbf{A}}_n''(2) - (1-e^2)^{-1/2} \sum_{n=1}^{\infty} \frac{2}{n} J_n'(ne) \bar{\mathbf{B}}_n''(1) \right] \quad (6.26)$$

$$\begin{aligned} \bar{\bar{h}} = \frac{P_\Phi}{a_s^2 \sqrt{1-e_s^2}} \frac{a}{2m} \left[-3e \bar{\mathbf{A}}_0''(2) + \sum_{n=1}^{\infty} \left(\frac{2}{n^2} \right) J_n'(ne) \bar{\mathbf{A}}_n''(2) \right. \\ \left. - (1-e^2)^{1/2} \sum_{n=1}^{\infty} \frac{1}{n} (J_{n-1}(ne) + J_{n+1}(ne)) \bar{\mathbf{B}}_n''(1) \right] \quad (6.27) \end{aligned}$$

$$\begin{aligned} \bar{e} = \frac{P_\Phi}{a_s^2 \sqrt{1-e_s^2}} \frac{1}{2m} \left\{ \frac{2h}{\mu} \bar{\mathbf{A}}_0''(2) + \frac{a}{h} \left[\left(3e(1-e^2)^{1/2} \sum_{n=1}^{\infty} \left(\frac{1}{n} \right) J'_n(ne) \bar{\mathbf{B}}_n''(1) - \sum_{n=1}^{\infty} C_n \bar{\mathbf{B}}_n''(1) \right) \right. \right. \\ \left. \left. + \left(-3(1-e^2) \sum_{n=1}^{\infty} J_n(ne) \bar{\mathbf{A}}_n''(2) + 2F_0 \bar{\mathbf{A}}_0''(2) + \sum_{n=1}^{\infty} F_n \bar{\mathbf{A}}_n''(2) \right) \right. \right. \\ \left. \left. - (1-e^2)^{1/2} \sum_{n=1}^{\infty} \left(\frac{2}{n} \right) J_n(ne) \cdot \bar{\mathbf{B}}_n''(1) \right] \right\} \quad (6.28) \end{aligned}$$

Series expansions for these equations up to third order in eccentricity are included in Appendix A. Note here that if the force is a constant in the body frame as assumed in previous studies, then there will be secular growth in semi-major axis and eccentricity for eccentric orbits. However, it is clear that higher order coefficients become important for the orbit evolution in these cases.

The series expansion up to third order in eccentricity for the year averaged semi-major axis is,

$$\bar{a} = \frac{P_\Phi}{a_s^2 \sqrt{1-e_s^2}} \frac{ah}{m\mu} \left\{ \bar{a}_0 + e\bar{a}_1 + e^2\bar{a}_2 + e^3\bar{a}_3 + \dots \right\} \quad (6.29)$$

where the first 3 orders are,

$$\bar{a}_0 = -\bar{\mathbf{B}}_1''(1) + \bar{\mathbf{A}}_1''(2) \quad (6.30)$$

$$\bar{a}_1 = -\bar{\mathbf{B}}_2''(1) + \bar{\mathbf{A}}_2''(2) \quad (6.31)$$

$$\bar{a}_2 = -\frac{1}{8}\bar{\mathbf{B}}_1''(1) - \frac{9}{8}\bar{\mathbf{B}}_3''(1) - \frac{1}{8}\bar{\mathbf{A}}_1''(2) + \frac{9}{8}\bar{\mathbf{A}}_3''(2) \quad (6.32)$$

$$\bar{a}_3 = \frac{1}{6}\bar{\mathbf{B}}_2''(1) - \frac{4}{3}\bar{\mathbf{B}}_4''(1) - \frac{1}{3}\bar{\mathbf{A}}_2''(2) + \frac{4}{3}\bar{\mathbf{A}}_4''(2) \quad (6.33)$$

The series expansion up to third order in eccentricity for the year averaged angular momentum magnitude is,

$$\bar{h} = \frac{a}{2m} \frac{P_\Phi}{a_s^2 \sqrt{1-e_s^2}} \left\{ \bar{h}_0 + e\bar{h}_1 + e^2\bar{h}_2 + e^3\bar{h}_3 + \dots \right\} \quad (6.34)$$

where the first 3 orders are,

$$\bar{h}_0 = \bar{\mathbf{A}}_1''(2) - \bar{\mathbf{B}}_1''(1) \quad (6.35)$$

$$\bar{h}_1 = -3\bar{\mathbf{A}}_0''(2) + \frac{1}{2}\bar{\mathbf{A}}_2''(2) - \frac{1}{2}\bar{\mathbf{B}}_2''(1) \quad (6.36)$$

$$\bar{h}_2 = -\frac{3}{8}\bar{\mathbf{A}}_1''(2) + \frac{3}{8}\bar{\mathbf{A}}_3''(2) + \frac{5}{8}\bar{\mathbf{B}}_1''(1) - \frac{3}{8}\bar{\mathbf{B}}_3''(1) \quad (6.37)$$

$$\bar{h}_3 = -\frac{1}{3}\bar{\mathbf{A}}_2''(2) + \frac{1}{3}\bar{\mathbf{A}}_4''(2) + \frac{5}{12}\bar{\mathbf{B}}_2''(1) - \frac{1}{3}\bar{\mathbf{B}}_4''(1) \quad (6.38)$$

The series expansion up to third order in eccentricity for the year averaged eccentricity is,

$$\bar{e} = \frac{1}{2m} \frac{P_\Phi}{a_s^2 \sqrt{1-e_s^2}} \frac{a}{h} \left\{ \bar{e}_0 + e\bar{e}_1 + e^2\bar{e}_2 + e^3\bar{e}_3 + \dots \right\} \quad (6.39)$$

where the first 3 orders are,

$$\bar{e}_0 = \frac{2}{\mu} \frac{h}{a} \left[\overline{h\mathbf{A}_0''}(2) \right] + \left[\overline{\mathbf{A}_0''}(2) + \frac{1}{2}\overline{\mathbf{A}_2''}(2) - \frac{1}{2}\overline{\mathbf{B}_2''}(1) \right] \quad (6.40)$$

$$\bar{e}_1 = -\frac{57}{4}\overline{\mathbf{A}_1''}(2) + \frac{3}{4}\overline{\mathbf{A}_3''}(2) + \frac{55}{4}\overline{\mathbf{B}_1''}(1) - \frac{3}{4}\overline{\mathbf{B}_3''}(1) \quad (6.41)$$

$$\bar{e}_2 = -\overline{\mathbf{A}_0''}(2) - 15\overline{\mathbf{A}_2''}(2) + \overline{\mathbf{A}_4''}(2) + \frac{59}{4}\overline{\mathbf{B}_2''}(1) - \overline{\mathbf{B}_4''}(1) \quad (6.42)$$

$$\bar{e}_3 = \frac{385}{24}\overline{\mathbf{A}_1''}(2) - \frac{555}{32}\overline{\mathbf{A}_3''}(2) + \frac{125}{96}\overline{\mathbf{A}_5''}(2) - \frac{293}{24}\overline{\mathbf{B}_1''}(1) + \frac{549}{32}\overline{\mathbf{B}_3''}(1) - \frac{125}{96}\overline{\mathbf{B}_5''}(1) \quad (6.43)$$

6.1.3.2 J_2 Averaging

Many primary asteroids in a binary pair are expected to have large J_2 values due to a shape similar to KW4-alpha with a large equatorial bulge. In order to more realistically model the secular evolution of such systems, the effect of J_2 on the secular dynamics must be considered.

For our system of equations, we will need to investigate the effect of both SRP and J_2 on the orbit energy, angular momentum, and eccentricity. Initially, these effects can be expressed as,

$$\dot{\mathcal{E}} = \dot{\mathcal{E}}_{BYORP} + \dot{\mathcal{E}}_{J_2} \quad (6.44)$$

$$\dot{\mathbf{h}} = \dot{\mathbf{h}}_{BYORP} + \dot{\mathbf{h}}_{J_2} \quad (6.45)$$

$$\dot{\mathbf{e}} = \dot{\mathbf{e}}_{BYORP} + \dot{\mathbf{e}}_{J_2} \quad (6.46)$$

As was done with SRP alone, these equations are averaged over an orbit to get the secular expressions per orbit as,

$$\bar{\mathcal{E}} = \bar{\mathcal{E}}_{BYORP} + \bar{\mathcal{E}}_{J_2} \quad (6.47)$$

$$\bar{\mathbf{h}} = \bar{\mathbf{h}}_{BYORP} + \bar{\mathbf{h}}_{J_2} \quad (6.48)$$

$$\bar{\mathbf{e}} = \bar{\mathbf{e}}_{BYORP} + \bar{\mathbf{e}}_{J_2} \quad (6.49)$$

The effects of the two forces are averaged independently and then added at this level, which is valid to first order because the averaging is a linear operator over independent disturbing accelerations, and the orbital elements are assumed constant over that averaging period.

In order to first determine the secular effects of J_2 over an orbit, we begin with the well known results from the Lagrange equations averaged over an orbit. These show that the secular effects of J_2 on the classical orbit elements is [111],

$$\bar{\dot{\Omega}}_p = -\frac{3nR_P^2 J_2}{2p^2} \cos i_p \quad (6.50)$$

$$\bar{\dot{\omega}}_p = \frac{3nR_P^2 J_2}{4p^2} (4 - 5 \sin^2 i_p) \quad (6.51)$$

$$\bar{\dot{i}}_p = 0 \quad (6.52)$$

$$\bar{\dot{a}} = 0 \quad (6.53)$$

$$\bar{\dot{e}} = 0 \quad (6.54)$$

where Ω_p is the right ascension of the ascending node, ω_p is the argument of perigee, i_p is the inclination (Ω_p , ω_p , and i_p are relative to a primary fixed reference frame), n is the mean motion, R_P is the radius of the primary, and p is the semi-latus rectum. We do not give the change in mean anomaly, as this aspect of the secular orbit evolution can be ignored. Clearly, the fact that J_2 does not change the semi-major axis in a secular manner also means that $\bar{\dot{e}}_{J_2} = 0$. Therefore any secular change in the energy will be caused by SRP only, and will not need to be addressed further in this section.

As our theory uses different orbital elements, we derive the effects of J_2 on \mathbf{e} and \mathbf{h} in terms of the classical orbit elements. First, taking the derivative with respect to time of these quantities we get,

$$\bar{\dot{\mathbf{e}}}_{J_2} = e\bar{\dot{\mathbf{e}}}_{J_2} + \bar{e}_{J_2}\mathbf{e} \quad (6.55)$$

$$\bar{\dot{\mathbf{h}}}_{J_2} = h\bar{\dot{\mathbf{h}}}_{J_2} + \bar{h}_{J_2}\mathbf{h} \quad (6.56)$$

It is also known that under the action of J_2 , $\dot{h}_{J_2} = 0$. Combined with Eq. (6.54), the above equations

simplify to,

$$\bar{\mathbf{e}}_{J_2} = e\bar{\hat{\mathbf{e}}}_{J_2} \quad (6.57)$$

$$\bar{\mathbf{h}}_{J_2} = h\bar{\hat{\mathbf{h}}}_{J_2} \quad (6.58)$$

Due to the induced rates, $\bar{\Omega}_p$ and $\bar{\omega}_p$, J_2 has the effect of making the angular momentum and eccentricity unit vectors circulate in inertial space. The angular momentum unit vector traces out a cone about the primary spin axis direction, while the eccentricity unit vector will follow a more complicated path as it circulates in the orbit plane while the plane rotates in inertial space. If this motion is averaged over the J_2 induced rates, then the average unit vectors will not be meaningful any longer; the average angular momentum unit vector will only have a component in the primary spin axis direction and the eccentricity unit vector will average to zero (unless the inclination is such that $\bar{\Omega}_p = \bar{\omega}_p$, in which case there will be a non-zero averaged eccentricity unit vector in the inertial $\hat{\mathbf{x}} - \hat{\mathbf{y}}$ plane as well).

When there is a non-zero inclination between the orbit angular momentum and the primary spin axis, the circulation of the angular momentum vector in inertial space will cause a variation in the solar latitude (δ_s) and longitude (λ_s), which will change the Fourier coefficients used to determine the SRP acceleration. For a system with a small inclination, this variation will be small as well, and therefore there will generally be a small variation in the Fourier coefficients. However, if systems with a large inclination are to be studied, the variation in the Fourier coefficients over the J_2 induced circulation must be considered. At this point, we assume that the inclination is small so that the variation in the Fourier coefficients is minimal and can be ignored.

At this point, we should note that we have averaged out three of the classical orbital elements: mean anomaly, argument of perigee, and the right ascension of the ascending node. This has had the effect of causing our variational equations for angular momentum and the eccentricity vectors to be reduced to their magnitudes. However, our three variational equations are no longer independent orbital elements given that,

$$h = \sqrt{\mu p} = \sqrt{\mu a(1 - e^2)} \quad (6.59)$$

Therefore there is one more degree of freedom left in the problem that we haven't addressed, and that is the inclination of the orbital plane.

The inclination, i_p , can be computed as,

$$\cos i_p = \frac{\mathbf{h} \cdot \hat{\mathbf{z}}}{h} \quad (6.60)$$

and therefore the rate of change of the inclination can be computed as,

$$\dot{i}_p = \frac{\dot{h}\mathbf{h} \cdot \hat{\mathbf{z}} - h\dot{\mathbf{h}} \cdot \hat{\mathbf{z}}}{h^2 \sin i_p} \quad (6.61)$$

however note that $\mathbf{h} = h\hat{\mathbf{h}}$, and under the averaged influence of BYORP and J_2 , $\dot{\mathbf{h}} = \dot{h}\hat{\mathbf{h}}$, so that

$$\dot{i}_p = 0 \quad (6.62)$$

Thus we can conclude that under the averaging of J_2 , the only orbit elements to track are any two of the energy, angular momentum magnitude, and eccentricity.

6.1.3.3 Long-term Averaging

The solar node (Ω_{s0}) can be made to circulate due to J_2 , 3rd body perturbations from the planets or due to the 3rd body effects of the Sun on the mutual orbit. In this section we discuss how this circulation occurs and average the secular rates over the circulation of the node by averaging the year-averaged coefficients in Eqs. (5.25) - (5.29).

First, the effects of J_2 on the solar node can be seen from the rates in Eqs. (6.50) and (6.51) with the definition of the solar node given by

$$\begin{aligned} \tan(\Omega_{s0}) &= \frac{\hat{\mathbf{Z}}_H \cdot \hat{\mathbf{e}}}{-\hat{\mathbf{Z}}_H \cdot \hat{\mathbf{e}}_\perp} \\ &= \frac{\cos(\omega) \sin(i_H) \sin(\Omega_H - \Omega) + [\cos(i_H) \sin(i) - \cos(i) \cos(\Omega_H - \Omega) \sin(i_H)] \sin(\omega)}{-\cos(i_H) \cos(\omega) \sin(i) + [\cos(i) \cos(\Omega_H - \Omega) \cos(\omega) + \sin(\Omega_H - \Omega) \sin(\omega)] \sin(i_H)} \end{aligned} \quad (6.63)$$

where i_H and Ω_H are the inclination and right ascension of the ascending node of the heliocentric orbit, and i , Ω , and ω are the inclination, right ascension of the ascending node, and argument of periape of the binary system's mutual orbit. All of these angles are measured with respect to the inertial frame. The definition of the solar node is illustrated in Fig. 2.1. Note however, that the J_2 induced rates are on the argument of periape and right ascension of the ascending node in the primary fixed frame, while the definition of the solar node depends up these values with respect to the inertial frame. Therefore, in general, the J_2 induced

rates can cause a variation in Ω , ω , and i with respect to the inertial frame if the primary's spin axis is not perpendicular to the ecliptic plane. However, as mentioned in the previous section, the inclination with respect to the primary, i_p , is often near zero for binary asteroid systems. In this case, Ω_p is undefined, and the periaapse direction circulates due to $\dot{\Omega}_p + \dot{\omega}_p$. Because the angular momentum vector is effectively fixed in inertial space, this combined rate will directly map to a rate in ω . The circulation of periaapse due to J_2 will dominate in smaller orbits, however as the orbit grows its importance will shrink as it depends on $a^{-5/2}$.

In the case of the NEA population, the Sun's influence will dominate over planetary perturbations. The period of circulation for NEA binaries due to the Sun's 3rd body effects is on the order of 500 years [97], whereas the circulation due to 3rd body perturbations from the planets is on the order of $10^4 - 10^5$ years [73].

The secular change of the node and periaapse of the mutual orbit (averaged over the secondary orbit and the heliocentric orbit) due to the 3rd body effect of the Sun were found in [97, 42] to be,

$$\frac{d\Omega}{dt} = -\frac{3}{8} \frac{N_s^2}{n\sqrt{1-e_s^2}} \frac{\cos i}{\sqrt{1-e^2}} (2 + 3e^2 - 5e^2 \cos 2\omega) \quad (6.64)$$

$$\frac{d\omega}{dt} = \frac{3}{8} \frac{N_s^2}{n\sqrt{1-e_s^2}} \frac{1}{\sqrt{1-e^2}} (5 \cos^2 i - 1 + 5 \sin^2 i \cos 2\omega + e^2(1 - 5 \cos 2\omega)) \quad (6.65)$$

where Ω is the right ascension of the ascending node, ω is the argument of periaapse and i is the inclination, all relative to the heliocentric orbit, e is the eccentricity, n is the mean motion, all of these orbital elements being for the mutual orbit of the binary asteroid system. N_s and e_s are the mean motion and eccentricity of the heliocentric orbit. As the orbit becomes larger, these effects will overtake the circulation due to J_2 .

The non-linearity in the definition of the solar node given in Eq. (6.63) means that the solar node does not vary uniformly as is typically assumed when averaging over an angular quantity. However, the rates of circulation for Ω and ω are typically disparate, which will result in complicated short term behavior of Ω_{s0} , but the long term behavior approaches that predicted by a uniform circulation. Therefore, we carry out the averaging of our evolutionary equations as if Ω_{s0} does evolve uniformly.

By inspection of Eqs. (5.25) - (5.29), it is immediately apparent that for all $n \geq 1$, the coefficients are multiplied by $\cos(n\Omega_{s0})$ or $\sin(n\Omega_{s0})$, and therefore average to zero over the circulation of the solar node. The only coefficient that survives this averaging with a non-zero value is $\overline{\overline{\mathbf{A}}_0}'' = \overline{\mathbf{A}}_0' = \overline{\mathbf{A}}_0$. This propagates

to the double-prime coefficients so that the only surviving coefficients after this averaging are,

$$\overline{\overline{\mathbf{A}}_0}'' = \begin{bmatrix} 0 \\ 0 \\ \overline{\mathbf{A}}_0'(3) \end{bmatrix} \quad (6.66)$$

$$\overline{\overline{\mathbf{A}}_1}'' = \begin{bmatrix} \overline{\mathbf{A}}_0'(1) \\ \overline{\mathbf{A}}_0'(2) \\ 0 \end{bmatrix} \quad (6.67)$$

$$\overline{\overline{\mathbf{B}}_1}'' = \begin{bmatrix} -\overline{\mathbf{A}}_0'(2) \\ \overline{\mathbf{A}}_0'(1) \\ 0 \end{bmatrix} \quad (6.68)$$

These results can be inserted into the year-averaged equations to find the secular evolutionary equations for the energy, angular momentum magnitude, and eccentricity under the influence of the BYORP effect, J_2 , and the 3rd body perturbation of the Sun. The circular equations become,

$$\overline{\overline{\dot{a}}_{\Omega_{s0}}} = 2 \frac{P_{\Phi}}{a_s^2 \sqrt{1-e_s^2}} \frac{ah}{m\mu} \overline{\mathbf{A}}_0(2) \quad (6.69)$$

$$\overline{\overline{\dot{h}}_{\Omega_{s0}}} = \frac{P_{\Phi}}{a_s^2 \sqrt{1-e_s^2}} \frac{a}{m} \overline{\mathbf{A}}_0(2) \quad (6.70)$$

$$\overline{\overline{\dot{e}}_{\Omega_{s0}}} = 0 \quad (6.71)$$

Therefore the secular evolution of a circular orbit under the influence of the BYORP effect and J_2 is that it will stay circular and expand or contract based on the single year-averaged coefficient $\overline{\mathbf{A}}_0(2)$.

The elliptical equations become,

$$\overline{\overline{\dot{a}}_{\Omega_{s0}}} = \frac{P_{\Phi}}{a_s^2 \sqrt{1-e_s^2}} \frac{ah}{m\mu} \left[\left(1 + \frac{1}{\sqrt{1-e^2}}\right) J_0(e) + \left(1 - \frac{1}{\sqrt{1-e^2}}\right) J_2(e) \right] \overline{\mathbf{A}}_0(2) \quad (6.72)$$

$$\overline{\overline{\dot{h}}_{\Omega_{s0}}} = \frac{P_{\Phi}}{a_s^2 \sqrt{1-e_s^2}} \frac{a}{2m} \left[\left(1 + \sqrt{1-e^2}\right) J_0(e) + \left(\sqrt{1-e^2} - 1\right) J_2(e) \right] \overline{\mathbf{A}}_0(2) \quad (6.73)$$

$$\overline{\overline{\dot{e}}_{\Omega_{s0}}} = \frac{P_{\Phi}}{a_s^2 \sqrt{1-e_s^2}} \frac{1}{2m} \frac{a}{h} \left[\sqrt{1-e^2} \left(-\frac{3}{2} e J_0(e) + [2 - 3\sqrt{1-e^2}] J_1(e) + \frac{3}{2} e J_2(e) \right) + C_1 + F_1 \right] \overline{\mathbf{A}}_0(2) \quad (6.74)$$

As with the circular equations, the elliptical equations also depend only on one coefficient, $\overline{\mathbf{A}}_0(2)$.

In this case, however, the eccentricity will evolve. Due to the presence of the Bessel functions and the

coefficients C_1 and F_1 , it is hard to determine from these expressions exactly how the secular evolution depends on the eccentricity. In order to clarify this situation, Eqs. (6.72) - (6.74) are expanded as a series in terms of eccentricity up to fourth order to get,

$$\bar{\bar{a}}_{\Omega_{s0}} \simeq \frac{P_{\Phi}}{a_s^2 \sqrt{1-e_s^2}} \frac{ah}{m\mu} \left[2 + \frac{7}{32} e^4 \right] \bar{\mathbf{A}}_0(2) \quad (6.75)$$

$$\bar{\bar{h}}_{\Omega_{s0}} \simeq \frac{P_{\Phi}}{a_s^2 \sqrt{1-e_s^2}} \frac{a}{2m} \left[2 - e^2 - \frac{e^4}{32} \right] \bar{\mathbf{A}}_0(2) \quad (6.76)$$

$$\bar{\bar{e}}_{\Omega_{s0}} \simeq \frac{P_{\Phi}}{a_s^2 \sqrt{1-e_s^2}} \frac{1}{2m} \frac{a}{h} \left[-e + \frac{13e^3}{8} \right] \bar{\mathbf{A}}_0(2) \quad (6.77)$$

Note that if $e = 0$ we quickly recover Eqs. (6.69) - (6.71).

It is very interesting at this point to compare the results in Eqs. (6.75) and (6.77) to those given by Goldreich [37]. If we take the zeroth order term from Eq. (6.75) and compare it to the first order term from Eq. (6.77), and use the zeroth order approximation $h = \sqrt{\mu a}$, we can reproduce the result,

$$\frac{1}{e} \bar{\bar{e}}_{\Omega_{s0},1} = -\frac{1}{4a} \bar{\bar{a}}_{\Omega_{s0},0} \quad (6.78)$$

where the “,1” and “,0” subscripts refer to the order of the eccentricity approximation used. After averaging over the secondary orbit, the heliocentric orbit, and the rotation of the node, the result is the same as applying an average force to the dynamics [3, 5].

The dynamical implications of Eqs. (6.75) - (6.78) are worth discussing. These clearly indicate that over the long-term averaging of a system, the semi-major axis and the eccentricity will evolve in opposite directions; when the semi-major axis grows, the eccentricity will be damped. Likewise, when the semi-major axis is contracting, the eccentricity is growing. This situation is illustrated with simulation results in §6.1.4.2.

6.1.4 Application to Binary System 1999 KW4

The binary asteroid system 1999 KW4 is one of the best characterized systems to date. Excellent observations were made in 2001 which allowed good estimates of the binary orbit, and shape models of both asteroids to be constructed [76]. Due to the fact that this system is so well characterized, it is a good first system for application of this model.

6.1.4.1 KW4 Physical Model

The shape of KW4 Beta (the secondary) as constructed from the shape models produced from the radar observations [76] is shown in Figs. 6.2 - 6.5. This shape model is constructed of 2292 triangular facets. The body frame associated with the single-prime coefficients is oriented such that $\hat{\mathbf{x}}_b$ is pointed away from the primary, $\hat{\mathbf{z}}_b$ is the rotation axis which is parallel to $\hat{\mathbf{h}}$, and $\hat{\mathbf{y}}_b$ is roughly along the velocity vector, to complete the frame. In the case of a circular orbit, $\hat{\mathbf{x}}_b$ will always be parallel to the radius vector, but for eccentric orbits these vectors are only parallel at apoapsis and periapsis due to the synchronous rotation assumption.

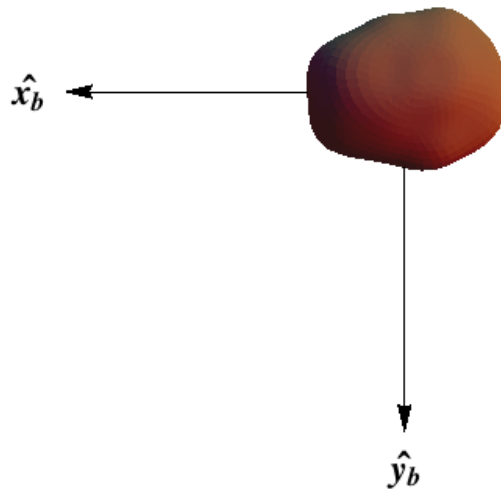


Figure 6.2: Top view of the KW4 Beta shape model with the body axes illustrated.

The facets from the shape model were used to compute the Fourier coefficients. Computation of the Fourier coefficients also requires the optical properties of the surface. We assume the body is uniform and dull, meaning that there is no specular reflection ($s = 0$ in Eqs. (2.30) and (2.31)). We have also assumed that there is zero thermal inertia to the body, although our theory is able to handle this if we want to add it later. The Fourier coefficients in the body frame are shown in Figs. 6.6 - 6.8, plotted against the zenith angle, which is equal to $90^\circ - \delta_s$. Note that for this case, we have developed the body frame coefficients, and set up our simulation such that $\phi_0 = 0$ and $\lambda_{s0} = 0$, so that the no-prime and single-prime coefficients are all equivalent. Also, it is interesting to point out that the effect of the insolation term $(\hat{\mathbf{u}}\hat{\mathbf{u}} \cdot \hat{\mathbf{n}}_i H_i(\hat{\mathbf{u}}) A_i)$

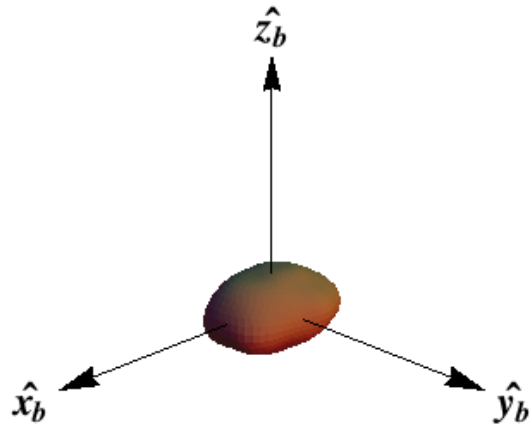


Figure 6.3: Isometric view of the KW4 Beta shape model with the body axes illustrated.

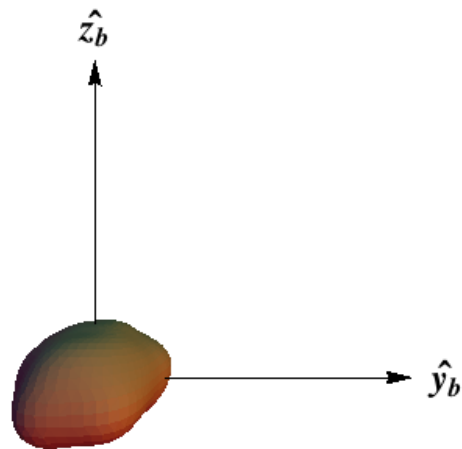


Figure 6.4: Front view of the KW4 Beta shape model with the body axes illustrated.

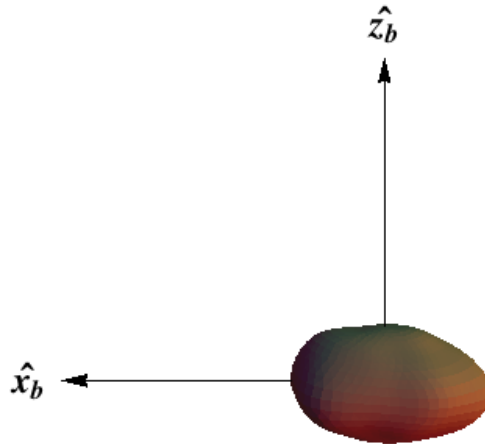


Figure 6.5: Side view of the KW4 Beta shape model with the body axes illustrated.

disappears over the year averaging of the coefficients, and therefore we have not included that term in for following plots. Due to these assumptions, the coefficient of Lambertian scattering ($B = 2/3$) has been pulled outside of the coefficients illustrated in the figures in this section so that they illustrate only the geometric qualities of the secondary body.

Note that for Figs. 6.7, 6.8, 6.10, and 6.11 the following colors define the first four orders: $n = 1$ is blue; $n = 2$ is green; $n = 3$ is red; $n = 4$ is cyan.

The double-prime coefficients are defined in the orbit frame, and are therefore a combination of the single-prime coefficients. These coefficients are shown in Figures 7-9.

One benefit of our theory is that given the heliocentric orbit of the binary system, the year-averaged coefficients can be computed independently of integration of the secular equations. Given the solar inclination in the body-frame, which for KW4 is computed to be $i_s = 168$, the year averaged no-prime coefficients are computed to be single values by averaging the coefficients over the range of zenith angles the Sun takes over the heliocentric orbit. These values are shown in Figs. 6.12 and 6.13. Only the coefficients up to order $n = 5$ are shown, since higher orders are very small comparatively and do not show up on this scale.

As discussed in §2.2, the year averaged double-prime coefficients depend on the location of the solar node in the body frame. The current solar node is given in Table 6.2. Table 6.1 lists all the physical

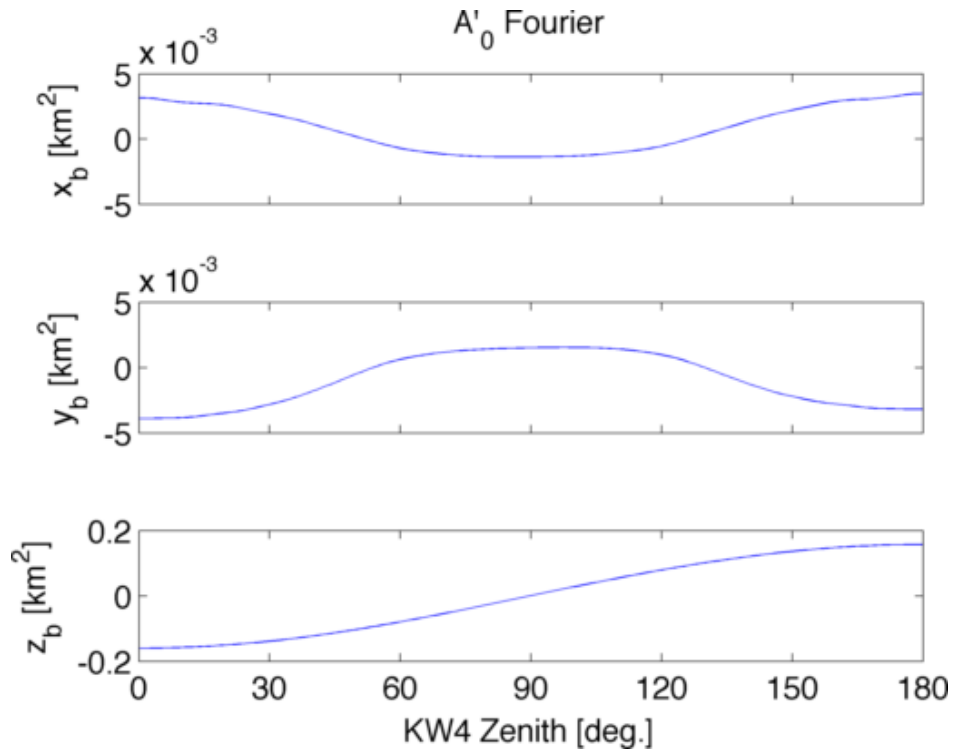


Figure 6.6: Plot of A'_0 over zenith angle (measured from the body's north pole) in body frame components denoted by the basis vectors \hat{x}_b , \hat{y}_b , \hat{z}_b .

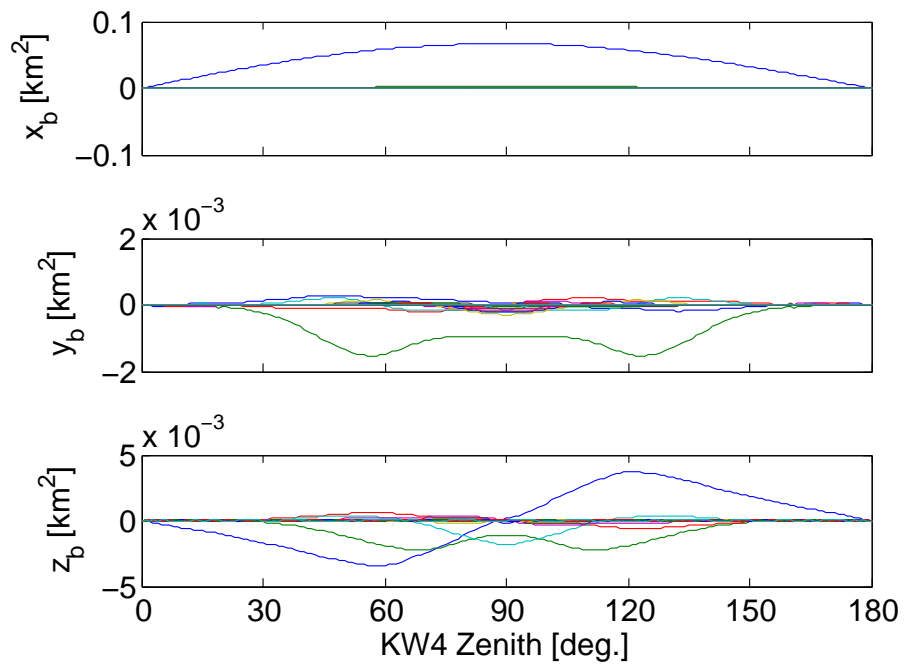


Figure 6.7: Plot of A'_n for KW4 over zenith angle in body frame components. The first four orders are defined by the following color scheme: $n = 1$ is blue; $n = 2$ is green; $n = 3$ is red; $n = 4$ is cyan.

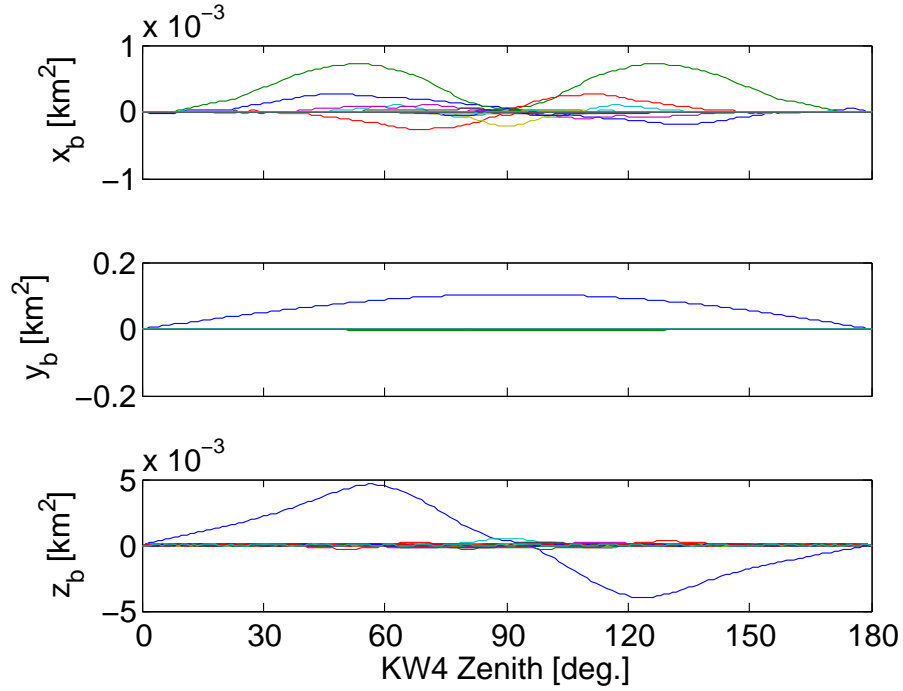


Figure 6.8: Plot of B'_n for KW4 over zenith angle in body frame components. The first four orders are defined by the following color scheme: $n = 1$ is blue; $n = 2$ is green; $n = 3$ is red; $n = 4$ is cyan.

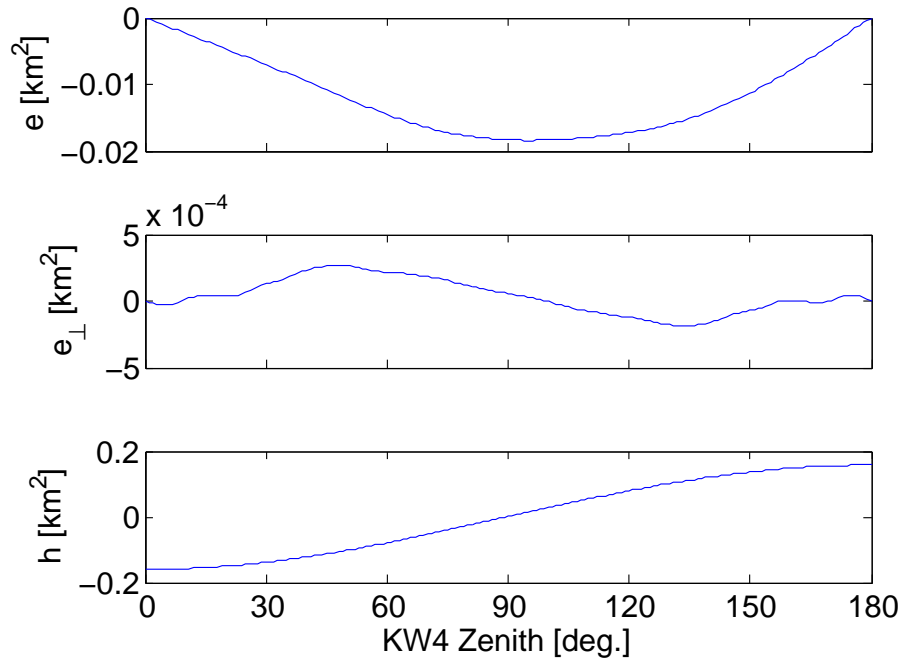


Figure 6.9: Plot of A''_0 over zenith angle (measured from the body's north pole) in orbit frame components denoted by the basis vectors \hat{e} , \hat{e}_{\perp} , \hat{h} .

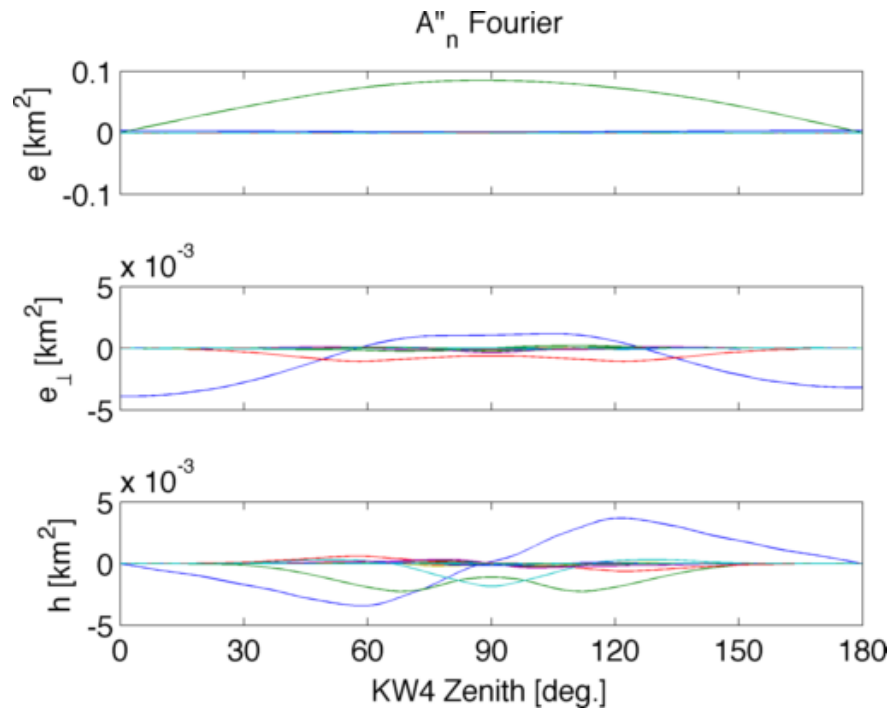


Figure 6.10: Plot of \mathbf{A}_n'' for KW4 over zenith angle in body frame components. The first four orders are defined by the following color scheme: $n = 1$ is blue; $n = 2$ is green; $n = 3$ is red; $n = 4$ is cyan.

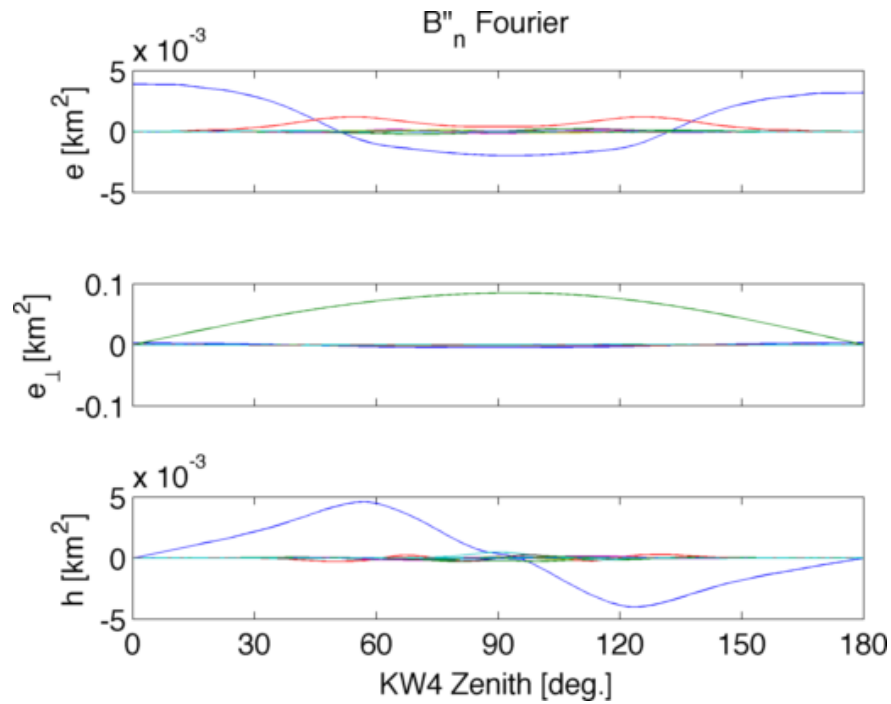


Figure 6.11: Plot of \mathbf{B}_n'' for KW4 over zenith angle in body frame components. The first four orders are defined by the following color scheme: $n = 1$ is blue; $n = 2$ is green; $n = 3$ is red; $n = 4$ is cyan.

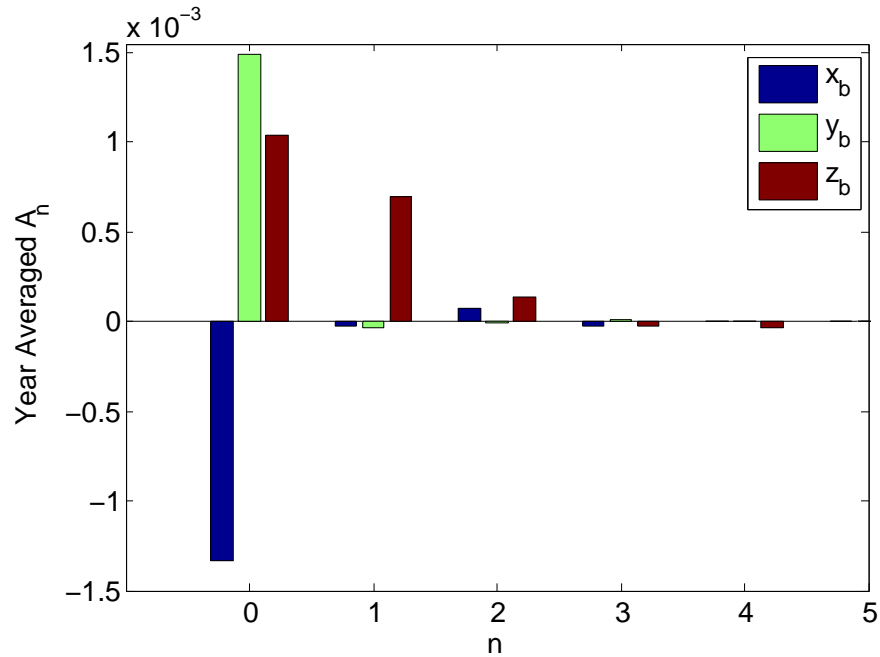


Figure 6.12: This figure shows the body-frame components of $\bar{\mathbf{A}}_n$, the year-averaged Fourier coefficients of KW4. These values were computed with a fixed heliocentric inclination and rotation pole (values are given in Table 6.1). Only the first few orders are shown as these are the dominant terms.

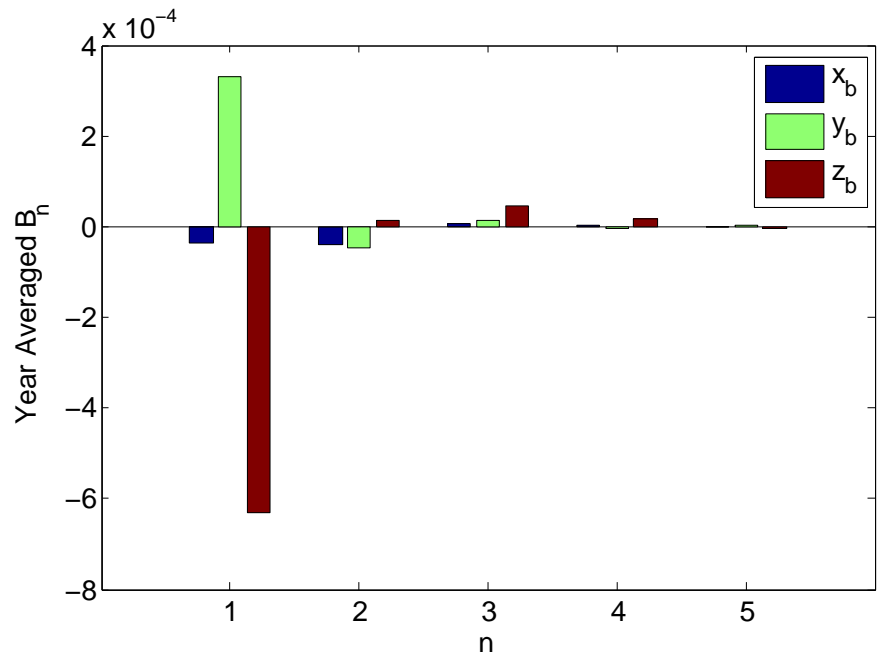


Figure 6.13: This figure shows the body-frame components of $\bar{\mathbf{B}}_n$, the year-averaged Fourier coefficients of KW4. These values were computed with a fixed heliocentric inclination and rotation pole (values are given in Table 6.1). Only the first few orders are shown as these are the dominant terms.

properties of the KW4 system of interest to this study. Included in this table are the orbital elements of KW4 Beta’s orbit, the masses of the system, and the definition of the KW4 system’s heliocentric orbit. The sources for each of these values is listed in the caption. Note that while these are estimated parameters, in this study we use only the mean values.

Table 6.1: Physical properties of the KW4 system. All data is reproduced from [76], except those marked with a * which are from [73], and those marked with a # which are from [92].

Description	Symbol	Units	Value
Semi-major axis	a	[km]	2.548
Eccentricity	e	[]	0.0004
Inclination	i	[deg.]	156.1
Long. of asc. node	Ω	[deg.]	105.4
Arg. of perigee	ω	[deg.]	319.7
Mass of Alpha	m_α	[kg]	2.353×10^{12}
Mass of Beta	m	[kg]	0.135×10^{12}
Rotation pole longitude	α	[deg.]	326
Rotation pole latitude	δ	[deg.]	-62
Alpha obliquity gravity	J_2	[km ²]	-0.02728
Heliocentric semi-major axis	a_s	[AU]	0.642
Heliocentric eccentricity	e_s	[]	0.6884
Heliocentric inclination	i_H	[deg.]	38.89
Heliocentric long. of asc. node	Ω_H	[deg.]	244.93
Solar node drift rate*	$\dot{\Omega}_H$	[arcsec/year]	-16.898
Solar radiation constant#	G_1	[kg km/s ²]	1×10^{14}

6.1.4.2 KW4 Predictions

In this section we present the results of simulations for the secular evolution of the KW4 mutual orbit under the influence of BYORP, J_2 , and 3rd body perturbations from the Sun. The initial conditions used in the simulations are shown in Table 6.2. Note that the inclination of the mutual orbit to the primary equator is generally small, and always less than 10 [29]. A value 3 was used for calculation of the J_2 rates shown in Table 6.2.

It should be noted that this simulation is intended only to show how the BYORP effect can change the KW4 orbit under the influence of the considered dynamics. This simulation is not representative of the “true” evolution of the KW4 orbit as we neglect many dynamical processes, such as close planetary approaches, which will change the smooth evolution found in this simulation.

The first simulation integrates Eqs. (6.72) - (6.74) which represent the evolution of the system in

Table 6.2: These values have either been derived from the previously cited data according to equations in [65], or they were set arbitrarily for the simulation. The vectors are expressed in inertial coordinates.

Description	Symbol	Units	Value
Initial energy	\mathcal{E}	[km ² /s ²]	-3.2586×10^{-8}
Initial angular momentum vector	$\mathbf{h}(1)$	[km ² /s]	2.540×10^{-4}
	$\mathbf{h}(2)$	[km ² /s]	6.998×10^{-5}
	$\mathbf{h}(3)$	[km ² /s]	-5.947×10^{-4}
Initial angular momentum magnitude	h	[km ² /s]	6.505×10^{-4}
Initial eccentricity vector	$\mathbf{e}(1)$	[]	-3.090×10^{-4}
	$\mathbf{e}(2)$	[]	2.314×10^{-4}
	$\mathbf{e}(3)$	[]	-1.048×10^{-4}
Initial J_2 rates	$\dot{\Omega}$	[rad./s]	-5.7724×10^{-7}
	$\dot{\omega}$	[rad./s]	-1.0037×10^{-6}
Gravitational parameter	μ	[km ³ /s ²]	1.6606e-07
Solar inclination in body frame	i_s	[deg.]	168.07
Solar node	Ω_{s0}	[deg.]	-28.1487
Initial solar longitude	λ_{s0}	[deg.]	0
Initial Beta rotation angle	ϕ_0	[deg.]	0

its most fully averaged form. The results of the simulation show growth in the semi-major axis, as seen in Fig. 6.14. The current year averaged growth rate for the semi-major axis is computed to be approximately 7 cm per year. The predicted times for the orbit to double in size and for it to reach the Hill Sphere are indicated in the figure. The evolution of the eccentricity is shown in Fig. 6.15. As discussed in §6.1.3.3, the eccentricity is damped as the semi-major axis grows.

These trends were confirmed for the case when Eqs. (6.26) - (6.28) are simulated and the solar node varies according to the dynamics discussed in §6.1.3.3. In that case, while the major trend is clearly a damping of eccentricity while the semi-major axis grows, there are significant periods where the eccentricity is growing at the same time as the semi-major axis. Therefore, observations of a system with growing semi-major axis and eccentricity would not rule out BYORP as the driver of the system evolution.

The second simulation that was run has the secondary body flipped 180° in space to see what would happen in the opposite orientation. As expected, the semi-major axis decreases as shown in Fig. 6.16. While the semi-major axis decreases, the eccentricity is growing, as shown in Fig. 6.17. Again, these trends were confirmed by simulating Eqs. (6.26) - (6.28) while the solar node is slowly circulating.

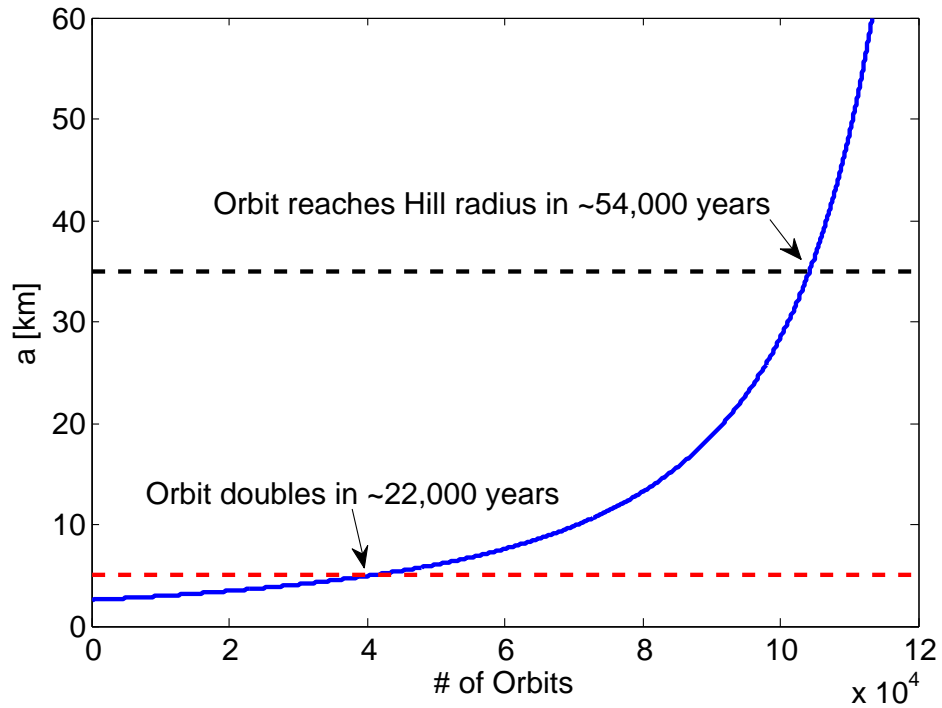


Figure 6.14: Predicted evolution of the semi-major axis under BYORP, J_2 , and 3rd body perturbations from the Sun. This integration was carried out with the long-term averaged evolutionary equations.

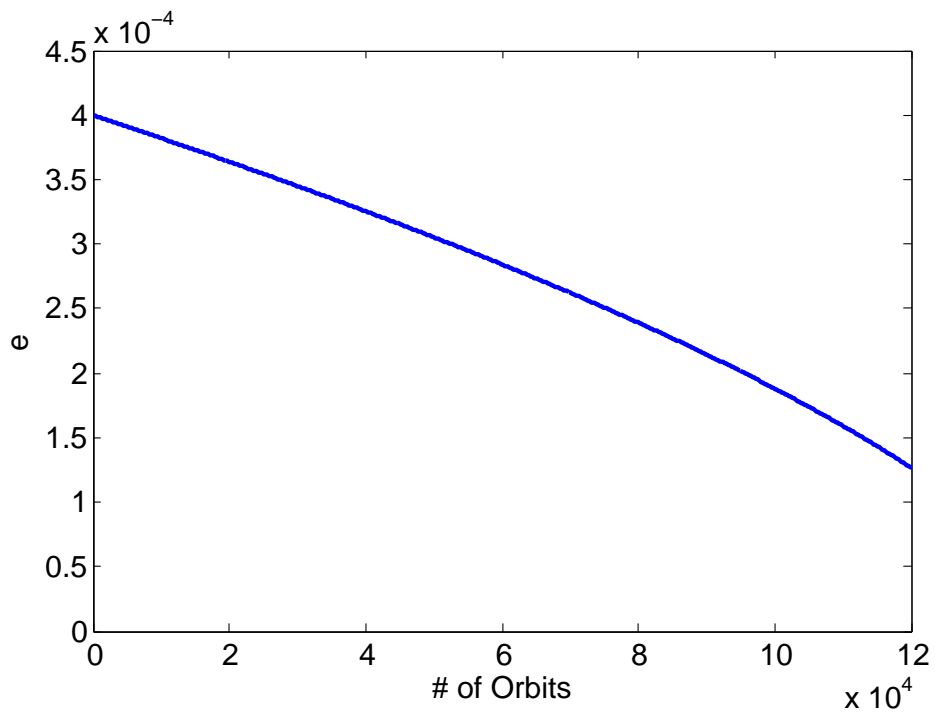


Figure 6.15: Predicted evolution of the eccentricity under BYORP, J_2 , and 3rd body perturbations from the Sun. This integration was carried out with the long-term averaged evolutionary equations.

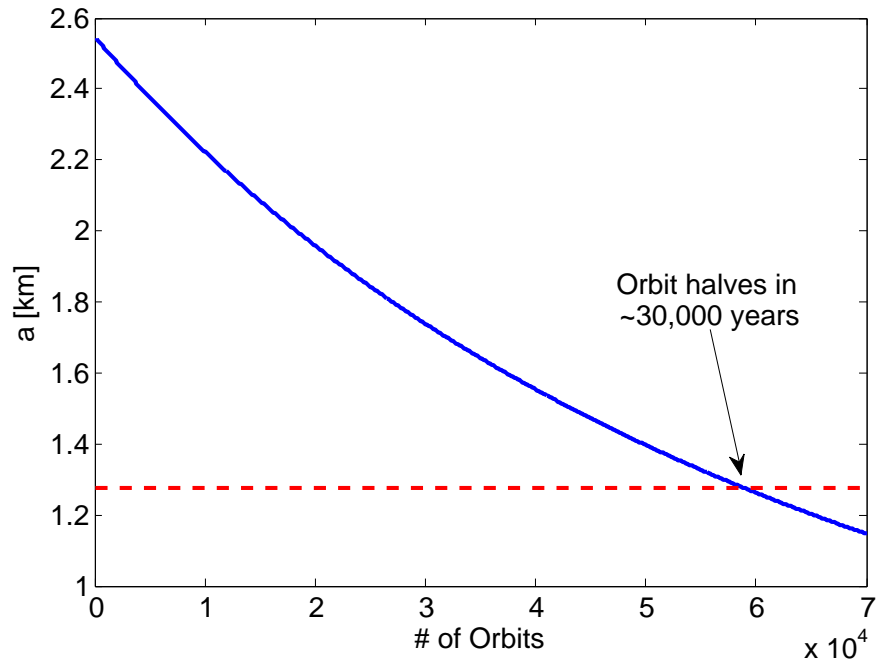


Figure 6.16: Predicted evolution of the semi-major axis under BYORP, J_2 , and 3rd body perturbations from the Sun. This integration was carried out with the long-term averaged evolutionary equations, and the secondary body flipped 180.

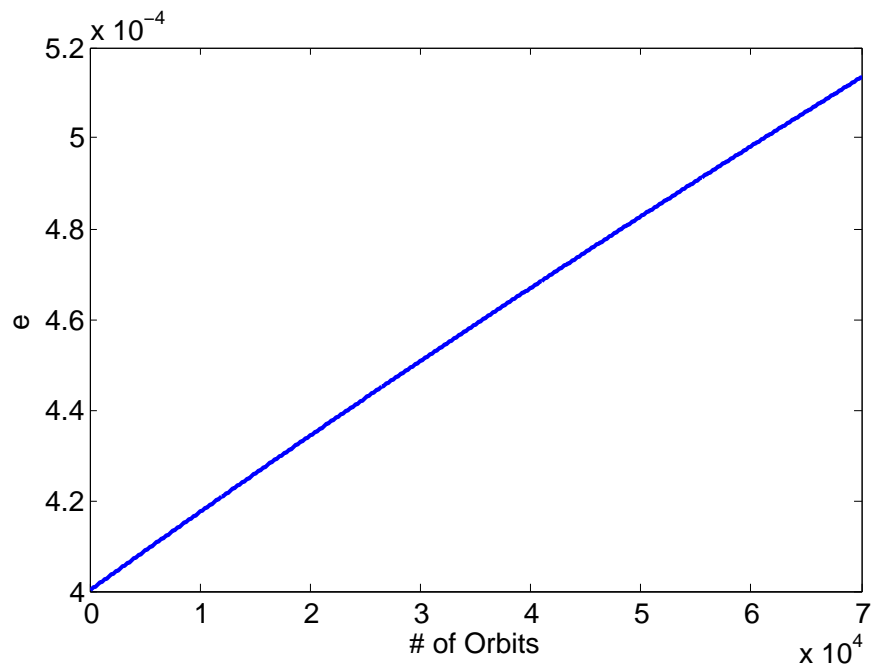


Figure 6.17: Predicted evolution of the eccentricity under BYORP, J_2 , and 3rd body perturbations from the Sun. This integration was carried out with the long-term averaged evolutionary equations, and the secondary body flipped 180.

6.1.4.3 Estimation of BYORP Predictions

We have shown that BYORP can cause significant secular changes in binary orbits. The current secular rates depend on the shape and optical properties of the asteroids as expressed by the Fourier coefficients, along with the current orbit state. Specifically, the results of §6.1.4.2 show that the 1999 KW4 orbit should be expanding at an appreciable rate. This naturally leads to the question of whether or not this effect can be observed through observation of a binary system.

While the BYORP induced expansion may be significant, it is much smaller than what is currently observable. In the case of KW4, the observations that allowed the orbit to be characterized and the shape models to be developed were of very high quality, but the standard errors on the semi-major axis fit is ± 15 m. Given the predicted expansion rate of 7 cm per year, one can see that it would take many years between observations to see if there is a drift, and this would still not constrain the drift rate very accurately.

However, there are two observable components which are influenced by the orbit expansion that may be measured; the orbit period and the mean anomaly. The mean anomaly for a Keplerian orbit is,

$$M = n(t - t_0) \quad (6.79)$$

where n is the mean motion, t_0 is the time of periape passage such that $M_0 = 0$, and t is the current time.

Taking the time derivative of this give,

$$\dot{M} = n + \dot{n}(t - t_0) \quad (6.80)$$

This can be directly integrated to get,

$$M = n(t - t_0) + \frac{1}{2}\dot{n}(t - t_0)^2 \quad (6.81)$$

Eq. (6.81) tells us that when the mean motion is changing, then the mean anomaly changes with a quadratic rate. It is clear that when the orbit is expanding, this causes the mean motion to change as well. The mean motion is defined as,

$$n = \sqrt{\frac{\mu}{a^3}} \quad (6.82)$$

so that the time derivative is,

$$\dot{n} = -\frac{3}{2}\sqrt{\frac{\mu}{a^5}}\dot{a} = -\frac{3n\dot{a}}{2a} \quad (6.83)$$

This result is inserted into Eq. (6.81) so that the value of M at a given time, t , becomes,

$$M = n(t - t_0) - \frac{3n\dot{a}}{4a}(t - t_0)^2 \quad (6.84)$$

Therefore, the drift in mean anomaly compared to a Keplerian system can be expressed as,

$$\Delta M = \frac{1}{2}\dot{n}(t - t_0)^2 = -\frac{3n\dot{a}}{4a}(t - t_0)^2 = \Delta M_d(t - t_0)^2 \quad (6.85)$$

Note that the constant offset to the period from the effect of J_2 is ignored, however this doesn't affect the quadratic growth of mean anomaly due to expansion of the orbit.

Likewise, one can compute a rate of change in the period to be,

$$\dot{T} = \frac{3T\dot{a}}{2a} \quad (6.86)$$

Given that the change in mean anomaly is quadratic with time due to orbit expansion, this should be the easiest to detect.

One possible way to estimate the mean anomaly is to fit the observed mean anomalies to the quadratic function shown in Eq. (6.81). If the measured values are M_i and t_i , the difference in these values since the epoch time, and we want to estimate n and \dot{n} , the cost functional can be written as,

$$J = \frac{1}{2\sigma_M^2} \sum_{i=1}^N \left(\Delta M_i - n\Delta t_i - \frac{1}{2}\dot{n}\Delta t_i^2 \right)^2 \quad (6.87)$$

where σ_M is the measurement sigma on the mean anomaly measurements, which can be computed by eclipse observations using photometry.

The least squares problem can now be set up as,

$$\Lambda \begin{bmatrix} n \\ \dot{n} \end{bmatrix} = Z \quad (6.88)$$

where the information matrix is written as,

$$\Lambda = \frac{1}{\sigma_M^2} \begin{bmatrix} \sum_i \Delta t_i^2 & \frac{1}{2} \sum_i \Delta t_i^3 \\ \frac{1}{2} \sum_i \Delta t_i^3 & \frac{1}{4} \sum_i \Delta t_i^4 \end{bmatrix} \quad (6.89)$$

and the measurement vector is,

$$Z = \frac{1}{\sigma_M} \begin{bmatrix} \sum_i \Delta M_i \Delta t_i \\ \frac{1}{2} \sum_i \Delta M_i \Delta t_i^2 \end{bmatrix} \quad (6.90)$$

From this formulation, we can approximate the sigma values for n and \dot{n} as,

$$\sigma_n = \frac{\sigma_M}{\sqrt{\sum_i \Delta t_i^2}} \quad (6.91)$$

$$\sigma_{\dot{n}} = \frac{2\sigma_M}{\sqrt{\sum_i \Delta t_i^4}} \quad (6.92)$$

The accuracy of the estimates of n and \dot{n} depend largely on the t_i for the measurements. Specifically, since the terms both depend on the sum of higher orders of these measurement times, the largest time term will dominate, so the time between the epoch and the latest measurement will dominate the accuracy of the estimates.

Given these relationships, the question is if this estimation is possible or not. To illustrate the feasibility of the measurement, we will use the KW4 system. Given the values for KW4 in Tables 6.1 and 6.2, and the relationships in Eqs. (6.82) and (6.83), along with the current semi-major expansion rate, we find that the current values for KW4 are,

$$n = 1.002 \times 10^{-4} \text{ rad/sec} \quad (6.93)$$

$$\dot{n} = -1.29 \times 10^{-16} \text{ rad/sec}^2 \quad (6.94)$$

If we assume $\sigma_M = 1$, we can find σ_n and $\sigma_{\dot{n}}$ assuming that one measurement is made at 1, 5, and 10 years after the initial measurement. These values are listed in Table 6.3, along with the amount of drift expected in the mean anomaly and period over these time spans. The results show that given this accuracy on measurements of the mean anomaly, we should easily be able to detect the quadratic drift in the mean anomaly due to BYORP.

Table 6.3: Drift in mean anomaly and period computed using the current KW4 expansion rate, along with estimation errors for n and \dot{n} over these time spans.

	Mean Anomaly	Period	σ_n	$\sigma_{\dot{n}}$
1 Year	-3.70	2.59 s	5.53×10^{-10} rad/s	3.51×10^{-17} rad/s ²
5 Years	-92.52	12.96 s	1.11×10^{-10} rad/s	1.40×10^{-18} rad/s ²
10 Years	-370.07	25.92 s	5.53×10^{-11} rad/s	3.51×10^{-19} rad/s ²

6.1.4.4 Scaled BYORP Predictions for Other Binaries

For comparison, we have included scaled results for other binary systems, using the semi-major axis expansion rate from KW4 as a starting point. This rate can be scaled directly for other systems by using the following equation,

$$\dot{a}_j = \left[\frac{D_{s,j}^2}{D_{s,KW4}^2} \right] \left[\frac{\nu_{KW4} a_{KW4}^3 T_j^3}{T_{KW4}^3 \nu_j a_j^3} \right] \left[\frac{a_{s,KW4}^2 \sqrt{1 - e_{s,KW4}^2}}{a_{s,j}^2 \sqrt{1 - e_{s,j}^2}} \right] \dot{a}_{KW4} \quad (6.95)$$

where j refers to a different binary, D_s is the secondary mean diameter, T is the orbit period, and ν is the mass fraction, which can be computed by,

$$\nu_j = \frac{D_s^3}{D_p^3 + D_s^3} \quad (6.96)$$

where D_p is the primary mean diameter. Note that if one wanted to determine the scaled coefficients for the KW4 system using Eqs. (6.1) and (6.2), the mean radius can be obtained from $r_m = D_s/2$.

Results for scaling the orbit expansion rate for a number of well observed binaries are shown in Table 4. We note that these expansion rates range from 10^4 to less than 10^6 years in most cases, in accord with the approximate predictions found in [20]. As indicated in Eq. (6.95), these scaled results only account for differences in size and mass of the other binary systems. However scaled coefficients are not recomputed to account for the different obliquities of these systems. This is mainly due to a lack of good information on pole directions of the binary asteroids. Furthermore because the KW4 results are simply scaled, these results show that every orbit is expanding; it is understood that in reality the orbits could be shrinking at these rates. Therefore the computed expansion rates should be considered only as indications of the possible effects, not predictions.

Table 6.4: Scaled orbit expansion results for well observed binaries. Binary data including heliocentric orbit semi-major axis (a_s) and eccentricity (e_s), primary and secondary diameters (D_{pri} and D_{sec} respectively), orbit semi-major axis (a) and orbit period (T_{orb}) obtained from [117]. Mass fraction (ν) derived by Eq. (6.96). Semi-major axis growth rate (\dot{a}) for all binaries scaled from KW4 according to Eq. (6.95). Mean anomaly drift calculated from Eq. (6.85). Time for the orbit to expand to the Hill radius (Δt_{Hill}) calculated based on the Hill radius at perihelion and the assumption that the expanding orbit remains circular. Comparison to KW4 simulation results in §6.1.4.2 gives an idea of the difference expected from this assumption.

Binary	a_s (AU)	e_s	D_{pri} (km)	a (km)	D_{sec} (km)	T_{orb} (d)	ν	\dot{a} (cm/yr)	ΔM_d (deg/yr ²)	Δt_{Hill} (10 ⁴ yr)
(66391) 1999 KW4	0.64	0.69	1.28	2.55	0.42	0.73	0.0347	6.934	-3.70	5.4
1999 HF1	0.82	0.46	3.50	6.00	0.80	0.58	0.0118	1.466	-0.41	67.5
(5381) Sekhmet	0.95	0.30	1.00	1.54	0.30	0.52	0.0263	2.687	-3.46	9.8
(66063) 1998 RO1	0.99	0.72	0.80	1.40	0.38	0.61	0.0968	3.086	-3.75	7.2
1996 FG3	1.05	0.35	1.50	2.80	0.46	0.67	0.0280	1.747	-0.93	27.2
(88710) 2001 SL9	1.06	0.27	0.80	1.50	0.22	0.68	0.0204	3.602	-3.53	7.1
1994 AW1	1.10	0.08	1.00	2.40	0.48	0.93	0.0996	1.917	-0.85	21.1
2003 YF1	1.11	0.29	1.00	3.20	0.18	1.53	0.0058	8.995	-1.84	5.8
(35107) 1991 VH	1.14	0.14	1.20	3.60	0.45	1.36	0.0501	2.975	-0.61	20.0
2000 DP107	1.37	0.38	0.80	2.90	0.33	1.75	0.0656	3.702	-0.72	12.7
(65803) Didymos	1.64	0.38	0.75	1.14	0.17	0.50	0.0115	1.442	-2.54	14.0
(69230) Hermes	1.66	0.62	0.60	1.20	0.54	0.58	0.4216	0.631	-0.91	32.8
(162000) 1990 OS	1.68	0.46	0.30	0.70	0.04	0.88	0.0034	8.187	-12.30	1.5
(5407) 1992 AX	1.84	0.28	3.90	6.50	0.80	0.56	0.0086	0.261	-0.07	445.4
(85938) 1999 DJ4	1.85	0.48	0.35	0.70	0.17	0.74	0.1028	1.913	-3.82	6.4
2006 GY2	1.86	0.50	0.40	0.60	0.08	0.49	0.0079	2.505	-8.53	4.3
2000 UG11	1.93	0.57	0.26	0.56	0.15	0.77	0.1611	2.040	-4.71	4.8
(7088) Ishtar	1.98	0.39	1.20	2.70	0.50	0.86	0.0675	0.575	-0.24	82.3
(31345) 1998 PG	2.02	0.39	0.90	1.50	0.34	0.58	0.0512	0.619	-0.74	43.3
2005 NB7	2.04	0.52	0.50	0.90	0.20	0.64	0.0602	1.145	-2.03	13.9
(3671) Dionysus	2.20	0.54	1.50	4.00	0.30	1.16	0.0079	1.171	-0.25	58.7
2007 DT103	2.21	0.57	0.30	0.55	0.10	0.64	0.0357	1.904	-5.31	5.1
2002 CE26	2.23	0.56	3.45	4.70	0.30	0.65	0.0007	1.522	-0.76	55.5
2005 AB	3.22	0.66	1.90	3.80	0.46	0.75	0.0140	0.256	-0.09	263.7

6.1.5 Discussion of Binary Asteroid Results

The Binary YORP effect may be a fundamental process for the evolution of small asteroids in the NEA and MBA populations. The relative speed at which this effect works suggests a rapid tempo for the rate at which small asteroids undergo rotational fission. The statistics for this are instructive to review, especially for NEA binaries which are relatively well observed. The nominal lifetime of an asteroid in the NEA population has been predicted to be 10 million years [36]. The fraction of asteroids which are binary in the NEA population has been predicted to be 16% [60], a prediction that has held up under the addition of new observations. Finally, we bring to these numbers the predicted lifetime of a binary due to the BYORP effect, which was predicted to be on the order of 0.1 Myr [20], a number which is consistent with the more detailed computations in this dissertation. This rapid time scale has significant implications for the formation rate of binary asteroids. To maintain a population of 16% over a 10Myr lifetime means that the average asteroid (if binarity is shared across all asteroids) is in a binary state for 1.6 Myrs. However, each time a binary forms, the current predictions from the BYORP effect indicates that it is disrupted in only 0.1 Myrs. Thus, to maintain this fraction a single asteroid must, on average, be reformed as a binary on the order of 16 times, or conversely, become a binary asteroid every 600Kyr. If asteroids which can form into binaries form a sub-set of the total NEA population, then this production rate must be even faster.

This is a striking prediction and if true would have major implications for the morphology of NEA, and would also imply that early planetesimals in the solar system could have been subject to similar processes. The key result arises from the predicted lifetime due to the BYORP effect, however there are several issues with this effect that must still be addressed, some of which could slow the BYORP evolution and change the implicit formation rate. First and foremost is that BYORP has not been verified, although the theoretical predictions seem well established. In this dissertation we lay out a relatively simple approach to detection of this effect, although precise verification of it will require **in situ** observations of a binary system. Even if BYORP is effective at the rates predicted for asynchronous binaries, there are other ways in which BYORP could be shut down or delayed. One such pathway would be loss of synchronization when the bodies are relatively distant from each other, which would cause the secondary to spin at a non-synchronous rate and

shut down the BYORP process. It is significant to note that there exist some binary asteroids, with a larger separation distance, which display a distinctly asynchronous secondary [78]. However, once a binary is at a larger separation distance it is also more susceptible to being disrupted by a relatively distant flyby of a planet [93, 118], which should enhance the disruption rate of binaries. Finally, the expansion rates caused by the BYORP effect could be very sensitive to changes in surface morphology (as has been proposed for the YORP effect [96, 103]), causing the evolution to change over time due to impact events.

Another possibility is that the binary system can alternately grow and shrink in size as the secondaries cycle in and out of synchronicity and vary the synchronous attitude of the secondary by 180 degrees [22]. The interesting implication of the work here, however, is that the eccentricity changes in the opposite direction of the semi-major axis. Given that the synchronous rotation of the secondary is more stable on a circular orbit, and the orbit will tend to stay circular when it is expanding and become elliptic when it is shrinking, it is possible that this would allow the system to keep BYORP in effect longer when the orbit is expanding than when it is contracting, leading to a net outward evolution of the secondary.

Beyond the formation and destruction rate of binary asteroids, the BYORP effect could also provide a physical mechanism for the creation or maintenance of contact binary asteroids. As discussed in [94, 95] shows, if a contact binary asteroid has a mass fraction greater than 0.2 between its components, when it fissions it cannot undergo a mutual escape and the components remain bound to each other. Under energy dissipation such systems may devolve to a doubly-synchronous state, such as has been observed for the asteroid Hermes [59]. As noted in this dissertation, a doubly-synchronous binary can experience an even greater BYORP effect which, in addition to making the system grow, could also cause the system to contract. The final dynamics of such a contraction have been speculated on [108], and could conceivably result in the maintenance of the system as a contact binary system, as proposed in [94].

Taken together, the implications of BYORP paint a picture of dynamic and rapidly evolving systems in the NEA environment, even including the possible factors which would degrade this effect. These predictions are all based on relatively simple and well understood physical effects, yet the macroscopic evolution of asteroids that are implied by these effects do not fit with traditional understanding of the NEA population, or other small body populations. This disparity between classical assumptions of how these systems evolve

over time and the implications of the BYORP effect are fundamentally interesting and must be further studied and understood in the future.

Specifically, the goals for the research by the authors are to develop theories for the evolution of binary systems, which will help to lend insight into the lifetime of these systems and how they may become disrupted. In order to pursue these goals, there are several areas of this theory which need to be advanced. One of the most important factors will be how librations in the attitude motion effect BYORP. Another important aspect of our theory that needs to be explored is how uncertainties in the Fourier coefficients (caused by inaccurate models etc.) will affect our predictions. Previous work [103] has shown that the coefficients for predicting YORP rates are very sensitive to moving small surface features to different locations on the body. The YORP coefficients can be generated from the BYORP coefficients for each surface facet, crossed with the location of that facet on the body. The dependence of the YORP coefficients on the body location of surface features leads directly to the strong dependence of the total coefficients on the location of different surface features. It is expected that because the BYORP coefficients do not depend as strongly on the body location, the sensitivities to these types of shape model errors will not be as severe, however this certainly needs to be investigated in detail. Finally, the use of this analytical model for the BYORP effect, combined with the other major perturbations present in binary systems (e.g. solar resonances), will enable an efficient combination of numerical and analytical models to investigate the evolution of binary systems.

6.2 Effects of Libration

The natural dynamics of an elongated secondary asteroid in synchronous orbit will generally lead to some amount of librational motion in the plane of the orbit. This type of libration is illustrated in Fig. 6.18. The case of a librating secondary asteroid is especially interesting for several reasons. First, it does not nicely fit into any of the attitude motion categories laid out in Chapter 4; as long as the libration is bounded, the average motion is still synchronous, however the total attitude motion is not strictly synchronous. Second, because the BYORP effect depends on the secondary being in synchronous rotation so that the same coefficients can cause long-term secular effects, if the libration becomes unbounded then the secondary can begin spinning, breaking the average synchronous rotation and stopping the BYORP

effect. In this section, it is shown how librational motion changes the BYORP evolution, but as long as the librational motion is small enough the orbit can still expand to the Hill radius.

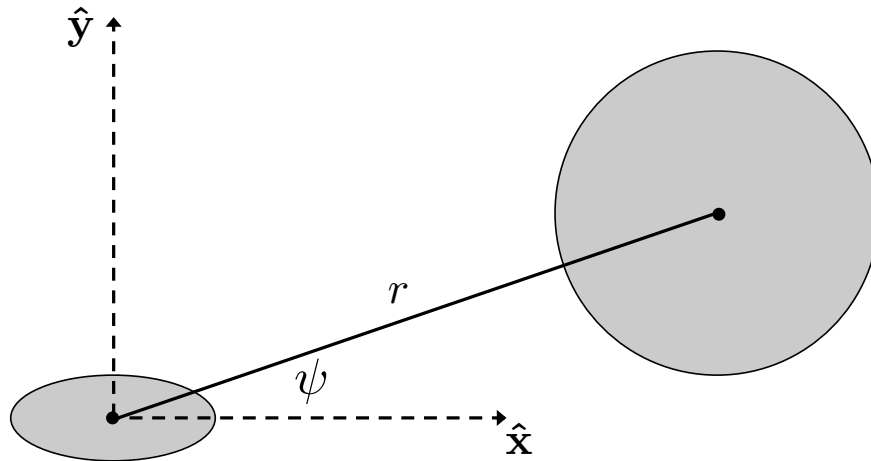


Figure 6.18: Illustration showing the libration angle of an elongated secondary asteroid in the plane of its orbit. The libration angle is defined as the angle between the long axis of the secondary and the orbital radius vector.

6.2.1 Librational Dynamics

Consider a pitch only libration (roll and yaw have no initial libration, and are not excited by the pitch motion) for a body in circular orbit, with the gravity gradient torque represented to first order in $\epsilon = l/R_c$. The equation of motion for pitch is then [41],

$$\ddot{\psi} + \frac{3}{2}n^2k_2 \sin(2\psi) = 0 \quad (6.97)$$

where ψ is the pitch libration angle, n is the mean motion of the circular orbit, and the inertia ratio,

$$k_2 = \frac{I_y - I_x}{I_z} \quad (6.98)$$

where the I 's are the principal axis moments of inertia. We assume that for this analysis to be valid, the secondary is in a stable orientation where $I_z > I_y > I_x$.

The energy integral for this system is given by,

$$\dot{\psi}^2 + 3n^2k_2 \sin^2(\psi) = a^2 = 3n^2k_2\hat{a}^2 \quad (6.99)$$

where the amplitude terms a or \hat{a} are calculated from the initial conditions. The basic relationship is $\hat{a} = \sin(\psi_{max})$, therefore the main thing to note is the when $\hat{a} < 1$, the motion is libration, which is what we will consider.

The closed form solution to this problem, which is a simple pendulum, is known to be,

$$\sin \psi = \hat{a} \operatorname{sn} \left[\frac{a\Delta t}{\hat{a}}; \hat{a} \right] = \hat{a} \operatorname{sn} \left[\sqrt{3k_2} n \Delta t; \hat{a} \right] \quad (6.100)$$

where Δt is the time since $\psi = 0$, and the term after the semi-colon is the parameter to be used with the Jacobian elliptic function sn .

Finally, the period can be shown to be,

$$T_{lib} = \frac{4\hat{a}K(\hat{a})}{a} = \frac{4K(\hat{a})}{n\sqrt{3k_2}} \quad (6.101)$$

where $K()$ is Legendre's complete elliptic integral of the first kind. The libration period is equal to the orbit period if $T = 2\pi/n$, in other words if

$$K(\hat{a}) = \frac{1}{2}\pi\sqrt{3k_2} \quad (6.102)$$

The solution to this condition is shown in Fig. 6.19. The immediate condition to notice is that the orbit period and libration period can not be equal if $k_2 < 1/3$. This is illustrated in Fig. 6.19.

This situation is rare in nature, as is illustrated for the possible k_2 values for 1999 KW4, as it only occurs for a particular libration amplitude as shown in Fig. 6.20.

6.2.2 Fourier Coefficients for a Librating Secondary

To handle libration about the spin axis, we begin with our body-fixed (no-prime) set of Fourier coefficients ,

$$\mathbf{F}_{SRP} = P(R) \sum_{n=0}^{\infty} [\mathbf{A}_n(\delta_s) \cos(n\lambda_s) + \mathbf{B}_n(\delta_s) \sin(n\lambda_s)] \quad (6.103)$$

Typically we change to the single-prime set by using $\lambda_s = \lambda_{s_0} - (\phi + \phi_0)$ so that,

$$\mathbf{F}_{SRP} = P(R) \sum_{n=0}^{\infty} [\mathbf{A}'_n \cos(n\phi) + \mathbf{B}'_n \sin(n\phi)] \quad (6.104)$$

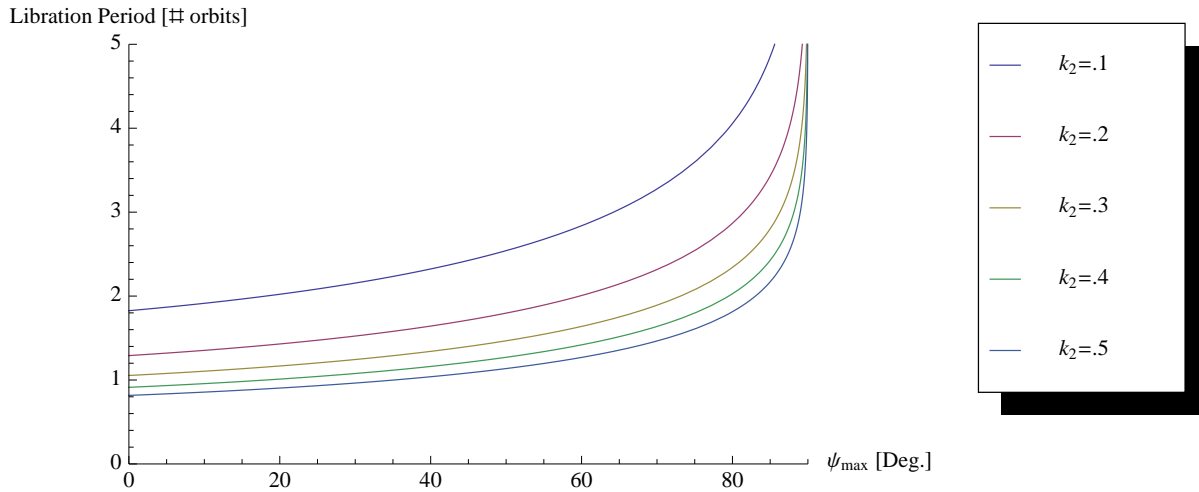


Figure 6.19: Necessary condition for the libration period to be the same as the orbit period. Note that the range of values for KW4 show that it is possible for there to be a periodic libration.

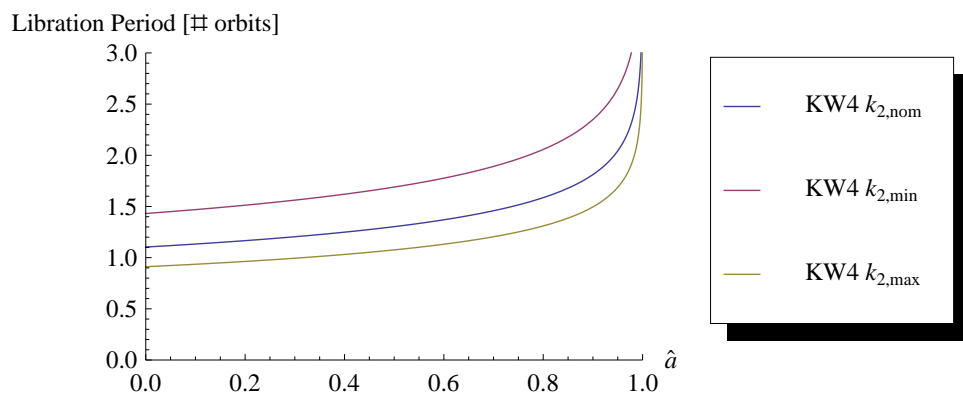


Figure 6.20: Libration periods for varying libration amplitude.

where the single-prime Fourier coefficients are given by,

$$\mathbf{A}'_n = \cos(n(\lambda_{s_0} - \phi_0))\mathbf{A}_n + \sin(n(\lambda_{s_0} - \phi_0))\mathbf{B}_n \quad (6.105)$$

$$\mathbf{B}'_n = \cos(n(\lambda_{s_0} - \phi_0))\mathbf{B}_n - \sin(n(\lambda_{s_0} - \phi_0))\mathbf{A}_n \quad (6.106)$$

In the case of libration, the relationship for the Sun's longitude is modified to be,

$$\lambda_s = \lambda_{s_0} - (\phi + \phi_0 + \psi) \quad (6.107)$$

where ψ is the libration angle, measured from the actual $\hat{\mathbf{x}}_b$ axis and the x-axis of the synchronously rotating frame, and it is positive in the same direction as ϕ .

Using Eq. (6.107), the expression for the SRP force will now be,

$$\mathbf{F}_{SRP} = P(R) \sum_{n=0}^{\infty} [\mathbf{A}'_n \cos(n(\phi + \psi)) + \mathbf{B}'_n \sin(n(\phi + \psi))] \quad (6.108)$$

Recall that the variational equations depend on the SRP acceleration in the orbit frame. This is achieved by rotating the acceleration from Eq. (6.108). Now, however, the rotation has also changed due to the libration angle, and it can be expressed as a dyad,

$$T = \cos(\phi + \psi)\hat{\mathbf{e}}\hat{\mathbf{x}}_b - \sin(\phi + \psi)\hat{\mathbf{e}}\hat{\mathbf{y}}_b + \sin(\phi + \psi)\hat{\mathbf{e}}_{\perp}\hat{\mathbf{x}}_b + \cos(\phi + \psi)\hat{\mathbf{e}}_{\perp}\hat{\mathbf{y}}_b + \hat{\mathbf{h}}\hat{\mathbf{z}}_b \quad (6.109)$$

Previously we determined the double-prime coefficient set by distributing the rotation directly into the acceleration. The same process is used here to get a double-prime set including the effect of libration.

Start by expressing,

$$T \cdot \mathbf{a}_{SRP} = T \cdot \frac{P(R)}{m} \sum_{n=0}^{\infty} [\mathbf{A}'_n \cos(n(\phi + \psi)) + \mathbf{B}'_n \sin(n(\phi + \psi))] \quad (6.110)$$

By distributing the rotation dyad through, we are left with,

$$\begin{aligned} T \cdot \mathbf{a}_{SRP} = & \frac{P(R)}{m} \sum_{n=0}^{\infty} \left\{ \left[\cos(\phi + \psi) \cos(n(\phi + \psi))A'_n(1) - \sin(\phi + \psi) \cos(n(\phi + \psi))A'_n(2) \right. \right. \\ & \left. \left. + \cos(\phi + \psi) \sin(n(\phi + \psi))B'_n(1) - \sin(\phi + \psi) \sin(n(\phi + \psi))B'_n(2) \right] \hat{\mathbf{e}} \right. \\ & \left. + \left[\sin(\phi + \psi) \cos(n(\phi + \psi))A'_n(1) + \cos(\phi + \psi) \cos(n(\phi + \psi))A'_n(2) \right. \right. \\ & \left. \left. + \sin(\phi + \psi) \sin(n(\phi + \psi))B'_n(1) + \cos(\phi + \psi) \sin(n(\phi + \psi))B'_n(2) \right] \hat{\mathbf{e}}_{\perp} \right. \\ & \left. + \left[\cos(n(\phi + \psi))A'_n(3) + \sin(n(\phi + \psi))B'_n(3) \right] \hat{\mathbf{h}} \right\} \end{aligned} \quad (6.111)$$

Using the trigonometric identities listed in Appendix A and separating the different orders, gives the following relationships for the new libration double-prime coefficients,

$$\mathbf{A}''_{lib,0} = \mathbf{A}''_0 \quad (6.112)$$

$$\mathbf{A}''_{lib,1} = \cos(\psi)\mathbf{A}''_1 + \sin(\psi)\mathbf{B}''_1 \quad (6.113)$$

$$\mathbf{B}''_{lib,1} = \cos(\psi)\mathbf{B}''_1 - \sin(\psi)\mathbf{A}''_1 \quad (6.114)$$

$$\mathbf{A}''_{lib,n} = \cos(n\psi)\mathbf{A}''_n + \sin(n\psi)\mathbf{B}''_n \quad (6.115)$$

$$\mathbf{B}''_{lib,n} = \cos(n\psi)\mathbf{B}''_n - \sin(n\psi)\mathbf{A}''_n \quad (6.116)$$

for $n = 2, 3, \dots, \infty$. The interesting things to note are that the zeroth-order coefficient is not changed at all, and the original double-prime coefficients for all higher orders have been multiplied by $\cos(n\psi)$, while a new term multiplied by $\sin(n\psi)$ also appears in each of the higher orders.

The resulting expression for the acceleration in terms of the new double-prime coefficients is,

$$\mathbf{a}_{SRP} = \frac{P(R)}{m} \sum_{n=0}^{\infty} [\mathbf{A}''_{lib,n} \cos(nM) + \mathbf{B}''_{lib,n} \sin(nM)] \quad (6.117)$$

which can be used directly in the variational equations as before.

6.2.3 Libration Averaging

As a first order approximation, let us average the librational motion separately from the orbital motion. In this case, we are assuming that the frequencies are independent, and therefore we can average in either order. It is easier to average the librational motion first, which corresponds to averaging over ψ in Eqs. (6.112) - (6.116).

In the case of a circular orbit, the averaging is straightforward. Given the solution of the libration from Eq. (6.100), we average over one libration period. It is known that the Jacobi elliptic function, sn , is

odd about it's half period, and therefore $\sin(\psi)$ will average to zero over the period of libration. This should also hold for all orders of $\sin(n\psi)$ because ψ is itself an odd valued argument about the half period. On the other hand, $\cos(n\psi)$ will in general not average to zero. The result is that all of the Fourier coefficients from Eqs. (6.112) - (6.116) of order $n \geq 1$ will be equal to the original double-prime coefficients, multiplied by a scaling determined by the average of $\cos(n\psi)$; this scaling will be denoted by C_n . The values for C_1 and C_2 for given libration amplitudes are shown in Fig. 6.21.

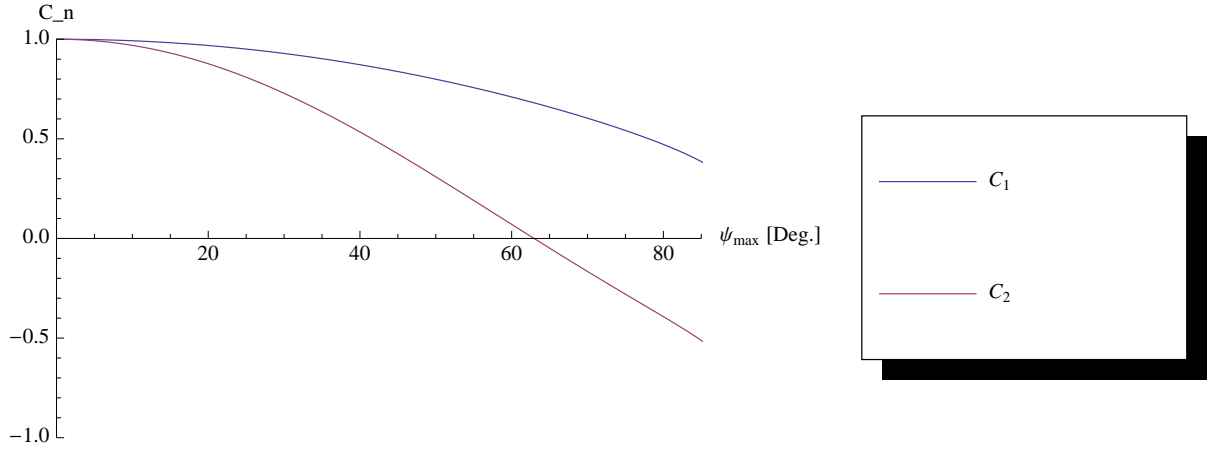


Figure 6.21: Averaged values of libration angle coefficients.

Inserting this into the circular orbit variational equations, and then averaging over the orbit and the libration results in,

$$\bar{\mathcal{E}}_{lib} = \frac{P(R)}{m} \frac{h}{2a} C_1 \left[-\hat{\mathbf{a}} \cdot \mathbf{B}_1'' + \hat{\mathbf{b}} \cdot \mathbf{A}_1'' \right] \quad (6.118)$$

$$\bar{\mathbf{h}}_{lib} = \frac{P(R)}{m} \frac{a}{2} C_1 \left[\tilde{\hat{\mathbf{a}}} \cdot \mathbf{A}_1'' + \tilde{\hat{\mathbf{b}}} \cdot \mathbf{B}_1'' \right] \quad (6.119)$$

$$\begin{aligned} \bar{\mathbf{e}}_{lib} = \frac{P(R)}{m} \frac{h}{2\mu} \left[-2\tilde{\hat{\mathbf{h}}} \cdot \mathbf{A}''_0 - \frac{1}{2} C_2 \hat{\mathbf{a}} \hat{\mathbf{a}} \cdot \mathbf{B}_2'' - \hat{\mathbf{b}} \hat{\mathbf{a}} \cdot \mathbf{A}_0'' \right. \\ \left. + \frac{1}{2} C_2 \hat{\mathbf{b}} \hat{\mathbf{a}} \cdot \mathbf{A}_2'' + \hat{\mathbf{a}} \hat{\mathbf{b}} \cdot \mathbf{A}_0'' + \frac{1}{2} C_2 \hat{\mathbf{a}} \hat{\mathbf{b}} \cdot \mathbf{A}_2'' + \frac{1}{2} C_2 \hat{\mathbf{b}} \hat{\mathbf{b}} \cdot \mathbf{B}_2'' \right] \end{aligned} \quad (6.120)$$

The long term evolution of the orbit will average the same way as discussed in §6.1.3.3, with the addition of the correction terms for the libration. Therefore the expansion equations for a circular orbit

become,

$$\bar{\bar{a}}_{\Omega_{s0}} = 2C_1 \frac{P_\Phi}{a_s^2 \sqrt{1-e_s^2}} \frac{ah}{m\mu} \bar{\mathbf{A}}_0(2) \quad (6.121)$$

$$\bar{\bar{h}}_{\Omega_{s0}} = C_1 \frac{P_\Phi}{a_s^2 \sqrt{1-e_s^2}} \frac{a}{m} \bar{\mathbf{A}}_0(2) \quad (6.122)$$

$$\bar{\bar{e}}_{\Omega_{s0}} = 0 \quad (6.123)$$

or for orbits with small eccentricity we have,

$$\bar{\bar{a}}_{\Omega_{s0}} \simeq C_1 \frac{P_\Phi}{a_s^2 \sqrt{1-e_s^2}} \frac{ah}{m\mu} \left[2 + \frac{7}{32} e^4 \right] \bar{\mathbf{A}}_0(2) \quad (6.124)$$

$$\bar{\bar{h}}_{\Omega_{s0}} \simeq C_1 \frac{P_\Phi}{a_s^2 \sqrt{1-e_s^2}} \frac{a}{2m} \left[2 - e^2 - \frac{e^4}{32} \right] \bar{\mathbf{A}}_0(2) \quad (6.125)$$

$$\bar{\bar{e}}_{\Omega_{s0}} \simeq C_1 \frac{P_\Phi}{a_s^2 \sqrt{1-e_s^2}} \frac{1}{2m} \frac{a}{h} \left[-e + \frac{13e^3}{8} \right] \bar{\mathbf{A}}_0(2) \quad (6.126)$$

The remaining question for this scenario is how will the libration evolve, and therefore how will C_1 change with the orbit evolution? This question is answered through the application of adiabatic invariance to the linearized libration dynamics given by,

$$\ddot{\psi} + 3n^2 k_2 \psi = 0 \quad (6.127)$$

where the frequency of libration is given by,

$$\omega = n\sqrt{3k_2} \quad (6.128)$$

In this case, the mean motion changes very slowly compared to the frequency of oscillation. Therefore, the ratio of the systems energy to the frequency is an adiabatic invariant as with a pendulum [2]. The system energy is given by,

$$H = \frac{1}{2}\dot{\psi}^2 + \frac{3}{2}n^2 k_2 \psi^2 \quad (6.129)$$

If the initial libration amplitude is designated by, ψ_0 , then the maximum potential energy is

$$h = \frac{3}{2}n^2 k_2 \psi_0^2 \quad (6.130)$$

Therefore the adiabatic invariant can be written as

$$I = \frac{H}{\omega} = \frac{h}{\omega} = \frac{1}{2}\sqrt{3k_2} n_0 \psi_0^2 = c \quad (6.131)$$

where c is a constant. Assuming that the mass properties of the body do not change, we can therefore write that,

$$n_0 \psi_0^2 = n \psi^2 \quad (6.132)$$

or by inserting the definition for n in terms of a ,

$$\psi = \left(\frac{a}{a_0} \right)^{3/4} \psi_0 \quad (6.133)$$

which defines the adiabatic evolution of the libration amplitude as the orbit size changes slowly. By using this evolution law, the value for C_1 can be determined as the semi-major axis changes, and the effect of libration on the orbit evolution can be simulated. This is illustrated for 1999 KW4 in Fig. 6.22 and Table 6.5.

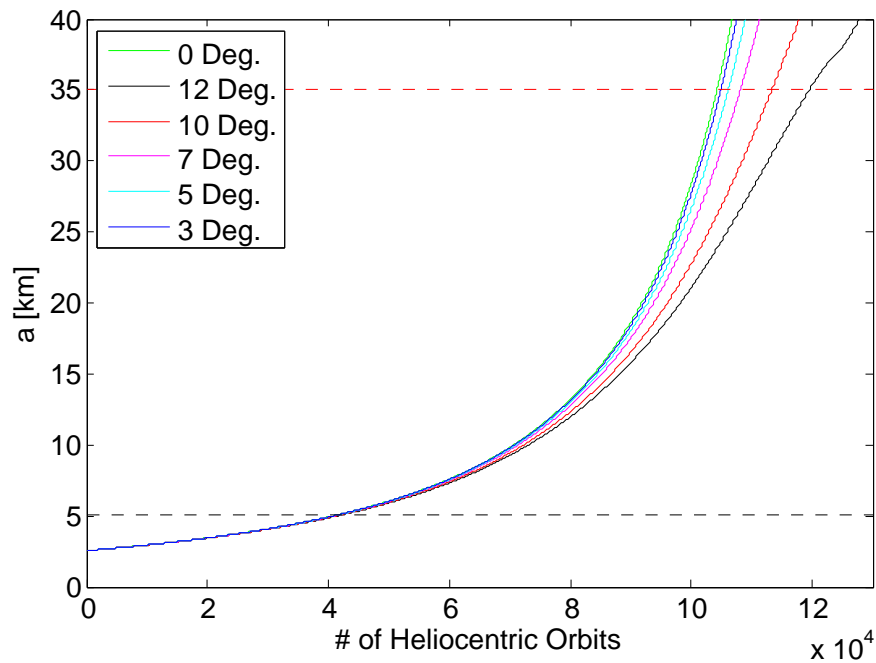


Figure 6.22: Orbit expansion for KW4 with different initial libration amplitudes. The libration amplitude is evolved adiabatically following Eq. (6.133).

Table 6.5: Time for the orbit of 1999 KW4 to expand to a given semi-major axis based on an initial libration amplitude that increases adiabatically as the orbit expands. The first row gives the nominal case with no libration at all, and the subsequent rows show how much longer the expansion takes given some initial libration amplitude.

ψ_0	Δt for $a \rightarrow 2a_0$	Δt for $a \rightarrow R_{Hill}$
0°	21528 yrs	53671 yrs
3°	+23 yrs	+327 yrs
5°	+70 yrs	+958 yrs
7°	+139 yrs	+2114 yrs
10°	+289 yrs	+4643 yrs
12°	+422 yrs	+7848 yrs

Chapter 7

Application to Artificial Bodies

There are a wide variety of solar radiation pressure (SRP) models used for spacecraft missions. The most widely used, due to its simplicity, is the cannonball model [53]. This model treats the spacecraft as a flat plat that is pointed directly at the Sun. While this can capture the basic effects of the SRP force, the model is insufficient for use in missions with more precise orbit accuracy requirements. For higher accuracy, spacecrafts are modeled to varying degrees of accuracy, from the macro models for TOPEX/Poseiden [61] or GRACE [17], to finite element models for GPS [124] or ICESat [80]. The former models use analytical expressions to derive the SRP force, while the latter use monte-carlo ray-tracing methods which simulate the path of each photon. Other models exist in the literature as well [33, 28], however all of these models suffer from the same weakness for orbit determination in that these models are used based on ground-measured data of the spacecraft. Once the spacecraft enters the space environment, however, many of the assumptions that go into these models will change in an unpredictable fashion, which will change the accelerations caused by the solar radiation pressure. Due to the manner in which these models are developed and used, it is nearly impossible to separate how errors in model parameters impact the spacecraft's orbit. The most common method to improve the model solution is to apply an estimated correction factor to all parts of the spacecraft equally, however this method cannot capture all possible model errors as it changes the accelerations in all directions proportionally.

A different type of model was developed independently by Springer et. al [102] and Bar-Sever [3] to model the SRP effect on the orbits of GPS satellites. These models were developed to be optimal models for the SRP effects on GPS satellites in terms of minimizing the residuals of the orbit fit. In other words,

this model was developed purely by looking at the orbital effects of SRP with no real attention being paid to the physics of the interaction that is causing these effects.

The approach presented in this dissertation combines these two methodologies. A precise, physics-based model of the SRP induced accelerations is combined with a perturbative theory of the accelerations on the orbit to create a system which combines a physical **a priori** model with a mathematical form that is conducive to studying the orbital effects and estimating the effect of SRP on the orbit.

The analysis presented here, which is based on the theory developed through Chapter 5, has several features. First, the model is derived in a way that analytically accounts for the main physical processes by which the SRP interaction induces a force on the spacecraft. This model also allows for a variation in how precise or rough of a shape model for the satellite will be used. Second, this model is written as a spatially periodic function, which highlights how the solar radiation pressure interacts with the spacecraft's periodic orbit and rotation. While we base our Fourier series on the analytical model for the SRP interaction mentioned above, the process for deriving and using the series representation is not tied to this model so if a better physical model appears, it can be adopted into the same structure presented here for analyzing the orbital effects. Third, this model allows for a unique method for analyzing the effects of the Earth's shadow, which is not easily available with other models. Another main advantage of the application of this model is that the parameters of the model can be estimated from flight data, allowing the model to be updated more accurately than current models. Finally, the model is derived specifically so that the secular and short period effects on the orbit can be separated, which is nearly impossible with many other models. This will allow for better predictions to be made for how SRP will affect a spacecraft's orbit over long times.

In §7.1 a detailed example for a satellite based on GRACE is shown, including the effect of the Earth's shadowing. In §7.2 the model is applied to the GPS spacecraft and compared to the highly accurate JPL and University of Bern SRP models. The Fourier coefficients are derived from the JPL model, and a comparison of the performance for orbit determination are shown in §7.3. The application of the Fourier series SRP theory to orbital debris is discussed in §7.4, and the application to solar sails is discussed in §7.5.

7.1 Satellite Application Example: GRACE

A basic model based on the GRACE satellite was constructed as an extruded trapezoidal shape with size and radiative property data from the literature[17, 7]. The body axes are aligned with the orbit at the start of the simulation as follows: $\hat{\mathbf{z}}_b$ is parallel with $\hat{\mathbf{h}}$, $\hat{\mathbf{x}}_b$ is parallel with $\hat{\mathbf{e}}$, and $\hat{\mathbf{y}}_b$ is parallel to $\hat{\mathbf{e}}_\perp$. As was stated earlier, the relationship with $\hat{\mathbf{z}}_b$ is fixed throughout the simulation, while the other two body axes rotate synchronously with the orbit. If $\hat{\mathbf{x}}_b$ and $\hat{\mathbf{y}}_b$ are not aligned correctly to start, the phase angle ϕ_0 is used to rotate the body to the correct orientation.

The radiative properties used are reproduced in Table 7.1. On the GRACE spacecraft, the top and sloped sides were solar panels, thus they share the same optical properties. The same is true for the front and back of the spacecraft.

Table 7.1: GRACE optical properties.

Side	s	ρ
Front and Back ($\pm\hat{\mathbf{y}}_b$)	0.4	0.26
Top and Sides ($+\hat{\mathbf{x}}_b, \pm\hat{\mathbf{z}}_b$)	0.05	0.3
Bottom ($-\hat{\mathbf{x}}_b$)	0.68	0.2

Following the methodology described by Scheeres [[92]] and the data from Table 7.1, the Fourier coefficients for this model were derived. The coefficients are plotted in Figs. 7.2 - 7.4. However, due to the symmetry of this shape, $\mathbf{A}_n(2)$, $\mathbf{B}_n(1)$, and $\mathbf{B}_n(3)$ are zero for all n , and therefore are not plotted. The zenith angle is defined as the angle between $\hat{\mathbf{z}}_b$ and the spacecraft-Sun unit vector. In each of these plots, all orders up to $n = 25$ are plotted, however in most cases the magnitude falls off as n increases.

Several interesting relationships appear that are worth pointing out. First we note that $\mathbf{A}_0(2) = 0$. This means, by Eq. (5.43), that there is no secular growth in energy for a circular orbit with any zenith angle. Also, notice that in Figs. 7.2 - 7.4 there is a kink in the coefficients near zenith angles of 50 degrees and 130 degrees. Between these zenith angles, both of the sloped sides of GRACE can see the Sun, while outside those angles only one side is illuminated. Finally, it is interesting to notice that all orders of the $\mathbf{A}_n(3)$ coefficients go to zero at a zenith angles or 90 degrees. This will cause the secular rate for all components of the angular momentum vector to go to zero via Eq. (5.44) when the orbit is oriented in that manner.

Figs. 7.2 - 7.4 show what can be considered the ideal values of the coefficients based on the available data before launch. However, the coefficients will almost certainly take on non-ideal values due to space weathering once the vehicle is on orbit. In particular, one can imagine the properties of the leading side ($+\hat{\mathbf{y}}_b$) to change differently than the trailing side. This would immediately impact the $\mathbf{A}_0(2)$ coefficient, which would then give rise to a secular change in energy. This idea illustrates how the Fourier coefficients are observable to be estimated once the craft is launched.

These coefficients were used to model the perturbative effects on the orbit caused by the solar radiation. This simulation was run for 10 orbits, and compares the numerical results with the secular results from the orbit averaging. This orbit is based on the nominal GRACE orbit, and has an altitude of 500 km and an inclination of 90 degrees. This simulation assumes that the Sun is at a zenith angle of 60 degrees.

The results of this simulation are shown in Figs. 7.5 - 7.7. These plots compare a numerical integration of the equations of motion using a point mass gravity model for Earth plus the full Fourier series up to $n = 25$ with the orbit averaged theory described by Eqs. (5.43) - (5.45). The secular theory includes the offsets from §5.2.2, which is why the two simulations have a difference at the initial time. The secular theory does follow the average of the numerical integration closely. Also note that the predicted bounds of the short period variations almost perfectly match those seen in the numerical simulation. The slight differences are due to the non-zero eccentricity that appears due to the secular variation, as well as higher order drift that is not taken into account in our averaging methodology.

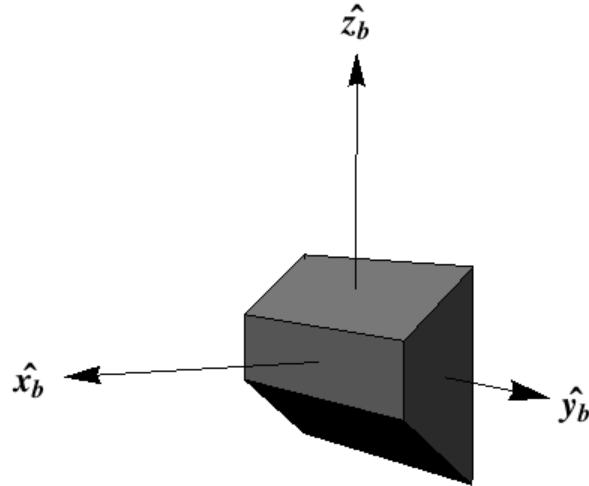


Figure 7.1: Illustration of the GRACE model, with the body axes shown.

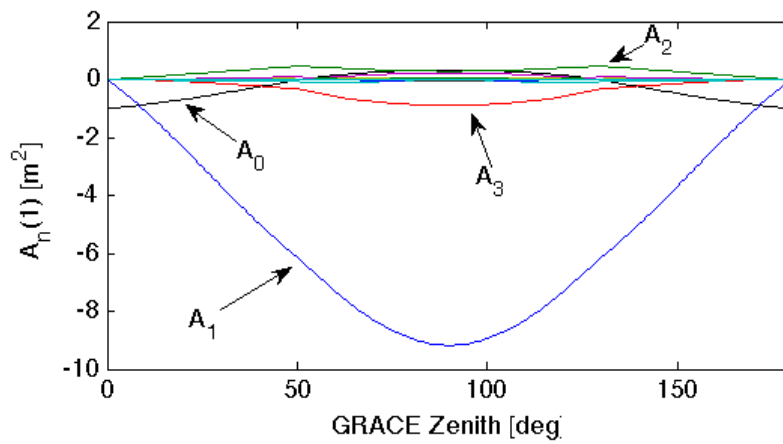


Figure 7.2: $A_n(1)$ coefficient components. The most prominent orders are labeled.

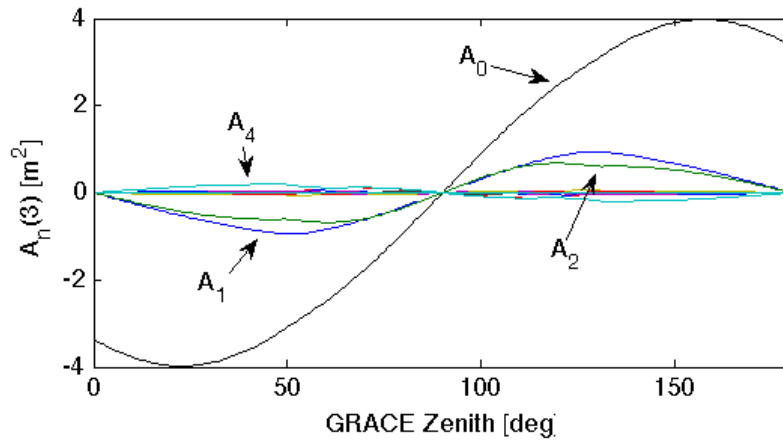


Figure 7.3: $A_n(3)$ coefficient components. The most prominent orders are labeled.

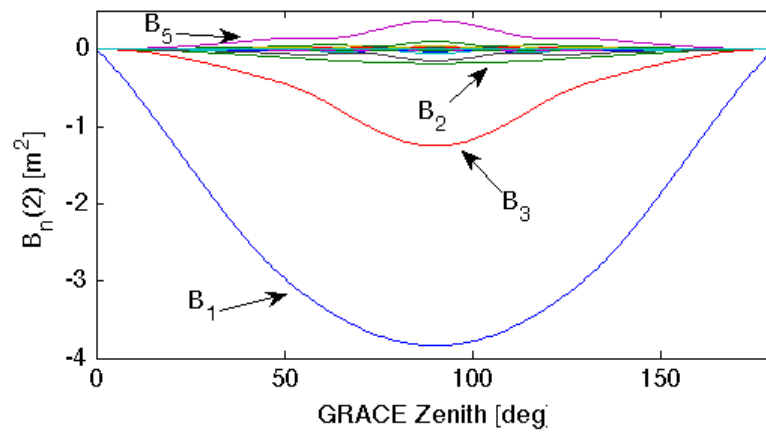


Figure 7.4: $B_n(2)$ coefficient components. The most prominent orders are labeled.

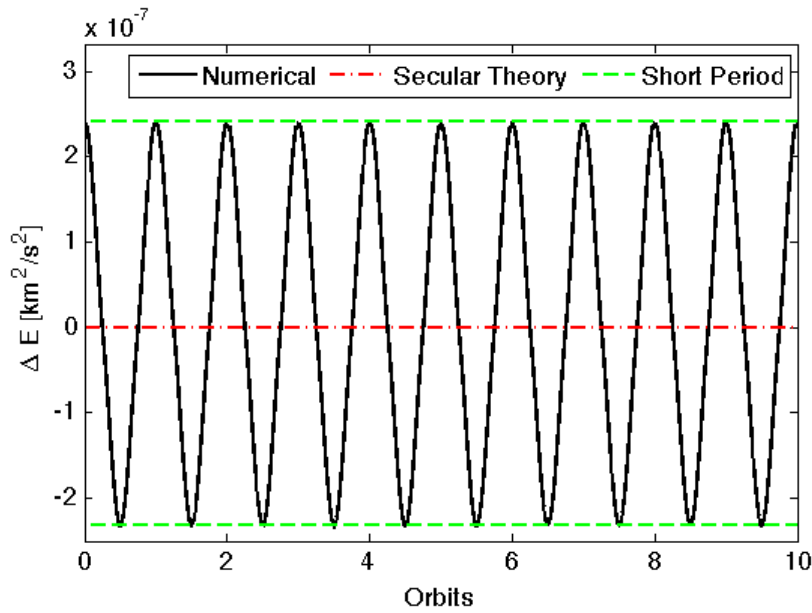


Figure 7.5: Change in the orbital energy from its initial mean value over 10 orbits for the numerical integration and the orbit averaged theory. The initial mean value is approximately $-28.98 \text{ km}^2/\text{s}^2$. The dashed lines represent the bounds of the short period variations.

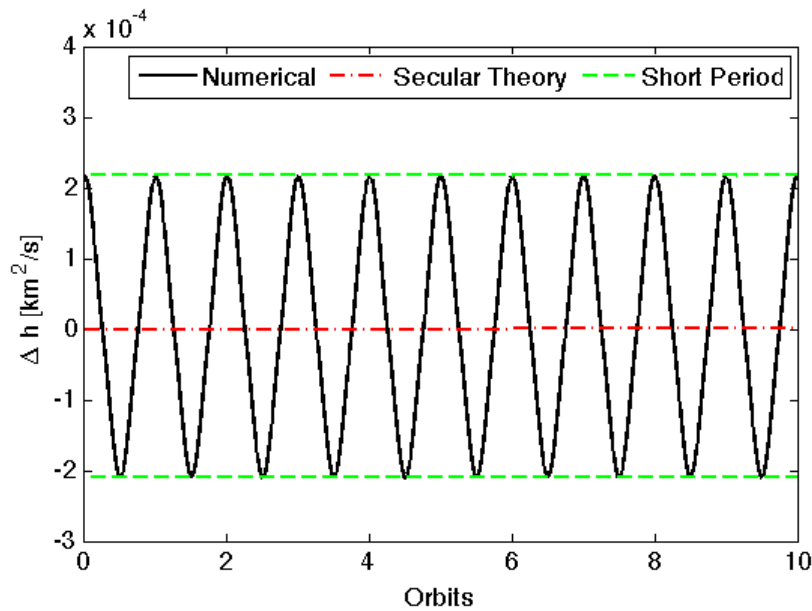


Figure 7.6: Change in the orbital angular momentum magnitude from its initial mean value over 10 orbits for the numerical integration and the orbit averaged theory. The initial mean value is approximately $52,360 \text{ km}^2/\text{s}$. The dashed lines represent the bounds of the short period variations.

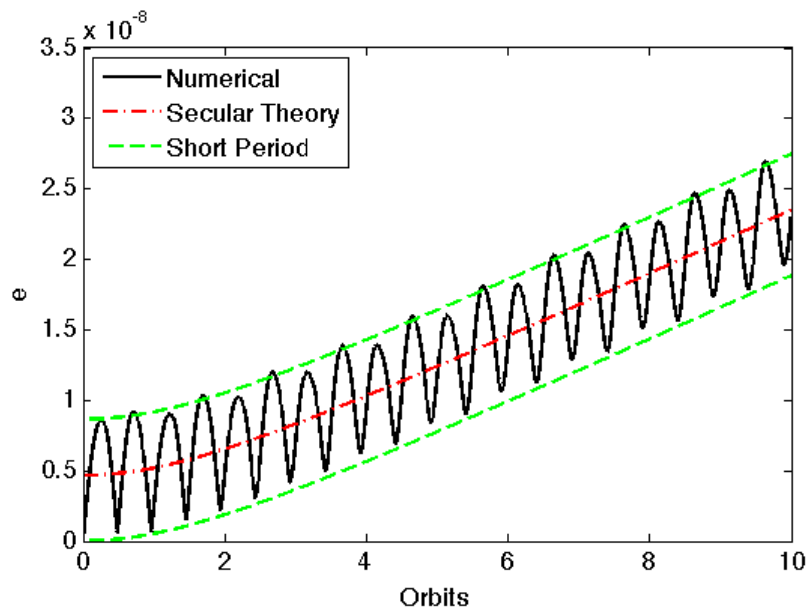


Figure 7.7: Orbital eccentricity over 10 orbits for the numerical integration and the orbit averaged theory. The dashed lines represent the bounds of the short period variations.

7.1.1 Shadowing

The theory thus far has not accounted for the effect of the shadow from the primary body. When in the shadow, the Sun is obscured from the view of the spacecraft (so that $P(R) = 0$), which results in the SRP force becoming zero while the spacecraft is in the shadow. When the orbit is orientated so that the spacecraft is passing through the shadow of the Earth, the Fourier coefficients used to describe the force will be different than those in Eq. (2.35).

To analyze the effects of the shadow on the orbit evolution, we create a “shadow force” to apply to the spacecraft when the orbit passes through the shadow. This shadow force is equal and opposite of the solar radiation force during the shadowing period, and zero elsewhere. By adding the original SRP model together with the shadow force model, the total effect will be to have the normal SRP acting on the satellite outside of the shadow, while having zero acceleration inside the shadow. Using this methodology has two benefits. First, the original set of Fourier coefficients, which are functions of the spacecraft’s physical properties and attitude motion, are not modified. Second, the shadow force can be described by its own set of Fourier coefficients which can then be used to determine how the presence of the eclipse changes to orbital effects of SRP.

7.1.2 Shadow Approach

The shadow force is defined as

$$\mathbf{F}_{sh} = \begin{cases} 0 & 0 \leq M < M_1 \\ -\mathbf{F}_{SRP} & M_1 \leq M \leq M_2 \\ 0 & M_2 < M \leq 2\pi \end{cases} \quad (7.1)$$

where M_1 is the mean anomaly at which the spacecraft enters the umbra, and M_2 is the mean anomaly where the spacecraft emerges from the umbra. The total force acting on the spacecraft due to SRP is now given by

$$\mathbf{F}_{tot} = \mathbf{F}_{SRP} + \mathbf{F}_{sh} = \begin{cases} \mathbf{F}_{SRP} & 0 \leq M < M_1 \\ 0 & M_1 \leq M \leq M_2 \\ \mathbf{F}_{SRP} & M_2 < M \leq 2\pi \end{cases} \quad (7.2)$$

This is illustrated in Fig. 7.8.

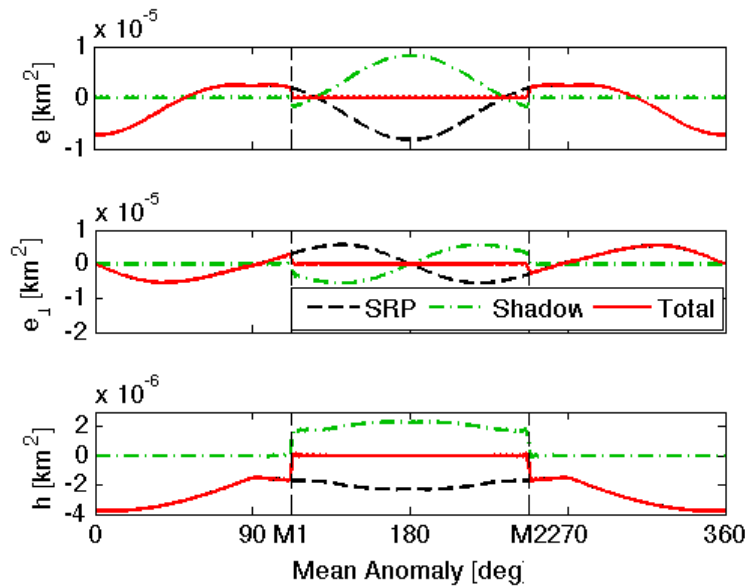


Figure 7.8: Example of the effect of the Earth's shadow on GRACE in orbit frame coordinates. The shadow acceleration cancels out the original SRP acceleration for $M_1 \leq M \leq M_2$ so that the total acceleration is zero over this range. The mean anomaly is measured from the sub-solar point on the orbit.

The shadow force can be expressed as a new Fourier series in the mean anomaly as

$$\mathbf{F}_{sh} = P(R) \sum_{n=0}^{\infty} [\mathbf{S}_n \cos(nM) + \mathbf{R}_n \sin(nM)] \quad (7.3)$$

where the coefficients can be derived as

$$S_0 = \frac{1}{2\pi} \int_{M_1}^{M_2} \frac{-\mathbf{F}_{SRP}}{P(R)} dM \quad (7.4)$$

$$S_n = \frac{1}{\pi} \int_{M_1}^{M_2} \frac{-\mathbf{F}_{SRP}}{P(R)} \cos(nM) dM \quad (7.5)$$

$$R_n = \frac{1}{\pi} \int_{M_1}^{M_2} \frac{-\mathbf{F}_{SRP}}{P(R)} \sin(nM) dM \quad (7.6)$$

for $n = 1, 2, \dots, \infty$. The integration bounds can be changed from 0 and 2π due to the fact that the shadow acceleration is zero outside of the umbra.

7.1.3 Orbital Effect of the Shadow

One of the main benefits of creating the shadow force is that we are able to decompose it into a Fourier series, and then insert those coefficients directly into the equations for the orbital effects. The averaging

theory we have applied to find the secular effects is a linear process; therefore we are able to find the total average effects by adding the commensurate Fourier coefficients from the original SRP force and the shadow force in the secular results given in Eqs. (5.43) - (5.45). The total secular effects are

$$\bar{\mathcal{E}} = \frac{P(R)}{m} \frac{h}{a} \hat{\mathbf{q}} \cdot (\mathbf{S}_0 + \mathbf{A}'_0) \quad (7.7)$$

$$\bar{\mathbf{h}} = \frac{P(R)}{m} \frac{a}{2} \left[\hat{\mathbf{a}}\hat{\mathbf{h}} \cdot (\mathbf{R}_1 + \mathbf{B}'_1) - \hat{\mathbf{b}}\hat{\mathbf{h}} \cdot (\mathbf{S}_1 + \mathbf{A}'_1) + 2\hat{\mathbf{h}}\hat{\mathbf{q}} \cdot (\mathbf{S}_0 + \mathbf{A}'_0) \right] \quad (7.8)$$

$$\bar{\mathbf{e}} = \frac{P(R)}{m} \frac{h}{2\mu} \left[\hat{\mathbf{a}}\hat{\mathbf{p}} \cdot (\mathbf{R}_1 + \mathbf{B}'_1) + 2\hat{\mathbf{a}}\hat{\mathbf{q}} \cdot (\mathbf{S}_1 + \mathbf{A}'_1) - \hat{\mathbf{b}}\hat{\mathbf{p}} \cdot (\mathbf{S}_1 + \mathbf{A}'_1) + 2\hat{\mathbf{b}}\hat{\mathbf{q}} \cdot (\mathbf{R}_1 + \mathbf{B}'_1) \right] \quad (7.9)$$

While these expressions have the same form as the original expressions, they are not as simple. In the non-shadow case, only seven coefficients are required to describe the secular effects. The shadow coefficients are technically functions of all of the original Fourier coefficients, however, and therefore the secular results now effectively depend on all of the Fourier coefficients.

The shadow coefficients can also be used to describe the short term dynamics. For example, using Eq. (5.72), the short term dynamics for the energy evolution are now described as

$$\begin{aligned} \bar{\mathcal{E}}_p = & \frac{P(R)}{m} \frac{h}{a} \sqrt{\frac{a^3}{\mu}} \hat{\mathbf{q}} \cdot \frac{1}{2\pi} \int_0^{2\pi} \left\{ (\mathbf{S}_0 + \mathbf{A}'_0) \cdot (M - M_0) + \sum_{n=1}^{\infty} \frac{1}{n} \left[(\mathbf{S}_n + \mathbf{A}'_n) \sin(nM) \right. \right. \\ & \left. \left. - (\mathbf{R}_n + \mathbf{B}'_n) \cos(nM) - (\mathbf{S}_n + \mathbf{A}'_n) \sin(nM_0) + (\mathbf{R}_n + \mathbf{B}'_n) \cos(nM_0) \right] \right\} dM \\ & - \pi \sqrt{\frac{a^3}{\mu}} \bar{\mathcal{E}}(\mathbf{x}_0) \end{aligned} \quad (7.10)$$

where $\bar{\mathcal{E}}(\mathbf{x}_0)$ is determined from Equation 7.7.

The shadow of the planet will change the secular rates and the short period dynamics of the satellite. The total effect the shadow is dependent on many factors, most notably the shape and optical properties of the satellite, what part of the orbit the satellite is obscured for, and for how long.

7.1.4 Penumbra Models

The theory so far has not included a penumbra, however this can be added easily in the same manner. There are two models of interest for the penumbra. The first is the most simple model which decreases the solar radiation force in proportion of the amount of the solar disk that is occluded by the solid Earth. The

second, more accurate model, which was developed by Vokrouhlicky et al [[113]], models the effect of the Earth's atmosphere in decreasing the solar radiation pressure, as well as the classical penumbra caused by the solid Earth.

No matter which form for the penumbra model is used, the shadow acceleration will be changed slightly to be derived as follows. The piecewise function will now be

$$\mathbf{F}_{sh} = \begin{cases} 0 & 0 \leq M < M_{p1} \\ -C_{pen}(M)\mathbf{F}_{SRP} & M_{p1} \leq M \leq M_1 \\ -\mathbf{F}_{SRP} & M_1 \leq M \leq M_2 \\ -C_{pen}(M)\mathbf{F}_{SRP} & M_2 \leq M \leq M_{p2} \\ 0 & M_{p2} < M \leq 2\pi \end{cases} \quad (7.11)$$

where M_{p1} is the mean anomaly at which the penumbra begins, M_{p2} is the mean anomaly where the penumbra ends, and $C_{pen}(M)$ is the scale factor for the penumbra model which depends on the mean anomaly. In this case, the shadow acceleration coefficients are determined by adding the integral of each of the three parts of the above piecewise function.

In the preliminary testing, the penumbra impact is insignificant on the secular rates assuming that the penumbra ($\Delta M \sim 0.5^\circ$) is small compared to the umbra ($\Delta M \sim 40^\circ$), and that it is symmetric about the umbra. However, if the penumbra is non-symmetric, meaning that the penumbra on one side of the umbra is bigger than the other side for the same orbit, there can be arbitrarily large changes in the secular rates, including sign changes. However, whether this is physically possible or not is beyond the scope of this dissertation. Future investigations applying the shadowing theory to the GRACE example will help to quantify the realistic effects.

7.2 GPS SRP Model

There are a wide variety of solar radiation pressure (SRP) models used for the GPS satellites. The most complicated numerical methods use ray-tracing methods [124] to attempt to predict the details of the physical interactions which cause the SRP accelerations. Simpler models, such as those by Fliegel and Gallini [30], use geometric primitives to try and capture the main effects at a much smaller computational cost. In this section, we define the Fourier coefficients for the GPS IIR-M satellites so that the orbit determination can be carried out with the rotating frame model. Application of the rotating frame model to the GPS spacecraft is of interest due to the fact that their attitude varies with respect to the rotating frame, unlike the GRACE spacecraft which was previously analyzed[66]. The GPS satellites are constantly yawing in a manner which is periodic with the orbit, as illustrated in Fig. 7.9, and the solar panels are also rotating to track the Sun. This makes a much more complicated representation in the rotating frame. In Section 7.2 7.2.1, we review the body-fixed SRP model for the GPS IIR-M satellites from JPL derived in Ref. [4]. Likewise, the form of the Bern model[102] is shown in Section 7.27.2.2. Section 7.2 7.2.3 discusses the conversion of the JPL model into the rotating frame model, and the necessary Fourier coefficients needed to use our theory are defined.

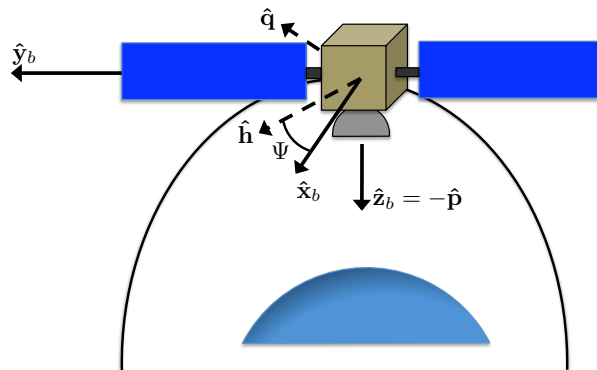


Figure 7.9: The nominal GPS II/IIA frame is illustrated, along with the rotating frame from Chapter 2. The yaw angle, that between \hat{h} and \hat{x}_b , is shown here to have a negative value. Note that the GPS IIR frame has the \hat{x}_b and \hat{y}_b body axes in the negative directions of those illustrated here, however the yaw angle can still be defined between the vectors shown.

7.2.1 JPL Model

The body-fixed SRP model for the GPS satellites is defined in Ref. [4] (with more details on the derivation in Ref. [3]) to be,

$$\mathbf{a}_{SRP} \cdot \hat{\mathbf{x}}_b = \left(\frac{AU}{R}\right)^2 \frac{s}{m} \left[S_{X1} \sin \varepsilon + S_{X2} \sin 2\varepsilon + S_{X3} \sin 3\varepsilon + S_{X5} \sin 5\varepsilon + S_{X7} \sin 7\varepsilon \right] \quad (7.12)$$

$$\mathbf{a}_{SRP} \cdot \hat{\mathbf{y}}_b = C_{Y0} + \left(\frac{AU^2}{R^2 m}\right) \left[C_{Y1} \cos \varepsilon + C_{Y2} \cos 2\varepsilon \right] \quad (7.13)$$

$$\mathbf{a}_{SRP} \cdot \hat{\mathbf{z}}_b = \left(\frac{AU}{R}\right)^2 \frac{s}{m} \left[C_{Z1} \cos \varepsilon + C_{Z3} \cos 3\varepsilon + C_{Z5} \cos 5\varepsilon \right] \quad (7.14)$$

where $AU = 1.4959787066 \times 10^8$ km, R is the distance between the spacecraft and the Sun, m is the mass of the spacecraft, and ε is the Sun-spacecraft-Earth angle. The body frame is illustrated in Fig. 7.9. The coefficients for GPS IIR-M spacecraft have the values shown in Table 7.2. The angle β is defined as the angle between the radius vector of the closest point to the Sun in the orbit plane, and the Sun unit vector ($\hat{\mathbf{u}}$). In this model, two parameters are estimated, s , which is a scale factor applied to the $\hat{\mathbf{x}}_b$ and $\hat{\mathbf{z}}_b$ directions, and the coefficient C_{Y0} , which represents the Y-bias acceleration.

Table 7.2: Parameter values for JPL SRP model for GPS IIR-M spacecraft, from Ref. [4].

Name	Value [10^{-5} N]
S_{X1}	10.9310
S_{X2}	$0.0172 + 0.0022 \sin \beta - 0.0016 / \sin \beta + 0.1477 \cos \beta$
S_{X3}	0.2476
S_{X5}	-0.2283
S_{X7}	-0.0140
C_{Y1}	$-0.0195 - 0.0172 \sin \beta - 0.0119 / \sin \beta + 0.0272 \cos \beta$
C_{Y2}	-0.0064
C_{Z1}	-11.6411
C_{Z3}	0.0583
C_{Z5}	0.0571

It is interesting to note that in this model, only two parameters are a function of the β angle, S_{X2}

and C_{Y1} . The values are fixed to the value at $|\beta| = \pm 14.5^\circ$ when the actual value of $|\beta| < 14.5^\circ$ (keeping the same sign as β). Also note that the Y-bias value, C_{Y0} , is nominally equal to zero.

7.2.2 University of Bern

The Bern model [102] is used to estimate the solar radiation pressure acting on GPS satellites for the Center for Orbit Determination in Europe (CODE). The SRP induced acceleration is assumed to have the form

$$\begin{aligned} \mathbf{a}_{SRP} = & D(\beta)\hat{\mathbf{u}} + Y(\beta)\hat{\mathbf{y}}_b + B(\beta)\hat{\mathbf{e}}_B \\ & + Z_1(\beta)\sin(u - u_0)\hat{\mathbf{z}}_b \\ & + [X_1(\beta)\sin(u - u_0) + X_3(\beta)\sin(3u - u_0)]\hat{\mathbf{x}}_b \end{aligned} \quad (7.15)$$

where $\hat{\mathbf{e}}_B = \hat{\mathbf{u}} \times \hat{\mathbf{y}}_b$, u is the satellite's argument of latitude, and u_0 is the argument of latitude of the Sun position projected onto the orbital plane. The coefficients (D , Y , B , X_1 , X_3 , and Z_1) are defined as,

$$D(\beta) = D_0 + D_{C2}\cos(2\beta) + D_{C4}\cos(4\beta) \quad (7.16)$$

$$Y(\beta) = Y_0 + Y_{C2}\cos(2\beta) \quad (7.17)$$

$$B(\beta) = B_0 + B_{C2}\cos(2\beta) \quad (7.18)$$

$$\begin{aligned} Z_1(\beta) = & Z_{10} + Z_{C2}\cos(2\beta) + Z_{S2}\sin(2\beta) \\ & + Z_{C4}\cos(4\beta) + Z_{S4}\sin(4\beta) \end{aligned} \quad (7.19)$$

$$X_1(\beta) = X_{10} + X_{1C}\cos(2\beta) + X_{1S}\sin(2\beta) \quad (7.20)$$

$$X_3(\beta) = X_{30} + X_{3C}\cos(2\beta) + X_{3S}\sin(2\beta) \quad (7.21)$$

In general, CODE estimates only D and Y from Eq. (7.15).

Reference [102] includes values for GPS II and IIA spacecraft, however that paper was published before most of the IIR or IIR-M spacecraft were in operation, and so these values are not available for comparison at this time.

7.2.3 Rotating Frame Coefficients

In order to determine the rotating frame Fourier coefficients, we must express the SRP acceleration in the rotating frame first. To do this, we note that $\hat{\mathbf{z}}_b$ is aligned with $-\hat{\mathbf{p}}$. The body is then rotated about this axis by the yaw angle, Ψ , which is nominally defined as,

$$\tan \Psi = \frac{-\tan \beta}{\sin M} \quad (7.22)$$

as illustrated in Fig. 7.9. The rotation from the body-frame to the rotating frame is then defined by the rotation matrix,

$$[B2R] = \begin{bmatrix} 0 & 0 & -1 \\ -\cos(\Psi) & \sin(\Psi) & 0 \\ \sin(\Psi) & -\cos(\Psi) & 0 \end{bmatrix} \quad (7.23)$$

The Bern model also uses two other unit vectors, $\hat{\mathbf{u}}$ and $\hat{\mathbf{e}}_B$. The Sun direction can be defined in the rotating frame as,

$$\hat{\mathbf{u}} = -\cos(\beta) \cos(M) \hat{\mathbf{p}} + \cos(\beta) \sin(M) \hat{\mathbf{q}} + \sin(\beta) \hat{\mathbf{h}} \quad (7.24)$$

assuming that the mean anomaly is measured from the orbit's midnight direction. Finally, we use $\hat{\mathbf{e}}_B = \hat{\mathbf{u}} \times \hat{\mathbf{y}}_b$.

To fully express the SRP acceleration in the rotating frame, we must also determine representations for the solar latitude and the mean anomaly in terms of β and ε . These are given as the following relationships

$$\delta_s = \beta \quad (7.25)$$

$$\cos \varepsilon = \cos M \cos \beta \quad (7.26)$$

Note that elsewhere in the literature [46], Eq. (7.26) includes a negative on the right hand side. In our case, this is not included in order to properly map to our rotating frame which has its origin at the spacecraft midnight, not spacecraft noon as in the GIPSY software.

The spacecraft's argument of latitude can be defined as,

$$u = u_0 + 180 \quad (7.27)$$

so that,

$$\sin(u - u_0) = -\sin(M) \quad (7.28)$$

and

$$3u = 3u_0 + 540M \quad (7.29)$$

so that,

$$\sin(3u - u_0) = -\sin(2u_0 + 3M) \quad (7.30)$$

Table 7.3: Relationship between JPL coefficients and single-prime coefficients when attitude motion is nominal.

JPL	Related Single-prime Coefficients
S_X_1	$A'_0(3), B'_1(2)$
S_X_2	$A'_1(3), B'_2(2)$
S_X_3	$A'_0(3), A'_2(3), B'_1(2), B'_3(2)$
S_X_5	$A'_0(3), A'_2(3), A'_4(3), B'_1(2), B'_3(2), B'_5(2)$
S_X_7	$A'_0(3), A'_2(3), A'_4(3), A'_6(3), B'_1(2), B'_3(2), B'_5(2)$
C_Y_0	$A'_0(2), A'_2(2), A'_4(2), A'_6(2), B'_1(3), B'_3(3), B'_5(3)$
C_Y_1	$A'_1(2), A'_3(2), A'_5(2), B'_2(3), B'_4(3), B'_6(3)$
C_Y_2	$A'_0(2), A'_2(2), A'_4(2), A'_6(2), B'_1(3), B'_3(3), B'_5(3)$
C_Z_1	$A'_1(1)$
C_Z_3	$A'_1(1), A'_3(1)$
C_Z_5	$A'_1(1), A'_3(1), A'_5(1)$

Using the nominal values given in Table 7.2, and Eqs. (7.22) - (7.26), we can compute the values of the Fourier coefficients in the rotating frame. The summary of which of our Fourier coefficients are influenced by the JPL coefficients is given in Table 7.3. The full values of the rotating frame coefficients as a function of β are presented in Figs. 7.10 - 7.12. Note that the areas between $-14.5^\circ \leq \beta \leq 14.5^\circ$ is shaded out to represent those orbits that are in shadow. In the case of a spacecraft in an orbit that is experiencing eclipse, we use a linear interpolation between the coefficient values at $\pm 14.5^\circ$, and have no SRP force acting on the spacecraft when it is the Earth's shadow.

The JPL Y-bias coefficient, C_Y_0 , is nominally set to zero when we computed these coefficient values. It is interesting to explore where this coefficient appears in the rotating frame. Fig. 7.13 illustrate the values of the rotating frame coefficients as a function of β when only the coefficient $C_Y_0 = 10^{-9}$ N is used to compute them. Clearly, the Y-bias shows up mainly in the $A'_0(2)$ and $B'_1(3)$ coefficients.

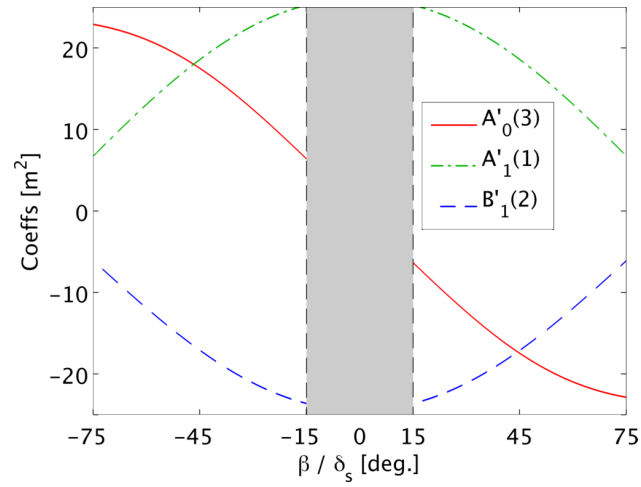


Figure 7.10: Rotating frame coefficients for GPS IIR-M plotted as a function of β (or δ_s) as computed using the JPL body-fixed SRP model and the nominal attitude motion. (Part I)

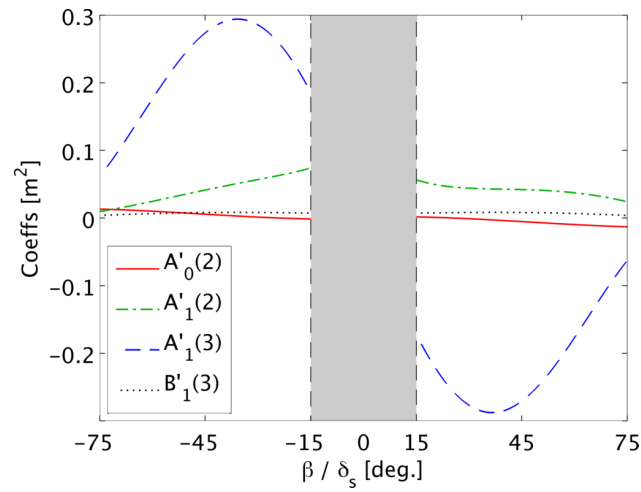


Figure 7.11: Rotating frame coefficients for GPS IIR-M plotted as a function of β (or δ_s) as computed using the JPL body-fixed SRP model and the nominal attitude motion. (Part II)

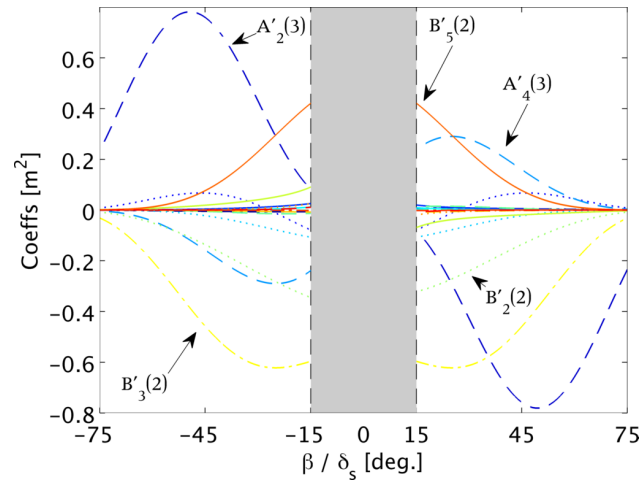


Figure 7.12: Rotating frame coefficients for GPS IIR-M plotted as a function of β (or δ_s) as computed using the JPL body-fixed SRP model and the nominal attitude motion. (Part III)

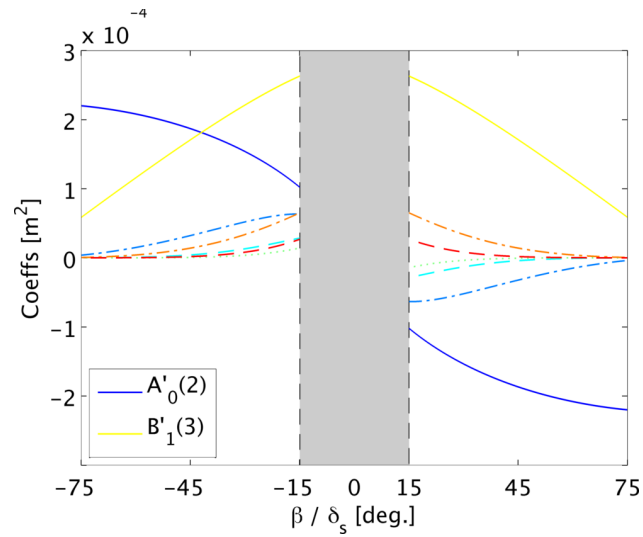


Figure 7.13: Rotating frame coefficients for GPS IIR-M due to $C_{Y_0} = 10^{-9} \text{ m/s}^2$ plotted as a function of β (or δ_s) as computed using the JPL body-fixed SRP model and the nominal attitude motion.

7.3 SRP Estimation for GPS Orbit Determination

The rotating frame coefficients derived in Section 7.2.3 are tested against the JPL model using the methodology from Ref. [4] to compare the performance of the SRP models. The JPL IGS solutions were used as the input data for the Trajedy orbit estimation process of the GIPSY-OASIS II (version 5) software from JPL. This software was configured with the nominal GPS templates, meaning that the following force models were used: 12 x 12 Earth gravity field, relativity, solid tide, ocean tide, polar tide, and of course solar pressure. Note that for these cases, the 3D RMS used for convergence was set to 1 mm with a max of 5 iterations. Convergence could also be satisfied if the estimated parameters change by less than the default tolerance.

There are two aspects of testing that we were interested in to test the feasibility of using the rotating frame SRP model for orbit determination. First, we tested different arcs as laid out in Ref. [4] - single day arcs, 10 day arcs, and fitting 4 day arcs and propagating the solution forward 4 more days. For these tests, we chose an arbitrary 10 day period of August 5-14, 2009. This gives us 10 separate single day arcs, one 10 day arc, and 3 four day arcs plus 4 days of propagation. Note that we are mainly concerned with the satellites which are not experiencing eclipse, those listed in Table 7.4, along with the range of β values of their orbits over the 10 day period of interest. We did also run the orbit determination for the other GPS IIR-M satellites which are in eclipse (GPS 41, 43, and 60) to see how they would perform.

Table 7.4: GPS IR-M satellites not in eclipse and their associated β values on August 5 and 14, 2009.

GPS No.	β° on 8/5	β° on 8/14
44	-18.1°	-26.6°
45	69.2°	62.4°
46	61.1°	52.7°
47	39.6°	45.7°
51	42.4°	48.3°
54	39.9°	46.0°
56	-18.5°	26.9°
59	30.1°	20.5°
61	68.9°	61.8°

Second, we tried a number of different combinations of which parameters from the rotating frame model to estimate to see how the model performed. In Case 1, we estimated $A'_0(2)$ and $B'_1(3)$ and a scale

factor which was applied equally to the remaining coefficients. This is the most similar case to the JPL methodology since the $A'_0(2)$ and $B'_1(3)$ coefficients represent the majority of the Y-bias influence, and then the rest of the model is modified by a scale factor, where JPL estimates the scale factor and the Y-bias acceleration directly. In Case 2, we estimate each of the seven coefficients which cause secular changes to the orbit outlined in Chapter 5, along with a scale factor that is applied to all of the other coefficients in the SRP model. Finally, Case 3 is the same as Case 2 except that the scale factor is not estimated. Each of these cases was used to successfully fit one-day orbit arcs. An example of the fits for all four estimation schemes (including JPL) is shown in Fig. 7.14.

A summary all of the one-day arc results for each of the four different estimation schemes is shown in Table 7.5. The goodness of fit is determined by comparing the estimated orbit to the input orbit, which as mentioned above is the JPL IGS orbit for each of these days. The RMS of the fit over the course of the arc is taken by comparing the solution at each hour. The table shows the RSS of the RMS fits for each of the 10 individual day arcs, which gives an idea of how each scheme performs over the whole 10 day period. It is clear that each of the schemes works quite well in fitting the orbits of each daily arc to the centimeter level, as seen in Fig. 7.14. Note the one outlier for GPS 54 with Case 3; this RSS is made up entirely of the fact that the fit for August 12th with this scheme has an RMS of 7.6 m. Excluding that point, the RSS for the other 9 days is 0.170 m. Based on these results alone, one could conclude that Case 2 with the rotating frame model performs better than the JPL model. In fact, out of all 120 single day arcs analyzed (12 satellites for 10 days) there was only a single day arc where the JPL model had a better fit than Case 2.

Tables 7.6 - 7.9 show the results for the 10 day arc fit, and the three separate 4 day arc plus 4 day prediction fits. The JPL models performs well across the board, as expected. In general, using Case 1 with the rotating frame model gives the best performance on the longer arcs. Cases 2 and 3 have some arcs where they perform quite well, and others where they have terrible performance.

In order to gain some insight into the performance of the rotating frame cases, the estimated parameters from the Case 1 single day arcs are plotted in Figs. 7.15 - 7.17. Taking each of the parameters in turn, Fig. 7.15 shows a significant issue. It is immediately obvious that the estimate of $A'_0(2)$ is extremely unstable, especially for the three satellites called out in the figure. These three satellites correspond to those

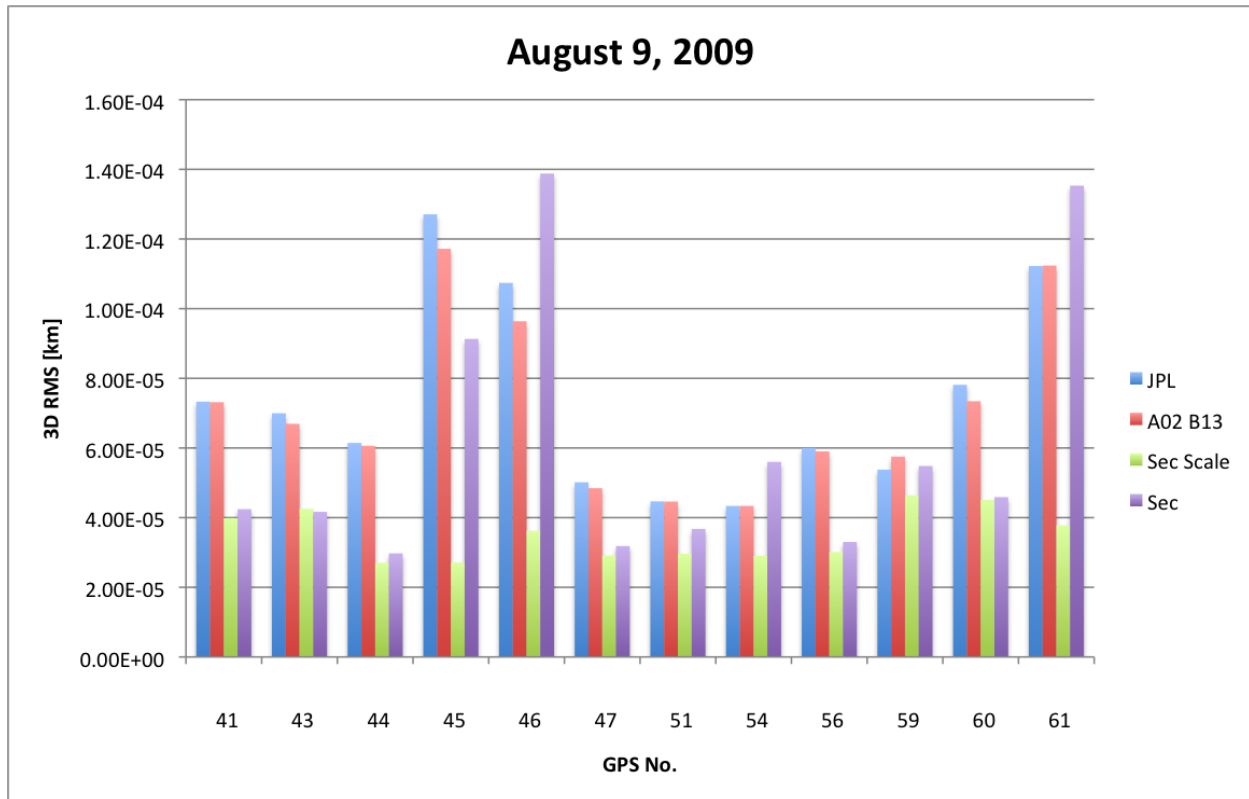


Figure 7.14: The RMS values for each of the four estimation schemes tested for August 9, 2009

Table 7.5: RSS [m] for 10 days August 5 - 14, 2009. The outlier marked with a * is discussed in the text.

GPS	JPL	Case 1	Case 2	Case 3
41	0.243	0.242	0.132	0.154
43	0.208	0.202	0.128	0.135
44	0.192	0.177	0.112	0.116
45	0.367	0.328	0.113	0.254
46	0.365	0.335	0.125	0.461
47	0.187	0.164	0.127	0.137
51	0.220	0.221	0.130	0.173
54	0.174	0.168	0.135	7.663*
56	0.213	0.197	0.122	0.143
59	0.203	0.202	0.131	0.159
60	0.256	0.236	0.142	0.144
61	0.388	0.385	0.116	0.455

Table 7.6: 10 day arc RMS [m] for August 5 - 14, 2009.

GPS	JPL	Case 1	Case 2	Case 3
41	0.451	0.881	50.858	50.986
43	0.433	0.622	191.262	214.672
44	0.207	1.783	0.146	0.211
45	0.194	0.777	0.094	0.150
46	0.341	0.923	33.506	29.748
47	0.194	0.988	8.241	0.503
51	0.255	1.345	45.820	45.785
54	0.174	0.563	41.704	47.348
56	0.372	2.452	59.822	37.370
59	0.192	18.014	1.027	39.637
60	0.617	0.631	0.099	0.109
61	0.239	0.243	0.099	0.174

Table 7.7: 4 day arc plus 4 day prediction RMS [m] for August 12, 2009.

GPS	JPL	Case 1	Case 2	Case 3
41	0.457	1.115	0.868	1.010
43	0.445	1.114	52.331	52.325
44	0.212	2.960	2.360	2.515
45	0.373	0.845	0.210	0.180
46	0.423	0.410	22.872	0.299
47	0.199	3.865	3.858	3.819
51	0.257	5.238	5.178	5.217
54	0.225	2.010	1.999	2.001
56	0.411	3.239	28.893	29.512
59	0.213	19.118	12.114	12.069
60	0.771	0.687	0.311	0.231
61	0.433	0.590	0.494	0.751

Table 7.8: 4 day arc plus 4 day prediction RMS [m] for August 13, 2009.

GPS	JPL	Case 1	Case 2	Case 3
41	0.515	0.798	0.784	0.904
43	0.460	1.025	54.770	47.905
44	0.226	3.656	2.258	2.060
45	0.227	0.826	0.238	0.476
46	0.604	0.702	22.460	0.530
47	0.249	3.562	3.494	3.514
51	0.389	4.814	4.577	4.577
54	0.219	1.862	15.822	17.437
56	0.475	4.527	29.395	40.738
59	0.339	25.827	13.054	13.052
60	0.785	0.719	0.225	0.226
61	0.259	0.321	0.150	0.233

Table 7.9: 4 day arc plus 4 day prediction RMS [m] for August 14, 2009.

GPS	JPL	Case 1	Case 2	Case 3
41	0.582	0.790	0.547	0.544
43	0.490	0.969	0.982	50.479
44	0.272	4.696	2.214	1.875
45	0.206	0.596	0.319	0.740
46	0.753	0.575	22.528	17.997
47	0.236	3.403	3.366	3.357
51	0.608	4.137	4.146	4.144
54	0.240	1.759	22.830	19.889
56	0.599	6.103	38.502	30.292
59	0.443	40.045	12.809	13.058
60	0.775	0.714	0.251	0.253
61	0.319	0.504	0.150	0.196

in Table 7.6 that do not fit the orbits. Fig. 7.16 shows an equally concerning trend where the estimate of $B'_1(3)$ for 11 of 12 satellites switches sign, as well as changing magnitude greatly over the course of the 10 days. On the other hand, Fig. 7.17 shows that the scale factor applied to all other Fourier coefficients behaves well over the course of the 10 days.

There are two issues at work here that can cause the variations in the parameters seen here and similar issues seen in the estimates of other parameters in Cases 2 and 3. First, the y-bias acceleration varies by spacecraft, as is illustrated in Table 7.10. Recall that the y-bias is largely represented in the $A'_0(2)$ and $B'_1(3)$ coefficients. A given y-bias will create values for these coefficients that are a combination of the functions shown in Figs. 7.10 and 7.13. Clearly, this could result in functional forms that are significantly different for each spacecraft, however the estimation schemes of Cases 1, 2, and 3 only allow for $A'_0(2)$ and $B'_1(3)$ to have the function form shown in Fig. 7.10 modified by a scale factor. The second problem is similar and related; the mapping between the JPL and the rotating frame coefficients is non-linear. Therefore, if a scale factor is adequate to represent the true SRP force with the JPL coefficients, this does not translate directly to a scale factor on each of the rotating frame coefficients (except for the simple case when the same scale factor is applied to all coefficients and there is no y-bias). These issues need to be addressed if this model is to be used operationally for GPS orbit determination. They can likely be resolved by allowing a different functional form for each spacecraft for the $A'_0(2)$ and $B'_1(3)$ coefficients either **a priori**, or by estimating a time-varying function like a linear fit for each coefficient instead of a scale factor only.

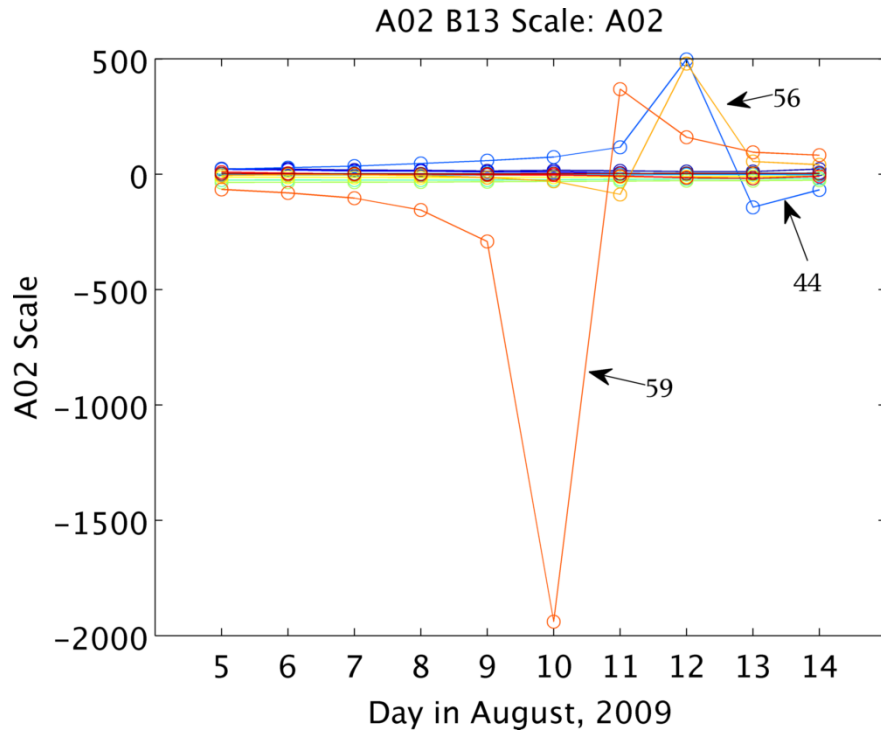


Figure 7.15: The $A'_0(2)$ scale factors estimated for each 1 day arc for each of the satellites in Case 1.

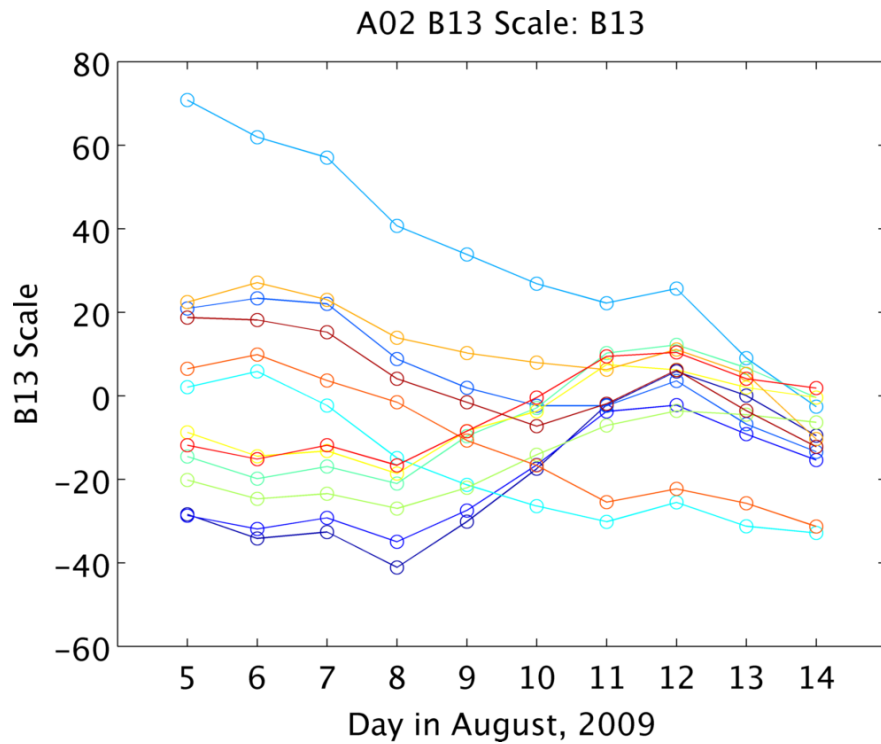


Figure 7.16: The $B'_1(3)$ scale factors estimated for each 1 day arc for each of the satellites in Case 1.

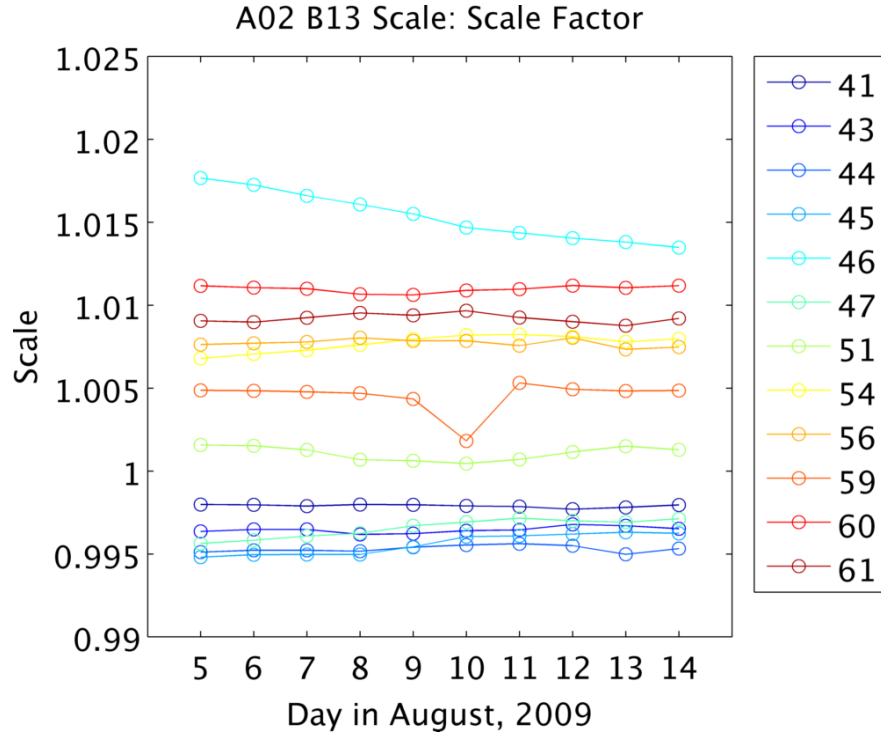


Figure 7.17: The general scale factors estimated for each 1 day arc for each of the satellites in Case 1.

Table 7.10: Y-bias values ($\times 10^{-9}$ m/s²) estimated by the JPL model estimation for August 9, 2009.

GPS	Y-bias
41	-0.4466
43	-0.2916
44	-0.1983
45	-0.2179
46	0.0675
47	-0.5998
51	-0.8855
54	-0.3518
56	0.0566
59	-0.4204
60	0.0121
61	0.0321

7.4 Orbital Debris

Current analytical studies [110], [100] and numerical studies [1] use the cannonball model to analyze the effect of solar radiation pressure on high area-to-mass ratio debris objects. While these studies have shown that using this simple model can cause huge variations in debris orbits over short time-spans, there is little justification for using the cannonball model. Here, we show that when a piece of debris is tumbling at a different rate than the orbits, the effective force due to solar radiation pressure will collapse to the well known cannonball model, where the force acts as a constant along the Sun-spacecraft direction that will vary on the order of the heliocentric orbit. We will also discuss what happens when this is not the case, and the debris' attitude is moving at rates similar to one of the orbit rates.

7.4.1 Tumbling Debris at Unique Rates

When a piece of debris is tumbling with a rate different than that of the orbit, the resulting dynamics will allow us to separately average the force and the perturbed orbit dynamics because there is no resonance or very long-period frequencies between the two types of dynamics. When the debris is tumbling rapidly compared to the orbit, it makes sense to average the SRP force over the tumbling motion and then use this averaged force in the perturbed orbital dynamics. On the other hand, when the debris is tumbling slower than the orbit average over the orbit with a constant SRP force for the current debris orientation, then average the result over the tumbling of the debris.

Either way, after averaging both the tumbling of the debris, and over the orbit, will yield the same result. In fact, in first order averaging theory, we can choose to apply the averaging in either order since this is a linear process. In this section we will average the force due to SRP over the tumbling motion of the debris, the results of which can be averaged over an orbit to determine the averaged dynamics.

To model a tumbling piece of debris, we assume that the body can be oriented in inertial space with equal probability. Therefore, the expected value of the force is precisely equal to the average force. Using the Fourier series expression for the SRP force from Eq. (2.28), the average force is obtained by integrating

over the solar latitude and longitude, and dividing by the range of the angles,

$$\overline{\mathbf{F}}_{SRP} = \frac{1}{4\pi} \int_0^\pi \int_0^{2\pi} \mathbf{F}_{SRP} d\lambda_s d\delta_s \quad (7.31)$$

where the line indicates the average value of the vector. However, note that the inner integral over the solar longitude is exactly the defining the zeroth order Fourier coefficient, so that

$$\overline{\mathbf{F}}_{SRP} = \frac{P(R)}{2} \int_0^\pi \mathbf{A}_0(\delta_s) d\delta_s \quad (7.32)$$

In this case, since the body is tumbling, it is useful to think of the spherical coordinate frame defined so that δ_s is measured from $\hat{\mathbf{u}}$, and λ_s is measured around that direction, so that

$$\hat{\mathbf{u}} = \begin{bmatrix} 0 \\ 0 \\ 1 \end{bmatrix} \quad (7.33)$$

and a general facet normal vector can be described as,

$$\hat{\mathbf{n}} = \begin{bmatrix} \cos \lambda_s \sin \delta_s \\ \sin \lambda_s \sin \delta_s \\ \cos \delta_s \end{bmatrix} \quad (7.34)$$

where the angles describe the current orientation of the facet with respect to the Sun.

Using this convention, \mathbf{f} for a given facet becomes,

$$\mathbf{f}_i = - \left\{ 2\rho_i s_i \cos^2 \delta_s \hat{\mathbf{n}}_i + (1 - \rho_i s_i) \cos \delta_s \hat{\mathbf{u}} + a_{2i} \cos \delta_s \hat{\mathbf{n}}_i \right\} H_i(\hat{\mathbf{u}}) A_i \quad (7.35)$$

Averaging this expression over λ_s gives,

$$\langle \mathbf{f}_i \rangle_{\lambda_s} = - \left\{ 2\rho_i s_i \cos^3 \delta_s + (1 - \rho_i s_i) \cos \delta_s + a_{2i} \cos^2 \delta_s \right\} H_i(\hat{\mathbf{u}}) A_i \cdot \hat{\mathbf{u}} \quad (7.36)$$

This result means that we can represent the zeroth-order Fourier coefficient as,

$$\mathbf{A}_0(\delta_s) = \sum_{i=1}^N \langle \mathbf{f}_i \rangle_{\lambda_s} \quad (7.37)$$

since we assume that the integration over each facet is independent.

In general, if there is no self shadowing, the visibility function has the simple definition,

$$H_i(\hat{\mathbf{u}}) = \begin{cases} 1 & \delta_s \geq 0 \\ 0 & \delta_s < 0 \end{cases} \quad (7.38)$$

which has the effect of changing the integration bounds for the averaging over the latitude. Therefore the averaging over the latitude for each facet becomes,

$$\bar{\mathbf{f}}_i = \frac{1}{2} \int_0^{\pi/2} \langle \mathbf{f}_i \rangle_{\lambda_s} \sin \delta_s \, d\delta_s = -\frac{1}{4} \left\{ 1 + \frac{2}{3} a_{2i} \right\} A_i \cdot \hat{\mathbf{u}} \quad (7.39)$$

and the average force due to SRP acting on the body is,

$$\bar{\mathbf{F}}_{SRP} = P(R) \sum_{i=1}^N \bar{\mathbf{f}}_i \quad (7.40)$$

A piece of debris that is modeled as a sum of facets, will therefore have a total average force in the $-\hat{\mathbf{u}}$ direction as it will equal the sum of the expected value of the force for each facet.

This result has produced the commonly used cannonball model, which is typically defined as,

$$\mathbf{F}_{SRP} = -C_R P(R) A \hat{\mathbf{u}} \quad (7.41)$$

where C_R is a scale factor and A is the projected area perpendicular to $\hat{\mathbf{u}}$. In our case, we would set

$$C_R \times A = \frac{1}{4} \sum_{i=1}^N \left\{ 1 + \frac{2}{3} a_{2i} \right\} A_i \quad (7.42)$$

Any piece of debris that is tumbling at a rate that is not near the orbit rate or the heliocentric orbit rate can be modeled with the cannonball model if the averaged force is then used to model the averaged orbit dynamics. The main assumption made here is that the piece of debris is tumbling so that there is a uniform probability of any orientation occurring between the piece of debris and the Sun direction. If this assumption is not proper, then the expected value of the SRP force can be determined by using a different probability density function to properly represent the attitude dynamics. The main outcome of violating this assumption is that the averaged force can be in a direction other than the Sun-spacecraft direction.

7.4.2 Tumbling Debris with Resonant Rates

If the debris is tumbling at one of the orbit rates, than a myriad of effects can appear that do not exist when using the cannonball model. If the debris is in a stable attitude motion that repeats every orbit,

secular terms will appear that can change any aspect of the orbit, depending on the shape of the body and the attitude motion. If the debris is tumbling, so that the attitude motion is not the same every orbit, then the secular rates that appear will change each orbit depending on the attitude motion over that orbit. These secular rates can make drastic changes to the orbit, or can largely cancel out; it depends on the specific shape and attitude motion. This case has been thoroughly explored in Chapters 5, 6, and 7.

Debris which is tumbling at near orbit rates requires special attention as well. In this case, the long-period rates will not be purely secular, however the periods can be very long so that they would appear nearly secular for time periods of interest. In this case, more specific analysis must be made for two reasons. First, the separation of the averaging processes over the orbit and the attitude motion can no longer be separated, as was done in the previous section. Second, since the period will be so long, the orbit averaging can not assume that the orbital elements are constant over that period. These issues were discussed in further detail in Chapter 4.

7.5 Solar Sails

The use of solar sails has been discussed for a number of missions and applications which typically fall into interplanetary mission or halo orbit applications. One of the earliest discussions of Earth escape using a solar sail was by Sands.[90] This basic analytical discussion was extended by Swartwout[106] to an optimal framework. Similarly, the majority of the current work in this area involves different optimization methods for Earth escape. [104, 58, 41] Other recent work considers more realistic near-optimal control laws with further constraints [57] and the influence of aerodynamic drag. [68]

Halo orbit applications are another popular area of research for using sailcraft as the continuous force created by the sail can be used to effectively modify gravity. This idea was introduced for Earth applications by Forward, [32] and was continued by Bookless, Waters, and McInnes. [120, 121, 8] The halo orbit application has also been used for control around the Sun-Earth Lagrange points. [9]

Outside of the halo applications, there have been a minimal number of papers for using solar sails in Earth orbit. One application that has been researched is an optimal formulation for controlling orbital elements for an Earth orbit. [56] There has also been a discussion of using sailcraft to explore the geomagnetic

tail, which requires a Sun-synchronous orbit. [63, 49]

Most solar sail work which considers the orbital effects of solar sail propulsion does not consider realistic attitude dynamics as well. In these cases, the attitude is generally considered as an optimization variable, and therefore the solutions often times require large control torques and high slew rates which may be unreasonable in real satellite systems.

On the other hand, there is a body of literature discussing the attitude dynamics and control of solar sails. Wie [122, 123] has covered a wide variety of methods for solar sail attitude control. Modi and Pande [69] discuss analytical solutions for spinning sailcraft under the influence of solar and gravity gradient torques. Others [16] have extended this research with an eye toward attitude stabilization using the aerodynamic torque.

Lawrence and Whorton [50] extend this idea further. They have determined that under the influence of gravity gradient, aerodynamic, and solar torques, there are natural equilibrium points for the solar sail attitude in the LVLH frame (equivalently the rotating frame from Chapter 2) which is defined at any given time by the basis set $\{\hat{\mathbf{r}}, \hat{\mathbf{v}}, \hat{\mathbf{h}}\}$, which are the radial, velocity, and angular momentum direction vectors respectively, in a circular orbit. If a sail's attitude is fixed at one of these equilibrium points only the orbit energy can be changed. The change in the angular momentum and eccentricity vectors is averaged out as the LVLH frame rotates. By coning the solar sail normal vector about a stable equilibrium point in the LVLH frame such that one coning rotation is completed per orbit, a wide variety of orbital effects can be created with zero control torque needed and minimal excitation of structural dynamics.

This section provides a structured discussion of the effects on the spacecraft orbit due to stable attitude motions about equilibrium points in the LVLH frame for circular orbits, combining the typically disparate areas of attitude and orbital dynamics. The goal is to provide a detailed analytical framework to show the usefulness of solar sails in low Earth orbits where they have typically not been considered.

7.5.1 System Definition

One of the key ideas for this dissertation is that attitude equilibria exist in the LVLH frame. The LVLH frame is defined by $\hat{\mathbf{r}}$, the unit vector along the radius vector, $\hat{\mathbf{h}}$, the unit vector along the angular

momentum vector, and $\hat{\mathbf{v}}$, the unit vector along the velocity vector. Note that in this dissertation we are discussing only circular orbits, in an elliptical orbit the third unit vector is only aligned with the velocity vector at the apse points.

The attitude of the sail is described by two angles with respect to the LVLH frame. The cone angle, β , is the angle between the solar sail normal vector and $\hat{\mathbf{h}}$. The clock angle, ϕ , is the angle between the projection of the normal vector into the $\hat{\mathbf{r}}-\hat{\mathbf{v}}$ plane, measured from $\hat{\mathbf{v}}$.

The solar sail normal vector can then be described in the LVLH frame by the cone and clock angles. It is a unit vector with the form,

$$[\hat{\mathbf{n}}]_{LVLH} = \begin{bmatrix} -\sin(\beta)\sin(\phi) \\ \sin(\beta)\cos(\phi) \\ \cos(\beta) \end{bmatrix} \quad (7.43)$$

The LVLH frame, the solar sail normal, and the cone and clock angles are illustrated in Fig. 7.18.

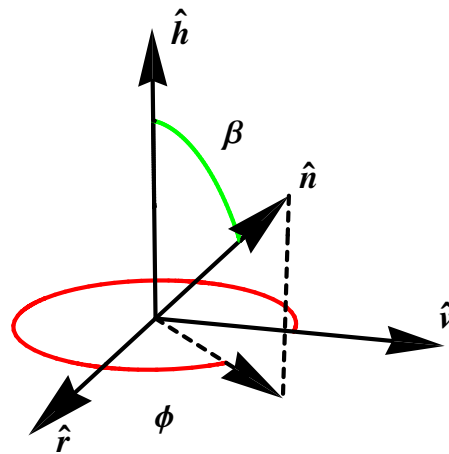


Figure 7.18: Illustration of the LVLH frame and the cone (β) and clock (ϕ) angles.

7.5.2 Attitude Motion

The equilibrium points in the LVLH frame found in Reference [50] that we will investigate motion about in this dissertation are those where the normal vector lies in the $\hat{\mathbf{v}} - \hat{\mathbf{h}}$ plane. For those equilibrium points, the clock angle, ϕ , is equal to 0 or π . The placement of the equilibrium point in terms of the cone

angle is then defined by the sail parameters and its spin rate about the solar sail normal. To start, we assume that the necessary combination is made to have any cone angle be an equilibrium point in turn, and we study the properties for each combination.

There are two reasons to study these equilibrium points. First, these attitudes were noted by Lawrence and Whorton to produce orbit raising ($\phi = \pi$) or lowering ($\phi = 0$) effects. The second reason to investigate these equilibria is that these are neutrally stable equilibria with closed orbits around them. This allows us to investigate the effects of a sail that is coning about an equilibrium point in the LVLH frame. An example of this type of coning is shown in Fig. 7.19. The cone half-angle is defined by θ and we assume that one attitude cone is completed in one solar sail orbit at a constant rate. The normal motion around the cone begins at $\hat{\mathbf{n}}_0$, the point on the cone with the smallest value of β , and rotates in a positive sense about $\hat{\mathbf{n}}_{eq}$.

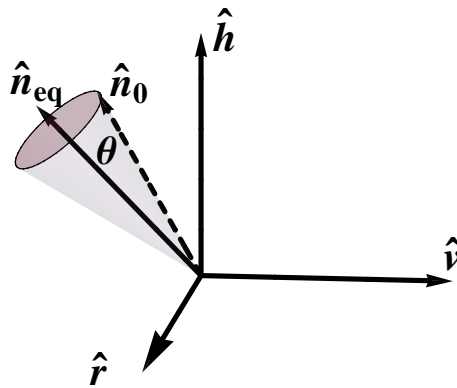


Figure 7.19: Illustration of the normal vector coning in the LVLH frame for $\phi_{eq} = \pi$.

7.5.3 Orbital Effects

The effects of a perturbing acceleration on an orbit can be described by the change in energy (\mathcal{E}), angular momentum (\mathbf{h}), and the eccentricity vector (\mathbf{e}) which are given in Eqs. (3.7) - (3.9). Given an inertial orbital acceleration vector, \mathbf{a} , the effect on the orbit can be determined.

A first order model of the acceleration created by the solar sail due to only specular reflection is,

$$\mathbf{a} = -a_c \cos^2(\beta) \hat{\mathbf{n}} \quad (7.44)$$

where a_c is the characteristic acceleration for the sail. In general the angle between the normal vector and

the sail-sun vector is used in Eq. (7.44), however we assume that the sail-sun vector is parallel to $\hat{\mathbf{h}}$, and therefore this angle is equal to the cone angle β .

Substituting Eq. (7.44) into Eqs. (3.7) - (3.9), we get

$$\dot{\mathcal{E}} = -a_c \sqrt{\frac{\mu}{r}} \cos^2(\beta) \hat{\mathbf{v}} \cdot \hat{\mathbf{n}} \quad (7.45)$$

$$\frac{I d\mathbf{h}}{dt} = -a_c r \cos^2(\beta) \hat{\mathbf{r}} \times \hat{\mathbf{n}} \quad (7.46)$$

$$\frac{I d\mathbf{e}}{dt} = -a_c \sqrt{\frac{r}{\mu}} \cos^2(\beta) [\hat{\mathbf{n}} \times \hat{\mathbf{h}} + \hat{\mathbf{v}} \times (\hat{\mathbf{r}} \times \hat{\mathbf{n}})] \quad (7.47)$$

where the angular momentum magnitude $h = rv$, and the orbit velocity $v = \sqrt{\mu/r}$, due to the assumption of a circular orbit. In this representation, the variation of the orbit is expressed as a function of the solar sail properties through a_c , the orbit size (r), and the sail orientation through $\hat{\mathbf{n}}$ and β .

It will be convenient to represent these quantities in inertial coordinates, therefore we will use a perifocal frame. However, since perigee is not defined for a circular orbit, the $\hat{\mathbf{P}}$ vector simply points along the initial radius vector, the $\hat{\mathbf{Q}}$ vector points along the initial velocity vector, and the $\hat{\mathbf{R}}$ vector points along the initial angular momentum vector.

As has been mentioned, the solar sail normal vector is nominally expressed in the LVLH frame as shown in Eq. (7.43). To put this vector into the PQR frame, the following transformation is used,

$$[L2P] = \begin{bmatrix} \cos nt & -\sin nt & 0 \\ \sin nt & \cos nt & 0 \\ 0 & 0 & 1 \end{bmatrix} \quad (7.48)$$

where $n = \sqrt{\mu/a^3}$ is the mean motion and t is the time since starting the orbit at the $\hat{\mathbf{P}}$ vector. Applying this transformation, the sail normal can be described in the orbital frame as,

$$[\hat{\mathbf{n}}]_{PQR} = \begin{bmatrix} -\sin(\beta) \sin(\phi) \cos(nt) - \sin(\beta) \cos(\phi) \sin(nt) \\ -\sin(\beta) \sin(\phi) \sin(nt) + \sin(\beta) \cos(\phi) \cos(nt) \\ \cos(\beta) \end{bmatrix} \quad (7.49)$$

Finally, the coning is described by an equilibrium cone and clock angle, β_{eq} and ϕ_{eq} respectively, and also the cone half angle θ . This means that the cone and clock angles in Eq. (7.49) are not constant, but can

be described in terms of these three parameters and time. For the case where $\phi_{eq} = \pi$, the fully expanded sail normal vector can be written as,

$$[\hat{\mathbf{n}}]_{PQR} = \begin{bmatrix} -(1 + \cos(\beta_{eq})) \sin(\theta) \sin(nt) \cos(nt) + \sin(\beta_{eq}) \cos(\theta) \sin(nt) \\ -\sin(\theta) \sin^2(nt) + \cos(\beta_{eq}) \sin(\theta) \cos^2(nt) - \sin(\beta_{eq}) \cos(\theta) \cos(nt) \\ \sin(\beta_{eq}) \sin(\theta) \cos(nt) + \cos(\beta_{eq}) \cos(\theta) \end{bmatrix} \quad (7.50)$$

Another impact of the cone and clock angles being non-constant is seen for Eqs. (7.45) - (7.47). We can recognize from Eqs. (7.49) and (7.50),

$$\cos(\beta) = \sin(\beta_{eq}) \sin(\theta) \cos(nt) + \cos(\beta_{eq}) \cos(\theta) \quad (7.51)$$

and therefore,

$$\begin{aligned} \cos^2(\beta) &= \sin^2(\beta_{eq}) \sin^2(\theta) \cos^2(nt) + \cos^2(\beta_{eq}) \cos^2(\theta) \\ &\quad + 2 \sin(\beta_{eq}) \sin(\theta) \cos(nt) \cos(\beta_{eq}) \cos(\theta) \end{aligned} \quad (7.52)$$

Substituting Eqs. (7.52) and (7.50) into Eq. (7.44) allows us to write the acceleration as a Fourier series,

$$\mathbf{a} = -a_c \sum_{n=0}^4 \mathbf{A}_n'' \cos(nM) + \mathbf{B}_n'' \sin(nM) \quad (7.53)$$

where the double-prime coefficients are given by,

$$\begin{aligned} \mathbf{A}_0'' \cdot \hat{\mathbf{Q}} &= -\frac{1}{8} \sin^2(\beta_{eq}) \sin^3(\theta) + \frac{3}{8} \sin^2(\beta_{eq}) \sin^3(\theta) \cos(\beta_{eq}) - \frac{1}{2} \sin(\theta) \cos^2(\beta_{eq}) \cos^2(\theta) \\ &\quad + \frac{1}{2} \cos^3(\beta_{eq}) \sin(\theta) \cos^2(\theta) - \sin(\theta) \cos^2(\theta) \sin^2(\beta_{eq}) \cos(\beta_{eq}) \end{aligned} \quad (7.54)$$

$$\mathbf{A}_0'' \cdot \hat{\mathbf{R}} = \frac{3}{2} \sin^2(\beta_{eq}) \sin^2(\theta) \cos(\beta_{eq}) \cos(\theta) + \cos^3(\beta_{eq}) \cos^3(\theta) \quad (7.55)$$

$$\begin{aligned} \mathbf{A}_1'' \cdot \hat{\mathbf{Q}} &= -\frac{3}{4} \sin^3(\beta_{eq}) \sin^2(\theta) \cos(\theta) - \sin(\beta_{eq}) \cos^2(\beta_{eq}) \cos^3(\theta) \\ &\quad - \frac{1}{2} \sin^2(\theta) \sin(\beta_{eq}) \cos(\beta_{eq}) \cos(\theta) + \frac{3}{2} \sin^2(\theta) \sin(\beta_{eq}) \cos^2(\beta_{eq}) \cos(\theta) \end{aligned} \quad (7.56)$$

$$\mathbf{A}_1'' \cdot \hat{\mathbf{R}} = \frac{3}{4} \sin^3(\beta_{eq}) \sin^3(\theta) + \cos^2(\beta_{eq}) \cos^2(\theta) \sin(\beta_{eq}) \sin(\theta) + 2 \sin(\beta_{eq}) \sin(\theta) \cos^2(\beta_{eq}) \cos^2(\theta) \quad (7.57)$$

$$\begin{aligned} \mathbf{A}_2'' \cdot \hat{\mathbf{Q}} &= \frac{1}{2} \sin^3(\theta) \sin^2(\beta_{eq}) \cos(\beta_{eq}) + \frac{1}{2} \sin(\theta) \cos^2(\beta_{eq}) \cos^2(\theta) \\ &\quad + \frac{1}{2} \sin(\theta) \cos^3(\beta_{eq}) \cos^2(\theta) - \sin(\theta) \sin^2(\beta_{eq}) \cos(\beta_{eq}) \cos^2(\theta) \end{aligned} \quad (7.58)$$

$$\mathbf{A}_2'' \cdot \hat{\mathbf{R}} = \frac{3}{2} \sin^2(\beta_{eq}) \sin^2(\theta) \cos(\beta_{eq}) \cos(\theta) \quad (7.59)$$

$$\mathbf{A}_3'' \cdot \hat{\mathbf{Q}} = -\frac{1}{4} \sin^2(\theta) \sin^3(\beta_{eq}) \cos(\theta) + \frac{1}{2} \sin^2(\theta) \sin(\beta_{eq}) \cos(\beta_{eq}) \cos(\theta) + \frac{1}{2} \sin^2(\theta) \sin(\beta_{eq}) \cos^2(\beta_{eq}) \cos(\theta) \quad (7.60)$$

$$\mathbf{A}_3'' \cdot \hat{\mathbf{R}} = \frac{1}{4} \sin^3(\beta_{eq}) \sin^3(\theta) \quad (7.61)$$

$$\mathbf{A}_4'' \cdot \hat{\mathbf{Q}} = \frac{1}{8} \sin^3(\theta) \sin^2(\beta_{eq}) [1 + \cos(\beta_{eq})] \quad (7.62)$$

$$\mathbf{B}_1'' \cdot \hat{\mathbf{P}} = \frac{1}{4} \sin^2(\theta) \sin^3(\beta_{eq}) \cos(\theta) + \sin(\beta_{eq}) \cos^2(\beta_{eq}) \cos^3(\theta) - \frac{1}{2} \sin^2(\theta) \sin(\beta_{eq}) \cos(\beta_{eq}) \cos(\theta) [1 + \cos(\beta_{eq})] \quad (7.63)$$

$$\mathbf{B}_2'' \cdot \hat{\mathbf{P}} = -\frac{1}{4} \sin^3(\theta) \sin^2(\beta_{eq}) [1 + \cos(\beta_{eq})] - \frac{1}{2} \cos^2(\beta_{eq}) \cos^2(\theta) \sin(\theta) [1 + \cos(\beta_{eq})] + \sin(\theta) \sin^2(\beta_{eq}) \cos(\beta_{eq}) \cos^2(\theta) \quad (7.64)$$

$$\mathbf{B}_3'' \cdot \hat{\mathbf{P}} = \frac{1}{4} \sin^2(\theta) \sin^3(\beta_{eq}) \cos(\theta) - \frac{1}{2} \sin^2(\theta) \sin(\beta_{eq}) \cos(\beta_{eq}) \cos(\theta) [1 + \cos(\beta_{eq})] \quad (7.65)$$

$$\mathbf{B}_4'' \cdot \hat{\mathbf{P}} = -\frac{1}{8} \sin^3(\theta) \sin^2(\beta_{eq}) [1 + \cos(\beta_{eq})] \quad (7.66)$$

and all other coefficients (including those with $n > 4$) are zero.

The final expression needed to write the variation equations in the PQR frame is the velocity, radius, and angular momentum unit vectors in the PQR frame, which are the columns of the rotation matrix in Eq. (7.48),

$$[\hat{\mathbf{r}}]_{PQR} = [\cos(nt) \ \sin(nt) \ 0]^T \quad (7.67)$$

$$[\hat{\mathbf{v}}]_{PQR} = [-\sin(nt) \ \cos(nt) \ 0]^T \quad (7.68)$$

$$[\hat{\mathbf{h}}]_{PQR} = [0 \ 0 \ 1]^T \quad (7.69)$$

Using Eqs. (7.50), (7.52), and (7.67) - (7.69), the Eqs. (7.45) - (7.47) are written in the PQR frame as,

$$\dot{\mathcal{E}} = -a_c \sqrt{\frac{\mu}{r}} \left[\left(-\cos(\theta) \sin(\beta_{eq}) + \cos(\beta_{eq}) \cos(M) \sin(\theta) \right) \cdot \left(\cos^2(\beta_{eq}) \cos^2(\theta) + 2 \cos(\beta_{eq}) \cos(M) \cos(\theta) \sin(\beta_{eq}) \sin(\theta) + \cos^2(M) \sin^2(\beta_{eq}) \sin^2(\theta) \right) \right] \quad (7.70)$$

$$\left[\frac{d\mathbf{h}}{dt} \right]_{PQR} = -a_c r \begin{bmatrix} \sin(M) \left(\cos(\beta_{eq}) \cos(\theta) + \cos(M) \sin(\beta_{eq}) \sin(\theta) \right) \\ \cdot \left(\cos^2(\beta_{eq}) \cos^2(\theta) + \cos^2(M) \sin^2(\beta_{eq}) \sin^2(\theta) \right) \\ + 2 \cos(\beta_{eq}) \cos(M) \cos(\theta) \sin(\beta_{eq}) \sin(\theta) \\ - \cos(M) \left(\cos(\beta_{eq}) \cos(\theta) + \cos(M) \sin(\beta_{eq}) \sin(\theta) \right) \\ \cdot \left(\cos^2(\beta_{eq}) \cos^2(\theta) + \cos^2(M) \sin^2(\beta_{eq}) \sin^2(\theta) \right) \\ + 2 \cos(\beta_{eq}) \cos(M) \cos(\theta) \sin(\beta_{eq}) \sin(\theta) \\ (-\cos(\theta) \sin(\beta_{eq}) + \cos(\beta_{eq}) \cos(M) \sin(\theta)) \\ \cdot \left(\cos^2(\beta_{eq}) \cos^2(\theta) + \cos^2(M) \sin^2(\beta_{eq}) \sin^2(\theta) \right) \\ + 2 \cos(\beta_{eq}) \cos(M) \cos(\theta) \sin(\beta_{eq}) \sin(\theta) \end{bmatrix} \quad (7.71)$$

$$\left[\frac{d\mathbf{e}}{dt} \right]_{PQR} = -a_c \sqrt{\frac{r}{\mu}} \begin{bmatrix} - \left(2 \cos(M) \cos(\theta) \sin(\beta_{eq}) - 2 \cos(\beta_{eq}) \cos^2(M) \sin(\theta) \right. \\ \left. + \sin^2(M) \sin(\theta) \right) \cdot \left(\cos^2(\beta_{eq}) \cos^2(\theta) \right) \\ + 2 \cos(\beta_{eq}) \cos(M) \cos(\theta) \sin(\beta_{eq}) \sin(\theta) \\ \left. + \cos^2(M) \sin^2(\beta_{eq}) \sin^2(\theta) \right) \\ \sin(M) \left((1 + 2 \cos(\beta_{eq})) \cos(M) \sin(\theta) - 2 \cos(\theta) \sin(\beta_{eq}) \right) \\ \cdot \left(\cos^2(\beta_{eq}) \cos^2(\theta) + \cos^2(M) \sin^2(\beta_{eq}) \sin^2(\theta) \right) \\ + 2 \cos(\beta_{eq}) \cos(M) \cos(\theta) \sin(\beta_{eq}) \sin(\theta) \\ 0 \end{bmatrix} \quad (7.72)$$

where M is the mean anomaly of the orbit and the relationship for a circular orbit,

$$M = nt \quad (7.73)$$

has been used. The mean anomaly is ill-defined for a circular orbit since perigee is not defined. Therefore,

we choose the initial position, which corresponds to $M = 0$, to be the ascending node.

The total effect of the sail completing one cone about the equilibrium attitude is obtained by averaging the variational equations in the PQR frame,

$$\overline{\dot{\mathcal{E}}} = \frac{1}{2\pi} \int_0^{2\pi} \dot{\mathcal{E}} dM \quad (7.74)$$

$$\overline{\dot{\mathbf{h}}} = \frac{1}{2\pi} \int_0^{2\pi} \dot{\mathbf{h}} dM \quad (7.75)$$

$$\overline{\dot{\mathbf{e}}}} = \frac{1}{2\pi} \int_0^{2\pi} \dot{\mathbf{e}} dM \quad (7.76)$$

Carrying out the averaging gives the following results,

$$\overline{\dot{\mathcal{E}}} = a_c \sqrt{\frac{\mu}{r}} \left[\frac{1}{16} \pi \left[\cos(\theta) \left(7 \sin(\beta_{eq}) + 3 \sin(3\beta_{eq}) \right) + \cos(3\theta) \left(\sin(\beta_{eq}) + 5 \sin(3\beta_{eq}) \right) \right] \right] \quad (7.77)$$

$$\overline{\dot{\mathbf{h}}} = a_c r \begin{bmatrix} 0 \\ \frac{3}{64} \pi \left[\sin(\theta) \left(13 \sin(\beta_{eq}) + \sin(3\beta_{eq}) \right) + \sin(3\theta) \left(\sin(\beta_{eq}) + 5 \sin(3\beta_{eq}) \right) \right] \\ \frac{1}{16} \pi \left[\cos(\theta) \left(7 \sin(\beta_{eq}) + 3 \sin(3\beta_{eq}) \right) + \cos(3\theta) \left(\sin(\beta_{eq}) + 5 \sin(3\beta_{eq}) \right) \right] \end{bmatrix} \quad (7.78)$$

$$\overline{\dot{\mathbf{e}}} = -a_c \sqrt{\frac{r}{\mu}} \begin{bmatrix} \frac{1}{32} \pi \left[\sin(\theta) \left(-7 + 13 \cos(\beta_{eq}) - \cos(2\beta_{eq}) + 3 \cos(3\beta_{eq}) \right) \right. \\ \left. + \sin(3\theta) \left(-3 + \cos(\beta_{eq}) - 5 \cos(2\beta_{eq}) + 15 \cos(3\beta_{eq}) \right) \right] \\ 0 \\ 0 \end{bmatrix} \quad (7.79)$$

Note that while these rates have been averaged over an orbit, the results shown in Eqs. (7.77) - (7.79) are the secular rates of change per second.

These results can also be used to investigate what happens on average to an orbit where the solar sail normal remains at a stable equilibrium with $\phi_{eq} = \pi$ and some β_{eq} . In this case, $\theta = 0$ because there

is no coning motion, and therefore there is a secular change in energy and the $\hat{\mathbf{R}}$ component of angular momentum. This was predicted by Lawrence and Whorton [50].

When coning motion is implemented, a wide variety of orbital effects can be generated based on the coning which is used. Figs. 7.20 - 7.21 show the scaled orbital effects for all coning motions with $\phi_{eq} = \pi$. The results are scaled based on the coefficients outside the square brackets in Eqs. (7.77) - (7.79). These coefficients are where the orbit size and solar sail dependence comes in, and therefore the Figures shown can be applied to any sail and orbit combination. Note that $\dot{\mathbf{h}} \cdot \hat{\mathbf{P}}$, $\dot{\mathbf{e}} \cdot \hat{\mathbf{Q}}$, and $\dot{\mathbf{e}} \cdot \hat{\mathbf{R}}$ average to zero for all coning motions as shown in Eqs. (7.78) and (7.79), and therefore are not plotted.

A mirroring set of figures can be generated for the coning cases where $\phi_{eq} = 0$. In that case, the $\bar{\mathbf{h}} \cdot \hat{\mathbf{Q}}$, $\bar{\mathbf{h}} \cdot \hat{\mathbf{R}}$, and $\bar{\mathcal{E}}$ plots are precisely inverted, having the opposite sign everywhere. On the other hand, the results for $\bar{\mathbf{e}} \cdot \hat{\mathbf{P}}$ are exactly the same.

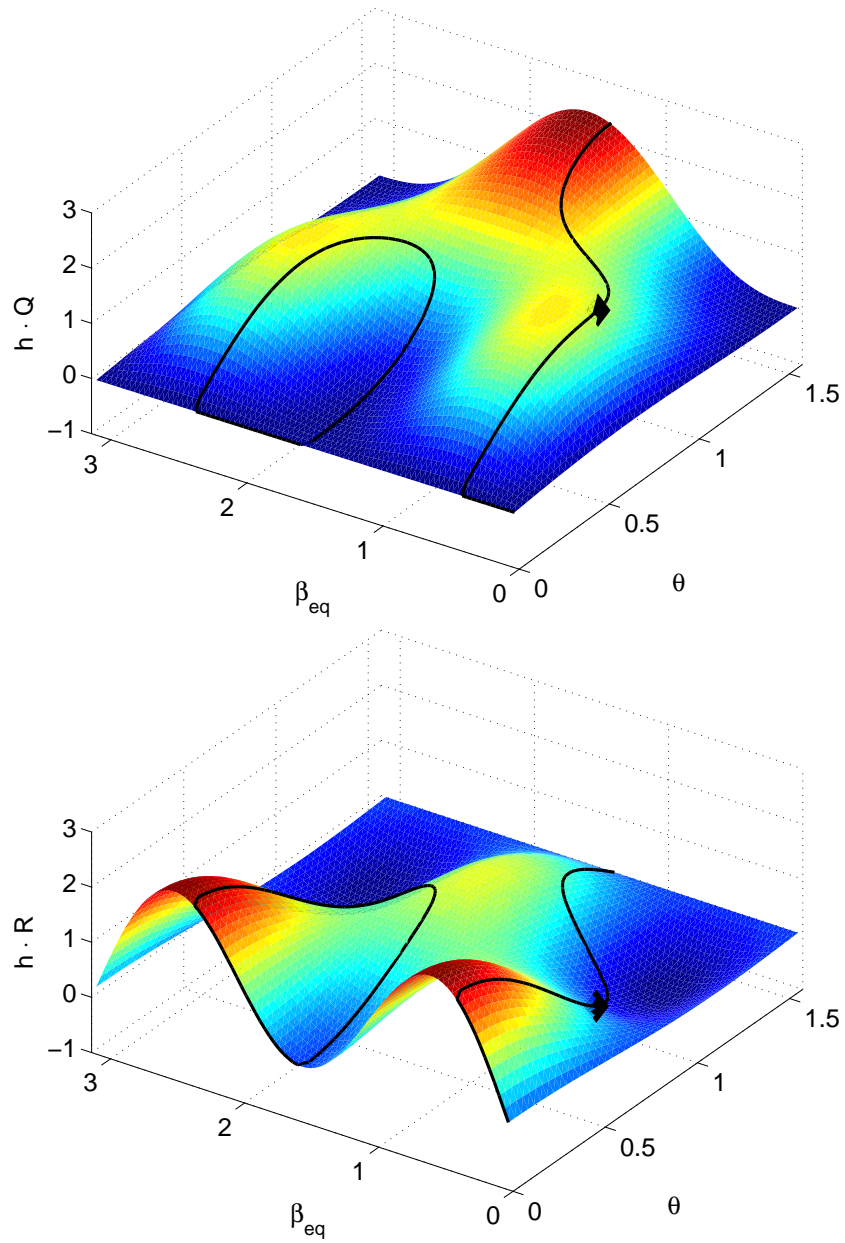


Figure 7.20: Scaled change of the angular momentum vector components, $\bar{\mathbf{h}} \cdot \hat{\mathbf{Q}} / (a_c r)$ (top) and $\bar{\mathbf{h}} \cdot \hat{\mathbf{R}} / (a_c r)$ (bottom), for coning cases with $\phi_{eq} = \pi$.

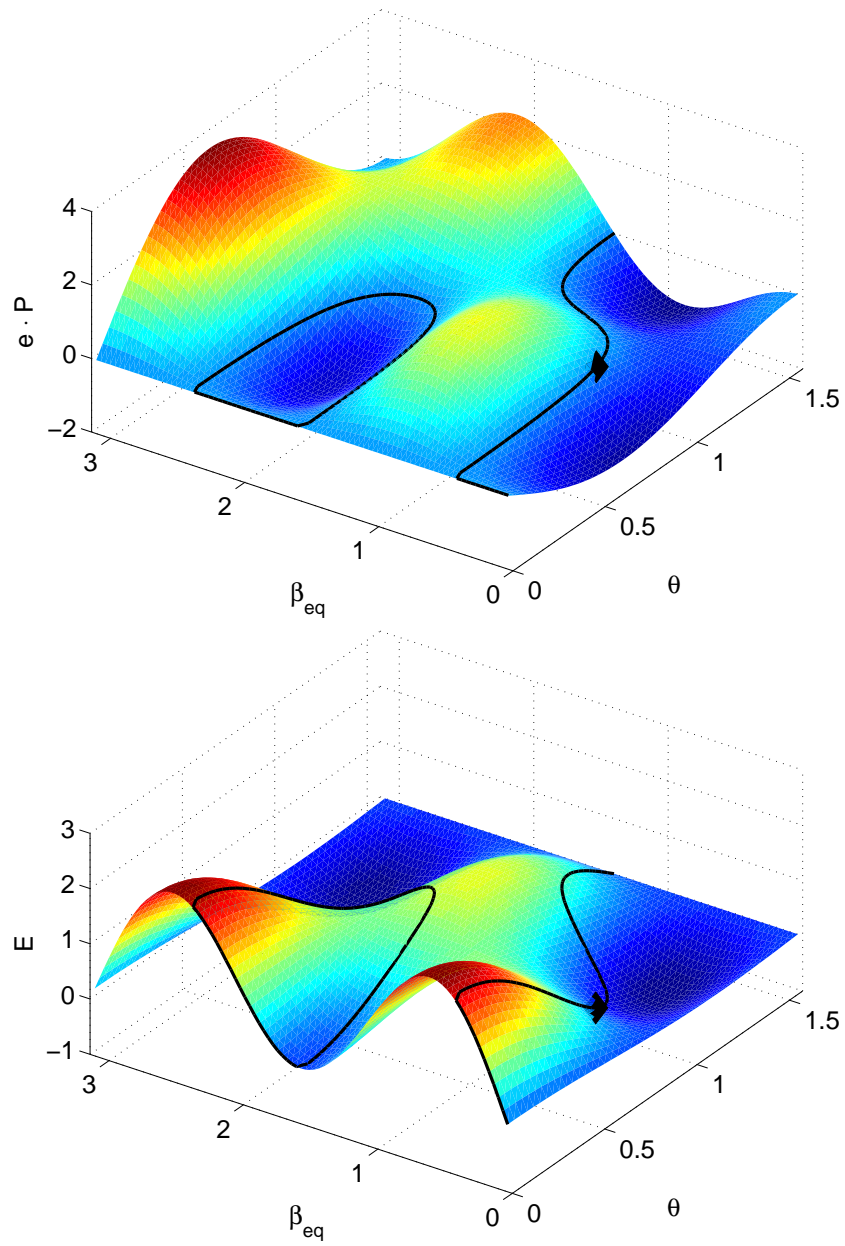


Figure 7.21: Scaled change of the eccentricity vector $\bar{\mathbf{e}} \cdot \hat{\mathbf{P}} / \left(a_c \sqrt{\frac{r}{\mu}} \right)$ (top), and the energy $\bar{E} / \left(a_c \sqrt{\frac{\mu}{r}} \right)$ (bottom) for coning cases with $\phi_{\text{eq}} = \pi$.

7.5.4 Applications

In this section, we investigate specific applications to Sun-synchronous orbits. Several issues will be investigated, including whether new Sun-synchronous orbits can be created for different orbital conditions if the solar sail accelerations can counteract/enforce the J_2 effect. A second, related, investigation will look at how large of an injection error can be overcome by the solar sail to place the spacecraft into a nominal Sun-synchronous orbit.

For the application of Sun-synchronous orbits, we are concerned with the comparison of nodal drift rates caused by J_2 and the solar sail. The expression for the nodal drift rate caused by J_2 from Vallado [111] is,

$$\dot{\Omega} = -\frac{3R_E^2 J_2 \sqrt{\mu}}{2a^{7/2}(1-e^2)^2} \cos(i) \quad (7.80)$$

where R_E is the Earth's radius, e is the orbit eccentricity, a is the semi-major axis, and i is the inclination.

The simplest case for the solar sail effects occurs when the PQR frame is aligned so that $\hat{\mathbf{P}}$ points to the minimum latitude position and $\hat{\mathbf{R}}$ points to the ascending node. Alternatively, if the cone is started at the maximum latitude instead of the minimum latitude, the node is rotated in the opposite direction. The $\bar{\mathbf{h}} \cdot \hat{\mathbf{Q}}$ rate works to rotate the orbital plane such that the node will be modified by,

$$\Delta\Omega = \arctan\left(\frac{(\bar{\mathbf{h}} \cdot \hat{\mathbf{Q}})T}{h \sin(i)}\right) \quad (7.81)$$

where $\Delta\Omega$ is the nodal drift in one orbit and T is the orbit period in seconds.

For the applications discussed here, we use a coning motion such that only the $\bar{\mathbf{h}} \cdot \hat{\mathbf{Q}}$ has a non-zero value; all other rates are zero. This is illustrated in Figs. 7.20 - 7.21. The black line on each surface represents the coning motions where $\bar{\mathbf{e}} \cdot \hat{\mathbf{P}} = 0$. This is seen most clearly in Fig. 7.21. The diamond then represents the particular coning motion where $\bar{\mathbf{h}} \cdot \hat{\mathbf{R}} = 0$ and $\bar{\mathcal{E}} = 0$. This particular case is a cone with $\beta_{eq} = 0.52$ radians and $\theta = 0.83$ radians.

In the following applications, we use a circular orbit with a radius of 8008 km for the scaling in the secular equations except where otherwise noted. Since this is a circular orbit, this fixes the velocity and angular momentum. The inclination is chosen by the Sun-synchronous relationship in Eq. (7.80), and turns out to be approximately 102.7° .

7.5.4.1 Sun-synchronous Errors

The first application of this motion for Sun-synchronous orbits is to use the solar sail to overcome undesired nodal drift from errors in the semi-major axis or inclination. Eq. (7.80) shows how errors in the desired semi-major axis and inclination values change the nodal drift rate. By executing the proper coning motion, the solar sail can be used to offset the undesired drift rate to keep the spacecraft in a Sun-synchronous orbit.

Fig. 7.22 illustrates this nodal drift situation for the particular case outlined above. Depending on the characteristic acceleration of the solar sail, larger errors can be matched or overcome by the coning motion. The outer edge of each color band is where the solar sail can exactly offset the error, and anywhere between the bands of matching color the error can be overcome by the solar sail. Note that the bands of errors do not actually end with the limits of this plot. They extend along the same diagonal outside of these arbitrary limits.

For comparison, the same results shown in Fig. 7.22 have been computed for orbits with a radius of 6600 km and 9900 km. These results are shown in Fig. 7.23. Notice that a solar sail with the same characteristic acceleration has the ability to counter more nodal drift at higher orbits.

This application has an interesting corollary application, which is the creation of new Sun-synchronous orbits which are not viable with only the J_2 effects. The potential for this idea is illustrated in Fig. 7.24. Even with a sail of a characteristic acceleration of 0.10 mm/s^2 , the orbit size at 10,000 km could be changed by 50 km and the Sun-synchronous property could be retained.

7.5.4.2 Launch Vehicle Injection Errors

The second application is very similar to the first. In this case, we explore how much injection error from launch can be overcome by a solar sail in this orbit executing coning motion. Fig. 7.25 shows the results here, which are similar in nature to those shown in Fig. 7.22. Here, a red box is drawn which represents the 3σ errors from a Pegasus launch vehicle. These errors encompass the published 3σ injection errors for many other launch vehicles for LEO orbits, including Delta II, Delta IV, Atlas V, Falcon I, Minotaur I and IV, and Taurus. In this application, it is shown that a solar sail with a characteristic acceleration of 0.20 mm/s^2

could basically overcome the entire 3σ envelope.

7.5.5 Conclusion

In this dissertation, we have shown that certain cheap and stable attitude motions can potentially be used to modify the solar sail's orbit in a wide variety of ways. By using these attitude motions about natural equilibrium points, the required control authority necessary is greatly decreased. Specific example of maintaining a sun-synchronous orbit was shown to be achievable and useful.

Given the promising results shown here, there are a number of future goals to extend this work. First, we would like to relax the assumptions made in the work so far. This will naturally lead to combining the attitude and orbital dynamics. In both dynamic regimes, more complicated motions will be investigated. In the attitude motion, there may be heteroclinic orbits of the normal vector around multiple equilibrium points that do not form a perfect cone in the LVLH frame. In the orbital motion, executing multiple coning motions in succession can be used to modify the orbit in almost any manner.

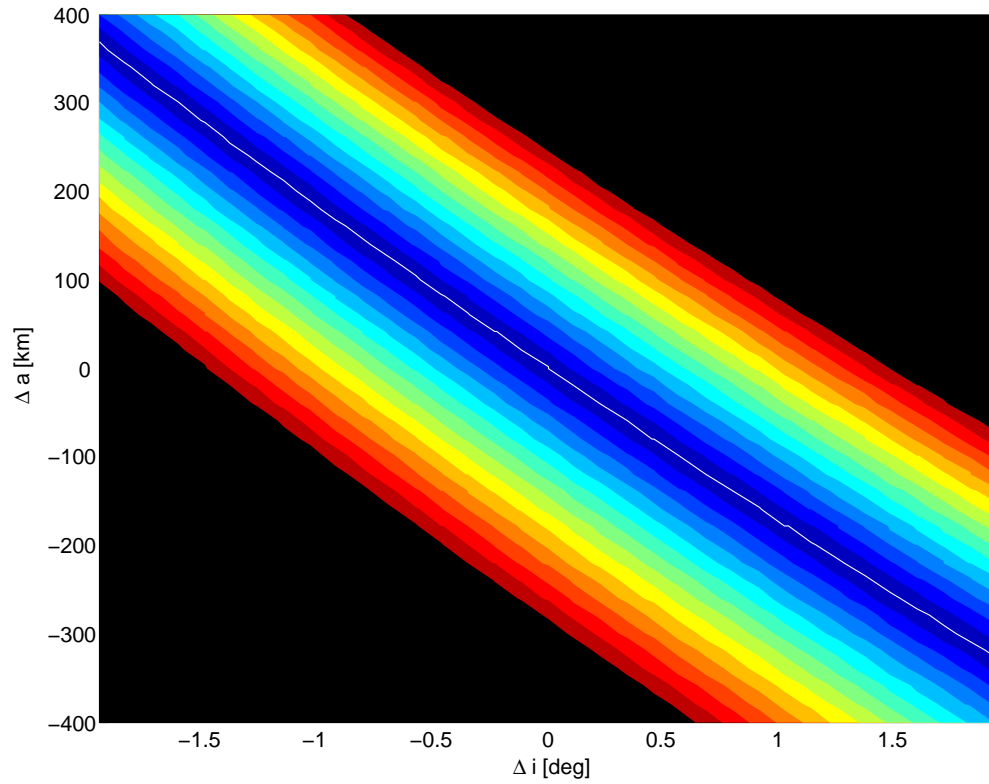


Figure 7.22: Nodal drift errors caused by off-nominal semi-major axis and inclination values that can be overcome by a solar sail with a variety of characteristic accelerations. a_c varies from 0.05 mm/s^2 (dark blue) to 0.75 mm/s^2 (dark red). The solar sail can overcome the error if it lies between the bands of the same color. The white line indicates where the semi-major axis and inclination errors offset each other. The orbit radius used to obtain these results was 8008 km.

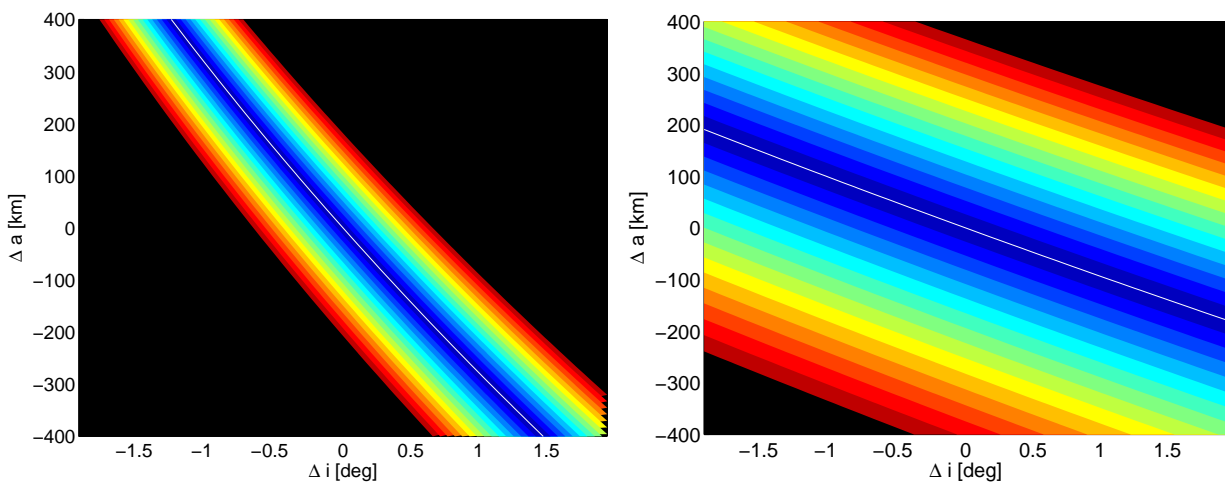


Figure 7.23: Nodal drift error plot for a 6600 km orbit (left) and a 9900 km orbit (right).

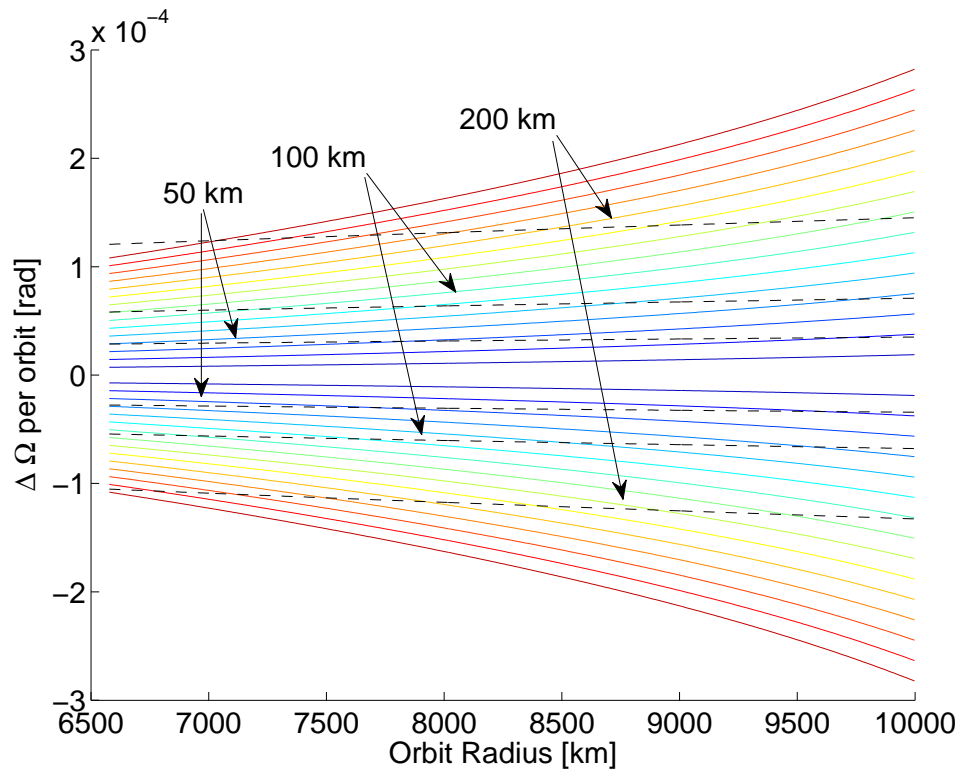


Figure 7.24: The nodal drift per orbit created for solar sails of varying characteristic accelerations over a variety of altitudes are shown as solid lines with the same color scheme as Fig. 7.22. The dotted lines represent the nodal drift that would need to be overcome for given changes in the orbit radius to keep the orbit Sun-synchronous.

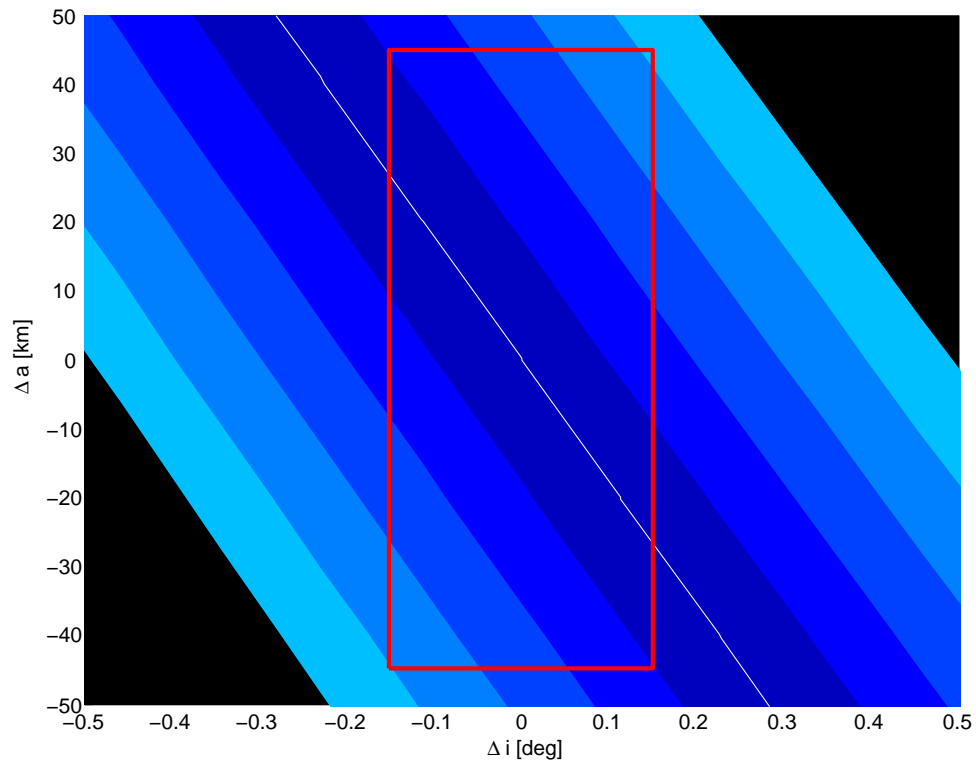


Figure 7.25: Nodal drift caused by 3σ injection errors from a Pegasus launch vehicle are drawn as a red box. Solar sails moving in coning motion can overcome errors within each color band, varying from $a_c = 0.05 - 0.25 \text{ mm/s}^2$

Chapter 8

Conclusion and Future Work

This dissertation presents a new approach to analyzing the effects of solar radiation pressure on the orbits of natural and artificial objects. The approach presented gives an analytical representation of the solar radiation pressure force which is derived from first principles of the solar radiation pressure interaction. This model bridges the gap in previous literature between the simple analytical models (e.g. the cannonball model) and the high-fidelity numerical models (based on ray-tracing techniques). This can be thought of as analogous to the role the spherical harmonics models of planetary gravity fields; an analytical representation that is much better than a point-mass model and captures the effects of high-fidelity numerical models.

Given the analytical representation for the solar radiation pressure perturbations, mathematical tools can be applied to explore the effects of this force on objects in orbit. A major complication of representing the solar radiation pressure effects is that they depend on the location of the Sun with respect to orbiting body. This is incorporated into the analytical theory through assumptions of the body's attitude motion during its orbit. Averaging theory is applied to variational equations for a convenient set of orbital elements in order to determine the short-period and secular effects under the action of solar radiation pressure.

The main contributions of this work concern the applications of this theory to binary asteroid systems, Earth orbiting spacecraft, orbital debris and solar sail spacecraft. The effect of solar radiation pressure on binary asteroid system orbit evolution had already been proposed prior to this work. Here, the detailed analytical theory has been applied to these systems which allows for determination of the evolution of a system based upon the actual physical properties of the system. The resulting predictions, which were made based on the actual shape of the binary asteroid 1999 KW4 were scaled and applied to other near-Earth

binary asteroids, can be tested by ground based observations. Finally, the analytical theory was expanded to account for the effects of J_2 and the libration of the secondary asteroid.

Application of this theory to Earth orbiting spacecraft has resulted in two main contributions. First, this theory has been able to easily accommodate the presence of the Earth's shadow. By adding a second set of Fourier coefficients depending on the shadow location, the same analytical framework can describe the orbital evolution with or without the shadow. The second contribution concerns the use of this solar radiation pressure model for orbit determination. It was shown that this model can achieve similar performance to JPL's GPS solar radiation pressure model. The contribution, however, is in the fact that the methodology given here can be applied to any spacecraft, whereas the JPL model is applicable to the GPS spacecraft only. Also, this model has analytical solutions for the orbit evolution.

The problem of orbital debris is a combination of the previous two problems as there are aspects of both natural and artificial bodies present. In the current literature the evolution of orbital debris is analyzed with the simple cannonball model. The contribution to this field made in the present analysis shows under what assumptions it is appropriate to use the cannonball model; this also reveals when it is not appropriate to use such a model.

Solar sails are subject to torques due to gravitational, aerodynamic, and solar radiation pressure forces in Earth orbit. The analysis here determines how the solar sail acceleration modifies the orbit when the sail cones naturally in the local horizontal frame due to the natural torques present. Taking advantage of these natural dynamics allows modification of the orbit while minimizing excitation of structural modes and fuel usage.

Given these contributions, there are still a number of other areas where application of this theory will lead to new results. In the study of binary asteroid evolution, there are two important extensions that should be investigated. First, an understanding of how the shape model estimation impacts the derived Fourier coefficients and therefore the orbit evolution predictions should be carried out. Second, a more detailed extension of the effect of the libration on the BYORP predictions, including actual simulation of the attitude dynamics, should be conducted. The spacecraft applications can also benefit from an extension and further study of the orbital determination applications, in particular the performance for estimating

the coefficients given an a priori model constructed from the theory given in Chapter 2. A new application of this theory is for analyzing the differential SRP forces on a formation of spacecraft given their shapes and attitude motion. In this work, the problem of orbital debris was studied only to the extent that the cannonball model was justified for certain situations. However, it may be important to extend this analysis to the cases where the cannonball model can not be used, in which case the orbital evolution can change dramatically. The study of the solar sail dynamics can be improved by extending the shape model beyond the flat, specular model used in this work. Extending the work to include a more detailed coupling of the attitudinal equations of motion will also be necessary for making accurate predictions of the sail effects. Finally, the framework presented here for studying the effects of solar radiation pressure can be used to study other perturbative effects which are periodic with the orbit such as the effect of atmospheric drag or the Earth albedo effect.

Bibliography

- [1] L. Anselmo and C. Pardini. Long-term dynamical evolution of high area-to-mass ratio debris released into high earth orbits. Acta Astronautica, 67(1-2):204–216, 2010.
- [2] V. I. Arnold. Mathematical Methods of Classical Mechanics. Springer-Verlag, second edition, 1989.
- [3] Y. E. Bar-Sever. New and improved solar radiation pressure models for gps satellites based on flight data. Technical report, Jet Propulsion Laboratory, Pasadena, CA, 1997.
- [4] Y. E. Bar-Sever and D. Kuang. New empirically derived solar radiation pressure model for global positioning system satellites. The Interplanetary Network Progress Report, 42(159):1–11, November 2004.
- [5] R. Bate, D. Mueller, and E. White. Fundamentals of Astrodynamics. Dover Publications, 1971.
- [6] Richard H. Battin. An Introduction to the Mathematics and Methods of Astrodynamics. AIAA, revised edition edition, 1999.
- [7] Srinivas Bettadpur. Grace: Product specification document. Technical Report GRACE 327-720, Center for Space Research, The University of Texas at Austin, 2007.
- [8] J. Bookless and C.R. McInnes. Dynamics and control of displaced periodic orbits using solar sail propulsion. Journal of Guidance, Control, and Dynamics, 29(3):527–537, May-June 2006.
- [9] J. Bookless and C.R. McInnes. Control of lagrange point orbits using solar sail propulsion. Acta Astronautica, 62:159–176, 2008.
- [10] W. F. Bottke et al. Asteroids III, chapter The Effect of Yarkovsky Thermal Forces on the Dynamical Evolution of Asteroids and Meteoroids. University of Arizona Press, 2003.
- [11] D. Brouwer. Solution of the problem of artificial satellite theory without drag. The Astronomical Journal, 64:378–397, 1959.
- [12] D. Brouwer and G. Clemence. Methods of Celestial Mechanics. Academic Press, New York, NY, 1961.
- [13] D. Brouwer and G. Hori. Theoretical evaluation of atmospheric drag effects in the motion of an artificial satellite. The Astronomical Journal, 66:193–225, 1961.
- [14] C.C. Chao and R. A. Gick. Long-term evolution of navigation satellite orbits: Gps/glonass/galileo. Advances in Space Research, 34:1221–1226, 2004.
- [15] J. Chen and J. Wang. Models of solar radiation pressure in the orbit determination of gps satellites. Chinese Astronomy and Astrophysics, 31:66–75, 2007.
- [16] Y. Chen, Z. Hong, C. Lin, and J. Chern. Aerodynamic and gravity gradient stabilization for microsatellites. Acta Astronautica, 46(7):491–499, 2000.

- [17] M. Cheng, J. Ries, and B. Tapley. Assessment of the solar radiation model for grace orbit determination. Advances in the Astronautical Sciences, 129:501–510, 2008.
- [18] D. G. Cook. Solar radiation pressure modeling issues for high altitude satellites. Master’s thesis, Air Force Institute of Technology, 2001.
- [19] G. E. Cook. Satellite drag coefficients. Planetary and Space Sciences, 13:929–946, 1965.
- [20] M. Čuk. Formation and destruction of small binary asteroids. The Astrophysical Journal, 659:L57–L60, 2007.
- [21] M. Čuk and J. Burns. Effects of thermal radiation on the dynamics of binary neas. Icarus, 176:418–431, 2005.
- [22] M. Čuk and D. Nesvorný. Orbital evolution of small binary asteroids. Icarus, 207:732–743, 2010.
- [23] D. A. Danielson, B. Neta, and L. W. Early. Semianalytic satellite theory (sst): Mathematical algorithms. Technical Report NPS-MA-94-001, Naval Postgraduate School, 1994.
- [24] R. Vilhena de Moraes. Non-gravitational disturbing forces. Advances in Space Research, 14(5):45–68, 1994.
- [25] A. Deprit. Canonical transformations depending on a small parameter. Celestial Mechanics, 1:12–30, 1969.
- [26] A. Deprit and A. Rom. The main problem of artificial satellite theory for small and moderate eccentricities. Celestial Mechanics, 2:166–206, 1970.
- [27] J.C. Van der Ha and V. J. Modi. Orbital perturbations and control by solar radiation forces. Journal of Spacecraft, 15(2):105–112, March-April 1978.
- [28] Eelco Doornbos. Modeling of non-gravitational forces for ers-2 and envisat. Master’s thesis, Delft Institute for Earth-Oriented Space Research, Delft University of Technology, July 2001.
- [29] E. G. Fahnestock and D. J. Scheeres. Simulation and analysis of the dynamics of binary near-earth asteroid (66391) 1999 kw4. Icarus, 194:410–435, 2008.
- [30] H. F. Fliegel and T. E. Gallini. Solar force modeling of block iir global positioning system satellites. Journal of Spacecraft and Rockets, 33(6):863–866, November-December 1996.
- [31] H. F. Fliegel, T. E. Gallini, and E. R. Swift. Global positioning system radiation force model for geodetic applications. Journal of Geophysical Research, 97(B1):559–568, January 1992.
- [32] R.L. Forward. The statite: A non-orbiting spacecraft. In Proceedings of the AIAA/ASME/SAE/ASEE 25th Joint Propulsion Conference, Malibu, CA, July 10-12 1989.
- [33] Bent Fritsche and Heiner Klinkrad. Accurate prediction of non-gravitational forces for precise orbit determination. part i: Principles of the computation of coefficients of force and torque. In Proceedings of the AIAA/AAS Astrodynamics Specialist Conference and Exhibit, number 2004-5461, Providence, RI, August 16 - 19 2004.
- [34] Bent Fritsche and Heiner Klinkrad. Accurate prediction of non-gravitational forces for precise orbit determination. part ii: Determination of perturbing forces and torques in an orbital environment. In Proceedings of the AIAA/AAS Astrodynamics Specialist Conference and Exhibit, number 2004-5462, Providence, RI, August 16 - 19 2004.
- [35] J. Fuller and R. Tolson. Improved method for estimation of spacecraft free-molecular aerodynamic properties. Journal of Spacecraft and Rockets, 46(5):938–948, September-October 2009.

- [36] B. Gladman, P. Michel, and Ch. Froeschlé. The near-earth object population. Icarus, 146:176–189, 2000.
- [37] P. Goldreich and R. Sari. Tidal evolution of rubble piles. The Astrophysical Journal, 691:54–60, 2009.
- [38] Richard Haberman. Applied Partial Differential Equations. Pearson Prentice Hall, fourth edition, 2004.
- [39] W. K. Hartmann et al. Reviewing the yarkovsky effect: New light on the delivery of stone and iron meteorites from the asteroid belt. Meteorites and Planetary Science, 34:A161–A167, 1999.
- [40] J. Hudson and D. Scheeres. Reduction of low-thrust continuous controls for trajectory dynamics. Journal of Guidance, Control, and Dynamics, 32(3):780–787, May-June 2009.
- [41] G.W. Hughes and C.R. McInnes. Solar sail hybrid trajectory optimization for non-keplerian orbit transfers. Journal of Guidance, Control, and Dynamics, 29(3):602–604, May-June 2006.
- [42] K. A. Innanen, J. Q. Zheng, S. Mikkola, and M. J. Valtonen. The kozai mechanism and the stability of planetary orbits in binary star systems. The Astronomical Journal, 113(5):1915–1919, May 1997.
- [43] JAXA. Ikaros mission webpage. <http://www.jaxa.jp/projects/sat/ikaros/index.e.html>, 2011.
- [44] M. Kaasalainen et al. Acceleration of the rotation of asteroid 1862 apollo by radiation torques. Nature, 446:420–422, 2007.
- [45] P. Knocke, J. Ries, and B. Tapley. Earth radiation pressure effects on satellites. In AIAA/AAS Astrodynamics Conference, number 88-4292-CP, pages 577–587, 1988.
- [46] J. Kouba. A simplified yaw-attitude model for eclipsing gps satellites. GPS Solutions, 13:1–12, 2009.
- [47] Yoshihide Kozai. The motion of a close earth satellite. The Astronomical Journal, 64:367–377, 1959.
- [48] Yoshihide Kozai. Second-order solution of artificial satellite theory without air drag. The Astronomical Journal, 67(7):446–461, September 1962.
- [49] V. Lappas and et. al. Microsolar sails for earth magnetotail monitoring. Journal of Spacecraft and Rockets, 44(4):840–848, July-August 2007.
- [50] D.A. Lawrence and M.S. Whorton. Solar sail dynamics and coning control in circular orbits. Journal of Guidance, Control, and Dynamics, TBD:TBD, 2009.
- [51] A. Long, J. Cappellari Jr., et al. Goddard trajectory determination system (gtlds) mathematical theory revision 1. Technical report, National Aeronautics and Space Administration, 1989.
- [52] S. C. Lowry et al. Direct detection of the asteroidal yorp effect. Science, 316:272–274, 2007.
- [53] D. Lucchesi. Reassessment of the error modelling of non-gravitational perturbations on lagesos ii and their impact in the lense-thirring determination. part i. Planetary and Space Science, 49:447–463, 2001.
- [54] K. Luu and C. Sabol. Effects of perturbations on space debris in supersynchronous storage orbits. Technical Report AFRL-VS-PS-TR-1998-1093, Air Force Research Labs, Space Vehicles Directorate, October 1998.
- [55] R. H. Lyddane. Small eccentricities or inclinations in the brouwer theory of the artificial satellite. The Astronomical Journal, 68(8):555–558, 1963.
- [56] M. Macdonald and C.R. McInnes. Analytical control laws for near-optimal geocentric solar sail transfers. Advances in the Astronautical Sciences, 109.3:2393–2411, 2001.

- [57] M. Macdonald and C.R. McInnes. Realistic earth escape strategies for solar sailing. Journal of Guidance, Control, and Dynamics, 28(2):315–320, March-April 2005.
- [58] M. Macdonald, C.R. McInnes, and B. Dachwald. Heliocentric solar sail transfers with locally optimal control laws. Journal of Spacecraft and Rockets, 44(1):273–276, January-February 2007.
- [59] J. L. Margot. Hermes as an exceptional case among binary near-earth asteroids. In Proceedings of the IAU Symposium, number S236-35, Prague, Czech Republic, 2006.
- [60] J.L. Margot et al. Binary asteroids in the near-earth object population. Science, 296:1445–1448, 2002.
- [61] J. A. Marshall and S. B. Luthcke. Modeling radiation forces acting on topex/poseidon for precision orbit determination. Journal of Spacecraft and Rockets, 31(1):99–105, January-February 1994.
- [62] Colin R. McInnes. Solar Sailing. Praxis Publishing, 1999.
- [63] C.R. McInnes, M. Macdonald, V. Angelopolous, and D. Alexander. Geosail: Exploring the geomagnetic tail using a small solar sail. Journal of Spacecraft and Rockets, 38(4):622–629, July-August 2001.
- [64] Jay McMahon and D. J. Scheeres. Detailed prediction for the byorp effect on binary near-earth asteroid (66391) 1999 kw4 and implications for the binary population. Icarus, 209:494–509, 2010.
- [65] Jay McMahon and Daniel Scheeres. Secular orbit variation due to solar radiation effects: A detailed model for byorp. Celestial Mechanics and Dynamical Astronomy, 106:261–300, 2010.
- [66] Jay McMahon and Daniel J. Scheeres. A new solar radiation pressure force model for navigation. Journal of Guidance Control and Dynamics, In press, June 2010.
- [67] S. Ferraz Mello. Analytical study of the earth’s shadowing effects on satellite orbits. Celestial Mechanics, 5:80–101, 1972.
- [68] G. Mengali and A. Quarta. Near-optimal solar-sail orbit-raising from low earth orbit. Journal of Spacecraft and Rockets, 42(5):954–958, September-October 2005.
- [69] V. Modi and K. Pande. On the periodic solutions and resonance of spinning satellites in near circular orbits. Celestial Mechanics, 11:195–212, 1975.
- [70] V. J. Modi and S. K. Shrivastava. Satellite attitude dynamics and control in presence of environmental torques - a survey. In AIAA/AAS Astrodynamics Conference, number AIAA-82-1414, 1982.
- [71] S. Mohan, J. Breakwell, and B. Lange. Interaction between attitude libration and orbital motion of a rigid body in a near keplerian orbit of low eccentricity. Celestial Mechanics, 5:157–173, 1972.
- [72] A. Morbidelli et al. Asteroids III, chapter Origin and Evolution of Near-Earth Objects. University of Arizona Press, 2003.
- [73] NEODyS. Neodys website. <http://unicorn.eis.uva.es/neodys/index.php?pc=1.1.6&n=66391>, 2010.
- [74] Isaac Newton. Newton’s Principia. Daniel Adee, 45 Liberty Street, New York, NY, 1846.
- [75] J. A. O’Keefe. Tektites and Their Origin. Elsevier, 1976.
- [76] S. J. Ostro et al. Radar imaging of binary near-earth asteroid (66391) 1999 kw4. Science, 314:1276–1280, November 2006.
- [77] S.J. Paddack. Rotational bursting of small celestial bodies: Effects of radiation pressure. Journal of Geophysical Research, 74(17):4379–4381, 1969.
- [78] P. Pravec et al. Photometric survey of binary near-earth asteroids. Icarus, 181:63–93, 2006.

- [79] V. V. Radzievskii. A mechanism for the disintegration of asteroids and meteorites. Doklady Akademii Nauk SSSR, 97:49–52, 1954.
- [80] H. Rim et al. Radiation pressure modeling for icesat precision orbit determination. In Proceedings of the AIAA/AAS Astrodynamics Specialist Conference and Exhibit, number 2006-6666, Keystone, CO, August 2006.
- [81] L. Rios-Reyes and D. J. Scheeres. Generalized model for solar sails. Journal of Spacecraft and Rockets, 42(1):182–185, January-February 2005.
- [82] L. Rios-Reyes and D. J. Scheeres. Solar-sail navigation: Estimation of force, moments, and optical parameters. Journal of Guidance, Control, and Dynamics, 30(3):660–668, May-June 2007.
- [83] E. A. Roth. The gaussian form of the variation-of-parameter equations formulated in equinoctial elements - applications: Airdrag and radiation pressure. Acta Astronautica, 12(10):719–730, 1985.
- [84] A. E. Roy. Orbital Motion. Taylor and Francis, 4th edition, 2004.
- [85] D. P. Rubincam. Lagesos orbit decay due to infrared radiation from earth. Journal of Geophysical Research, 92(B2):1287–1294, 1987.
- [86] D. P. Rubincam. Yarkovsky thermal drag on lagesos. Journal of Geophysical Research, 93(B11):13805–13810, November 1988.
- [87] D. P. Rubincam. Asteroid orbit evolution due to thermal drag. Journal of Geophysical Research, 100(E1):1585–1594, January 1995.
- [88] D. P. Rubincam. Radiative spin-up and spin-down of small asteroids. Icarus, 148:2–11, 2000.
- [89] J. A. Sanders, F. Verhulst, and J. Murdock. Averaging Methods in Nonlinear Dynamical Systems, volume 59 of Applied Mathematical Sciences. Springer, 2nd edition, 2007.
- [90] N. Sands. Escape from planetary gravity fields by use of solar sails. ARS Journal, 31:527–531, 1961.
- [91] Hanspeter Schaub and John Junkins. Analytical Mechanics of Space Systems. AIAA Education. AIAA, 2nd edition, 2009.
- [92] D. J. Scheeres. The dynamical evolution of uniformly rotating asteroids subject to yorp. Icarus, 188:430–450, 2007.
- [93] D. J. Scheeres. The dynamics of neo binary asteroids. In A. Milani, G. Valsecchi, and D. Vokrouhlicky, editors, Near Earth Objects, our Celestial Neighbors: Opportunity and Risk, number 236 in Proceedings of the IAU Symposium, 2007.
- [94] D. J. Scheeres. Rotational fission of contact binary asteroids. Icarus, 189:370–385, 2007.
- [95] D. J. Scheeres. Stability of the planar full 2-body problem. Celestial Mechanics and Dynamical Astronomy, 104:103–128, 2009.
- [96] D. J. Scheeres, M. Abe, M. Yoshikawa, R. Nakamura, R. Gaskell, and P. Abell. The effect of yorp on itokawa. Icarus, 188:425–429, 2007.
- [97] D. J. Scheeres, M. D. Guman, and B. F. Villac. Stability analysis of planetary satellite orbiters: Application to the europa orbiter. Journal of Guidance, Control, and Dynamics, 24:778–787, July-August 2001.
- [98] D. J. Scheeres and S. Mirrahimi. Rotational dynamics of a solar system body under solar radiation torques. Celestial Mechanics and Dynamical Astronomy, 101:69–103, 2008.

- [99] D. J. Scheeres, A. Rosengren, and J. McMahon. The dynamics of high area-to-mass ratio objects in earth orbit: The effect of solar radiation pressure. In Proceedings of the AAS/AIAA Space Flight Mechanics Meeting, number AAS 11-178, 2011.
- [100] D.J. Scheeres. Satellite dynamics about small bodies: Averaged solar radiation pressure effects. Journal of the Astronautical Sciences, 47(1):25–46, 1999.
- [101] T. Schildknecht, R. Musci, and T. Flohrer. Properties of the high area-to-mass ratio space debris population at high altitudes. Advances in Space Research, 41(7):1039–1045, 2008.
- [102] T.A. Springer, G. Beutler, and M. Rothacher. A new solar radiation pressure model for gps satellites. GPS Solutions, 2(3):50–62, 1999.
- [103] T. S. Statler. Extreme sensitivity of the yorp effect to small-scale topography. Icarus, 202:502–513, 2009.
- [104] P.V. Subba Rao and R.V. Ramanan. Optimal three-dimensional heliocentric solar-sail rendezvous transfer trajectories. Acta Astronautica, 29(5):341–345, 1993.
- [105] E. Sutton. Normalized force coefficients for satellites with elongated shapes. Journal of Spacecraft and Rockets, 46(1):112–116, January-February 2009.
- [106] M.A. Swartwout. Earth escape using a slowly rotating, doubly reflective sail. Journal of Guidance, Control, and Dynamics, 28(2):374–377, March-April 2005.
- [107] L. Taff. Celestial Mechanics; A Computational Guide for the Practitioner. John Wiley and Sons, New York, NY, 1985.
- [108] P. A. Taylor. Preferential production of contact binary asteroids with components of similar mass via angular momentum loss. In Bulletin of the American Astronomical Society, volume 41, page 905. American Astronomical Society, 2009.
- [109] P. A. Taylor et al. Spin rate of asteroid (54509) 2000 ph5 increasing due to the yorp effect. Science, 316:274–277, 2007.
- [110] S. Valk, A. Lemaître, and L. Anselmo. Analytical and semi-analytical investigations of geosynchronous space debris with high area-to-mass ratios. Advances in Space Research, 41:1077–1090, 2008.
- [111] D. Vallado. Fundamentals of Astrodynamics and Applications. Microcosm Press, 2nd edition, 2001.
- [112] D. Čapek and D. Vokrouhlický. The yorp effect with finite thermal conductivity. Icarus, 172:526–536, 2004.
- [113] D. Vokrouhlicky, P. Farinella, and F. Mignard. Solar radiation pressure perturbations for earth satellites. part i: A complete theory including penumbra transitions. Astronomy and Astrophysics, 280:295–312, 1993.
- [114] D. Vokrouhlicky, P. Farinella, and F. Mignard. Solar radiation pressure perturbations for earth satellites. part ii: An approximate method to model penumbra transitions and their long-term orbital effects on lageos. Astronomy and Astrophysics, 285:333–343, 1994.
- [115] D. Vokrouhlicky, P. Farinella, and F. Mignard. Solar radiation pressure perturbations for earth satellites. part iii: Global atmospheric phenomena and the albedo effect. Astronomy and Astrophysics, 290:324–334, 1994.
- [116] D. Vokrouhlicky, P. Farinella, and F. Mignard. Solar radiation pressure perturbations for earth satellites. part iv: Effects of the earth’s polar flattening of the shadow structure and the penumbra transitions. Astronomy and Astrophysics, 307:635–644, 1996.

- [117] K. Walsh and D. Richardson. Binary near-earth asteroid formation: Rubble pile model of tidal disruptions. Icarus, 180:201–216, 2006.
- [118] K. Walsh and D. Richardson. A steady-state model of nea binaries formed by tidal disruption of gravitational aggregates. Icarus, 193:553–566, 2008.
- [119] L. Wang, P. Krishnaprasad, and J. Maddocks. Hamiltonian dynamics of a rigid body in a central gravitational field. Celestial Mechanics and Dynamical Astronomy, 50:349–386, 1991.
- [120] T.J. Waters and C.R. McInnes. Periodic orbits above the ecliptic in the solar-sail restricted three-body problem. Journal of Guidance, Control, and Dynamics, 30(3):687–693, May-June 2007.
- [121] T.J. Waters and C.R. McInnes. Invariant manifolds and orbit control in the solar sail three-body problem. Journal of Guidance, Control, and Dynamics, 31(3):554–562, May-June 2008.
- [122] B. Wie. Solar sail attitude control and dynamics, part 1. Journal of Guidance, Control, and Dynamics, 27(4):526–535, July-August 2004.
- [123] B. Wie. Solar sail attitude control and dynamics, part 2. Journal of Guidance, Control, and Dynamics, 27(4):536–544, July-August 2004.
- [124] Marek Ziebart. Generalized analytical solar radiation pressure modeling algorithm for spacecraft of complex shape. Journal of Spacecraft and Rockets, 41(5):840–848, September-October 2004.

Appendix A

Mathematical Relationships

A.1 Trigonometric Functions

There are a number of trigonometric relationships which are used repeatedly in this article. The angle sum and difference identities are given by,

$$\sin(\alpha \pm \beta) = \sin \alpha \cos \beta \pm \cos \alpha \sin \beta \quad (\text{A.1})$$

$$\cos(\alpha \pm \beta) = \cos \alpha \cos \beta \mp \sin \alpha \sin \beta \quad (\text{A.2})$$

The product-to-sum identities are,

$$\cos \alpha \cos \beta = \frac{\cos(\alpha - \beta) + \cos(\alpha + \beta)}{2} \quad (\text{A.3})$$

$$\sin \alpha \sin \beta = \frac{\cos(\alpha - \beta) - \cos(\alpha + \beta)}{2} \quad (\text{A.4})$$

$$\cos \alpha \sin \beta = \frac{\sin(\alpha + \beta) - \sin(\alpha - \beta)}{2} \quad (\text{A.5})$$

$$\sin \alpha \cos \beta = \frac{\sin(\alpha + \beta) + \sin(\alpha - \beta)}{2} \quad (\text{A.6})$$

The integrals of cosine and sine functions over the range 0 to 2π is,

$$\int_0^{2\pi} \cos(nx) dx = 0 \quad (\text{A.7})$$

$$\int_0^{2\pi} \sin(nx) dx = 0 \quad (\text{A.8})$$

where $n \in \{x|x \in \mathbb{Z}, x \geq 1\}$.

The orthogonality relationships for the sine and cosine functions are,

$$\int_0^{2\pi} \cos(nx) \cos(mx) dx = \pi \delta_{nm} \quad (\text{A.9})$$

$$\int_0^{2\pi} \sin(nx) \sin(mx) dx = \pi \delta_{nm} \quad (\text{A.10})$$

$$\int_0^{2\pi} \cos(nx) \sin(mx) dx = 0 \quad (\text{A.11})$$

where δ_{nm} is the Kronecker delta, and $m \in \{x|x \in \mathbb{Z}, x \geq 1\}$. These can be derived through application of Eqs. (A.3) - (A.8).

A.2 Fourier Series

A Fourier series is an infinite series used to represent a function, $f(x)$, which is periodic over the interval $-L \leq x \leq L$ [38] as ,

$$f(x) = A_0 + \sum_{n=1}^{\infty} \left[A_n \cos\left(\frac{n\pi x}{L}\right) + B_n \sin\left(\frac{n\pi x}{L}\right) \right] \quad (\text{A.12})$$

where the Fourier coefficients are defined as,

$$A_0 = \frac{1}{2L} \int_{-L}^L f(x) dx \quad (\text{A.13})$$

$$A_n = \frac{1}{L} \int_{-L}^L f(x) \cos\left(\frac{n\pi x}{L}\right) dx \quad (\text{A.14})$$

$$B_n = \frac{1}{L} \int_{-L}^L f(x) \sin\left(\frac{n\pi x}{L}\right) dx \quad (\text{A.15})$$

The Fourier coefficients are derived through application of the trigonometric orthogonality conditions, Eqs. (A.9) - (A.11).

A.3 Bessel Functions

A Bessel function of the first kind can be defined as a series by the following equation [12], [107]

$$J_s(x) = \sum_{\beta=0}^{\infty} (-1)^\beta \frac{(x/2)^{s+2\beta}}{(s+\beta)! \beta!} \quad (\text{A.16})$$

The partial derivative of a Bessel function with respect to its argument ($J'_s(x) = \partial J_s(x)/\partial x$) can be defined in three equivalent ways,

$$J'_s(x) = \frac{1}{2}[J_{s-1}(x) - J_{s+1}(x)] \quad (\text{A.17})$$

$$J'_s(x) = J_{s-1}(x) - \frac{s}{x}J_s(x) \quad (\text{A.18})$$

$$J'_s(x) = \frac{s}{x}J_s(x) - J_{s+1}(x) \quad (\text{A.19})$$

due to the fact that

$$sJ_s(x) = \frac{x}{2}[J_{s-1}(x) + J_{s+1}(x)] \quad (\text{A.20})$$

It is worth pointing out here that in this work, the specific forms used are typically $J_n(ne)$, but the partials used are take with respect to e only as,

$$J'_n(ne) = \frac{\partial J_n(ne)}{\partial e} \quad (\text{A.21})$$

and **not** with respect to the full argument ne . This is important because they are not the same, and are in fact related by

$$\frac{\partial J_n(ne)}{\partial e} = n \frac{\partial J_n(ne)}{\partial ne} \quad (\text{A.22})$$